Title
Thermodynamics and Dynamics of Block Copolymer Electrolytes

Author
loo, whitney

Publication Date
2020

Peer reviewed|Thesis/dissertation

Thermodynamics and Dynamics of Block Copolymer Electrolytes

By
Whitney Loo

A dissertation submitted in partial satisfaction of the

requirements for the degree of

Doctor of Philosophy

in

Chemical Engineering

in the

Graduate Division

of the

University of California, Berkeley

Committee in charge:

Professor Nitash P. Balsara, Chair
Professor Bryan D. McCloskey
Professor Kristin Persson

Summer 2020

Thermodynamics and Dynamics of Block Copolymer Electrolytes

Abstract

Thermodynamics and Dynamics of Block Copolymer Electrolytes

by

Whitney Loo

Doctor of Philosophy in Chemical Engineering

University of California, Berkeley

Professor Nitash P. Balsara, Chair

It is becoming increasingly clear that the next generation of rechargeable batteries for the emerging clean energy landscape will require electrolytes that are fundamentally different from those used in today's lithium-ion batteries. In addition, it has been shown that the most promising approach to significantly increase the energy density of rechargeable batteries is through the implementation of the Li metal anode. Current electrolytes consist of mixtures of organic carbonates and a lithium salt. They pose safety concerns due to their flammability and are also incompatible with Li metal. Polymer electrolytes, which are mixtures of polymers and a lithium salt, are both less flammable than the organic solvents used currently and have been shown to be compatible with Li metal. Although linear polymers are able to exert some stress on the battery electrodes, which is essential to enabling rechargeable batteries with Li metal anodes, their viscoelastic nature prevents them from enduring stress in the long-time limit. One approach to improving the mechanical properties of polymer electrolytes is to use microphase separated block copolymers, which allows for decoupling of the ionically conducting and mechanically reinforcing properties.

The phase behavior of block copolymers, wherein two chemically distinct homopolymer chains are covalently bound, is dependent on two properties: segregation strength, χN, and copolymer composition, f_A. Segregation strength is the product of the Flory-Huggins interaction parameter, χ, and the overall chain length, N; it combines both enthalpic contributions from the monomer-monomer interactions, as well as entropic contributions which are directly related to chain length through the configurational entropy. The copolymer composition is measured in terms of the volume fraction of "block A", f_A, and dictates the degree of curvature needed to minimize the areal contact between the unlike phases. For a given copolymer composition, when a copolymer has a segregation strength less than $(\chi N)_{odt}$, the copolymer melt will form a homogeneous disordered mixture. When the same copolymer has $\chi N \geq (\chi N)_{odt}$, the copolymer will microphase separate into an ordered morphology such as body center cubic spheres, hexagonally packed cylinders, gyroid phases, or lamellae. The addition of salt to block copolymers allows them to conduct ions, but significantly alters their thermodynamics and resulting phase behavior. It is well-known for symmetric block copolymers, wherein the volume fractions of the two blocks are equal to 0.5, that

the addition of salt will increase the segregation strength of the copolymer. For example, a copolymer that forms a disordered morphology in the salt-free state will undergo a disorder-to-order transition and form an ordered lamellar phase once a critical salt concentration is reached. In the simplest case, the increase in χ is linear with respect to salt concentration.

It is well-known that ion transport in polymer electrolytes is linked to the segmental motion of the polymer backbone. At short times, the polymer repeat units can be modeled as beads linked together by springs that are characterized by a friction coefficient, ζ. Motion in this regime is known as Rouse dynamics. At longer times, the motion of a segment of a polymer chain is influenced by the presence of neighboring chains that form entanglement constraints represented by tubes of diameter, *d.* As time progresses, the polymer chain must reptate through the entanglement constraints until it is fully free of its tube and can undergo self-diffusion. The motion of the polymer chain while it is entirely or partially constrained by its tube is known as reptation. Previous studies of dynamics in the Rouse regime have shown that the monomeric friction coefficient decreases as salt concentration increases in polymer electrolytes due to the coordination between the polymer backbone and the cations. In fact, for some polymer electrolytes, the ionic conductivity can be explained entirely by the segmental motion of the polymer. However, no studies have been conducted on polymer electrolytes at time-scales that correlate with reptation.

The block copolymer electrolyte used in this research is a well-studied model system: polystyrene-*block*-poly(ethylene oxide) mixed with lithium bis(trifluoromethanesulfonyl) imide (LiTFSI). SEO/LiTFSI was chosen as the model system because it is well-known that the Li salt preferentially segregates into the poly(ethylene oxide) (PEO) domains and the electrochemical properties of PEO/LiTFSI have been fully characterized. The objective of this dissertation is to develop a molecular-level understanding of the effect of salt on block copolymer self-assembly, thermodynamics, and dynamics. Specifically, I will use theories developed for salt-free polymer systems and apply them to data collected on block copolymer electrolytes to determine how the presence of salt changes polymer behavior. In cases where the original theories cannot explain the new data, I will derive new theories to describe the observed phenomenon.

In order to conduct these studies, a library of SEO copolymers with precise molecular weights and a wide range of copolymer compositions was synthesized. The first section describes the methods used to synthesize the SEO copolymers with precise molecular weights and compositions and low polydispersities.

The research in this dissertation covers a large area of polymer science; therefore, several different experimental techniques were used. Coincidentally, all experimental techniques were centered around scattering applications of both X-rays and neutrons. The second section provides an introduction to the fundamentals of scattering as well as a brief review on the specific techniques used in these studies.

The phase behavior of SEO/LiTFSI was determined using small angle X-ray scattering (SAXS). We studied the effect of salt concentration, molecular weight, copolymer composition, and

temperature on the morphology of SEO/LiTFSI in sections four and five. In SEO copolymers with a majority polystyrene phase, the addition of salt induced the formation of ordered morphologies. However, unique phase behavior was seen in one copolymer, with a PEO volume fraction, f_{EO}, of 0.20. In this sample, a reentrant phase transition was found such that the disordered copolymer first formed an ordered morphology, followed by a disordered morphology, followed by a different ordered morphology with increasing salt concentration. The first ordered morphology seen at a low salt concentration was a novel type of coexistence wherein two distinct lattices of the same lattice type was observed. The nature of this type of coexistence was further probed with electron tomography to visualize the lattice structure and resonant soft X-ray scattering (RSoXS) to quantify the volume of salt in each lattice.

The goal of section five was to use the morphology data gathered from the SAXS experiments and assemble large experimental datasets of the phase behavior of SEO/LiTFSI. For simplicity, the phase diagrams were constructed at a single temperature of 100 °C. A simple framework based upon of mean-field theory developed for salt-free block copolymers was used to create a phase diagram plotting copolymer morphology as a function of χN and the volume fraction of the salt-containing phase, $f_{EO,salt}$. It was found that the phase behavior of SEO/LiTFSI is qualitatively similar to that of salt-free block copolymer systems. In addition, the effect of copolymer composition and salt concentration was examined on the domain spacing of SEO mixed with two different Li salts. Expressions for the domain spacing as a function of copolymer chain length, composition and salt concentration were developed for both the weak ($\chi N \leq 10$) and strong segregation regimes ($\chi N > 10$).

The following section focuses on the quantification of the thermodynamics of SEO/LiTFSI. Through application of Leibler's Random Phase Approximation, the Flory-Huggins interaction parameter of the neat, $\chi_{0,SC}$, and salt-containing, $\chi_{eff,SC}$, SEO copolymers were measured. An expression for $\chi_{eff,SC}$ was developed as a function of N, f_{EO} and salt concentration. It was then used in conjunction with mean-field theory to calculate the critical chain length for ordering, N_{crit}, as a function of copolymer composition and salt concentration. Two regimes of phase behavior emerged: at $f_{EO} > 0.27$, the addition of salt stabilizes the ordered phase and at $f_{EO} < 0.27$, the addition of salt stabilizes the disordered phase. The copolymer composition wherein segregation is independent of salt concentration ($f_{EO} = 0.27$) was termed the "isotaksis point" and simple theoretical model to predict this composition was developed.

The preceding sections focused on the effect of salt on the morphology of the block copolymer electrolytes, which corresponds to length-scales on the order of magnitude of the domain spacing of the microphases, ~10 nm. The effect of salt concentration on the polymer conformation of the corresponding homopolymer electrolyte, PEO/LiTFSI, was determined using small angle neutron scattering (SANS), which corresponds to length-scales less than 1 nm. Kratky analysis of the SANS profiles was used to determine the statistical segment length as a function of salt concentration. All parameters in the analysis were determined independently. It was found that the effect of salt concentration in non-monotonic: at low salt concentrations, the chain sizes decreases before reaching a minimum at intermediate salt concentrations and then increasing at higher salt

concentrations. This relationship is hypothesized to be related to the preferred environment of Li ions within PEO where each Li ion prefers to be coordinated by six ether oxygens. As salt concentration increases, the ether oxygens become saturated with Li ions, which are hypothesized to lead to the formation of ion clusters, which could increase the chain dimensions. Additional SANS studies were used to probe the nature of the ion clusters and found that the clusters had a characteristic size of 0.6 nm.

The final section of this dissertation focuses on the effect of salt concentration on the polymer chain dynamics of SEO/LiTFSI. Neutron spin echo (NSE) spectroscopy was used to measure the segmental dynamics in the Rouse regime ($t \leq 10$ ns) and the polymer chain dynamics in the reptation regime ($t \geq 50$ ns). In both regimes, the dynamics slow down as salt concentration increases. This is quantified through an increase in monomer friction seen at low times and a decrease in tube diameter seen at longer times. The NSE results were used to calculate a normalized longest molecular relaxation time and it was found that block copolymers will flow more slowly with increasing salt concentration. This is important in a battery operating at high current wherein the diffusion of salt ions in one direction must induce diffusion of polymer chains in the opposite direction.

Table of Contents

List of Figures

List of Tables

Acknowledgements

I would like to acknowledge the various funding sources that have supported the research presented in this dissertation. Primary funding for this work was provided by the National Science Foundation through Award DMR-1505444 as well as from the Joint Center for Energy Storage Research (JCESR), an Energy Innovation Hub funded by the U.S. Department of Energy (DOE), Office of Science, Basic Energy sciences (BES), under Contract No. DEAC02-06CH11357. A majority of the research presented in this dissertation was conducted at various User Facilities across the country. Work at the Advanced Light Source, which is a DOE Office of Science User Facility, was supported by Contract No. DE-AC02- 05CH11231. Work at the Stanford Synchrotron Radiation Light Source, a user facility at SLAC National Accelerator Laboratory, was supported by the U.S. Department of Energy, Office of Science, Office of Basic Energy Sciences under Contract No. DE-AC02-76SF00515. The National Institute of Standards and Technology, U.S. Department of Commerce provided access to the neutron research facilities used in this work. Access to NGB-30m as well as the NGA-NSE was provided by the Center for High Resolution Neutron Scattering, a partnership between the National Institute of Standards and Technology and the National Science Foundation under Agreement No. DMR-1508249. In addition, my tuition and stipend has been supported by funding from the National Science Foundation Graduate Student Research Fellowship DGE-1106400.

Now on to the less technical acknowledgements.

First, I would like to thank my family for their unconditional love and support. Even though they are all doctors, getting a PhD is a foreign experience to them. Thank you for learning about grad school and listening to my constant complaints about synthesis and beamtime. We are now a family of Doctors. Mom, you are my first and biggest role model. Growing up, I watched you run an independent medical practice while never missing a school pick-up. When you told me that “I could be anything I wanted when I grew up”, I believed you because I saw you do it every day. Thank you, Dad, for being my best friend. My sister, Megan, you are my biggest cheerleader. I hope you realize that I am also your biggest cheerleader as you become an amazing cardiothoracic surgeon. Mimi, you are my chosen family and I am eternally grateful for your love and support over the past nine years. I wouldn’t have survived MIT without you, so thank you for helping me get to and get through Berkeley. Thank you to my partner, Elliot, for always being by my side with snacks.

Next, I want to acknowledge the Balsara Lab. The Balsara Lab is an amazing environment to grow as an individual and a scientist. The support we provide each other is infinite and unwavering. I believe that the productivity of the group is a reflection of how much we care for each other as people and scientists.

To my enemy, synthesis partner and scallop, Jackie, thank you. I cannot imagine enduring graduate school without you by my side every step of the way. From late nights on the vacuum line to even later nights at the beamline, I knew that you had my back every single day. Looking back, it’s easy to see everything you taught me. Today, I am more patient, less reckless and more thoughtful

because of you. Thank you for being patient with my lack of patience. Thank you for not getting mad at me when I yelled at you. You are an amazing scientist and an even more amazing person. I cannot wait to see all you accomplish.

Deep, I am so amazed by the scientist you have become over the past five years. Honestly, I think today you are just as excited by fundamental science as I am. Your continuous commitment to work-life balance throughout graduate school inspired me. Without your example, I would have never pursued teaching yoga and never set boundaries. Without your example, I don't think I would have ever pulled myself out of the over-worked induced depression that I found myself in at the start of graduate school. Thank you.

Mike, thank you for never giving up on me. From our handicapped days to late nights at 7.3.3, I have thoroughly enjoyed working with you and getting to know you outside of lab. Never stop keeping Nitash in check at group meeting and going for ski jumps you know you can't land. Your confidence inspires me. Beamtime with Gumi was always a highlight. Your positivity was a much-needed light during the darkness of graduate school, so thank you. I am continuously impressed by your ferocity for both scientific discovery and life.

Thank you, Lorena, for being my Tan Hall buddy. Our daily lunch conversations were a highlight of my day. Your commitment to the Balsara Lab is inspiring. There was a time when I didn't think that we could be friends, and now I can't imagine my life without you. This is a reflection of honest work and communication from both of us. Thank you for not giving up on the lab and on me. Kevin, I am so glad I got to spend some quality time with you at NIST. You are one the brightest people I have ever met. I hope you continue to open up and let people in because you have so much to share with others.

Alec, Neel, and Zach: thank you for maintaining the Balsara Lab spirit. Your work hard, play hard attitude continuously reminds me that there is so much more to life than research. I know the Balsara Lab is in good hands with you three. Darby and Morgan: I wish we got to spend more time together, but the pandemic literally kept us apart. I am already impressed with the progress you have both made. Your tenacity will continue to serve you well throughout graduate school.

Professor Hee Jeung, thank you for being my first mentor in graduate school. You took valuable time away from your own projects to train Jackie and I, two good-for-nothing first years, on the vacuum line. Your selflessness is unmatched, and I know you will always put your students before yourself. They are lucky to have you. Kim, you brought me NIST and introduced me to neutrons. That first trip to NCNR drastically changed the trajectory of graduate school, and possibly my career. Thank you for taking me under your wing and letting me crash your beamtime. To the rest of the Balsara Lab postdocs, past and present, David, Didier, Irune, Louise, Mahesh, Saheli, Xiopeng and Youngwoo, thank you for being leaders in the Balsara Lab. Without your guidance and expertise, the graduate students would never be able to get anything done. Each of you brought leadership and scientific excellent to the lab and then shared it openly.

To the previous generation of Balsara Lab graduate students, thank you for creating an environment for future students to thrive in. Jacob, thank you for being a lifelong mentor. I am so happy that we still talk about science regularly despite being very far apart. Chaeyoung, I am so glad our friendship continued and deepened after graduate school and I am so proud of everything you have accomplished with Sugarlogix. Ksenia, I am so happy we have remained close friends after you graduated. You are my favorite adventure buddy and I cannot wait for a lifetime of adventures together. Mahati, Katherine, Kevin, Adriana, Alex, Doug, Rita and Danielle: thank you for being examples of what senior graduate students should be. I only hope that I have treated Morgan and Darby half as well as you treated us.

I would like to thank all of the beamline and instrument scientists I had the opportunity to work with during my graduate studies. Thank you, Eric and Chenhui from 7.3.3., Cheng, Isvar, and Greg from 11.0.1.2, and Chris and Tim from 1-5 for the X-ray expertise. I learned so much from running independent experiments at your beamlines. I would also like to thank all of the instrument and staff scientists I got to meet and work with at NCNR at NIST. NCNR is one of the most special places for science. Every office door is open, and everyone is willing to help out a lonely user. Thank you, Antonio, Paul, Susana, Madhu, and Michi for helping me run successful experiments. I look forward to working with you all in the future.

Congratulations to the Department of Chemical and Biomolecular Engineering UC Berkeley incoming class of 2015. Thank you for becoming my family over the last five years. From post-quals celebrations to trips to Mexico, I am so grateful that we celebrated all of the victories of grad school together. I am excited to continue to celebrate life's victories with all of you. Thank you to the senior students, especially Kyle and Kristen, for the much-needed coffee and lunch breaks as well as all of the scientific and grad school-related advice.

I want to thank the amazing group of strong women I met at Corepower Yoga including Lilla, DeShauna, Carolyn, Sharon and Leslie. Thank you for creating a space for me to escape the pressures of graduate school. Thank you, for reminding me that life has more to offer than what can be discovered in a lab. Teaching yoga reignited my passion for teaching when I desperately needed it and now as I embark on a journey towards becoming a lifelong teacher, I will keep the times we shared in the studio close to my heart for when I need some inspiration.

Finally, Nitash, thank you for being my mentor over the past five years. You let me dive into the deep end of polymer thermodynamics and somehow, I figured out how to swim. Thank you being an example of scientific integrity and sharing my love for fundamental science. It was a constant reassurance to know that you thought my work was interesting, even when the rest of the group, including myself at times, did not. Thank you for sending me to conferences early. Those experiences helped shape my path towards pursuing an academic career. You taught me not only how to be an effective researcher and scientific writer, but also how to be a mentor. Never once did you put my research output over my well-being and I always appreciated your candor and ability to admit your own mistakes. It was a pleasure to be your graduate student and I look forward to becoming your colleague in the polymer physics community in the future.

1. Introduction

Significant improvements in energy storage technology are required in order to make the transition from a fossil-fuel based economy to one based on renewable energy sources.[1] One strategy for achieving technology improvements, in both increased energy density as well as increased battery safety, is the development and implementation of electrolytes that are fundamentally different from those used in today's lithium-ion batteries.[2–4] Current electrolytes in lithium ion batteries are mixtures of cyclic and linear carbonates and a lithium salt. Polymer electrolytes, which are mixtures of polymers and a lithium salt, have the potential to improve battery safety, as they are less flammable than organic electrolytes, and can enable the use of Li metal anodes, which have higher energy densities than those used currently.[5,6] The goal of the research presented in this dissertation is the development of a molecular-level understanding of the thermodynamics and dynamics of polymer electrolytes to aid in the design of next-generation solid polymer-based-battery electrolytes.

1.1 Solid Polymer Electrolytes

The field of polymer electrolytes began in 1973 after Fenton, Parker and Wright published the first account of alkali metal ions being solvated by dry poly(ethylene oxide) (PEO).[7] In 1979, Armand and coworkers showed that these ion/polymer complexes could conduct ions and be used as battery electrolytes due to the development of highly delocalized salts, such as lithium bis(trifluoromethanesulfonyl) imide (LiTFSI).[8,9] It was also found that polymer electrolytes were stable against Li metal,[2] allowing for use of the Li metal anode, a promising approach to significantly increase the energy density of rechargeable batteries.[10,11] Since then, there has been considerable interest in understanding the ion transport mechanisms and structure of PEO-based electrolyte systems.[12,13] However, many challenges, such as low ionic conductivity at room temperatures as well as the formation of lithium dendrites, remain to be solved, which has prohibited polymer-electrolyte-based Li metal batteries from entering large-scale commercial markets.

The most widely studied polymer electrolyte system is PEO/LiTFSI. Molecular dynamics simulations have shown that the preferred conformation is the coordination of one Li ion to six ether oxygens and that each Li ion is solvated by at most two PEO chains.[14–16] This preferred coordination environment is thought to lead to the high ionic conductivity in the melt state seen in PEO/LiTFSI compared to other polymer electrolyte systems. The ionic conductivity of PEO/LiTFSI increases with increasing salt concentration due to an increase in charge carriers, until it reaches a maximum at moderate salt concentrations.[17] From there, the conductivity decreases with increasing salt concentration. Using concentrated solution theory, developed by John Newman[18], the electrochemical and transport properties of PEO/LiTFSI have been fully characterized.[19,20]

Another challenge that arises in rechargeable batteries with Li metal electrodes is the nonplanar deposition of Li during the charging and discharging cycles that leads to the formation of Li protrusions or dendrites. These dendrites can span the width of the electrolyte and lead to short-

circuit failure of the electrochemical cell.[21] Monroe and Newman proposed that dendrite growth could be suppressed if the battery electrolyte had a high enough shear modulus to "push-back" on to the growing protrusions. Linear polymers are viscoelastic liquids and thus are unable to withstand stress in the long-time limit. One approach for creating solid polymer electrolytes is through the self-assembly of block copolymers, which can microphase separate into ionically conductive and mechanically rigid domains.[22–25]

The most commonly studied block copolymer electrolyte, and the focus of the research presented in this dissertation, is polystyrene-*block*-poly(ethylene oxide) (SEO) mixed with LiTFSI salt, SEO/LiTFSI. Preliminary studies of SEO/LiTFSI have provided evidence that the presence of the polystyrene (PS) microphase suppresses dendrite growth.[26–28] The addition of a third component, PS, as well as the presence of nanostructure complicates the ion transport picture in SEO/LiTFSI. However, the assumption that the salt preferentially segregates into the PEO domains[29–31] simplifies this picture and the electrochemical and transport properties in a variety of SEO/LiTFSI copolymers have been fully characterized using concentrated solution theory.[20,25]

1.2 Block Copolymer Thermodynamics

The phase behavior of AB diblock copolymers wherein two dissimilar chains are covalently bonded is determined entirely by two parameters: segregation strength and composition.[32–37] Segregation strength is characterized by the product χN, where χ is the Flory-Huggins interaction parameter and measures the thermodynamic compatibility between A and B chains and N is the degree of polymerization of the block copolymer. Composition is quantified by the volume fraction of one of the polymer components, f_A. As segregation strength increases, block copolymers microphase separate from a homogeneous disordered phase (DIS) into ordered morphologies, such as lamellae (LAM), gyroid phases (GYR), hexagonally packed cylinders (HEX) and body center cubic spheres (BCC). The geometry of the resulting ordered phase depends on both χN and f_A.[38–41] The temperature dependence of the Flory-Huggins interaction parameter in salt-free binary polymer systems is generally expressed as

$$\chi = \frac{A}{T} + B \tag{1.1}$$

where A and B are empirically determined constants.[39,42] There are no analytical expressions for the boundary between disorder and order for block copolymers. Self-consistent field theory (SCFT) has been used to calculate the order-disorder boundary as well as the predicted ordered morphologies on a χN versus f_A plot.[41] The most common ways to determine the morphology of block copolymers is through reciprocal space techniques such as small angle X-ray scattering (SAXS)[43,44] or through real-space techniques such as transmission electron microscopy (TEM). The Flory-Huggins interaction parameter of block copolymers can be determined through application of the Random Phase Approximation to block copolymers, as developed by Leibler.[34]

In the weak segregation limit (WSL) *i.e.* in the vicinity of the order-disorder transition (ODT), the composition dependence of the periodic length-scale of ordered block copolymer phases, or the domain spacing, was calculated numerically by Leibler.[34] The length scale of the periodic phase in

an ordered block copolymer is a reflection of molecular size. In a homopolymer, molecular size is often characterized by the radius of gyration, $R_g = N^{\frac{1}{2}}b/6$, where b is the statistical segment length of the chain.[32,45] In the disordered regime as well as the WSL, the molecular size of each copolymer block can be approximated by the radius of gyration of that polymer block because the chains adopt a relaxed Gaussian conformation due to the favorable mixing between the two blocks.[39] As segregation strength increases and the strong segregation limit (SSL) is approached, the chains will stretch at the microphase interface due to the thermodynamic repulsion of mixing and increase the molecular size of the copolymer.[46–48] Relationships between the domain spacing, the statistical segment length and the interaction parameter have been determined for both segregation regimes.[49]

The addition of salt to block copolymers is known to alter their phase behavior due to the introduction of new interactions between the polymers and ions including electrostatic interactions, charge dissociation, ion solvation and physical cross-linking between the ions and polymer chains. There have been many theoretical studies that attempt to quantify the effects of these interactions on polymer phase behavior. Ions tends to cluster in the phase with the higher dielectric constant and this increases segregation strength. This was captured in models developed by Wang and coworkers using the concept of Born solvation energy wherein the ions were treated as reversibly bound to polymer chains.[50,51] In these models, the framework described in the previous section for salt-free systems can be applied to salty systems provided χ is replaced with an effective interaction parameter, χ_{eff}, which depends on salt concentration. In the simplest case, this dependence is linear and

$$\chi_{eff} = \chi_0 + mr \tag{1.2}$$

where χ_0 is the Flory-Huggins parameter for the salt-free system, r is a suitable measure of salt concentration and m is a system-dependent proportionality constant. This form for χ_{eff} in salty systems was first proposed in the pioneering work of Mayes and coworkers[52] and has been used successfully to model the thermodynamics in a variety of SEO-based electrolyte systems.[53–55]

While the aforementioned model was able to predict trends in the domain spacing[56] and order-disorder transition[57] of symmetric block copolymers with added salts, the theories did not match trends seen in asymmetric SEO/LiTFSI systems where $f_{EO} \neq f_S \neq 0.50$.[58] It was hypothesized that the discrepancy seen between theory and experiment was due to the lack of explicit ionic correlations in the model. Therefore, de la Cruz and coworkers introduced a hybrid liquid-state theory based correction for ionic correlations into a block copolyelectrolyte model.[59–61] This model produces phase block copolymer phase diagrams that are qualitatively different from those predicted by mean-field theory for salt-free systems. Most notably, this model predicts a stable "chimney-like" region where a narrow channel of ordered phases is predicted to be stable in diblock copolymers with a minority ion-containing phase (phase A). In addition, these stable phases contain inverted morphologies (e.g. cylinders of B in a matrix of A) are predicted in the chimney.[59] This behavior was attributed to "electrostatic cohesion" wherein the presence of ionic clusters stabilize the ordered morphologies in these regions of the phase diagram.

For simplicity, we have chosen to outline two of the many recently developed theories[62–64] on the phase behavior and thermodynamics of ion-containing copolymers. Although there has been significant work in developing new, and increasingly complex, theoretical frameworks, little has been done to directly compare these frameworks to experimental datasets. The data presented in this dissertation enables a critical examination of theories described above.

1.3 Polymer Dynamics

Several theoretical models have been developed to describe the motion of polymer chains in the absence of salt. They are well-described in ref 65. The short-time segemental dynamics of polymers can be described by the Rouse model.[66] In this model, the polymer segments are represented by beads connected to each other via springs characterized by a friction coefficient, ζ, and polymer relaxation occurs in a sub-diffusive matter. In this regime, the mean-squared displacement (MSD) of the polymer chain scales with $t^{1/2}$. At longer times, $t > \tau_e$ where τ_e is the crossover time, the motion of a polymer chain becomes influenced by the presence of neighboring chains. When the polymer chains are long enough to interact, or entangle with one another, the neighboring chains form dynamical constraints which are represented by a tube of diameter, d. At these molecular weights, the ionic conductivity of PEO/LiTFSI is independent of molecular weight.[67,68] The reptative motion of the polymer chain along this tube has been described by models proposed by de Gennes, Edwards, and Doi.[69,70] At intermediate times, $\tau_e < t < \tau_R$ where τ_R is the reptation time, the polymer chain reptates within the confined tube through a process known as local reptation. Here, the MSD scales with $t^{\frac{1}{4}}$. At longer times, $\tau_R < t < \tau_d$ where τ_d is the longest molecular relaxation time, one end of the chain "escapes" from the confined tube through a process known as pure reptation where the MSD scales with $t^{\frac{1}{2}}$. Finally, at sufficiently long times, $t > \tau_d$, the polymer chain undergoes diffusive motion where MSD scales with t.[71] In typical polymer chains, these time-scales span over 12 orders of magnitude of time with Rouse modes happening on the nanosecond time scale, reptative modes happening on 100 ns – 1 μs time scale, and diffusive modes happening on the second time-scale.[65] Therefore, a variety of experimental techniques are needed to measure polymer dynamics across the three regimes of polymer dynamics: Rouse, reptation and diffusive motion.

It is well known that the translation of ions in polymer electrolytes is coordinated to the segmental relaxation of the polymer chains.[15,65,80,72–79] Previous studies have used quasi-elastic neutron scattering (QENS) to probe the dynamics of the polymer backbone in the Rouse regime and extract the monomeric friction coefficient in the presence of salt.[15,73,74,80] In general, they have found that the monomeric friction coefficient increases with increasing salt concentration and that this increase is responsible for the decrease in ionic conductivity seen at high salt concentrations measured with ac impedance spectroscopy. It is currently unclear how the reptation and diffusive polymer dynamical modes influence ion transport in polymer electrolyte systems. Polymer dynamics at these time scales cannot be measured with QENS.

It is important to note that the aforementioned theories were developed for homopolymer systems in the absence of salt. The picture of polymer dynamics in block copolymers is more complex due to the anchoring of one or more chain ends due to microphase separation. Conformational relaxation of the chains in the ionically conducting domains is affected by connectivity to the rigid

domains.[81] The segmental composition profile within the conducting domains is also affected by mixing with the rigid domains, especially in the vicinity of the interface between the microphases.[39,62,63] Any of these effects could alter the dynamics of block copolymer electrolytes. There have been no studies on the effect of salt concentration on the dynamics of block copolymer electrolytes in the Rouse or reptation regimes. Previous studies on nanostructured block copolymer electrolytes are limited to studying the cooperative grain dynamics on the 10^{-2}-10^{2} s time-scale.[82]

1.4 Outline of Dissertation

In the enclosed work, I use quantitative X-ray and neutron scattering techniques to study the effect of salt concentration on the thermodynamics and dynamics of block copolymer electrolytes. The remainder of the dissertation is organized as followed. Chapter 2 outlines the procedures used to synthesize the block copolymers in this study. In Chapter 3, I outline the different X-ray and neutron scattering techniques used in this study and highlight recent advances in scattering technology as well as other applications for the techniques. Chapters 4-7 rely on X-ray scattering techniques and Chapters 7-8 rely on neutron scattering techniques. Chapters 4 and 5 focus on the effect of salt concentration on the phase behavior of SEO/LiTFSI. Chapter 4 focuses on systems with a majority PS-phase, which uncovered a new type of coexistence not previously seen in polymer systems. The nature of the coexistence is probed using a variety of techniques in Chapter 4. Chapter 5 focuses on developing an experimental dataset for the morphologies of SEO/LiTFSI system as a function of copolymer composition, molecular weight, and salt concentration. A literature review was also conducted to expand the experimental dataset to SEO systems that were previously studied as well as determine the effect of salt concentration on the domain spacing of SEO/LiTFSI systems in the weak and strong segregation limit. The phase diagrams presented in Chapter 5 will hopefully serve as benchmarks during the development of new theories on the phase behavior of ion-containing polymer systems. Chapter 6 focuses on the effect of salt concentration and copolymer composition on the thermodynamics of SEO/LiTFSI. Through careful measurements of the effective Flory-Huggins interaction parameters, the existence of a copolymer composition wherein the segregation is not affected by salt concentration was uncovered and a preliminary model was developed to describe its molecular underpinnings. Chapter 7, the only section of this dissertation that focuses on homopolymers, examines the effect of salt concentration on the statistical segment length of PEO/LiTFSI using neutron scattering. It was found that the relationship between salt concentration and chain dimensions was non-monotonic and that the presence of ion clusters might lead to the increase in statistical segment length at high salt concentrations. In addition, Chapter 7 uses a variety of scattering techniques to probe the presence of ionic clusters at high salt concentrations. Chapter 8 uses neutron spin echo spectroscopy to probe the effect of salt concentration on polymer dynamics in SEO/LiTFSI. This is the first study of polymer dynamics in block copolymer electrolytes and the first study that covers both the Rouse and reptation regime in block copolymers (with and without salt). Finally, Chapter 9 provides a summary of the study.

1.5 Nomenclature

1.5.1 Abbreviations:

BCC	body center cubic
DIS	disordered

GYR	gyroid
HEX	hexagonally packed cylinders
LAM	lamellae
LiTFSI	lithium bis(trifluoromethanesulfonyl) imide salt
MSD	mean-squared displacement
ODT	order-disorder transition
PEO	poly(ethylene oxide)
PS	polystyrene
QENS	quasi-elastic neutron scattering
SAXS	small angle X-ray scattering
SEO	polystyrene-*block*-poly(ethylene oxide)
SSL	strong segregation limit
TEM	transmission electron microscopy
WSL	weak segregation limit

1.5.2 Symbols:

d	domain spacing (nm)
f_A	volume fraction of species A
R_g	radius of gyration
r	salt concentration ($[Li^+]$ $[EO]^{-1}$)
t	time

1.5.3 Greek Symbols:

τ_d	longest molecular relaxation time
τ_e	crossover time
τ_R	reptation time
χ	Flory-Huggins interaction parameter
χ_0	Flory-Huggins interaction parameter in salt free state
χ_{eff}	effective Flory-Huggins interaction parameter
χN	segregation strength

2. Synthesis of Polystyrene-*block*-poly(ethylene oxide) via Anionic Polymerization

ABSTRACT

Polystyrene-*block*-poly(ethylene oxide) (SEO) was synthesized using anionic polymerization. Great care was taken to purify the solvents and monomers. Both polymerizations were done in benzene and terminated with methanol. A cryptand catalyst was used to dissociate the oxyanion and allow for ethylene oxide polymerization propagation. The copolymers were thoroughly purified to remove any unreacted monomer as well as residual cryptand catalyst. The molecular weights and molecular weight distributions were determined via gel permeation chromatography. The relative block fractions were determined using nuclear magnetic resonance.

2.1 Introduction

Polystyrene-*block*-poly(ethylene oxide) (SEO) was synthesized using anionic polymerization. The structure of SEO is shown in Figure 2.1 Anionic polymerization allows for precise control of molecular weights and narrow polydispersities through the use of high vacuum techniques.[83] In addition, complex polymer architectures, including block and star copolymers, can be synthesized through sequential polymerization on the "living chains".[84] The main drawback of anionic polymerization is the need for extremely pure solvents and monomers to reduce the concentration of known contaminants, such as water and other proton donors, which could terminate the chains resulting in non-ideal polymer molecular weights. The purification is typically done through thorough degassing of the reactors and the use of water-scavenging agents. Therefore, all synthetic steps are performed either on a high-vacuum Schlenk line on in a glovebox with an inert Ar atmosphere.

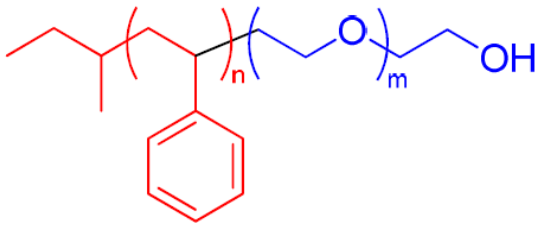

Figure 2.1. Structure of polystyrene-*b*-poly(ethylene oxide).

Below is a detailed account of the synthesis of SEO via anionic polymerization adopted from ref 85 and ref 86 and modified according to ref 87 and ref 88. Purification and characterization of the SEO copolymers was adopted from ref 85. A main synthetic advantage of anionic polymerization is the application of simplifying assumptions that (1) each initiator molecule will initiate a single chain and (2) each reaction will run to approximately 100% conversion. These assumptions

streamline the design of a given reaction and minimize the "trial-and-error" process typically associated with polymer synthesis.

2.2 Anionic Polymerization of SEO

Before beginning the synthesis, the high-vacuum Schlenk line must be tested for leaks and thoroughly cleaned via flame-drying. It is important to record the baseline, with all valves closed and no reactors on the vacuum line, of the vacuum gauge to determine the lowest pressure when degassing reactors during the synthesis. It is important that this baseline value is met after each reactor is added to the vacuum line to ensure that there are no leaks in the reactors and that all trace water from the atmosphere is evaporated. In addition, the vacuum pump oil should be changed prior to the synthesis to ensure that the pump is operating as efficiently as possible. All reactors should be thoroughly checked for microscopic cracks and sealing issues prior to use in the synthesis. Proper PPE and proper use of engineering safety controls is extremely important throughout the duration of the synthesis procedure. Also, due to the labor-intensity of anionic polymerization, it is not recommended for the following procedure to be done solo. Ideally, two people should be in the laboratory at all times and another colleague should be within earshot.

2.2.1 Benzene and Ethylbenzene Purification. Two solvents are used in the SEO synthesis: (1) benzene is used as the polymerization solvent and (2) ethylbenzene is used to dry the ethylene oxide monomer. Both solvents must be purified to remove any trace oxygen or water before adding additional reactants. One 2 L and one 1 L reactor are flame-dried on the vacuum line to evaporate off all residual water. One liter of benzene is added from the solvent column to the evacuated 2 L reactor. The 1 L reactor is taken into the glovebox and 500 mL of anhydrous ethylbenzene is added. Both reactors are returned to the vacuum line, frozen using liquid nitrogen, and degassed until the baseline pressure is reached. This process, referred to as "freeze-pump-thaw" or a hard degas, is repeated at least three times for each reactor or until the maximum pressure during the pump process is less than 10 mTorr. Both reactors are then taken into the glovebox. An appropriate quantity of *n*-butyllithium in cyclohexane was added to the benzene and ethylbenzene as a water scavenger; in general, 0.035 mol of *n*-butyllithium per 1000 mL of solvent should be sufficient to remove all traces of moisture. Styrene was then added in a roughly 10:1 molar ratio with *n*-butyllithium in order to ensure styrene oligomers grow which are heavy enough to prevent any possibility of entrainment in the subsequent solvent distillation. The mixture was allowed to stir in the glove box for 24 hours at room temperature. The solvent was determined to be clean if the bright red color characteristic of polystyryl lithium species appeared and persisted without fading. The solvents are stable for months in the glovebox stirring at room temperature to use in subsequent syntheses.

The benzene reactor was removed from the glovebox and returned to the vacuum line and degassed. The reactor was then hard degassed three times. The desired number of polymerization reactors (maximum three) were added to the vacuum line, degassed, and flame-dried. 200-300 mL of clean benzene from the 2 L reactor was distilled into each of the polymerization reactors. Each the of the polymerization reactors was then hard degassed once following the distillation.

2.2.2 Styrene Purification. One 500 mL reactor was added to the vacuum line, degassed and flame dried. It was then brought into the glovebox where a 1.25x excess of styrene needed for the polymerization(s) from a fresh bottle was added to the reactor. A drying agent, dibutyl magnesium (DBMg), was added to the reactor in a 1:20 DBMg to styrene by volume ratio. The reactor was returned to the vacuum line and degassed three times. The styrene mixture was stirred overnight at room temperature on the vacuum line and then hard degassed one additional time. The presence of a white solid might appear in the styrene. The solids indicate the presence of styrene oligomers that polymerized from contaminants originally present in the monomer and will not harm the synthesis.

2.2.3 Polystyrene Polymerization. The polymerization reactors containing clean benzene were hard degassed one time. A graduated ampoule was added to the vacuum line, degassed, and flame-dried. Styrene monomer was distilled from the 500 mL reactor to the ampoule and then degassed. The desired amount of styrene was distilled from the graduated ampoule to each polymerization reactor and then degassed. The volume of styrene distilled is determined from the volume levels of the graduated ampoule. The ampoule can be stirred to expedite the distillation process if necessary. The reactors were thawed to room temperature and then brought into the glovebox. The desired amount of *sec*-butyllithium was added to each reactor. The desired amount of initiator is calculated assuming that each initiator molecule will initiate exactly one chain. The reaction mixture will rapidly change from colorless to bright yellow, orange or red, depending on the concentration of chain ends. The intense colors are characteristic of the growing polystyrene chains capped with polystyrl anions. The more concentrated the ions, the darker the color. The reaction scheme for the initiation and propagation of the styrene polymerization is shown in Figure 2.2. The reaction was stirred in the glovebox for at least eight hours. After complete consumption of the styrene monomer, an aliquot of the reaction mixture was removed from each polymerization reactor for analysis. The aliquot was terminated by dry methanol and the molecular weight of the styrene block was determined by gel permeation chromatography (GPC).

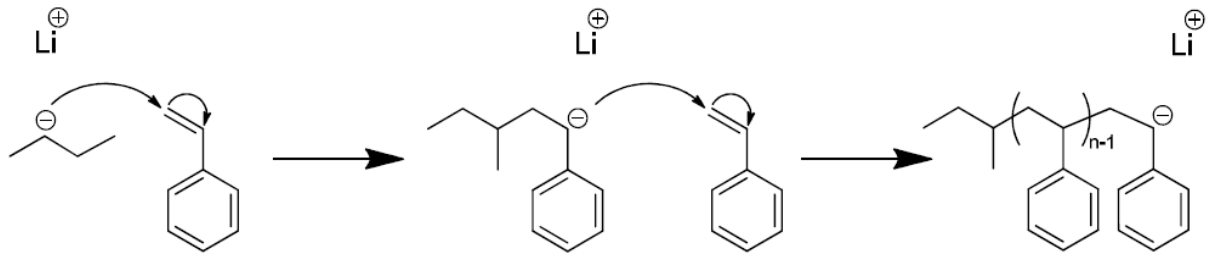

Figure 2.2 Styrene initiation and chain propagation scheme.

2.2.4 Ethylene Oxide Purification. Extreme caution is necessary when working with ethylene oxide, an acutely toxic gas. Ethylene oxide is first purified by stirring over calcium hydride, a material that is highly reactive with water. A long neck reactor containing crushed calcium hydride is added to the vacuum line and degassed overnight and flame-dried thoroughly to remove any residual water from the calcium hydride. Ethylene oxide is distilled from the cylinder on to calcium hydride frozen over liquid nitrogen and then degassed once. The calcium hydride/ethylene oxide

mixture is warmed on a mixture of dry ice and isopropanol slowly until the ethylene oxide monomer is a liquid and is then stirred vigorously for at least eight hours.

A 1 L reactor is added to the vacuum line, degassed and flame-dried. It is then brought into the glovebox and 0.075 mol of *n*-butyllithium was added to the reactor. This reactor, as well as the ethylbenzene reactor, was returned to the vacuum line and degassed. The ethylbenzene reactor was hard degassed three times prior to distillation of 300 mL of ethylbenzene on to the *n*-butyllithium. The ethylbenzene/*n*-butyllithium reactor was degassed thoroughly before being thawed to room temperature slowly. The ethylbenzene purification reactor was removed from the vacuum line and returned to the glovebox.

Ethylene oxide was distilled from the calcium hydride reactor into the ethylbenzene reactor. The source flask was cooled on a mixture of salted ice water (- 10 °C) and the destination reactor was cooled on mixture of dry ice and isopropanol. The distillation was stopped once all of the ethylene oxide was removed from the calcium hydride; the calcium hydride powder appeared dry and white. The ethylbenzene reactor was thawed to room temperature slowly and allowed to stir. The ethylene oxide monomer is now solvated by the ethylbenzene and is safe to store at room temperature for up to two weeks. Over time, white precipitate will form in the solution; these solids are slowly propagating PEO oligomers. The presence of these solids will not contaminate the pure ethylene oxide monomer, but overtime will consume the solvated monomer so it is important to use the monomer as soon as possible. Extreme caution is necessary when removing the calcium hydride reactor from the vacuum line in case residual amount of ethylene oxide monomer remain.

2.2.5 Ethylene Oxide Endcapping. A graduated ampoule was added to the vacuum line, degassed and flame-dried. The polymerization reactors were returned to the vacuum line and degassed one time each. A few milliliters of ethylene oxide were distilled from the ethylbenzene reactor to the ampoule. The destination reactor is chilled on a mixture of dry ice/isopropanol and the source reactor is chilled on salted ice water to minimize the amount of ethylbenzene that distills with the ethylene oxide monomer. 1 mL of ethylene oxide was subsequently distilled to each of the polymerization reactors and the reactors were allowed to thaw to room temperature over ice water slowly. One ethylene oxide moiety will react with each styrl anion, end-capping the chain with the oxygen anion (Figure 2.3). Further propagation of the ethylene oxide polymerization with the excess ethylene oxide monomer is suppressed due to the strong association of the oxyanion and the lithium cation. Once the reactors are thawed, the reaction mixture should turn colorless. If the reaction mixture remained yellow, additional ethylene oxide monomer was added until the thawed solution was colorless.

The polymerization reactors were left on the vacuum line at room temperature to stir overnight. They were then each degassed once to remove any excess ethylene oxide monomer and then brought into the glovebox. The cryptand catalyst *tert*-butyl phosphazene (P_4-*t*-Bu) in hexanes was added to the reactor in 10% stoichiometric excess relative to the number of calculated chains. The *tert*-butyl phosphazene "frees" the oxyanion for further ethylene oxide propagation. The

polymerization reactors were allowed to stir overnight at room temperature in the glovebox to ensure association of the catalyst to the lithium cations.

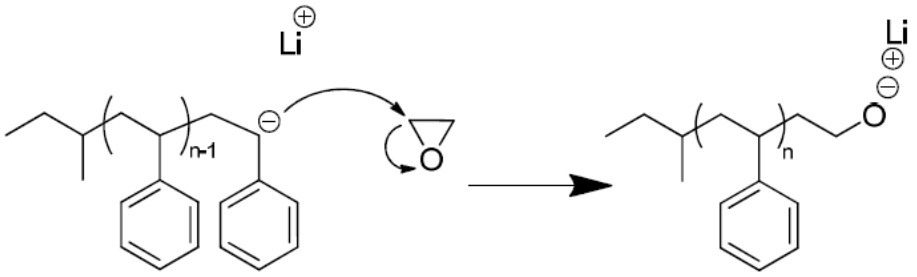

Figure 2.3 Styrene end-capping scheme.

2.2.6 Ethylene Oxide Polymerization. The polymerization reactors were returned to the vacuum line and degassed one time. A graduated ampoule was added to the vacuum line, degassed and flame-dried. Ethylene oxide was distilled from the ethylbenzene reactor to the graduated ampoule. The destination reactor is chilled on a mixture of dry ice/isopropanol and the source reactor is chilled on salted ice water to minimize the amount of ethylbenzene that distills with the ethylene oxide monomer. The ampoule was then hard degassed and thawed to -10 °C to note the total volume of ethylene oxide in the ampoule. The density of ethylene oxide is highly dependent on temperature; therefore, it is important to keep the ampoule at -10 °C to ensure that correct weight of monomer is distilled to the reactors. The desired volume of ethylene oxide was distilled from the ampoule to each polymerization reactor. The polymerization reactors were then slowly thawed and heated to 45 °C in oil baths. The polymerization reactors were stirred for four days. Depending on the concentration of oxyanions, the reaction mixture will develop a blue-purple-gray color with a bright fuchsia or magenta intermediate. Finally, the polymerization reactors were brought into the glove box. The chains were terminated with 1 mL of methanol while stirring. Additional methanol was added until the reaction mixture became clear, up to a maximum of 5 mL. The ethylene oxide polymerization propagation and termination are shown in Figure 2.4.

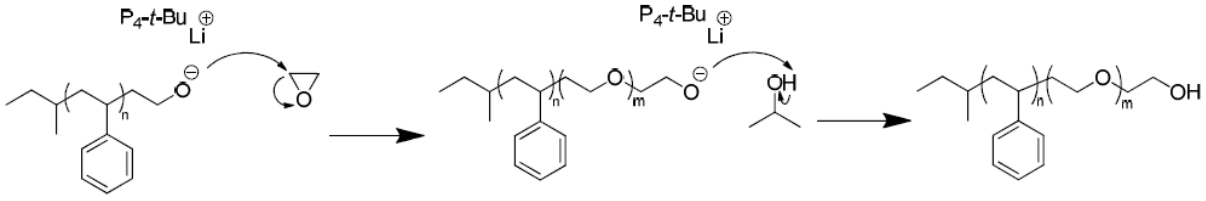

Figure 2.4 Ethylene oxide polymerization propagation and termination scheme.

2.3 Copolymer Purification

The residual salts and catalyst were removed by three cycles of precipitation in ice-cold hexanes, filtration through cellulose membranes, and redissolution in benzene. The volume of benzene needed to dissolve the copolymers was decreased during each round of purification. The *tert*-butyl

phosphazene base was removed by filtering the copolymer/benzene solution through neutral alumina and nylon membranes with an average pore size of 1 μm to remove any dust particulates. This process was repeated until the no evidence of the phosphazene base was present in the ^{1}H nuclear magnetic resonance (NMR) spectra. An example ^{1}H NMR spectra of SEO is provided in Figure 2.5. The intensities were normalized and offset to allow for a direct comparison. The ^{1}H NMR signature of the phozphazene base is highlighted as "e" and corresponds to chemical shifts of 2.6-2.8 ppm. After purification over alumina, the intensities of these peaks are significantly diminished such that their area accounts for less than 0.01% of total peak area. All copolymers were freeze-dried from benzene in a lyophilizer slowly over the course of seven days to remove solvent. Clean and dry copolymers are completely transparent and colorless in the melt state.

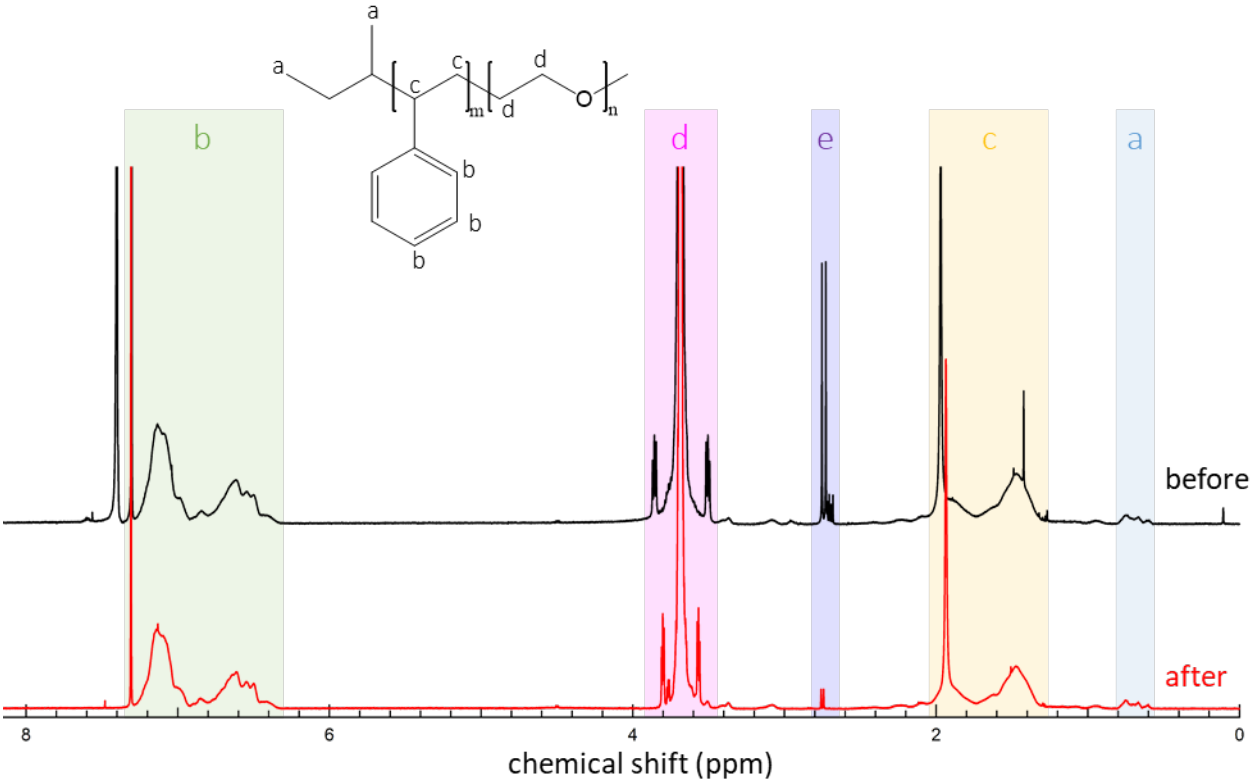

Figure 2.5 ^{1}H NMR Spectra of SEO(4.0-22.4) before and after purification over alumina.

2.4 Copolymer Characterization

2.4.1 Molecular Weight Characterization with GPC. Gel permeation chromatography (GPC) is a type of size exclusion chromatography (SEC) used to determine the relative molecular weight of a polymer sample. SEC uses a column with a large variety of pore sizes that a polymer chain must "navigate through" before reaching a detector, typically a refractive index detector or viscometer. The polymers with a larger molecular weight will occupy larger spaces in solution and therefore will not be able to enter some of the smaller pores within the column. Therefore, samples with larger volumes will elute prior to those with smaller volumes. A series of standards, typically homopolymer standards of known molecular weights, are used to calibration the elution volume

or time of a given instrument and solvent choice as it is well-known that the size of a given polymer is extremely dependent on polymer-solvent interactions.[45]

The terminated aliquot of the polystyrene block was characterized with GPC to determine the molecular weight of the first block of the copolymer. A Viskotek VE 2001 Separations Module and a Viscotek TDA 302 Triple Detector were used to determine the number- and weight- averaged molecular weights and the polydispersity indices of the homopolymer. The instrument was run at room temperature with tetrahydrofuran as the mobile phase. Samples were prepared at a concentration of 2-4 mg of polymer per mL of tetrahydrofuran removed from the reservoir. The samples were allowed to dissolve thoroughly and filtered before loading into the GPC. The calculations were performed by the OmniSEC software provided by Viscotek using a series of polystyrene standards purchased from PolymerSource.

It is impossible to determine the exact molecular weight of the SEO copolymer using SEC because of the (1) use of homopolymer standards and (2) large difference in solubility of polystyrene and poly(ethylene oxide) in most solvents. However, the total polydispersity of the SEO copolymer can be determined using GPC. The polydispersities of copolymers with a majority polystyrene phase were measured using GPC in the same manner as the polystyrene aliquots. The polydispersities of copolymers with a majority poly(ethylene oxide) phase as well as those with high molecular weights, $N > 2{,}000$, were measured with an Agilent 1260 Infinity Series fitted with Water Styragel HR 3 and 4 columns with N-Methyl-2-pyrrolidone/LiBr as the mobile phase. The polydispersity index (PDI) was measured by using a series of polystyrene standards purchased from PolymerSource.[89]

2.4.2 Copolymer Composition Characterization with ^{1}H NMR. NMR characterization of the block copolymers was performed on an AVB-400 Spectrometer. Samples were prepared by dissolving 10-20 mg of dried polymer in 1 mL of deuterated chloroform. Samples were stirred and heated to 40 °C to aid the dissolution of polymer. Figure 2.5 shows an example ^{1}H NMR spectra of an SEO copolymer with a majority PEO phase. Also included in Figure 2.5 is the structure of SEO where the relevant hydrogen atoms are labeled according to ^{1}H chemical shift. In SEO, the protons have three main chemical environments: the aromatic ring (6.3-7.3 ppm), the alkyl backbone (1.3-2.1 ppm) and the ether backbone (3.4-3.8 ppm), labeled with the letters b, c, and d, respectively in Figure 2.5. In the low molecular weight copolymers, the alkyl protons from the sec-butyl initiator can be seen at 0.8-0.95 ppm, labeled with the letter a in Figure 2.5. These peaks were used to determine the copolymer composition in deuterated SEO copolymers where ^{1}H NMR spectra of the PS block could not be obtained. We assume that no homopolymer was present in the block copolymer from the GPC results. We can then use the ratio of the peak integration of the ether backbone protons to that of the aromatic ring protons to determine the weight percent of each block.[90] The molecular weight of the polystyrene aliquot, determined from GPC, is then used to calculate the molecular weight of the poly(ethylene oxide) block.

The polymers are named SEO (*xx-yy*), where *xx* and *yy* are the number-averaged molecular weights of polystyrene, M_{PS}, and poly(ethylene oxide), M_{PEO}, in kg mol^{-1}. The volume fractions of each block of the copolymers are given by

$$f_{EO} = \frac{\nu_{EO}}{\nu_{EO} + \frac{M_{PS}M_{EO}}{M_S M_{PEO}}\nu_S} \quad (2.1)$$

where v_{EO} and v_S are the molar volumes of ethylene oxide and styrene monomer units, and M_{EO} and M_S are the molar masses of ethylene oxide (44.05 g mol^{-1}) and styrene (104.15 g mol^{-1}). Molar volumes were calculated by $\nu = M/\rho$. In this study, the densities of the poly(ethylene oxide) and polystyrene blocks were given by $\rho_{PEO} = 1.139 - 7.31 \times 10^{-4} \times T$ and $\rho_{PS} = 1.08665 - 6.19 \times 10^{-4} \times T + 1.36 \times 10^{-7} \times T^2$.[91] The overall degree of polymerization, N, was calculated by $N = N_{PS} + N_{PEO}$ where

$$N_i = \frac{M_i}{\rho_i(T) N_A \nu_{ref}} \quad (2.2)$$

and N_A is Avogadro's number and ν_{ref} was fixed at 0.1 nm^3. Table 2.1 contains polymer characteristics, including the polydispersity indices, of the block copolymers synthesized by the author. The neat copolymers are completely transparent and colorless.

2.5 Library of Copolymers

Table 2.1 lists the SEO copolymer synthesized by the author.

Lab Name	Polymer	M_{PS} kg mol^{-1}	M_{PEO} kg mol^{-1}	f_{EO}	N	PDI	Chapter Reference	Notes
SEO.WSL.1	SEO(9.4-2.4)	9.4	2.4	0.19	185	1.04	4, 5, 6	
SEO.WSL.2	SEO(9.7-1.7)	9.7	1.7	0.14	180	1.04		No scattering*
SEO.WSL.3	SEO(10.8-1.2)	10.8	1.2	0.09	190	1.04		No scattering*
SEO.WSL.4	SEO(9.4-4.0)	9.4	4.0	0.28	209	1.04	4, 5, 6	
SEO.WSL.5	SEO(17.4-3.9)	17.4	3.9	0.17	335	1.04	4, 5, 6	
SEO.WSL.6	SEO(17.4-2.6)	17.4	2.6	0.12	315	1.04		No scattering*
SEO.WSL.7	SEO(5.1-12.8)	5.1	12.8	0.70	271	1.04	5, 6	
SEO.WSL.8	SEO(4.0-22.4)	4.0	22.4	0.84	396	1.03	5, 6	
SEO.WSL.9	SEO(3.8-8.2)	3.8	8.2	0.67	182	1.04	5, 6	
SEO.WSL.10	SEO(5.1-14.4)	5.1	14.4	0.72	295	1.05	7	dPS-*b*-hPEO
SEO.WSL.12	SEO(4.9-23.6)	4.9	23.6	0.82	428	1.05	7	dPS-*b*-dPEO
SEO.JAM.2	SEO(250-694)	250	750	0.74	3980	1.15		Cylindrical*
SEO.JAM.3	SEO(18.5-17.5)	18.5	17.5	0.47	554	1.03		Lamellar*
SEO.JAM.5	SEO(115-172)	115	172	0.58	4380	1.10		Lamellar*
SEO.JAM.7	SEO(110-183)	110	183	0.61	4460	1.10		Lamellar*
SEO.JAM.8	SEO(200-222)	200	222	0.51	6470	1.08		Lamellar*
SEO.JAM.9	SEO(235-222)	235	222	0.47	7030	1.05		Lamellar*

**scattering/morphology in the neat state*

2.6 Nomenclature

2.6.1 Abbreviations

DBMg	dibutyl-magnesium
GPC	gel permeation chromatography
LiTFSI	lithium bis(trifluoromethanesulfonyl) imide salt
N_A	Avogadro's number

NMR	nuclear magnetic resonance
PDI	polydispersity index
PEO	poly(ethylene oxide)
P_4-*t*-Bu	*tert*-butyl phosphazene cryptand catalyst
PS	polystyrene
SEO	polystyrene-*block*-poly(ethylene oxide)
SEC	size exclusion chromatography

2.6.2 Symbols

f_{EO}	volume fraction of PEO phase
M_i	number-averaged molecular weight of species *i* (kg mol^{-1})
N	number-averaged degree of polymerization (sites chain^{-1})

2.6.3 Greek Symbols

ν_i	molar volume of species I i (cm^3 mol^{-1})
ν_{ref}	reference volume (nm^3 site^{-1})
ρ_i	density of spcies species i (g cm^{-3})

2.7 Supporting Information

2.7.2 Deuterated Monomers. Isotopically labeled copolymers are extremely valuable tools to selectively probe the dynamics and chain conformations of a given block. Most notably, is the substitution between hydrogenated and deuterated monomers to create copolymers with neutron contrast due to the large difference in neutron scattering lengths of ^{1}H and ^{2}H. These polymers enable the use of a variety of neutron scattering techniques.[92]

Deuterated monomers are often significantly more expensive and contaminated than typical hydrogenated monomers, and therefore it is important to take additional steps in their purification. Deuterated styrene is purified twice over DBMg and deuterated ethylene oxide is purified twice over calcium hydride before being dried over *n*-butyllithium as described above. It's important to note that even with these additional precautions, the synthesis with deuterated monomers resulted in molecular weights that were significantly "farther" from the target molecular weights. However, the polydispersities of the deuterated copolymers were still extremely low (Table 2.1)

2.7.3 High Molecular Weight SEO. The synthesis of high molecular weight SEO, SEO.JAM2-SEO.JAM.9 in Table 2.1, require extremely pure monomers and solvents. When synthesizing high molecular weight copolymers, the number of living chains decreases by over an order of magnitude, which means that each chain that is terminated by a water molecule will significantly alter the molecular weight of the resulting copolymer. Therefore, small adjustments were made to the synthesis procedure when synthesizing copolymers with $N > 2000$.

The most common point of synthesis failure during the synthesis of high molecular weight SEO is the propagation of the ethylene oxide polymerization, which results in a large volume fraction of polystyrene homopolymer in the final product and copolymer compositions with $f_{EO} \gg 0.50$.

Typically, the reaction mixture turns clear after addition of a few milliliters of ethylene oxide monomer, which indicates that the ethylene oxide endcapping process was successful. Therefore, a 25% stoichiometric excess of the *tert*-butyl phosphazene was added for oxyanion dissociation and the reactors were left to stir in the glovebox for at least twelve hours at room temperature. In addition, the ethylene oxide polymerization propagation reaction was left for six days stirring at 45 °C to ensure that the reaction reached ~100% conversion before termination. Typically, the reaction mixture was gray in color during this step of the reaction. Although a stoichiometric excess of the cryptand catalyst was used, the concentration of catalyst in the copolymer is so low that it cannot be detected by ^{1}H NMR. Therefore, high molecular weight SEO is only purified through three-round of precipitation in ice-cold hexanes and re-dissolution in benzene prior to lyophilization.

3. Review on X-ray and Neutron Scattering Techniques

ABSTRACT

X-ray and neutron scattering techniques have emerged as useful tools for probing structure and dynamics at relevant time- and length-scales in polymer-containing systems. In this chapter, a brief background on the basics of the physics of scattering is presented. Next, several scattering techniques relevant to polymer science are outlined, with a focus on providing the specific aims of each technique. Relevant time- and length-scales for each technique are discussed. The goal of this chapter is to create a basic user's guide to scattering experiments in polymer science and provide the necessary information to discriminate between scattering techniques.

3.1 Introduction

Experimental techniques in X-ray and neutron scattering have emerged as useful tools for probing structure and dynamics at small (sub-micron) length-scales through bulk measurements.[93] This chapter does not aim to provide a deep technical background to any given scattering technique, but rather aims to serve as a user's guide for discriminating between techniques, with a focus on applications in polymer science. Although each type of scattering experiment provides insight into the molecular picture at a specific time- or length-scale, acquired scattering data is always averaged over all of the scattering events within the sample, and can be thought of as a "mean-field" representation of the relevant physics present within the sample. Figure 3.1 presents a schematic of a typical scattering event. An incident beam of X-rays, neutrons or light, characterized by momentum, $\boldsymbol{k}$, and energy, E, intersects a sample. A majority of the particles in the incident beam do not interact with the sample and pass directly through it, as shown by the dashed line in Figure 3.1. Some of the particles interact with the sample and are scattered at an angle, θ. The resulting beam after the scattering event, now characterized by momentum, $\boldsymbol{k'}$, and energy, E', is collected by a detector for analysis.

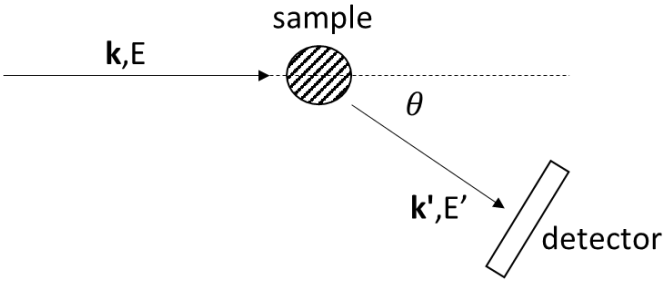

Figure 3.1 Schematic of a Scattering Event: Schematic of a scattering event wherein an incident beam characterized by momentum, $\boldsymbol{k}$, and energy, E, interacts with a sample. The incident beam is scattered at angle, θ, and has resulting momentum, $\boldsymbol{k'}$, and energy, E'. The scattered beam properties are collected on a detector for further analysis.

There are three main types of scattering events: elastic, inelastic, and quasi-elastic. The scattering vector, q, to describe the length-scales at which the scattering events occur can be universally defined as

$$q = \boldsymbol{k} - \boldsymbol{k}' \tag{3.1}$$

according to Figure 3.1. In an elastic scattering event, also known as "hard scattering", there is no energy transfer between the beam and the sample, and therefore, $E' = E$. Only information about sample structure is gathered during an elastic scattering event. In contrast, during an inelastic scattering event there is a transfer of momentum, and therefore energy, between the incident beam and the sample. The energy transfer can happen in either direction such that the scattered beam can have a higher or lower scattering intensity than the incident beam. One example of inelastic scattering is Raman spectroscopy wherein incident photons interact with the sample and shifts the frequency of the scattered photon beam. Raman spectroscopy provides information about different vibrational energy states that are present within a given molecule.[94] The energy and momentum transfer during an inelastic scattering event can be calculated according to

$$\hbar\omega = E - E' = \frac{\hbar^2}{2m_n}(\boldsymbol{k}^2 - \boldsymbol{k}'^2) \tag{3.2}$$

where $\hbar$ is reduced Planck's constant, ω is the angular frequency, and m_n is the mass of the scattered neutrons. In a quasi-elastic scattering event, there is also a transfer of energy, however, the change is typically small such that the approximation $\boldsymbol{k} \approx \boldsymbol{k}'$ can be used. Therefore, the magnitude of the scattering vector, q, can be defined as

$$|q| = q = 2k \sin\left(\frac{\theta}{2}\right) = \frac{4\pi}{\lambda} \sin\left(\frac{\theta}{2}\right) \tag{3.3}$$

for both elastic and quasi-elastic scattering events where λ is the wavelength of the incident beam. Typically, quasi-elastic scattering experiments are focused on measuring the change of momentum of the incident beam in order to learn about the dynamics of the sample. However, the energy exchange can also be ignored during quasi-elastic scattering events in order to gain information about local structure.

When probing structure, the scattering intensity can be broken down into three contributions: (1) form factor ($P(q)$), (2) structure factor ($S(q)$), and (3) contrast. The form factor and structure factor are q-dependent and are related to the probed length-scales. The form factor describes the scattering from interference resulting from different parts of the same object. It provides information on the structure of a given object within the sample and is related to the Fourier transform of the real-space density distribution. The structure factor arises from the different objects present within the sample and measures the correlation function between their centers of mass. $S(q)$ also contains information about the interactions between these objects. The scattering intensity scales with contrast which is given by

$$contrast = \nu_{ref}\left(B_i - B_j\right)^2 [=] cm^{-1} \tag{3.4}$$

where B_i is the scattering length densities of species i and ν_{ref} is an arbitrary reference volume. Similar to the structure factor, contrast is dependent on the different components present within the sample (i and j). The scattering length density is dependent on the type of incident beam used in the scattering experiment, which dictates what species the beam interacts with inside of the sample (electrons, nuclei, etc.). Although contrast is independent of q, how one defines species i and j is directly related to the probed length-scale. For example, in a small angle X-ray scattering experiment on a block copolymer sample, i and j could be the different polymer blocks present within the sample. In an analogous wide angle X-ray sample, which probes smaller length-scales, i and j could be the crystalline and amorphous domains within a given polymer.

Table 3.1 lists the X-ray and neutron scattering techniques that are discussed in the remainder of the chapter and whether they probe structure or dynamics. It is important to choose the right experiment in order to answer a given question. All of the techniques listed in Table 3.1 rely on basic scattering events depicted in Figure 3.1. However, they utilize different incident beams (X-rays versus neutrons as well as different beam energies), probe different length-scales (by changing θ), and collect information on either structure or dynamics (depending on the detectors used). This chapter describes the basics of each technique as well as a few relevant applications of each technique in polymer science. In addition, a brief discussion of the relevant pros and cons of each technique are provided. The aim of this chapter is to provide a general background to each scattering technique such that one can choose the correct technique to answer their given research question.

Table 3.1: Scattering Techniques described in this chapter

	X-ray	Neutron
Structure	SAXS, WAXS, RSoXS	SANS
Dynamics	XPCS	NSE, QENS

3.2 X-ray Scattering Techniques

X-ray scattering can be used to measure both structural and dynamical properties in polymeric systems.[93] X-rays interact with the electrons of the scattering object and the scattering length density is directly proportional to the electron density of the sample.[43] Therefore, according to Eq. 3.4, the attenuation is related to the difference in electron density between the different components of a given sample. This makes X-ray scattering extremely easy in inorganic compounds wherein the samples are often comprised of heavy elements. Polymers, on the other hand, are typically organic compounds comprised of elements with low, and similar, electron content such as carbon, hydrogen, and oxygen. However, there can be a large enough difference in electron density between the blocks of a given copolymer to see scattering from X-rays without synthetic modification of the monomers, such as in polystyrene-*block*-poly(ethylene oxide). The resulting contrast is typically high enough to permit fast time-resolved experiments to probe dynamic

processes including structural responses to external stimuli. In addition, the implementation of high energy X-rays from synchrotron sources has significantly reduced the exposure time needed to see scattering compared to bench-top equipment. In this section, we will discuss the basics and select applications of four X-ray scattering techniques: small angle X-ray scattering, wide angle-X-ray scattering, resonant soft X-ray scattering, and X-ray photoelectron spectroscopy. The first three techniques discussed probe structure and the fourth detects dynamics.

3.2.1 Small Angle X-ray Scattering (SAXS). Small angle X-ray scattering (SAXS) is the most commonly used scattering technique in polymer science. SAXS experiments provide valuable information about the structure of a given sample and measure the largest length-scales of any X-ray scattering technique.[95] Typical probed length-scales range from 2-100 nm, and there are some SAXS beamlines at synchrotron facilities that can probe length-scales up to 500 nm.[96] In SAXS, the incident beam of X-rays has a high intensity ($E = \frac{hc}{\lambda} > 8$ keV) and undergoes elastic scattering. Therefore, X-ray absorption is neglected in SAXS experiments.

The most common application of SAXS in polymer science is the study of the phase behavior and thermodynamics of block copolymers.[44] In microphase separated block copolymers, SAXS can be used to determine the ordered morphology due to the observed sequence of Bragg reflections of the primary scattering peak, q^*, The spacing of the higher-order scattering peaks correspond to the lattice structure of the ordered morphology as defined by the form factor. As segregation increases, the sharpness of the scattering peaks as well as the number of observed higher order peaks also increase. The full-width half-maximum of the q^* peak is related to the average grain size within the sample as given by the Scherrer equation.[97,98] In previous studies, SAXS has been combined with other techniques to measure the effect external stimuli have on polymer structure. For example, *in-situ* SAXS experiments were conducted in conjunction with electrochemical measurements to track changes in block copolymer morphology under an applied electric field.[99]

When a block copolymer forms a disordered morphology, the broad scattering peak, which corresponds to the correlation-hole phenomenon,[100] can be used to quantify the Flory-Huggins interaction parameter, χ, between the polymer blocks through application of the Random Phase Approximation (RPA) derived from Leibler.[34] Accurate conversion to absolute scattering intensities through the use of calibrated standards of known scattering intensity are necessary to extract χ.[101] In addition, there has been a recent push toward using machine learning techniques to predict the equilibrium structure of block copolymers provided a scattering profile and vice versa.[102–104] An excellent guide to quantitative X-ray scattering can be found in ref 105. These techniques are used throughout Chapters 4-6 in this dissertation. Chapters 4 and 5 use SAXS to determine the morphologies of a series of block copolymer electrolytes[106,107] while Chapter 6 applies RPA to disordered SAXS patterns to quantify the effect of salt concentration and copolymer composition on the thermodynamics of block copolymer electrolytes.[108]

3.2.2 Wide Angle X-ray Scattering (WAXS). Wide angle X-ray scattering (WAXS) is analogous to SAXS although it probes much smaller length-scales corresponding to ≤ 1 nm in size. This is typically achieved by moving the detector closer to the sample such that the angles probed, θ, are

much larger than those probed in SAXS. Despite probing almost atomic-level length-scales, the data obtained from WAXS experiments is still averaged over the entire scattered sample and represents the global average. Due to the sizes probed in WAXS, it is not commonly used to study the structure of polymer melts. Typically, WAXS is used to probe the semi-crystalline properties of polymeric materials because the crystalline structure is intra-chain. These experiments are similar to X-ray diffraction and the peaks are sharp in intensity and can be used to identify the crystal structure.[109] More recently, WAXS has been used to detect clusters of charged species in polyelectrolytes known as the "ionomer peak", which appears as a broad diffuse peak.[110] Interpretation of the diffuse peaks in WAXS is challenging, especially in multicomponent systems where contrast calculation, *i.e.* identification of species *i* and *j* as given by Eq. 3.4, is not straight-forward. Currently, no quantitative models exist to correlate diffuse WAXS peaks to atomic distributions within the polymer melt. It is likely that molecular dynamics simulations and atomistic simulations will serve as important complementary tools to decipher diffuse WAXS scattering profiles in the future.

3.2.3 Resonant Soft X-ray Scattering (RSoXS). Resonant soft X-ray scattering (RSoXS) is a relatively new technique that uses tunable incident X-ray energy to increase contrast within chemically heterogeneous systems with homogeneous electron density. RSoXS combines SAXS with Near Edge X-Ray Absorption Fine Structure, NEXAFS, spectroscopy to obtain energy-dependent scattering profiles.[111] The X-rays used in RSoXS experiments are low energy ($E < 1.5$ keV), where absorption by the sample can no longer be neglected. Therefore, samples used in RSoXS are typically thin films of less than 1 μm in thickness.

In RSoXS experiments, multiple scattering profiles are taken across a range of energies and used to determine the nano-scale structure of a heterogeneous system. In polymeric materials, this is commonly done by probing the absorption spectra around the carbon K-edge for features such as π^* resonance seen in polystyrene-containing materials.[112,113] This makes RSoXS an ideal characterization technique for conjugated polymer systems commonly used in organic photovoltaics.[114,115] In one previous study, Wang and co-workers used differences in absorption along the carbon K-edge in a triblock copolymer to take scattering profiles were one, two, or all three of the blocks were "visible" to the X-rays. They then used the resulting scattering patterns to piece together the overall morphology of the triblock copolymer system.[116] At some synchrotron facilities, the polarization of the incident beam can also be tuned, which can reveal information about molecular orientation within the sample.[117] In Chapter 4 of this dissertation, we take advantage of the elemental composition of our block copolymer electrolytes to probe the spatial distribution of the fluorine-containing lithium salt within the nanostructure. Instead of taking scattering profiles across a single elemental K-edge, RSoXS was conducted across the K-edge of carbon, oxygen, and fluorine to directly probe specific elements present within a single or both polymer blocks.

3.2.4 X-ray Photo Correlation Spectroscopy (XPCS). X-ray photo correlation spectroscopy (XPCS) is used to measure the dynamics of polymer-containing systems. Although XPCS is not used in the research presented in this dissertation, it is an emerging technique used to measure slow

dynamics in polymers. In essence, XPCS is just a time-resolved SAXS/WAXS experiment wherein many scattering snapshots are taken of the same sample over time and the intensity is tracked to provide insights into the dynamics of the system. More technically, XPCS quantifies the variation in the speckle pattern originated by the scattering of coherent light from a material with spatial inhomogeneities.[118] XPCS detects dynamics on similar length-scales as SAXS and WAXS. The temporal resolution of XPCS experiments is dictated by the instrument/hardware capabilities, most specifically the fastest frame rate that spectra can be collected with reasonable statistics. There have been significant improvements in the temporal resolution for XPCS through the development and implementation of ultra-fast X-ray cameras that allow for detection of dynamics at times as fast as 1 microsecond.[119]

Typically, in XPCS experiments, the dynamics are quantified at a q-vector that is identified by a speckle on the 2d scattering pattern. The speckle pattern is related to the spatial arrangement of the disordered scatterers. The change in intensity of the speckle pattern with respect to time is quantified by the autocorrelation function, $g_2(q_i, t)$. The decay of $g_2(q_i, t)$ is related to the relaxation time of the dynamics in the sample on the length-scale prescribed by q_i. Because XPCS relies on taking many spectra on the same sample spot over time, beam damage is large concern when conducting XPCS experiments.[120] XPCS has been previously used to study the cooperative grain dynamics of strongly segregated block copolymer electrolytes on the 10^{-2} - 10^{2} s time-scale,[82] as well as the relaxation processes in supercooled block copolymers[121] and multicomponent polymer blends.[122]

3.3 Neutron Scattering Techniques

Neutron scattering events are quasi-elastic and therefore provide both structural and dynamical information.[123] Currently, there are only three neutron research facilities in the United States: the National Center for Neutron Research at the National Institute of Standards and Technology in Gaithersburg, MD and the High Flux Isotope Reactor and Spallation Neutron Source both at Oak Ridge National Lab in Oak Ridge, TN.

Neutrons interact with the nuclei of the sample during a scattering event and therefore, the attenuation is isotope specific. The scattering intensity can be divided into two contributions, the coherent (I_{coh}) and incoherent (I_{incoh}) scattering intensity, and each elemental isotope has a specific coherent and incoherent scattering length density. The coherent scattering contributions provide information on the collective/pair dynamics and are typically used to provide information about structure since I_{coh} is q-dependent. In contrast, the incoherent scattering contributions are q-independent and therefore, do not provide any information about structure. Instead, I_{incoh} describes single-particle dynamics. Conveniently, hydrogen and deuterium have extremely different coherent and incoherent scattering length densities, and most often, a blend of hydrogenated and deuterated components is used to create neutron contrast. This synthetic scheme allows for neutron scattering experiments to be conducted on homogeneous or nearly-homogeneous systems such as homopolymers[124] or blends of polyolefins[125] without altering the interactions present within the system. In addition, ^{1}H has a large incoherent scattering cross

section, which allows for easy tracking of the dynamics of polymer chains. In this section we will cover three neutron scattering techniques, small angle neutron scattering, quasi-elastic neutron scattering, and neutron spin echo spectroscopy.

3.3.1 Small Angle Neutron Scattering (SANS). Small angle neutron scattering (SANS) is completely analogous to SAXS although it uses an incident neutron beam. In SANS experiments, the energy-exchange between the neutrons and the sample is ignored such that $S(q) = \int_{-\infty}^{\infty} S(q, \omega) d\omega$ is measured, which allows for detection of structure only. In the late 1980s, the introduction of pre-calibrated strongly scattering standards allowed for easy calibration of SANS instruments to absolute scattering.[126] This advancement, along with the development of easy-to-use data analysis software,[127,128] made SANS an extremely powerful tool to detect the thermodynamics of polymeric systems due to the ease of application of fundamental theories, such as RPA,[92,129] to scattering data. SANS has been used to measure the interaction parameters, χ, in multi-component polymer systems[130–133] as well as the statistical segment length of homopolymers in solutions[134,135] and the melt-phase.[136] In Chapter 7, SANS is used to determine the effect of salt concentration on the statistical segment length of homopolymer/salt mixtures.[137]

3.3.2 Quasi-Elastic Neutron Scattering (QENS). Quasi-elastic neutron scattering (QENS) measures the probability of a neutron scattering event as a function of space and energy, allowing for the detection of dynamics at specific length-scales.[138,139] The spatial and temporal range of QENS is dictated by the specific instrument, typically time-of-flight spectrometers or backscattering spectrometers. Time-of-flight spectrometers detect molecular vibrations at shorter times and therefore, do not cover relevant time-scales to study polymer dynamics. Backscattering spectrometers are used to study polymer dynamics and can detect dynamics at times as high as 2 ns. In backscattering experiments, the motions of the sample are probed by varying the energy of the incident neutrons and measuring their change in energy after interacting with the sample. The output function is therefore the dynamic structure factor in the energy domain, $S(q, \omega)$, which can be converted to the intermediate structure factor in the time domain, $S(q, t)$, through a Fourier transform.

QENS is sensitive to the incoherent scattering intensity and is, therefore, very useful in measuring the dynamics of hydrogen atoms. This allows for direct measurement of the dynamics of most polymer backbones without synthetic modification. QENS typically measures the segmental dynamics in polymers, which correlates to length-scales between 5 and 50 Å and time-scales between 0.1 and 2 ns.[140–142] The mean squared displacement, $< r^2(t) >$, of the hydrogen atoms can be readily calculated from the QENS data as given by[71]

$$S_{inc}(q, t) = \exp\left[-\frac{q^2}{6} < r^2(t) >\right] \tag{3.5}$$

The relationship between $< r^2(t) >$ and t provides insight into the mechanisms of the segmental dynamics, such as through the calculation of the monomeric friction coefficient, ζ, in the Rouse regime.[66] QENS has been used to study the dynamics in multicomponent polymer blends[140,143] and disordered block copolymer systems.[142] In polymer electrolytes, QENS has been used to measure ζ as a function of salt concentration. It has been shown that as salt concentration increases, the monomeric friction coefficient also increases.[15,80,144] Although QENS was not directly used in the

research presented in this dissertation, the aforementioned studies were instrumental in building a foundation for understanding polymer dynamics in the presence of ions.

3.3.3 Neutron Spin Echo (NSE) Spectroscopy. Neutron spin echo (NSE) spectroscopy is the newest technique discussed in this chapter. Instead of measuring the change in energy of the neutron beam before and after the scattering event, NSE measures the change in velocity of the neutrons through use of polarized neutrons. NSE takes advantage of the Larmor procession of the neutron's spin, which serves as an "internal clock" and stores information about the velocity of the neutron.[145] This strategy allows NSE to have the highest energy resolution among neutron spectrometers. In addition, NSE directly measures the intermediate scattering function in the time domain, $S(q,t)$, instead of the dynamic structure factor, $S(q,\omega)$. This makes NSE best suited to measure relaxation versus excitation processes.[71] In short, NSE covers the smallest q and E scales, which correspond to the longest length- and time-scales, making NSE extremely useful to measure polymer chain dynamics in both the Rouse and reptation regimes. For example, the two NSE instruments in the United States can measure dynamics up to 100 ns, and the best NSE spectrometer in the world can measure dynamics up to 500 ns.[146]

NSE probes single chain dynamics, which is related to $I_{coh}(q)$. Therefore, it is important to minimize the incoherent scattering intensity in NSE experiments. This is typically achieved through blends of hydrogenated and deuterated polymers in homogeneous systems or through selective deuteration of specific components in heterogeneous systems similar to the synthetic strategies used in designing SANS experiments. However, NSE includes contributions from both $I_{coh}(q)$ and $I_{incoh}(q)$ and, therefore, easy calculation of $< r^2(t) >$, according to Eq. 3.5, is not possible with NSE data. NSE samples typically require longer exposure times and the aforementioned synthetic modifications compared to QENS samples, which can limit the applicability of NSE experiments. NSE has been used extensively to study polymer dynamics in homopolymer[77,140,147–149] and nanocomposite[150,151] systems in both the Rouse and reptation regimes. There have only been a few studies using NSE on block copolymer systems, and these studies were limited to the Rouse regime ($t \leq 10$ ns).[152] In Chapter 8, NSE is used to probe the effect of salt concentration on the polymer chain dynamics of the salt-containing microphase of a model block copolymer electrolyte system.[153] This is the first study of the dynamics of ion-containing polymers in the reptation regime.

3.4 Conclusions

The goal of this chapter is to provide a basic background to scattering experiments and outline the most commonly used scattering techniques in polymer science, with a focus on X-ray and neutron techniques. Scattering experiments have emerged as powerful tools to gain insight on the structure and dynamics of polymer materials on the sub-micron length-scale. Through the advancement of particle physics instrumentation at synchrotron lightsources and neutron sources, the spatial and temporal ranges reached by scattering experiments have been significantly improved. Each scattering technique can answer a specific question, typically either structure or dynamics, at prescribed length- and time-scales, and thus, the use of a combination of scattering techniques is necessary to provide information on polymer behavior from the monomer to macroscopic length-scales.

3.5 Nomenclature

3.5.1 Abbreviations:

NEXAFS	Near Edge X-Ray Absorption Fine Structure
NSE	neutron spin echo
QENS	quasi-elastic neutron scattering
RSoXS	resonant soft X-ray scattering
RPA	random phase approximation
SANS	small angle neutron scattering
SAXS	small angle X-ray scattering
WAXS	wide angle X-ray scattering
XPCS	X-ray photon correlation spectroscopy

3.5.2 Symbols:

B_i	scattering length density of species *i*
E	energy of incident beam
E'	energy of scattered beam
$g_2(q_i, t)$	autocorrelation function
$\hbar$	reduced Planck's constant
I_{coh}	coherent scattering intensity
I_{incoh}	incoherent scattering intensity
k	momentum of incident beam
k'	momentum of scattered beam
m_n	mass of scattered neutrons
$P(q)$	form factor
q	scattering vector
q^*	primary scattering peak
$< r^2(t) >$	mean squared displacement
$S(q)$	structure factor
$S(q, t)$	intermediate scattering function
$S(q, \omega)$	dynamic structure factor
t	time

3.5.3 Greek Symbols:

θ	scattering angle
λ	wavelength of the incident beam
ζ	monomeric friction coefficient
ν_{ref}	reference volume
χ	Flory-Huggins interaction parameter
ω	angular frequency

4. Reentrant phase behavior and coexistence in asymmetric block copolymer electrolytes[†]

ABSTRACT

It is known that the addition of salts to symmetric block copolymers leads to stabilization of ordered phases and an increase in domain spacing; both trends are consistent with an increase in the effective Flory-Huggins interaction parameter between the blocks, χ. In this work, we show that the addition of salt to a disordered asymmetric block copolymer first leads to the formation of coexisting ordered phases which give way to a reentrant disordered phase at a higher salt concentration. The coexisting phases are both body centered cubic (BCC) with different domain spacings, stabilized by partitioning of the salt. Further increase in salt concentration results in yet another disorder-to-order transition; hexagonally packed cylinders are obtained in the high salt concentration limit. The coexisting phases formed at intermediate salt concentration, elucidated by electron tomography, showed the absence of macroscopic regions with distinct BCC lattices. This coexistence was further probed with resonant soft X-ray scattering to determine the relative salt concentration of each BCC lattice. A different asymmetric block copolymer with composition in the vicinity of the sample described above only showed only a single disorder-to-order transition. However, the dependence of domain spacing on salt concentration was distinctly non-monotonic, and similar to that of the sample with the reentrant phase behavior. This dependence appears to be an announcement of reentrant phase transitions in asymmetric block copolymer electrolytes. These results cannot be mapped on to the traditional theory of block copolymer electrolyte self-assembly based on an effective χ.

4.1 Introduction

Polystyrene-*block*-poly(ethylene oxide) (SEO) mixed with lithium bis(trifluoromethanesulfonyl) imide salt, SEO/LiTFSI, is a commonly studied block copolymer electrolyte system. The thermodynamic interactions in SEO/LiTFSI are often expressed in terms of an effective Flory-Huggins interaction parameter between the blocks, χ. Current work suggests that χ increases with increasing salt concentration.[53–55,58,154,155] The addition of salt to disordered block copolymers generally results in the formation of ordered phases.[57,156,157] Experimental work thus far focuses on symmetric (or nearly symmetric) block copolymers.[54,158,159] The purpose of this study is to describe the thermodynamic properties of a series of asymmetric block copolymer electrolytes with a majority polystyrene phase. Our work builds on previous studies on neat asymmetric block copolymers.[160–162] Particularly relevant is the limited long-range order observed in some asymmetric systems.[163–165] We report on disorder-order and order-order phase transitions that are very different from those reported in previous studies. In particular, we show that reentrant phase

[†] This chapter was reported in *Soft Matter*, **2018**, **14**, 2789 – 2795.

transitions are possible in these systems. The addition of salt to a disordered block copolymer first leads to the formation of ordered phases which give way to a reentrant disordered phase upon further salt addition. In the ordered state, we find two coexisting phases with the same geometry but different lattice constants.

4.2 Experimental Methods

4.2.1 Synthesis and preparation of the block copolymer electrolytes. The SEO copolymers were synthesized using methods described in ref. 83 and purified using methods described in ref. 58. The electrolytes were prepared according to methods described in ref. 166 using argon gloveboxes. SAXS samples were prepared by pressing/melting the polymer into a 1/8 in. diameter spacer made of 1/32 in. thick Aflas rubber and annealing them at 120 °C overnight followed by a 24 hour period of controlled cooling under vacuum to room temperature. The samples were sealed with Kapton windows.

4.2.2 Small Angle X-ray Scattering (SAXS). SAXS measurements were performed at beamline 7.3.3. at the Advanced Light Source (ALS) at Lawrence Berkeley National Laboratory[167] and beamline 1-5 at the Stanford Synchrotron Radiation Lightsource (SSRL) at SLAC National Accelerator Laboratory. Silver behenate was used to determine the beam center and sample-to-detector distance. The scattered intensity was corrected for beam transmission and empty cell scattering. Two-dimensional scattering patterns were integrated azimuthally using the Nika program for IGOR Pro to produce one-dimensional scattering profiles and are reported as scattering intensity, I, as a function of the scattering vector, q.[168] Measurements were taken in a custom-built 8-sample heating stage, starting at 132 °C and cooling in steps of about 10 °C to 75 °C. Samples were annealed for about 30 min at each temperature before taking measurements. A typical temperature scan takes about six hours (including time required to cool the sample stage). To a good approximation, the SAXS profiles of all our samples were independent of temperature in the range studied. We thus only discuss data obtained at the highest temperature in the main text. The temperature range of our SAXS experiments is well above the melting temperature of the crystallizable poly(ethylene oxide) (PEO) block. Data obtained at the lowest temperature, 75 °C, is shown in the Supporting Information.

4.2.3 Electron Tomography. A bulk sample, annealed using the same protocol used to prepare the SAXS samples, was sectioned at -120 °C using cryo-microtome (Leica Ultracut 6) to obtain an ultrathin film (~100nm). The ultrathin film was transferred to C-flat grid with ultrathin continuous carbon supporting film and stored in a glove box immediately after cryo-microtoming to minimize the effect of humidity. PEO domains were stained to increase contrast and stability under electron beam by exposing the ultrathin film to RuO_4 vapor for 10 minutes at room temperature. 5 nm gold colloid nanoparticles were deposited on the backside of the grid as fiducial markers. Dual-axis tomography was performed using Philps CM200 transmission electron microscope at 200 KV at the Donner Lab Electron Microscopy Facility at Lawrence Berkeley National Lab. The tilt series were collected with 1.5 degrees step from -65 to 65 degrees. Tomograms were reconstructed and

filtered (nonlinear anisotropic diffusion filter) in IMOD. The tomogram of a small area was binarized for segmentation by adjusting threshold.[169–171]

4.2.4 Resonant soft X-ray Scattering (RSoXS). RSoXS experiments were conducted on solvent-casted thin films of SEO/LiTFSI on 100 nm thick silicon nitride windows. Solutions of 5 mg/mL of SEO/LiTFSI were dissolved in n-methyl-2-pyrrolidone. The windows were heated to 120 °C and 4 μL of solution was dropped on to the heated window. The solvent was evaporated in the glovebox for 15 minutes before being transferred to a glovebox antechamber at 130 °C for 24 h under active vacuum. The antechamber was allowed to cool slowly to room temperature over 12 hr under active vacuum.

The RSoXS experiments were performed at beamline 11.0.1.2 at the Advanced Light Source.[111] Samples were measured using energies of 275-290 eV for C, 520-550 eV for O and 685-705 eV for F at a sample-to-detector distance of ~50 mm. Data were analyzed using a modified version of the same Nika program used in SAXS experiments. Data were normalized by incident beam intensity, blank window transmission and by subtracting out a dark image.

4.3 Phase Behavior

Table 4.1 Characteristics of polymers synthesized and used in this study

Polymer	M_{PS} (kg mol^{-1})	M_{PEO} (kg mol^{-1})	f_{EO}	PDI	N_{PS}	N_{EO}	N
SEO(17.4-3.9)	17.4	3.9	0.18	1.04	287	63	350
SEO(9.4-2.4)	9.4	2.4	0.20	1.04	155	39	194
SEO(9.4-4.0)	9.4	4.0	0.29	1.04	155	65	220

Parameters f_{EO}, N_{PS}, N_{EO} were evaluated at 140 °C

The properties of the polymers used in this study are given in Table 1. We refer to each copolymer by its molecular weight, for example, in SEO(9.4-4.0) the molecular weights of the polystyrene (PS) and PEO blocks are 9.4 kg mol^{-1} and 4.0 kg mol^{-1}. Figure 4.1 shows the scattering profiles of the block copolymer electrolytes at 132 °C at selected salt concentrations. LiTFSI concentrations are reported as the molar ratio of lithium ions to ethylene oxide moieties: $r = \frac{[Li]}{[EO]}$. For SEO(9.4-4.0), Figure 4.1a, we see that the addition of salt drives microphase separation, as previously reported.[55,58,172] The broad scattering peak obtained in the neat sample becomes sharper at r = 0.005. The scattering profiles obtained in this salt concentration regime ($0 \leq r \leq 0.005$) are consistent with a disordered state. Further increase of salt concentration to r = 0.01 results in dramatic sharpening of the primary scattering peak and the emergence of higher order scattering reflections at $\frac{q}{q^*} = \sqrt{3}$ and $\sqrt{4}$ where q^* is the location of the primary scattering peak, consistent with a hexagonally packed cylindrical phase (HEX). These reflections persist at all remaining salt concentrations, and at higher salt concentrations, $r \geq 0.025$, higher order reflections at $\frac{q}{q^*} = \sqrt{7}$ and $\sqrt{9}$ appear. For SEO(17.4-3.9), Figure 4.1b, the neat sample is also disordered, and the addition

of salt induces microphase separation at all measured salt concentrations ($0.005 \leq r \leq 0.075$). The higher order scattering reflections in this sample are located at $\frac{q}{q^*} = \sqrt{2}, \sqrt{3}$, and $\sqrt{6}$ indicative of a body center cubic spherical phase (BCC). The $\frac{q}{q^*} = \sqrt{2}$ peak is not detected for r = 0.01, 0.05, and 0.075 due to the broadening of the primary q^* peak.

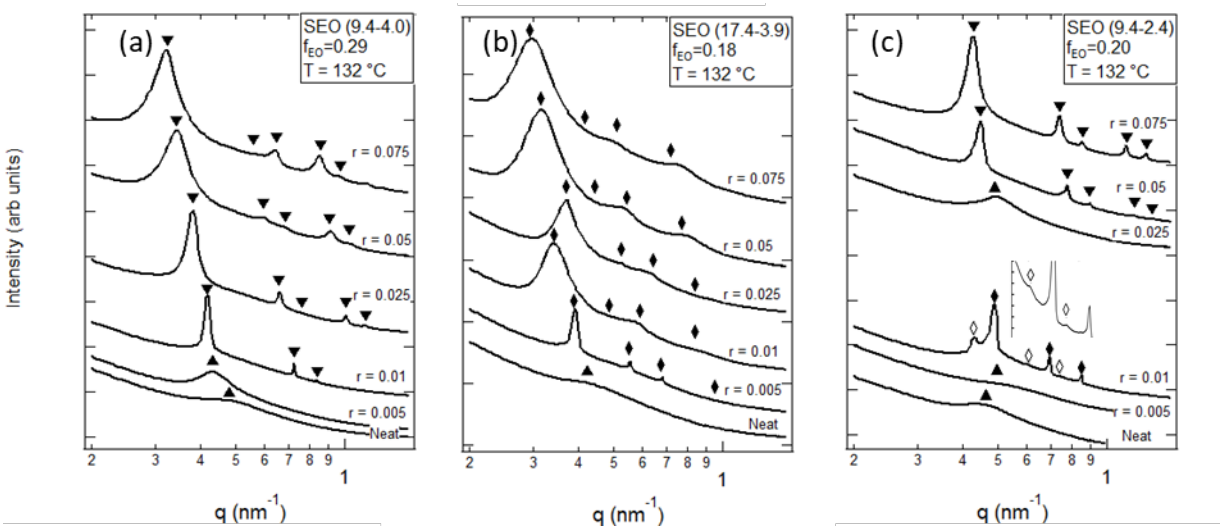

Figure 4.1. Salt Concentration Dependence of SAXS Profiles: SAXS profiles at 132 °C for (a) SEO(9.4-4.0), (b) SEO(17.4-3.9) and (c) SEO(9.4-2.4) at varying salt concentrations. The ▲, ▼, ◆ represent primary and higher ordering scattering peaks for morphologies DIS, HEX, BCC respectively. The presence of both filled and open symbols indicates coexistence between ordered phases.

More complex phase transformations are seen with SEO(9.4-2.4), Figure 4.1c. The neat polymer is disordered as is the mixture with r = 0.005. However, we see the emergence of two coexisting BCC phases at r = 0.01. The scattering signatures of the larger BCC lattice are indicated by open symbols while those of the smaller BCC lattice are indicated by filled symbols. Reflections at $\frac{q}{q^*} = \sqrt{2}$ and $\sqrt{3}$ corresponding to both lattices are seen in Figure 4.1c. To our knowledge, two coexisting lattices with the same symmetry have been neither observed nor predicted in block copolymer systems. The domain spacing, given by $d = \frac{2\pi}{q^*}$, of the two coexisting BCC lattices are 12.8 and 14.8 nm. It is apparent that the two BCC phases must have different salt concentrations; if this were not the case, it is impossible to rationalize the presence of two coexisting morphologies.[99] Further increase in overall salt concentration to r = 0.025 results in the formation of a reentrant disordered phase. Finally, at r = 0.05 and r = 0.075, a single HEX phase is obtained with higher order scattering reflections at $\frac{q}{q^*} = \sqrt{3}, \sqrt{4}, \sqrt{7}$ and $\sqrt{9}$. SEO(9.4-2.4) exhibits phase behavior that appears to be a combination of behaviors observed in SEO(9.4-4.0) and SEO(17.4-3.9). While SEO(9.4-4.0) and SEO(17.4-3.9) electrolytes exhibit HEX and BCC phases in the ordered state, SEO(9.4-2.4) electrolytes exhibit both ordered phases. For all three block copolymers, the addition of salt results in broadening of SAXS peaks associated with the ordered phase, suggesting a decrease in long-range order. In previous studies, we have used TEM to establish this effect, which

arises due to the formation of temporary crosslinks created by the coordination of PEO chains and Li^+ ions that impede chain motion.[173]

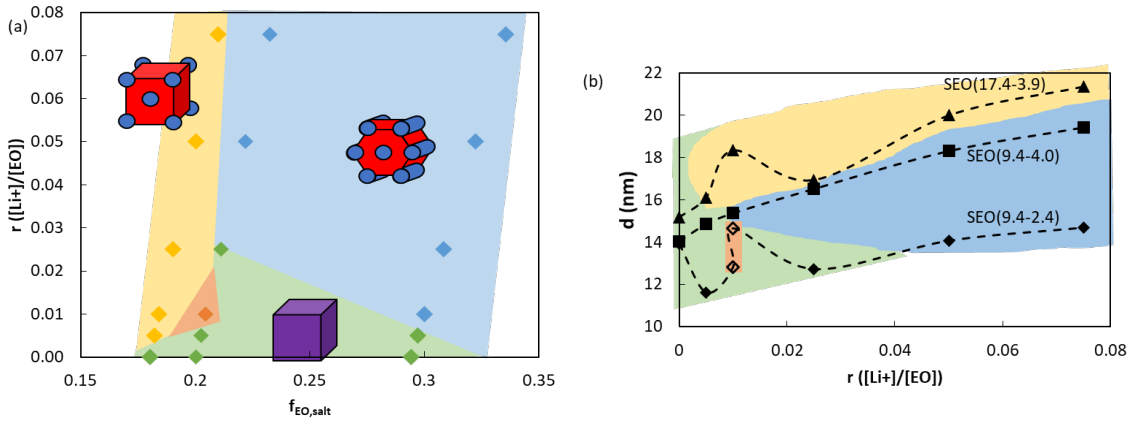

Figure 4.2. Phase Diagrams of SEO/LiTFSI: a) Phase behavior of SEO/salt mixtures on a plot of salt concentration versus volume fraction of the PEO-rich conducting microphase at 75 °C -132 °C. b) Domain spacing of a series of SEO block copolymers at 132 °C as a function of salt concentration. For both diagrams, the yellow, blue, green and orange regions correspond to BCC, HEX, DIS, and coexisting BCC phases, respectively.

The disordered and ordered morphologies of the block copolymer electrolytes are shown in Figure 4.2a on a plot of salt concentration in the PEO domains, r, versus volume fraction of the PEO-rich domains, $f_{EO,salt}$. We calculate $f_{EO,salt}$ based on the assumption that LiTFSI preferentially segregates into the PEO domains and from reported densities of LiTFSI/PEO mixtures in ref 19.[29,30] The phase diagram contains three sets of data points representing the three polymers; as salt is added to the copolymer, $f_{EO,salt}$ increases linearly with r for each polymer. SEO(9.4-4.0) and SEO(17.4-3.9) exhibit one salt-induced phase transformation from DIS to HEX and DIS to BCC respectively. SEO(9.4-2.4) exhibits three phase transformations: DIS to coexisting BCC lattices to DIS to HEX. The Gibbs phase rule requires coexistence at all phase boundaries. We conclude that the widths of all of the coexistence windows in the samples are smaller than our coarse steps in salt concentration; for example, the Gibbs phase rule necessitates coexistence of DIS and BCC phases at the disorder-order boundary.[157] The origin of the two coexisting BCC lattices, which were observed throughout the entire temperature window in two independently prepared samples, is thus not clear. Figure 4.2a thus applies to the entire temperature window. The fact that the morphologies of the copolymers listed in Table 1 can be represented on a simple r versus $f_{EO,salt}$ diagram (Figure 4.2a) is non-trivial.

The effect of added salt on block copolymer thermodynamics is due to two competing factors: (1) the addition of salt generally increases the effective χ between the blocks and induces ordering, (2) the salt molecules partition into and swell the PEO domains, thereby increasing f_{EO}. The f_{EO} of neat SEO(9.4-2.4) is 0.20, which is at the border between BCC and HEX phases. (Floudas et al. studied the phase behavior of poly(ethylene oxide)-block-polyisoprene block copolymers, where the BCC/HEX border was identified at $f_{EO} = 0.21$.[162]) Adding salt to SEO(9.4-2.4) at $r = 0.01$ results in the formation of coexisting BCC lattices consistent with (1). The salt concentration at this

composition does not result in sufficient swelling of the PEO domain to obtain hexagonally packed PEO cylinders. This phase is only formed at $r \geq 0.05$. The disordered phase at an intermediate salt concentration, $r = 0.025$, is due to the interplay between the two competing factors.

The dependence of domain spacing, *d,* on salt concentration, *r*, is shown in Figure 4.2b. The colors in the figure depict the morphology of the electrolytes. The simplest behavior is seen in SEO(9.4-4.0) wherein *d* increases monotonically with increasing *r* with no discontinuity at the DIS to HEX transition.[53,54,58] The domain spacing of neat SEO(9.4-2.4) is identical to that of neat SEO(9.4-4.0), but it decreases with increasing salt concentration before increasing at $r = 0.01$ where two coexisting BCC lattices are obtained. It is unusual that a salt-containing sample would have a lower *d* compared to its neat counterpart. Further increase of salt concentration results in a decrease in *d* as the sample disorders. At $r \geq 0.025$, *d* increases monotonically with increasing *r* with no discontinuity at the DIS to HEX transition. The dependence of *d* on *r* of SEO(17.4-3.9) is most interesting. This sample exhibits a simple DIS to BCC transition, but the dependence of *d* on *r* is non-monotonic, similar to that of SEO(9.4-2.4). These two copolymers have similar compositions but their chains lengths differ by a factor of 1.8. One may thus regard the non-monotonic dependence of *d* on *r* in SEO(17.4-3.9) as "announcements" of BCC coexistence at lower molecular weights in the same composition window.

The chains of SEO(9.4-2.4) at $r = 0.01$ exhibit different extents of chain stretching, depending on the BCC lattice they belong to. The reason for the fact that the coexisting morphology has a lower free energy than that of a single BCC phase with intermediate chain stretching remains to be determined. Computer simulations suggest that each lithium ion is associated with six coordinating oxygen atoms.[16,174,175] Perhaps, discrete chain conformations are preferred due to these interactions, and the free energy gain from adopting these conformations is large enough to offset the entropic penalty of heterogeneous salt distribution.

4.4 Probing Coexistence of Ordered Morphologies

The nature of the coexisting BCC lattices was further studied by transmission electron tomography. We are not aware of any prior studies wherein electron tomography has been used to study the morphology of weakly ordered block copolymers in the vicinity of order-disorder transitions. Three dimensional tomograms were obtained from the $r = 0.01$ sample of SEO(9.4-2.4)/LiTFSI stained with RuO_4. Figure 4.3a shows slices of the tomogram obtained from dual-axis reconstruction of the data. The dark domains represent the RuO_4 stained PEO/LiTFSI spherical domains. Electron tomography confirms that the sample contains only spheres, consistent with our interpretation of the SAXS profile. It is also evident, however, that our sample does not contain easily identifiable macroscopic regions with two different lattice constants. Some regions did, however, show evidence of BCC lattices with limited long-range order. One such region is shown in Figure 4.3b. Quantitative analysis of the entire tomogram is necessary to reveal correlations between the spherical domains.

The nature of the coexisting BCC lattices was further studied by transmission electron tomography. We are not aware of any prior studies wherein electron tomography has been used to study the morphology of weakly ordered block copolymers in the vicinity of order-disorder transitions. Three dimensional tomograms were obtained from the $r = 0.01$ sample of SEO(9.4-2.4)/LiTFSI

stained with RuO_4. Figure 4.3a shows slices of the tomogram obtained from dual-axis reconstruction of the data. The dark domains represent the RuO_4 stained PEO/LiTFSI spherical domains. Electron tomography confirms that the sample contains only spheres, consistent with our interpretation of the SAXS profile. It is also evident, however, that our sample does not contain easily identifiable macroscopic regions with two different lattice constants. Some regions did, however, show evidence of BCC lattices with limited long-range order. One such region is shown in Figure 4.3b. Quantitative analysis of the entire tomogram is necessary to reveal correlations between the spherical domains.

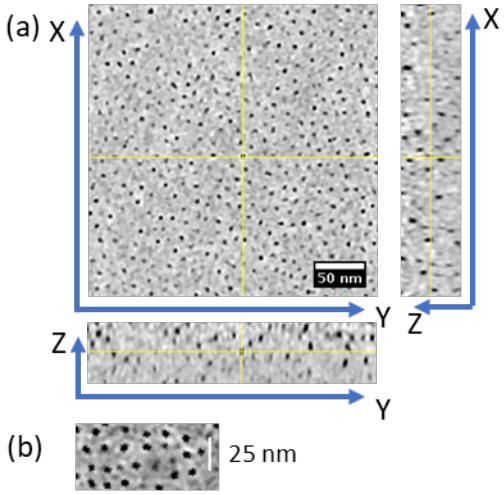

Figure 4.3. Electron Tomography of Coexisting Morphologies: (a) Tomogram obtained from dual-axis reconstruction of RuO_4 stained SEO/LiTFSI $r = 0.01$ sample. Dark domains represent the RuO_4 stained PEO block. (b) Region of tomogram with increased long-range order. Scale bar represents 25 nm.

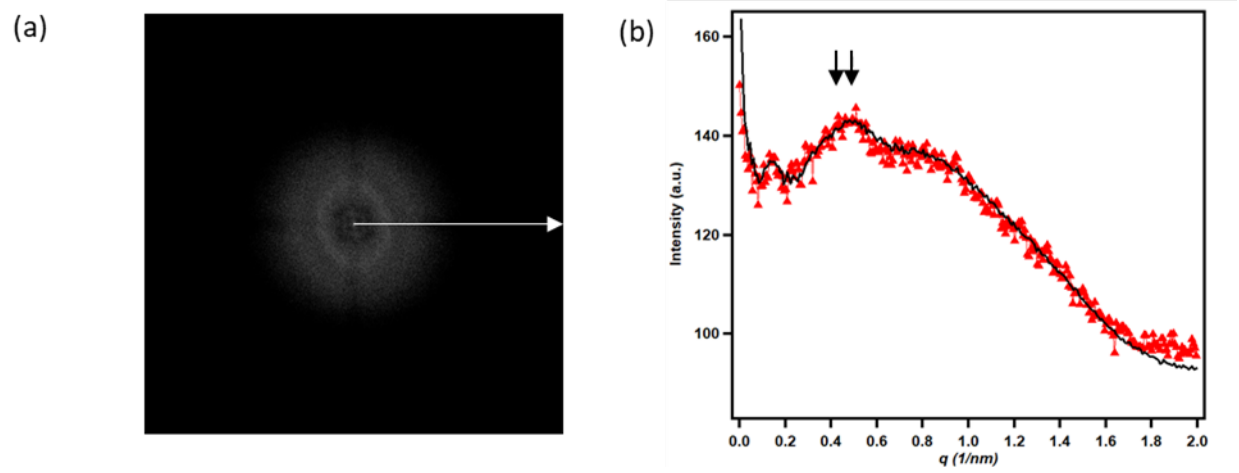

Figure 4.4. Inverse Space Representation of Tomogram: (a) FFT of single slice of tomogram. Sector average was performed along the white arrow. (b) Sector averaged (red triangles) and circular averaged (black line) intensity versus scattering vector, q. The black arrows indicate the locations of the observed primary SAXS peaks.

Figure 4.4a shows the Fourier transform (FT) of a typical slice obtained by electron tomography; e.g. see Figure 4.3a. The anisotropy of the FT is attributed to distortion due to compression along one axis during cryo-sectioning. Figure 4.4b shows a sector-averaged intensity versus scattering vector, q, for the FT. The averaging was conducted along the non-compressed axis, indicated by the white arrow in Figure 4.4a. The circularly averaged FT of the same slice, shown by a continuous black line in Figure 4.4b is qualitatively similar to the sector-averaged FT. The FT analysis was repeated for several slices and the results of three slices are given in Section 4.5 (Figure 4.7). All of the FTs are very similar to that given in Figure 4.4b. The arrows in Figure 4.4b indicate the positions of the primary peaks observed in SAXS; recall that SAXS revealed the presence of two BCC lattices. There is reasonable agreement between the FT peak and the SAXS data. The relatively subtle difference in the lattice constants of the coexisting BCC structures obtained by SAXS are lost in the FT analysis. We posit that this is due to complications related to the electron tomography experiments such as missing spheres due to incomplete staining and distortions during cryo-sectioning. While our TEM data provide support for our interpretation of the SAXS profile of SEO(9.4-2.4) $r = 0.01$, it also reveals the complexity of coexisting phases that are obtained in the vicinity of order-disorder transitions.

A new technique, resonant soft X-ray scattering (RSoXS), can be used to study the spatial distribution of salt within the nanostructured block copolymer. RSoXS combines SAXS with Near Edge X-Ray Absorption Fine Structure, NEXAFS, spectroscopy to obtain energy-dependent scattering profiles. Previous RSoXS studies have been conducted to determine complex morphologies in triblock copolymers by taking advantage of block-specific resonant signatures in absorption along the carbon K-edge.[116] We can view SEO/LiTFSI as a similar three-component system and can utilize the different elements in each component to extract structural information.

Our RSoXS experiments have shown that coexistence of ordered morphologies can be seen in SEO/LiTFSI thin film samples and the coexistence persists throughout the probed energy spectra. Figure 4.4 shows the scattering data for a 400 nm thin film of SEO(9.4-2.4) $r = 0.025$ at the C (282 eV), O (533 eV) and F (692 eV) K-edges. There are two peaks corresponding to ordered structures with domain spacings of 13 and 13.75 nm. We attribute the higher salt concentration necessary to induce coexistence, as compared to hard X-ray bulk experiments, to thin film effects. We also assume that this structure has the same ordered morphology as bulk samples and contains two coexisting BCC lattices; however, no higher order reflections are seen in the RSoXS profiles, so TEM micrographs will be necessary to confirm the thin film morphology. Although the domain spacings of the two lattices are consistent throughout the probed energies, the relative intensities and shapes of each peak change, suggesting that the local structure and elemental composition of the coexisting phases differ.

We can decipher specific structural information about the three-component system from the profiles taken at each probed energy. Separate NEXAFS experiments were conducted on pure PS, PEO as well as PEO/LiTFSI samples of various salt concentrations to determine the absorption spectra of each phase at each range of energies. The cartoons in Figure 4.5 depict what components of the BCC lattice are “seen” at each energy: red represents PS, blue PEO, and yellow TFSI. When the components are shown in gray, they are “invisible” at the probed energy. Because both PS and

PEO contain C, we can extract the size and relative amounts of each lattice from the C K-edge. O is only found in PEO and TFSI, and therefore is confined primarily to the spheres of the BCC lattice. It can be used to measure the degree of microphase separation within each lattice and the distance between spheres. Finally, the F K-edge is unique to TFSI and reveals how much salt is present in each lattice. It is important to note that when the F K-edge was probed for a SEO sample without salt, no scattering was observed.

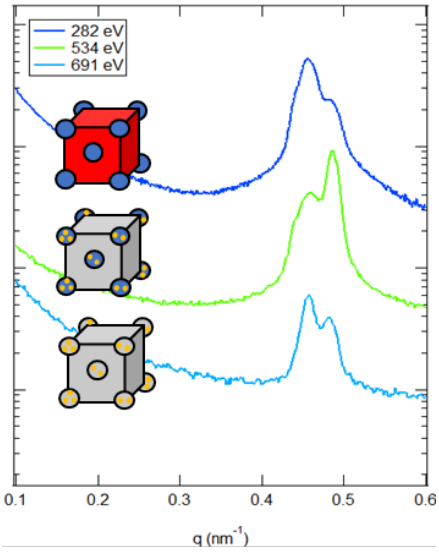

Figure 4.5 RSoXS Spectra: RSoXS scattering profiles of SEO(9.4-2.4) r = 0.025 at the C (282 eV, dark blue), O (533 eV, green), and F (692 eV, light teal) K-edges. Schematics show which species are "visible" at each energy.

In order to quantify these observations, we computed the scattering invariant (Q_i) of each peak for each probed energy:

$$Q_i = \int I_i(q) q^2 dq \text{ for } i = 1, 2 \tag{4.1}$$

where each BCC microphase is represented by one of the two ordered scattering peaks. For a heterogeneous system with two distinct phases, the invariant is independent of morphology and only depends on the volume of one of the phases.[93] It has been previously shown that this quantity is bounded and was used to determine the volume fraction of the ordered phase in an SEO/LiTFSI system exhibiting coexistence between disordered and lamellar phases near the order-disorder transition.[157] From the calculated scattering invariants, we can calculate the volume fraction of each ordered phase, $\phi_{i,j}$, for each element, j, within the system:

$$\phi_{i,j} = \frac{Q_{i,j}}{Q_{i,j}+Q_{i,j}} \text{ for } i = 1, 2 \text{ and } j = C, O, F \tag{4.2}$$

The resulting volume fraction information is provided in Table 4.2.

Based on this information, we can determine the elemental composition of each microphase. From the carbon volume fraction, it is clear that a majority of the polymer chains are segregated into the

microphase with a larger domain spacing. However, based on the fluorine volume fraction, we know that the volume of salt is evenly distributed between the two microphases. Therefore, phase 2, or that with a smaller domain spacing, must have a higher molar ratio, or *r*-value, of LiTFSI. This finding contradicts our original hypothesis and previous work showing that the domain spacing of block copolymer electrolytes scales with salt concentration.[53,58]

Table 4.2 Volume fractions of each element in each phase determined from RSoXS

	Phase 1	*Phase 2*
Carbon	0.73	0.27
Oxygen	0.45	0.55
Fluorine	0.45	0.55

It's important to note that the RSoXS data is preliminary and due to sample fabrication inconsistencies, it is also not reproduceable. Low molecular weight SEO copolymers do not form homogeneous thin films. It would be, perhaps, instrumental to run analogous RSoXS experiments on block copolymer electrolytes that can form homogeneous thin films such as PS-*b*-POEM.[30,31]

4.5 Conclusions

In conclusion, we have determined the morphology of mixtures of asymmetric block copolymers and a lithium salt by SAXS and electron tomography. SAXS results show that the addition of salt to a disordered asymmetric block copolymer first leads to the formation of coexisting BCC lattices, which give way to a reentrant disordered phase at a higher salt concentration. Further increase in salt concentration results in the formation of hexagonally packed cylinders. Electron tomography showed the absence of macroscopic regions with distinct BCC lattices. However, the Fourier transforms of tomogram slices were qualitatively consistent with the SAXS results. Doubling the chain length at fixed composition (or nearly so) resulted in a single disorder-to-order transition with added salt. Reducing the asymmetry at fixed chain length (or nearly so) also resulted in a single disorder-to-order transition with added salt. These results cannot be mapped on to any of the existing theories of the thermodynamics of block copolymer/salt mixtures.[51,59,176,177]

4.6 Nomenclature

4.6.1 Abbreviations:

BCC	body center cubic
DIS	disordered
FT	Fourier transform
HEX	hexagonally packed cylinders
LiTFSI	lithium bis(trifluoromethanesulfonyl) imide salt
NEXAFS	near edge X-ray absorption fine structure
PEO	poly(ethylene oxide)
PS	polystyrene
RSoXS	resonant soft X-ray scattering

SAXS	small angle X-ray scattering
SEO	polystyrene-*block*-poly(ethylene oxide)
TEM	transmission electron microscopy

4.6.2 Symbols:

d	domain spacing (nm)
$f_{EO,salt}$	volume fraction of the PEO/LiTFSI phase
f_{EO}	volume fraction of PEO phase
I	scattering intensity
M_{PEO}	number-averaged molecular weight of the PEO block (kg mol^{-1})
M_{PS}	number-averaged molecular weight of PS block (kg mol^{-1})
N	number-averaged degree of polymerization (sites chain^{-1})
q	scattering vector (nm^{-1})
q^*	scattering vector at the primary peak (nm^{-1})
Q_i	scattering invariant
r	salt concentration ([Li^+] [EO]$^{-1}$)

4.6.3 Greek Symbols:

$\phi_{i,j}$	volume fraction of each ordered lattice, *i*, for each element, *j*
χ	Flory-Huggins interaction parameter

4.7 Supporting Information

4.7.1 Small Angle X-ray Scattering

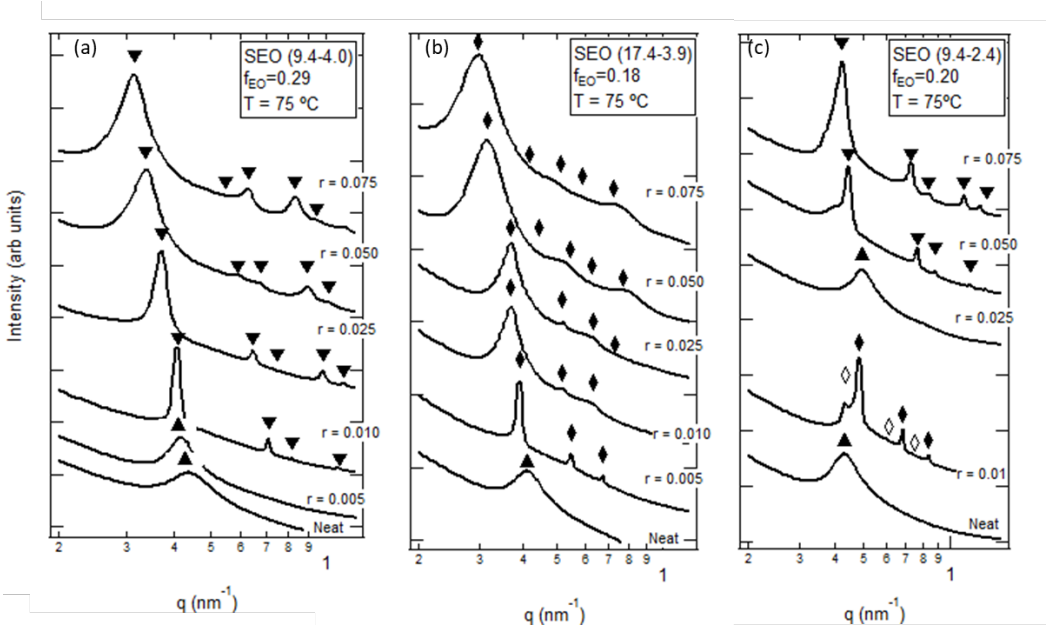

Figure 4.6. SAXS Profiles of SEO/LiTFSI at Low Temperature: SAXS profiles at 75 °C for a) SEO (9.4-4.0) b) SEO (17.4-3.9) and c) SEO (9.4-2.4) at varying salt concentrations. The symbols marking the primary peaks and higher order reflections match those used in the main text.

4.7.2 Electron Tomography

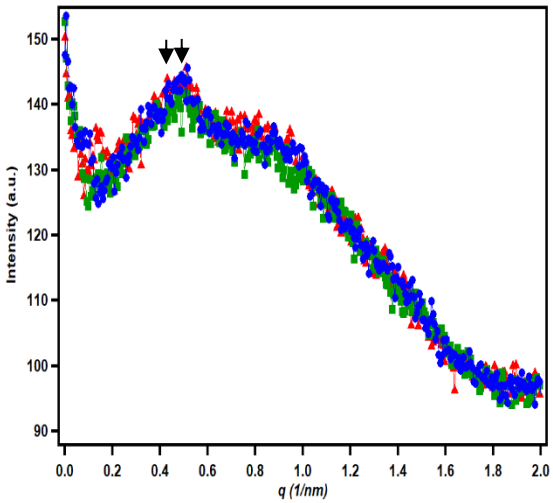

Figure 4.7. Inverse Space Representation of Tomogram: Sector-averaged FFT of tomogram slice 10 (red triangles), 20 (blue circles), and 30 (green squares) showing overall intensity as a function of q. The arrows indicate the primary peak positions of each BCC lattice detected in SAXS. There is good agreement in sphere-to-sphere spacing between TEM and SAXS throughout the tomogram.

5. Phase Behavior of Mixtures of Block Copolymers and a Lithium Salt[†]

ABSTRACT

We present experimental results on the phase behavior of block copolymer/salt mixtures over a wide range of copolymer compositions, molecular weights and salt concentrations. The experimental system comprises polystyrene- *block* -poly(ethylene oxide) and lithium bis(trifluoromethanesulfonyl) imide (LiTFSI) salt. It is well established that LiTFSI interacts favorably with poly(ethylene oxide) relative to polystyrene. The relationship between chain length and copolymer composition at fixed temperature is U-shaped, as seen in experiments on conventional block copolymers and as anticipated from the standard self-consistent field theory (SCFT) of block copolymer melts. The phase behavior can be explained in terms of an effective Flory-Huggins interaction parameter between the polystyrene monomers and poly(ethylene oxide) monomers complexed with the salt, χ_{eff}, which increases linearly with salt concentration. The phase behavior of salt-containing block copolymers, plotted on a segregation strength versus copolymer composition plot, is similar to that of conventional (uncharged) block copolymer melts, when the parameter χ_{eff} replaces χ in segregation strength.

5.1 Introduction

There is considerable interest in the potential use of microphase-separated block copolymers as solid electrolytes for lithium batteries.[22,24,178,179] A commonly studied system is polystyrene-*block*-poly(ethylene oxide) (SEO) mixed with lithium bis(trifluoromethanesulfonyl) imide salt (LiTFSI), SEO/LiTFSI. The transport of lithium ions in poly(ethylene oxide) (PEO) has been fully characterized[19], and polystyrene (PS) acts as the mechanical reinforcement for the solid electrolyte.

The phase behavior of pure diblock copolymers has been thoroughly investigated.[39,41] The equilibrium phase behavior is controlled by two parameters: the volume fraction of one polymer block, f_A, and the segregation strength, χN, where N is the overall degree of polymerization and χ is the Flory-Huggins interaction parameter, which measures the thermodynamic compatibility between the two blocks. At high temperatures, entropic contributions dominate and the system forms a homogeneous disordered phase. As temperature decreases, interactions between the two polymer blocks become more important, which leads to microphase separation into ordered morphologies. For a given block copolymer, characterized by f_A and N, the transition from disorder-to-order occurs at a critical value of χ, a parameter that generally increases as temperature decreases. The morphologies observed in neat block copolymers include lamellae (LAM), bicontinuous gyroid phases (GYR), hexagonally packed cylinders (HEX) and body center cubic spheres (BCC), among others.[40,180] Self-consistent field theory (SCFT)[180] and the Random Phase Approximation (RPA)[34] have emerged as powerful tools for understanding the relationship

[†] This chapter was reported in *J. Phy. Chem. B,* **2018**, 122 (33), 8065-8074 and *J Poly. Sci. B,* **2019**, *57*, 1177-1187.

between molecular structure, interactions, and phase behavior in conventional (uncharged) block copolymers.

In the weak segregation limit (WSL) *i.e.* in the vicinity of the order-disorder transition (ODT), the composition dependence of the periodic length-scale of ordered block copolymer phases, d, was calculated numerically by Leibler.[34] The length scale of the periodic phase in an ordered block copolymer is a reflection of molecular size. In a homopolymer, molecular size is often characterized by the radius of gyration, $R_g = N^{\frac{1}{2}}b/\sqrt{6}$, where b is the statistical segment length of the chain.[32,45] In Leibler's theory, d is given by the product $R_g D(f_A)$ where D is a dimensionless parameter that is a function of the composition of the block copolymer, f_A, and is provided in ref 34.

It has been shown experimentally that the addition of salt affects the phase behavior of block copolymers.[54,55,91,172,181] Several theoretical groups have worked on the molecular underpinnings of these observations.[62,155,176,177,182] The thermodynamics of these systems are affected by several factors that are not included in theoretical studies of conventional block copolymers. These factors include electrostatic interactions, charge dissociation, ion solvation, and physical cross-linking of chains due to the presence of ions. In early work, Wang and coworkers determined that ion solvation has the largest effect on the energetics of block copolymer/salt systems and added a term that they called "Born solvation energy" into a thermodynamic model.[50,51,155] This work suggests that the phase behavior of block copolymer/salt mixtures is similar to that of conventional block copolymers, provided χ is replaced by an effective interaction parameter, χ_{eff}, which accounts for the solvation energy contribution. In the simplest case, χ_{eff} increases linearly with salt concentration according to:

$$\chi_{eff} = \chi_0 + mr \tag{5.1}$$

where χ_0 is the Flory-Huggins interaction parameter of the neat system, r is the salt concentration given by $r = \frac{[Li]}{[EO]}$ and m is a proportionality constant. This form for χ_{eff} was anticipated nearly three decades ago in the pioneering experimental studies by Mayes et al.[52] More recent theoretical work that accounts for salt-induced physical crosslinking indicates that Equation 5.1 still holds, although m must be redefined to account for the coupled and non-additive effects of ion-crosslinking and solvation energy.[183]

Theoretical work by de la Cruz and coworkers uses SCFT in conjunction with a hybrid liquid-state theory to account for electrostatic interactions in ion-containing copolymers.[59,60,184] We refer to this theory as Ionic-SCFT. This theory attempts to correct for charge ordering induced by ion correlations by explicitly adding an electrostatics term in conjunction with χ_0.[60] The surprising conclusion of this work is that the phase behavior of ion-containing block copolymers is qualitatively different from that of conventional block copolymers. In particular, the ordered phase window at low values of $\chi_0 N$ contains a "chimney" at low values of f_A (where A is the ionic block).[61] In polymers with low dielectric constants, such as PS and PEO, ordered phases with inverted morphologies (e.g. cylinders of B in a matrix of A) are predicted in the chimney.[59] We note that the phase diagram of conventional block copolymers is devoid of any chimney-like feature.

The purpose of this study is to present experimental data on the phase behavior of SEO/LiTFSI mixtures in the vicinity of the ODT. The chain lengths of the SEO block copolymers were chosen such that the systems were disordered in the neat state. The volume fractions of the PEO blocks in our neat copolymers cover the range, $0.18 \leq f_{EO} \leq 0.84$, and focus on compositionally asymmetric systems ($f_{EO} \neq f_S \neq 0.50$) to supplement previous work on symmetric systems.[91] The ordered morphologies that emerged upon the addition of salt were determined primarily by small angle X-ray scattering (SAXS). Our data enables a critical examination of theories described above. In addition, this study includes a literature review of previously reported phase behavior on SEO copolymers mixed with two different lithium salts. Our objective is to organize literature data into a few simple plots where we examine the effect of added salt on the phase behavior and domain spacing of block copolymer electrolytes.

5.2 Experimental Methods

5.2.1 Polymer Synthesis and Characterization. The SEO copolymers in this study were synthesized, purified and characterized using methods described in ref 83,91. In this study, the polymers are named SEO (*xx-yy*), where *xx* and *yy* are the number-averaged molecular weights of PS, M_{PS}, and PEO, M_{PEO}, in kg mol^{-1}. The volume fractions of each block of the copolymers are given by

$$f_{EO} = \frac{\nu_{EO}}{\nu_{EO} + \frac{M_{PS}M_{EO}}{M_S M_{PEO}}\nu_S} \tag{5.2}$$

where v_{EO} and v_S are the molar volumes of ethylene oxide and styrene monomer units, and M_{EO} and M_S are the molar masses of ethylene oxide (44.05 g mol^{-1}) and styrene (104.15 g mol^{-1}). Molar volumes were calculated by $v = M/\rho$. In this study, the densities of the PEO and PS blocks were given by $\rho_{PEO} = 1.139 - 7.31 \times 10^{-4} \times T$ and $\rho_{PS} = 1.08665 - 6.19 \times 10^{-4} \times T + 1.36 \times 10^{-7} \times T^2$.[91] The overall degree of polymerization, N, was calculated by $N = N_{PS} + N_{PEO}$ where

$$N_i = \frac{M_i}{\rho_i(T) N_A \nu_{ref}} \tag{5.3}$$

and N_A is Avogadro's number and ν_{ref} was fixed at 0.1 nm^3. Table 5.1 contains polymer characteristics, including the polydispersity indices, of the block copolymers in this study. The neat copolymers are completely transparent and colorless.

5.2.2 Electrolyte Preparation. The salt-containing copolymers were prepared using methods described in ref 157. Due to the hygroscopic nature of the salt, Argon environment gloveboxes (Vacuum Atmosphere Company) with low oxygen and water levels were used for all sample preparation. The molar ratio of lithium ions to ethylene oxide (EO) moieties, *r,* is used in this study to quantify salt concentration. The number of EO units per polymer chain is calculated from M_{PEO} without correcting for end groups. We assume that the all of the salt resides in the PEO domain [29–31] and determine the volume fraction of the salty PEO domain by

$$f_{EO,salt} = \frac{\nu_{EO,salt}}{\nu_{EO,salt} + \left(\frac{M_{PS}M_{EO}}{M_S M_{PEO}}\right)\nu_S} \tag{5.4}$$

where $\nu_{EO,salt}$ is the molar volume of salt-containing PEO calculated by $\nu_{EO,salt} = \frac{M_{PEO}}{\rho_{EO,salt}(r)}$ where $\rho_{EO,salt}(r)$ is taken from ref 19. By using the measured density of salty PEO, we have accounted for the volume change of mixing within the PEO-rich domains. We assume that the monomer volume of PS is unaffected by the addition of salt; measured densities of SEO(5.1-12.8)/LiTFSI mixtures indicate that this is an excellent assumption. A full list of properties for the salt-containing samples used in this study can be found in Table 5.2.

Table 5.1: Characteristics of polymers used in this study.

Polymer	M_{PS} (kg mol^{-1})	M_{PEO} (kg mol^{-1})	f_{EO}	N
SEO(17.4-3.9)	17.4	3.9	0.18	350
SEO(9.4-2.4)	9.4	2.4	0.20	194
SEO(9.4-4.0)	9.4	4.0	0.29	220
SEO(3.8-8.2)	3.8	8.2	0.68	195
SEO(5.1-12.8)	5.1	12.8	0.72	291
SEO(4.0-22.4)	4.0	22.4	0.85	428
SEO(1.9-0.8)	1.9	0.8	0.29	47
SEO(1.4-1.6)	1.4	1.6	0.52	52
SEO(1.7-1.4)	1.7	1.4	0.44	54
SEO(2.9-3.3)	2.9	3.3	0.52	108
SEO(4.9-5.5)	4.9	5.5	0.52	181
SEO(16-16)	16.0	16.0	0.49	556

Data for SEO(1.9-0.8), SEO(1.4-1.6), SEO(1.7-1.4), SEO(2.9-3.3), SEO(4.9-5.5) are taken from a previous publication (ref 58*) and data for SEO(16-16) are taken from ref* 185*. N and f_{EO} were calculated at 140 °C.*

5.2.3 Small Angle X-ray Scattering (SAXS) Measurements. SAXS samples were prepared by and thermally pre-treated according to methods described in ref 106. SAXS measurements were conducted at the Advanced Light Source beamline 7.3.3 at Lawrence Berkeley National Lab[167] and Stanford Synchrotron Radiation Light Source beamline 1-5 at SLAC National Accelerator Laboratory. In order to compare data collected at each beamline, temperature calibrations were conducted to measure the absolute temperature of the samples by making separate electrolyte samples with a thermocouple running through the sample holder. The data presented in the main text reflects the absolute temperatures of the samples. Silver behenate was used to determine the beam center and sample-to-detector distance. The scattered intensity was corrected for beam transmission, empty cell scattering, as well as for unavoidable air gaps in the system. Two-dimensional scattering patterns were integrated azimuthally using the Nika program for IGOR Pro to produce one-dimensional scattering profiles.[168] Measurements were taken in a custom-built 8-sample heating stage, starting at 132 °C and cooling in steps of about 10 °C to 75 °C. Samples were annealed for about 30 min at each temperature before taking measurements.

5.2.4 Depolarized Light Scattering (DPLS). The samples for DPLS were prepared like SAXS samples but were sealed between quartz windows in custom-designed airtight aluminum sample holders.[186] The light source was a continuous-wave diode laser with a wavelength of 633 nm and an output power adjustable from 0 to 40 mW. The sample was placed between crossed polarizers in a heating block that was electrically heated by two heating elements, and the temperature of the sample was controlled by an Omega Engineering temperature controller (CN9111A).[187] In order to determine the order-disorder transition temperature (T_{odt}) of the sample, the birefringence method was employed.[188] In the order-to-disorder experiments, the total depolarized transmitted laser power was obtained as the sample was heated in approximately 10 °C increments from 80 °C to 110 °C. When the sample temperature is higher than the T_{odt}, the sample is completely disordered, and the total power decays to zero. At the end of every temperature step, a DPLS scattering pattern was captured with a CCD camera. For the coexistence experiments, the samples were heated to 80°C and the scattering patterns were recorded after 40 minutes at 80 °C. All scattering patterns were stored as 8-bit, 801 x 801 pixel TIFF image files. The intensity at each pixel was represented by a dimensionless number between 0 and 255. The total depolarized transmitted power was calculated from the image file by summing the intensities at every pixel, after subtracting a background noise image taken with a completely disordered sample.

Table 5.2 Characteristics of asymmetric SEO/LiTFSI mixtures used in this study

Polymer	r	$f_{EO,salt}$	Morphology	T_{odt}
SEO(5.1-12.8)	0.000	0.70	DIS	
	0.005	0.71	DIS	
	0.010	0.71	DIS to LAM	101 °C
	0.025	0.72	GYR	
	0.050	0.73	HEX	
	0.075	0.74	HEX	
	0.100	0.75	HEX	
	0.150	0.77	HEX	
	0.200	0.79	HEX	
	0.250	0.81	HEX	
	0.300	0.82	HEX	
SEO(4.0-22.4)	0.000	0.84	DIS	
	0.005	0.84	DIS	
	0.010	0.84	DIS	
	0.025	0.85	HEX	
	0.050	0.86	HEX	
	0.075	0.87	HEX/BCC	
	0.100	0.87	HEX/BCC	
	0.150	0.88	BCC	
	0.200	0.89	BCC	
	0.250	0.90	BCC	
	0.300	0.91	BCC	
SEO(3.8-8.2)	0.000	0.67	DIS	
	0.005	0.67	DIS	
	0.010	0.68	DIS	
	0.025	0.69	DIS to LAM	127 °C
	0.050	0.70	GYR	
	0.075	0.71	HEX	
	0.100	0.73	HEX	
	0.150	0.75	HEX	
	0.200	0.76	HEX	
	0.250	0.78	HEX	
	0.300	0.79	HEX	
SEO(9.4-2.4)	0.000	0.19	DIS	
	0.005	0.20	DIS	
	0.010	0.20	BCC/BCC	
	0.025	0.21	DIS	
	0.050	0.22	HEX	
	0.075	0.23	HEX	
SEO(9.4-4.0)	0.000	0.29	DIS	
	0.005	0.29	DIS	
	0.010	0.29	HEX	
	0.025	0.30	HEX	
	0.050	0.32	HEX	
	0.075	0.33	HEX	
	0.100	0.34	HEX	
	0.150	0.37	HEX	
	0.200	0.39	HEX	
	0.250	0.41	HEX	
	0.300	0.43	HEX	
SEO(17.4-3.9)	0.000	0.17	DIS	
	0.005	0.18	BCC	
	0.010	0.18	BCC	
	0.025	0.18	BCC	
	0.050	0.20	BCC	
	0.075	0.21	BCC	

5.3 SAXS Results

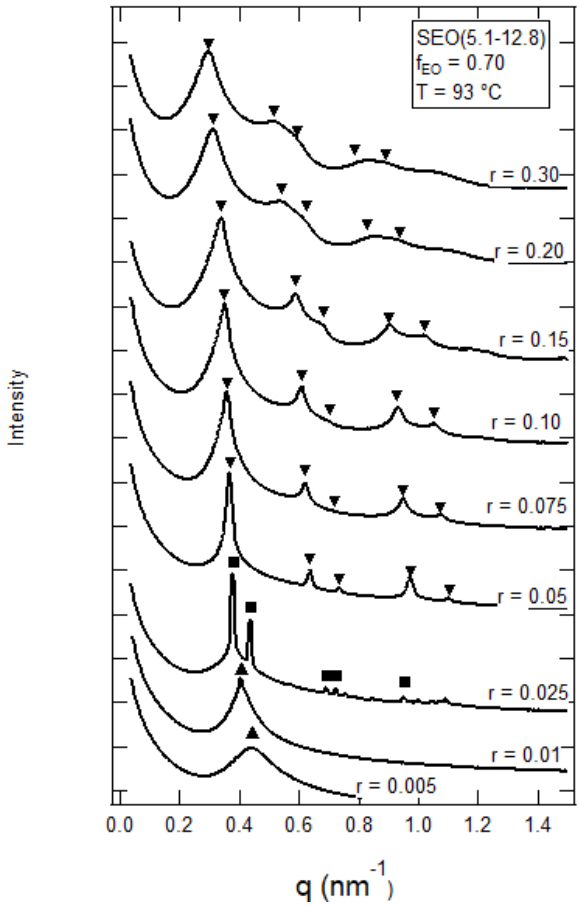

Figure 5.1 SAXS of SEO(5.1-12.8): SAXS profiles at 93 °C for SEO(5.1-12.8) at several salt concentrations. Profiles are offset vertically for clarity. The symbols represent the primary and higher order scattering peaks: Δ, □, and ∇ represent DIS, GYR, and HEX phases respectively.

Table 5.2 outlines the polymer characteristics and phase behavior for all salt-containing SEO copolymer samples. All six SEO copolymers are disordered in the neat state and SAXS profiles of the neat copolymers can be found in the Supporting Information (Figure 5.15). Figure 5.1 shows the SAXS profiles for SEO(5.1-12.8) at 93 °C for salt concentrations ranging from $0.005 \leq r \leq 0.300$. At the lowest salt concentration, $r = 0.005$, the electrolyte exhibits a single broad disordered peak at $q^* = 0.433$ nm^{-1}, where q^* is the location of the primary peak. At $r = 0.01$, the sample exhibits a weak signature of order; note the presence of a small, but noticeable, sharp primary peak at $q^* = 0.444$ nm^{-1} superimposed on a broad peak characteristic of a disordered phase. Upon further salt addition to $r = 0.025$, the sample forms a GYR state with higher order reflections at $\frac{q}{q^*} =$

$\sqrt{\frac{4}{3}}, \sqrt{\frac{8}{3}}$ and $\sqrt{\frac{11}{3}}$. At all higher salt concentrations, $0.025 \leq r \leq 0.30$, the electrolytes are in the HEX state with higher order reflections at $\frac{q}{q^*} = \sqrt{3}, \sqrt{4}, \sqrt{7}$ and $\sqrt{9}$.

SAXS was also conducted on all salt concentrations of SEO(5.1-12.8) from 75 °C $\leq T \leq$ 132 °C in approximately 10 °C increments. Only the sample with r = 0.01 shows temperature-dependent phase behavior. SAXS profiles of this sample at selected temperatures are shown in Figure 5.2a. At 85 °C, we see the scattering signature of LAM. At 93 °C, we see the scattering signature of coexisting LAM and DIS phases. At 113 °C, we see a pure DIS phase. The order-to-disorder transition in this sample was also studied by birefringence (Figure 5.2b). At temperatures below 87 °C, the birefringence signal is more or less independent of temperature. At temperatures between 87 °C $\leq T \leq$ 101 °C, the birefringence signal decreases smoothly to zero. We therefore determined the order-disorder transition temperature, $T_{odt,}$ to be 101 °C.[188] The smooth decrease is consistent with the presence of coexisting LAM and DIS phases in this temperature window, which has been seen previously in block copolymer salt mixtures.[57,157] Only the LAM phase contributes to the birefringence signal and the fraction of the sample occupied by the LAM phase decreases with increasing temperature and vanishes at T_{odt}.[189]

The phase behavior of salty SEO(5.1-12.8) is shown in Figure 5.2c as a function of temperature and salt concentration. The dashed lines represent the boundaries between two phases and the hatched pattern indicates coexistence between DIS and LAM. Phase boundaries are placed to bisect known phases when the coexistence window was not observed. The Gibbs phase rule requires coexistence across all phase boundaries,[55,57,156,190] however, the step-changes in salt concentration and temperature were too large to observe coexistence in most cases. We have chosen to omit the individual data points interpreted from SAXS to focus on the overall phase behavior.

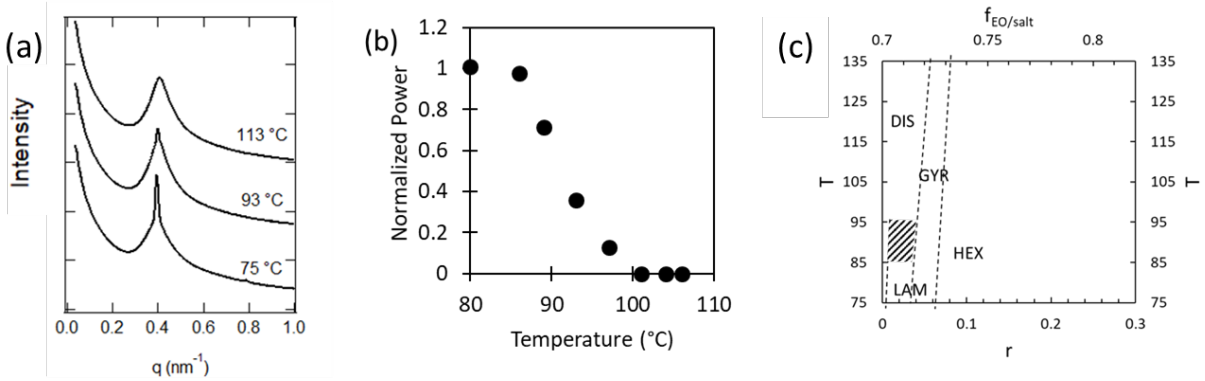

Figure 5.2 Temperature dependence of SEO(5.1-12.8)/LiTFSI: (a) SAXS profiles of SEO(5.1-12.8) r = 0.01 at different temperatures through the order-disorder transition. (b) Plot of normalized power versus temperature from birefringence measurements to determine the T_{odt} of the sample. (c) Phase diagram of SEO(5.1-12.8) as a function of temperature and salt concentration. Dashed lines mark phase boundaries and the hatched region indicate coexistence between phases.

Figure 5.3a shows the SAXS profiles for SEO(4.0-22.4) at 93 °C. SEO(4.0-22.4) is the most asymmetric and longest polymer studied with f_{EO} = 0.84 and N = 428. It remains disordered at $r \leq$ 0.01 before forming HEX at $0.025 \leq r \leq 0.05$ with higher order reflections at $\frac{q}{q^*} = \sqrt{3}$ and $\sqrt{4}$. At $0.075 \leq r \leq 0.10$, we see coexistence between HEX (open triangles) and BCC phases (filled diamonds). The presence of both filled and open symbols in Figure 5.3a indicates coexistence between two ordered phases. At a salt concentration of r = 0.075, the primary peak for the HEX phase appears at q^* = 0.324 nm^{-1} and that of the BCC phase at q^* = 0.347 nm^{-1}. The HEX phase has a larger domain spacing, given by $d = \frac{2\pi}{q^*}$, than the BCC phase: 19.4 nm versus 18.1 nm, respectively. The higher order reflections for the BCC phase are seen at $\frac{q}{q^*} = \sqrt{2}, \sqrt{3}, \sqrt{4}$, and $\sqrt{6}$. The relative intensities of the peaks associated with HEX and BCC morphologies change with salt concentration; for example, at r = 0.075, HEX is the majority component of the system and at r = 0.10, BCC becomes the majority phase. Since the HEX phase is optically anisotropic and the BCC phase is optically isotropic, the gradual transition from HEX to BCC with salt concentration can be studied by birefringence.[191] The dependence of the birefringence signal on salt concentration at 80 °C in the HEX/BCC coexistence window is given in the Supporting Information (Figure 5.16). The normalized signal decreases smoothly over a wide range of salt concentration to a value of 0.02 at r = 0.15, where only spheres are seen. The reason for obtaining the small signal from BCC remains to be established. It may arise from strain trapped within the sample as it was prepared. At the highest salt concentrations, $r \geq 0.15$, SEO(4.0-22.4) forms a pure BCC phase. The phase behavior of SEO(4.0-22.4) is independent of temperature at all salt concentrations.

Figure 5.3b shows the observed phase behavior of salty SEO(4.0-22.4) as a function of temperature and salt concentration. Dashed lines represent phase boundaries between morphologies and the hatched region represents coexistence of BCC and HEX phases. In this coexistence window, salt must be partitioned between these two phases. Based on the location of the coexistence window, we anticipate that the salt concentration is higher in regions where the BCC phase is found.

The phase behavior of SEO(3.8-8.2) is similar to that of SEO(5.1-12.8) and SAXS data obtained from this sample is shown in Supporting Information (Figure 5.17). The phase behavior for SEO(9.4-2.4), SEO(9.4-4.0) and SEO(17.4-3.9) has been previously reported in ref 106.

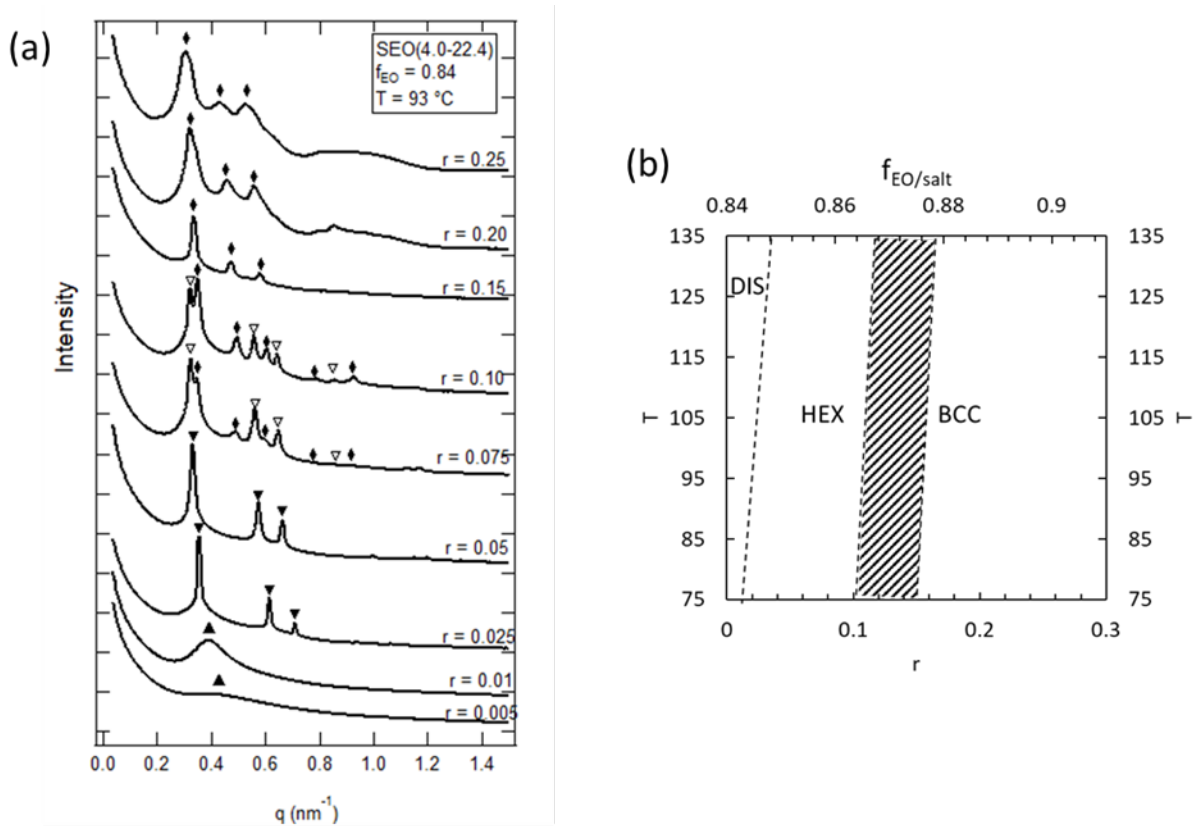

Figure 5.3 Temperature dependence of SEO(4.0-22.4)/LiTFSI: (a) SAXS profiles at 93 °C for SEO(4.0-22.4) at several salt concentrations. Profiles area offset vertically for clarity. The symbols represent the primary and higher order scattering peaks: Δ, ◊ and ∇ represent DIS, BCC, and HEX phases respectively. (b) Phase diagram of SEO (4.0-22.4)/LiTFSI as a function of salt concentration and temperature. Dashed lines mark phase boundaries and the hatched region indicate coexistence.

5.4 Phase Diagrams of SEO/LiTFSI

It is evident from the discussion above that the phase behavior of SEO/LiTFSI mixtures is a complex function of chain length, copolymer composition, salt concentration and temperature. Our objective is to compare our findings with prevailing theories directly. There are no established approaches for accomplishing this. The phase behavior of conventional block copolymers is usually reported on a χN versus f_A plot where χN reflects segregation strength. However, there is much debate in the literature about the relationship between experimentally determined χ and that demanded by theory.[42,192–194] Many more questions arise in the case of salty block copolymers wherein χ must be replaced by χ_{eff}.[50] If we assume that χ_{eff} for block copolymer/salt mixtures can be approximated by Equation 5.1, then the segregation strength in these mixtures is approximated as

$$\chi_{eff}N = \chi_0 N + mrN \tag{5.5}$$

Note that the segregation strength is proportional to the product *Nr*.

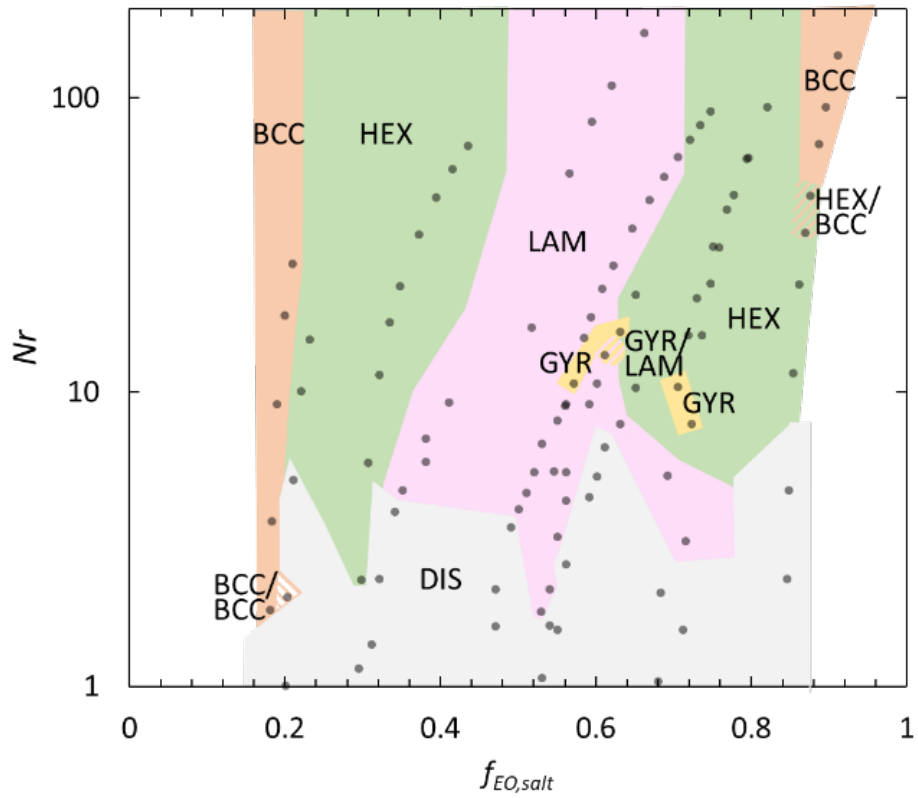

Figure 5.4 Phase diagram as a function of *Nr*: Morphology data for SEO/LiTFSI copolymers at 100 °C plotted as a function of *Nr* versus volume fraction of the salt containing phase, $f_{EO,salt}$. Gray symbols indicate a discrete sample where morphology was determined through SAXS. Phase boundaries were drawn to bisect known morphologies where no window of coexistence was observed. Coexistence is denoted by hatched colored regions.

As a first step, we present the phase behavior of all of the samples described above at 100 °C in Figure 5.4, where the product *Nr* is now used to represent the segregation strength and $f_{EO,salt}$, the volume fraction of the salt-containing PEO-rich microphase, is used to quantify composition. Also included in this figure is the phase behavior of nearly-symmetric SEO/LiTFSI mixtures at 100 °C found in Table 5.1, previously reported in ref 91,173. In Figure 5.4, phase boundaries are drawn to bisect the known morphologies when no coexistence is seen between phases. Regions of coexistence are denoted by the hatched pattern of the colors indicative of the two observed morphologies. Due to the broad range of *Nr* covered in this study, a log scale is used on the y-axis in Figure 5.4. Neat samples ($r = 0$) are therefore omitted from the phase diagram. Note that the dominant morphologies (BCC, HEX, LAM and DIS) are obtained in contiguous regions on the *Nr* vs $f_{EO,salt}$ plot. We see the DIS phase across all compositions at low values of *Nr*. The LAM phase is seen in the range of $0.4 < f_{EO,salt} < 0.6$, flanked by HEX phases on either side, which are in turn flanked by BCC phases. Two separate pockets of the GYR phase are found in the vicinity of LAM/HEX border. It is important to recognize that in Figure 5.4 we have succeeded in organizing

a large body of morphological data that is dependent on three independent parameters – N, r, f_{EO} – using just two parameters. We note that the is no evidence of a chimney region predicted in ref 61 at low values of $f_{EO,salt}$.

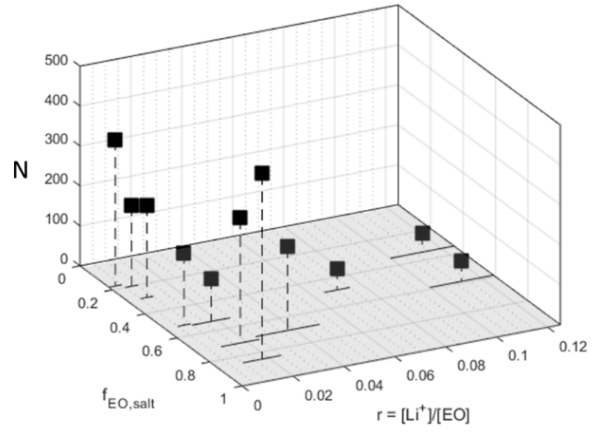

Figure 5.5 SEO/LiTFSI properties at the ODT: Chain lengths, N, at the order-disorder transition at 100 °C versus polymer composition, $f_{EO,salt}$ and critical salt concentration concentration, r, for the SEO/LiTFSI system.

For a given system characterized by N and f_{EO}, we have determined the critical salt concentration beyond which ordered phases are observed at 100 °C. This information is conveyed in Figure 5.5 where N is plotted as a function of r and $f_{EO,salt}$ on a three-dimensional plot. The step change in salt concentration that leads to order formation is used as the error bar on the $N = 0$ plane. As expected, shorter polymers order at higher salt concentrations. However, it is evident that the surface demarcating the order-to-disorder transition in N-r-$f_{EO,salt}$ space, the surface obtained by connecting the squares in Figure 5.5, is complex.

Cochran and Fredrickson have computed the boundary between ordered and disordered phases in neat block copolymers using SCFT.[41] They expressed their results on a χN vs f_A plot. We are interested in the relationship between N and f_A at a fixed temperature, or χ. Our objective is to compare the data presented in Figure 5.5 with the Cochran and Fredrickson predictions. In our experiments, the order-to-disorder transition was located over a range of $0.0025 < r < 0.125$. Over this range, χ_{eff} values reported in the literature range between 0.05 and 0.20.[91] In order to make connections between the Cochran-Fredrickson SCFT and experiments, we calculate N at the order-disorder transition as a function of f_A using these two values for χ. The results of these calculations are the two U-shaped curves in Figure 5.6. The symbols in Figure 5.6 represent the experimental SEO/LiTFSI systems in which salt-induced order-disorder transitions have been identified taken from Figure 5 at 100 °C. Generally, the experimental data points lie between the two SCFT curves and are consistent with SCFT. Figure 5.6 indicates that the phase behavior of salty SEO mixtures can be mapped on to the phase behavior of uncharged block copolymers.

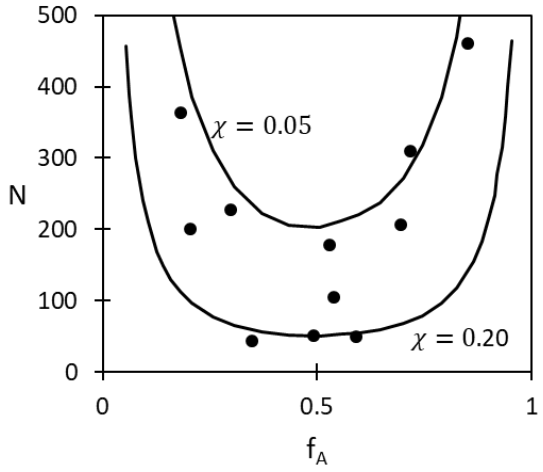

Figure 5.6 Critical Chain Length: Chain length, *N*, at the order-disorder transition as a function of volume fraction for the ion-containing phases (filled circles are SEO/LiTFSI with $f_{EO,salt}$ for the *x*-axis taken at 100 °C) and SCFT for conventional block copolymers at $\chi = 0.20$ and 0.05 (solid curves).

We use the experimentally measured locations of the order-disorder transitions and the Cochran-Fredrickson (ref 41) SCFT to estimate χ_{eff}. The Cochran-Fredrickson SCFT results for the order-disorder phase boundary can be recast in the form

$$(\chi N)_{ODT} = g(f_A) = 10.495 + C_1(f_A - 0.5)^2 + C_2(f_A - 0.5)^4 + C_3(f_A - 0.5)^6 + C_4(f_A - 0.5)^8 \quad (5.6)$$

(The coefficient values are given in the Supporting Information). For a given SEO/LiTFSI mixture, the value of χ at the order-disorder transition was calculated using Eq. 5.6 with the assumption that $f_A = f_{EO,salt}$, to obtain

$$\chi_{eff} = \frac{10.495 + C_1\left(f_{EO,salt} - 0.5\right)^2 + C_2\left(f_{EO,salt} - 0.5\right)^4 + C_3\left(f_{EO,salt} - 0.5\right)^6 + C_4\left(f_{EO,salt} - 0.5\right)^8}{N} \quad (5.7)$$

This enables taking each data point in Figure 5.5 where *N* at the ODT is given as a function of $f_{EO,salt}$ and *r*, and converting it into χ_{eff} for the given value of *r*. Our approach for determining χ_{eff} is similar to the time-honored method of determining phase boundaries in binary polymer solutions and blends and mapping these results onto the predictions of the Flory-Huggins theory to determine the interaction parameter.[42,195,196] The calculated values of χ_{eff} thus obtained are plotted versus salt concentration, *r*, in Figure 5.7. The estimates for χ_{eff} show a strong linear dependence with *r,* consistent with Equation 5.1. A least-squares fit through the data in Figure 5.7 gives $\chi_0 = 0.047$ and $m = 1.67$. These values match experimentally determined values of χ_0 and m in ref 55, where χ_{eff} was determined from RPA fits through SAXS data obtained from the disordered state. It is important to note that the salt concentration, *r,* is not explicitly used when determining χ_{eff}. The applicability of a linear relationship between χ_{eff} and *r* over a wide salt

concentration ($0.0025 \leq r \leq 0.125$) and EO volume fractions ($0.18 \leq f_{EO} \leq 0.84$) is noteworthy. In spite of these complexities, our work indicates that most of the important features of the SEO/LiTFSI phase diagram can be reproduced by combining the linear relationship in Fig. 5.7 with conventional block copolymer SCFT.

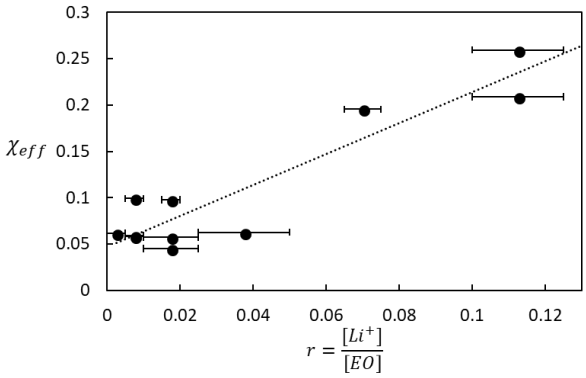

Figure 5.7 Salt Concentration Dependence of the Interaction Parameter: Calculated χ_{eff} from SCFT as a function of r for the salty SEO copolymers using the composition dependence of the order-disorder transition (Equation 5.7) at 100 °C. The data are consistent with $\chi_{eff} = \chi_0 + mr$ with $\chi_0 = 0.047$ and $m = 1.67$. The error bars represent the step change in salt concentration that leads to order formation.

We use our results for χ_0 and m from Figure 5.7 to calculate segregation strength according to Equation 5.5 such that

$$\chi_{eff}N = 0.047N + 1.67Nr \tag{5.8}$$

The morphology data for all SEO/LiTFSI mixtures, originally presented in Figure 5.4, is re-cast in Figure 5.8, using a semi-log plot with $\chi_{eff}N$ as the *y*-axis and $f_{EO,salt}$ as the *x*-axis. Figures 5.4 and 5.8 use the same color scheme. We have chosen to omit the discrete samples to focus on the phase boundaries. Phase boundaries were drawn to bisect known morphologies, when no window of coexistence was observed.

While Figures 5.4 and 5.8 appear similar, there are important differences. The jagged phase boundaries in Figure 5.4 are replaced by smooth lines in Figure 5.8. The boundaries between different morphologies in SEO/LiTFSI are straight but tilted to the right when plotted on a semi-log $\chi_{eff}N$ versus $f_{EO,salt}$ plot. A particularly satisfying aspect of using $\chi_{eff}N$ is that the two separate pockets of GRY seen in Figure 5.4 are merged in Figure 5.8. The appearance of small coexistence windows at the bottom of the BCC phases at both low and high $f_{EO,salt}$ values is clearly due to the presence of salt; they are not observed in conventional block copolymers. Aside from these differences, the phase behavior of SEO/LiTFSI is similar to that of conventional block copolymers.

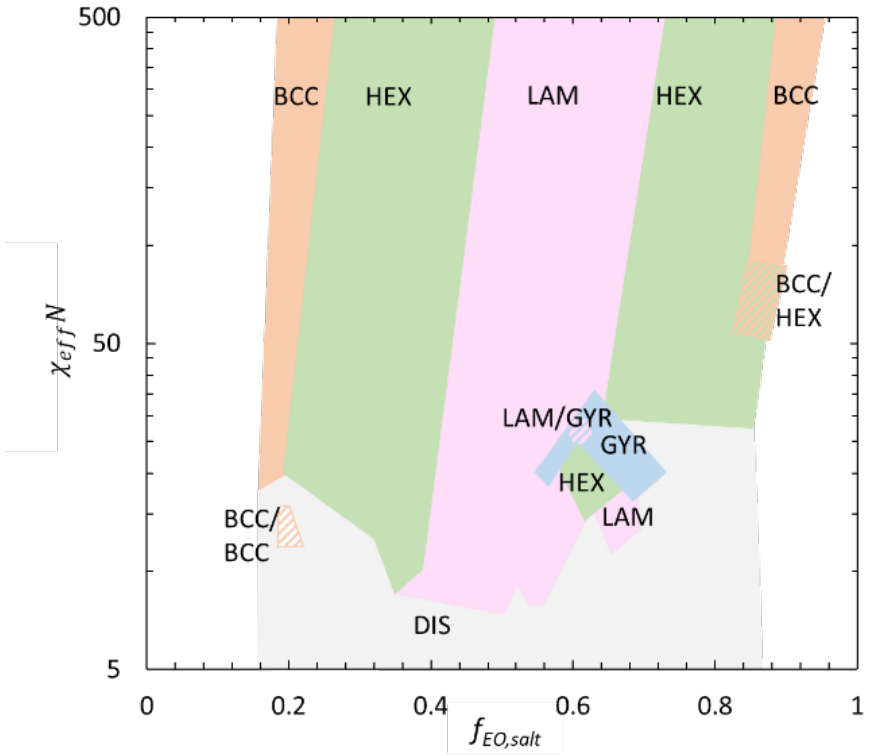

Figure 5.8 SEO/LiTFSI Phase Diagram: Morphology data for SEO/LiTFSI copolymers at 100 °C plotted as a function of $\chi_{eff}N$ versus volume fraction of the salt containing phase, $f_{EO/salt}$. Phase boundaries were drawn to bisect known morphologies where no window of coexistence was observed. Coexistence is denoted by hatched colored regions.

We can use the calculated segregation strength to compare the phase behavior of our salt-containing copolymers to that of conventional neat block copolymers. Figure 5.9 shows the phase diagram of a neat conventional block copolymer, polystyrene-block-polyisoprene (SIP), taken from ref 197. We have colored all of the ordered phases that are relevant to the present study (LAM, HEX, BCC and GYR) using the same color scheme as Figure 5.8. The *x*-axis in Figure 5. 9 is the volume fraction of the polyisoprene (PI) block and the *y*-axis is χN for SIP. Also shown in Figure 5.9 are five colored horizontal bars evenly spaced between $20 \leq \chi_{eff}N \leq 40$. These bars present the phase behavior of SEO/LiTFSI mixtures (Figure 5.8). We set $\chi_{eff}N = \chi N$ and $f_I = f_{EO,salt}$ in order to overlap the individual phase diagrams. Within each bar, the color represents the ordered phase using the same color scheme as Figure 5.8.

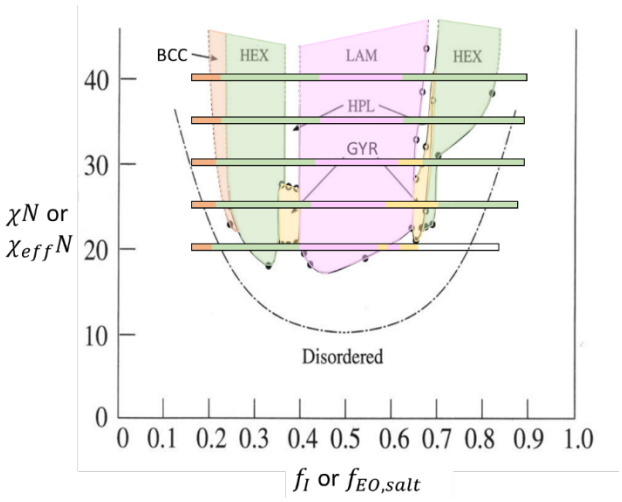

Figure 5.9 Comparisons to Literature: Phase behavior diagram of SIP reproduced from Khandpur et al (ref 197). The five colored bars represent the phase behavior of SEO/LiTFSI taken from Figure 5.8 at 100 °C. The colors match the morphologies labeled in Figure 5.8 with the DIS phase left unlabeled in white.

It is clear from Figure 5.9 that the phase behavior of salty block copolymers closely resembles that of conventional block copolymers. It does not contain a chimney-like feature that was predicted by Ionic SCFT.[61] The BCC phase is found at low values of segregation strength (25) for styrene-rich (S-rich) block copolymers in both SIP and SEO/LiTFSI. In both IP-rich and EO-rich systems, the BCC phase is absent at values of segregation strength as high as 40. This similarity is noteworthy given the chemical differences between PI and PEO/LiTFSI. The widths of the HEX phases in SEO/LiTFSI mixtures are similar in both S-rich and EO-rich systems, consistent with all of the theories on neat block copolymer self-assembly.[39] There is reasonable agreement between the widths of the LAM phases found in SIP and SEO/LiTFSI. The GYR pockets in SEO/LiTFSI are only found in the EO-rich side of the phase diagram. It is evident that the underlying simplicity of the phase behavior of SEO/LiTFSI mixtures is revealed by simple rescaling χ to account for the additional interactions due to the presence of salt in block copolymer/salt mixtures.

In order to verify our approach to organizing morphology data of SEO/LiTFSI on a plot of segregation strength versus copolymer composition using Eq. 5.8, we expanded our analysis to other SEO block copolymer electrolytes available in the literature. The copolymer properties are provided in Table 5.3. These systems include two different salts: LiTFSI and lithium trifluoromethanesulfonate (LiTf).

The discrete data points in Figure 5.10 represent morphologies determined by small angle X-ray scattering (SAXS) experiments for a given SEO electrolyte, characterized by N, $f_{EO,salt}$ and r. $\chi_{eff}N$ for a given SEO electrolyte is then calculated by Equation 5.8. The symbols for each electrolyte correspond to their morphology: BCC is given as circles, HEX as hexagons, GYR as plus signs, LAM as squares, and DIS as triangles. Due to the sparseness of data at $\chi_{eff}N > 100$, the figure is broken up into two panels. We assume that the phase boundaries are vertical when $\chi_{eff}N > 100$ in accordance with strong segregation theory.[41,46,47]

Table 5.3 Characteristics of polymers compiled.

Polymer	M_{PS} (kg mol^{-1})	M_{PEO} (kg mol^{-1})	f_{EO}	N	Salt Species	*Ref*
SEO(2.3-4.6)	2.3	4.6	0.65	104	LiTFSI	Wanakule[33]
SEO(3.1-5.1)	3.1	5.1	0.60	124	LiTFSI	Wanakule[33]
SEO(4.6-3.7)	4.6	3.7	0.43	127	LiTFSI	Wanakule[33]
SEO(5.3-3.0)	5.3	3.0	0.35	128	LiTFSI	Wanakule[33]
SEO(5.3-3.6)	5.3	3.6	0.39	137	LiTFSI	Wanakule[33]
SEO(6.4-7.2)	6.4	7.2	0.51	207	LiTFSI	Teran[32]
SEO(6.4-7.3)	6.4	7.3	0.52	210	LiTFSI	Teran[32]
SEO(10.0-4.5)	10	4.5	0.30	224	LiTf	Young[36]
SEO(9.5-8.0)	9.5	8.0	0.44	268	LiTf	Gunkel[35]
SEO(9.7-10.4)	9.7	10.4	0.50	307	LiTf	Zardalidis[37]
SEO(48.6-41.4)	48.6	41.4	0.44	1379	LiTf	Zardalidis[37]

Overall, there is agreement between SCFT calculations and the experimental data. The experimentally determined location of the order-disorder boundary is shown by a black curve in Figure 5.10. It was determined by locating the order-disorder transition at $f_{EO,salt} = 0.18, 0.29, 0.72,$ and 0.86 and joining these data points by lines. A large majority of the open triangles (but not all of them), corresponding to the DIS phase, in Figure 5.10 are located below the order-disorder curve. Similarly, there are a few ordered phases that fall below the experimental order-disorder curve; these samples are typically the highest salt concentration of a given low molecular weight SEO. The agreement is perhaps surprising given the simplicity of Equation 5.8. At low $f_{EO,salt}$ values (in the vicinity of 0.2), the experimental boundary between BCC and HEX occurs at slightly higher $f_{EO,salt}$ values than those predicted by theory. At $0.3 < f_{EO,salt} < 0.4$, the experimentally determined boundary between HEX and LAM also occurs at slightly higher $f_{EO,salt}$ values than those predicted by theory. In symmetric systems near $f_{EO,salt} = 0.5$, LAM is obtained as predicted by theory, especially when $\chi_{eff}N > 50$. As $f_{EO,salt}$ values approach 0.6, we obtained HEX experimentally, but theory predicts LAM. On the PEO-rich side of the phase diagram, there is excellent agreement between experimentally determined HEX phases and theoretical predictions between $0.7 < f_{EO,salt} < 0.8$. The data points that are filled with hatched patterns represent samples that exhibited coexistence between two ordered morphologies.[106,107] The phase boundary between HEX and BCC at values of $\chi_{eff}N > 60$ on the $f_{EO,salt} > 0.5$ side aligns extremely well with experiment. Pure BCC phases are seen in this region at $\chi_{eff}N > 100$, as predicted by theory.

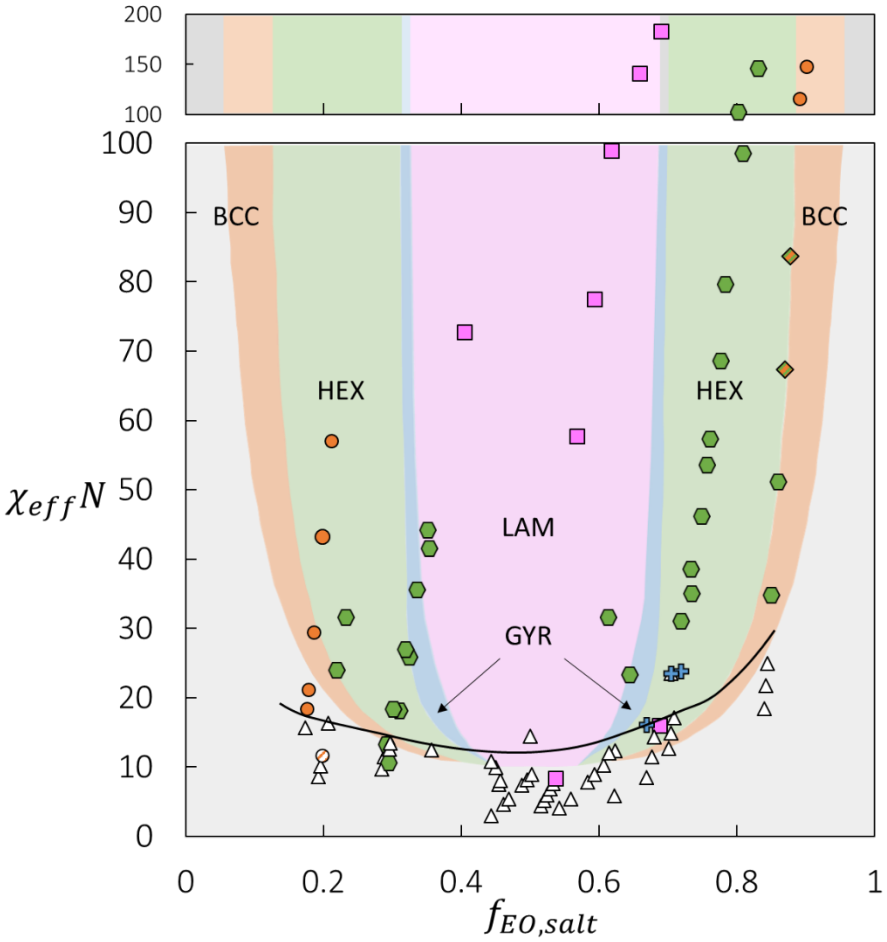

Figure 5.10 Compiled Phase Diagram from Literature. Phase diagram for salt-containing SEO block copolymers blends taken at 100 °C plotted as $\chi_{eff}N$ versus $f_{EO,salt}$. The shapes of the symbols correspond to the morphologies of the electrolytes: Δ for DIS (white), ○ for BCC (orange), □ for LAM (pink), ⬡ for HEX (green), and + for GYR (blue). The shaded regions represent phase boundaries calculated by mean-field SCFT for salt-free systems and the data points are discrete samples.

5.5 Domain Spacing

We conclude with a discussion on the effect of salt on the domain spacing of the SEO copolymers. Figure 5.11 shows selected data from a subset of SEO copolymers included in Tables 5.1 and 5.3. Domain spacing, *d*, is plotted as a function of volume fraction of the salt containing phase, $f_{EO,salt}$, and salt concentration, *r,* at 120 °C. The values of *N* are given in the legend. It is obvious from Figure 5.11 that the relationship between *d, N, r,* and $f_{EO,salt}$ is complicated. Figure 5.11 shows that $f_{EO,salt}$ increases monotonically as *r* increases; see the dashed curves in the bottom $f_{EO,salt} - r$ plane (i.e. $d = 0$ plane). The dashed curves in Figure 5.11, which are based on Equation 5.4, are slightly non-linear. It is also evident in Figure 5.11 that *d* increases with increasing *r* but the relationship between these variables is highly non-linear. It is thus helpful to account for the dependence of *d* on the two relevant variables ($f_{EO,salt}$ and *r*) independently.

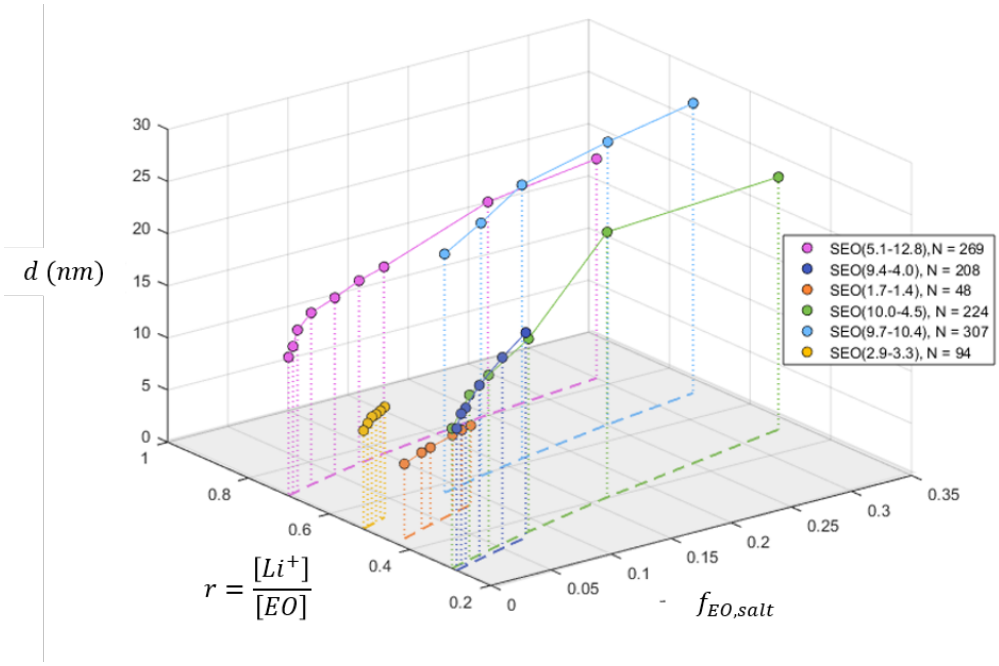

Figure 5.11 3D Plot of SEO Properties. 3D plot of volume fraction of PEO + salt, $f_{EO,salt}$, domain spacing, d, and salt concentration, r, for a sample of SEO copolymers used in this study at 120 °C. Dashed lines shown are a projection to the $d = 0$ plane.

To account for the dependence of d on $f_{EO,salt}$, we normalize d by D defined in the Introduction. D, taken from ref 34, can be re-cast into an equation in similar form of Equation 5.6 and the coefficients, C_i's, are provided in the Supporting Information. Figure 5.12 is a plot of normalized domain spacing ($\mathcal{D} = \frac{d}{D}$) versus salt concentration, r, at 120 °C. (We chose 120 °C because of the availability of published data. The plot would be much sparser if we used available data at 100 °C, the temperature used in the discussion of phase behavior. We do not expect qualitative differences due to this 20 °C discrepancy in temperature.) The data in Figure 5.12 are color coded with the same color scheme used to describe the morphologies of SEO block copolymers in Figure 5.10. The symbols for the discrete data points correspond to the morphology of a given electrolyte; they also match the symbols used in Figure 5.10. On this plot, the disordered systems (DIS) appear towards the lower half, and in this regime, $\mathcal{D}$ is more-or-less independent of r. In disordered systems, the reported value of d corresponds to the characteristic length scale of concentration fluctuations.[34] In the ordered state, $\mathcal{D}$ increases with r in a non-linear fashion, increasing more rapidly at higher values of r. When coexistence of ordered phases was observed for a single electrolyte, domain spacing for each morphology is presented. It is worth noting that in Figure 5.12, different morphologies are segregated into different pockets on the $\mathcal{D}$ versus r plot. The LAM pocket occurs at the upper right-hand corner of the diagram, GYR and HEX phases appear in the middle of the diagram above DIS but below BCC. Interestingly, the BCC pocket runs into the LAM pocket in the vicinity of $r = 0.1$. There are two outliers of LAM seen inside the DIS region. In these two electrolytes, the DIS phase was transformed into LAM by the addition of salt. In

contrast, the LAM phases presented in the upper right-hand corner of Figure 5.12 were obtained in electrolytes with inaccessible order-disorder transitions.

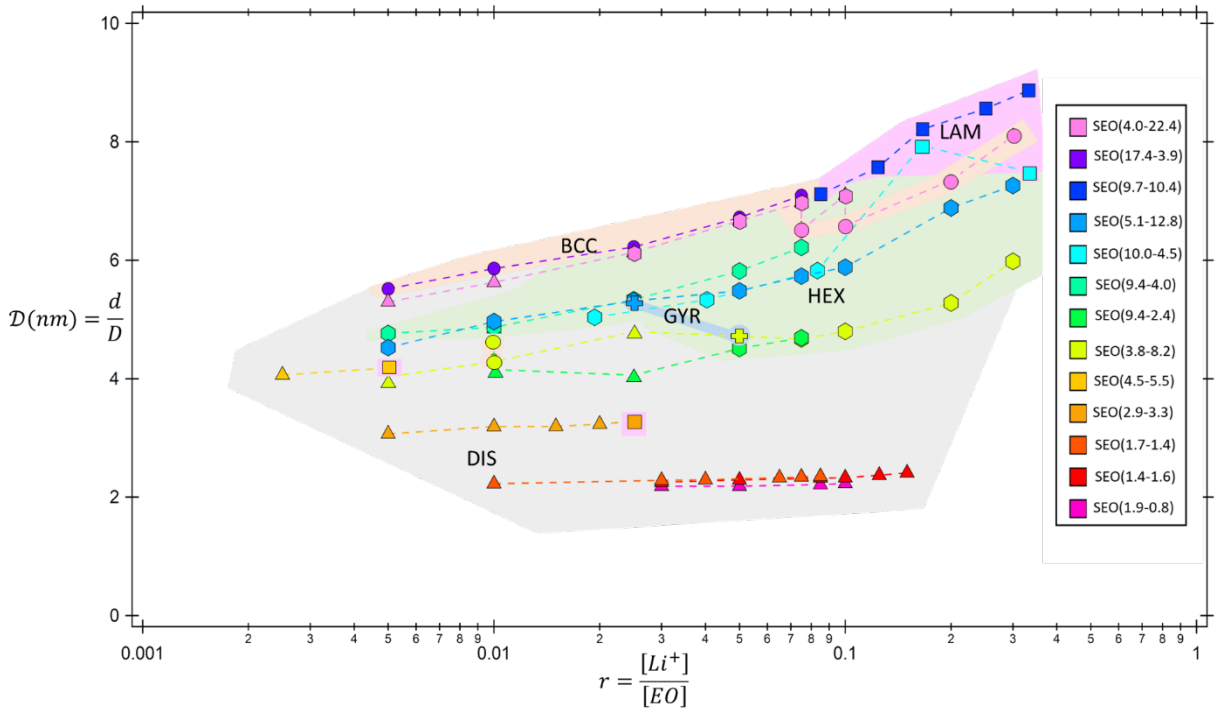

Figure 5.12 Normalized Domain Spacing. Dependence of normalized domain spacing, $\mathcal{D} = \frac{d}{D}$, on salt concentration, *r*, for salt-containing SEO block copolymers at 120 °C. Data from different morphologies cluster into "pockets" that are colored differently and match Figure 6: DIS (gray), BCC (orange), LAM (pink), HEX (green), and GYR (blue). The symbols indicate the morphology and also match those of Figure 5.10: Δ for DIS, ○ for BCC, □ for LAM, ⬡ for HEX, and + for GYR. Dashed lines are a guide for the eye.

If the change in domain spacing upon salt addition was only due to changes in $f_{EO,salt}$, then within our framework, $\mathcal{D}$ would be independent of salt concentration for each polymer as our normalization scheme accounts for this effect. It is, however, clear from Figure 5.12 that the changes in domain spacing upon salt addition are due to additional effects introduced by the presence of ions such as increased segregation. In each of the ordered morphologies, the junction between PS and PEO chains are located near the domain boundaries. Segregation strength is known to affect the area per junction.[198,199] It is evident that the addition of salt to ordered morphologies results in a decrease in the area per junction.

Figure 5.13 shows the relationship between normalized domain spacing, $\mathcal{D}$, chain length, *N*, and segregation strength, $\chi_{eff}N$, for the SEO copolymers with and without salt. The ordinate in Figure 5.13 is a dimensionless quantity: $\frac{\mathcal{D}}{bN^{\frac{1}{2}}}$; note that $\mathcal{D}$ has units of nm. The statistical segment length, *b,* was taken to be 0.5 nm, the nominal value that applies to a large number of flexible polymer chains.[200] All of the data in Figure 5.12 collapses on to two straight lines in Figure 5.13. The solid

lines are vertically shifted linear regressions through the dataset cut off at $\chi_{eff}N \leq 10$. The break in the data at $\chi_{eff}N = 10$ is expected as the systems cross-over from the weak to strong segregation limit.

Based on the $\chi_{eff}N \leq 10$ data set, we obtain

$$\frac{\mathcal{D}}{bN^{\frac{1}{2}}} = 0.63 \tag{5.9}$$

Based on the $\chi_{eff}N > 10$ data set, we obtain

$$\frac{\mathcal{D}}{bN^{\frac{1}{2}}} = 0.42\left(\chi_{eff}N\right)^{0.177} \tag{5.10}$$

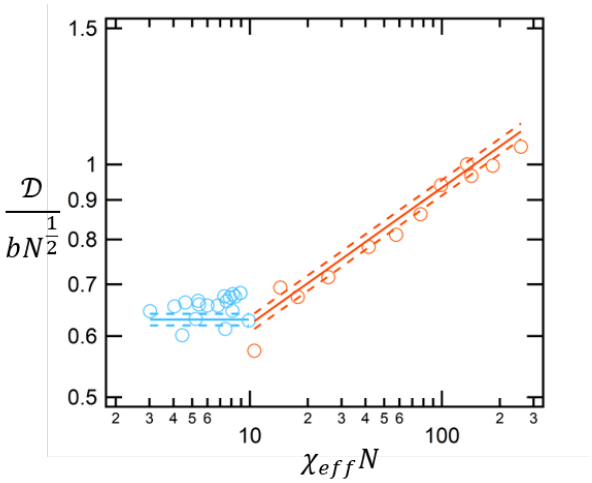

Figure 5.13 Crossover Regime of Normalized Domain Spacing. Relationship between normalized domain spacing, chain length, and segregation strength for the salt-containing SEO copolymers. In the WSL, $\chi_{eff}N > 10$, the normalized domain spacing is independent of segregation strength. In the SSL, $\chi_{eff}N > 10$, $\mathcal{D} \sim N^{\frac{2}{3}}$. Experimental data in the weak and strong segregation regimes are shown in blue and orange circles, respectively. The solid lines represent Equations 5.9 and 5.10, based on linear regressions as described in the text. The dashed lines represent a 95% confidence interval.

The constants in each regression were modified slightly to enforce continuity at $\chi_{eff}N = 10$ (from 0.656 to 0.63 in Equation 5.9 and from 0.404 to 0.420 in Equation 5.10). The dashed lines around each line represent 95% confidence intervals for the modified regressions. At low values of segregation strength, $\chi_{eff}N \ll 10$, the right side of Equation 5.10 is independent of $\chi_{eff}N$ and $\mathcal{D} \sim N^{\frac{1}{2}}$ as predicted by the mean field theory of Leibler.[34] At high values of segregation strength where ordered phases are obtained, $\chi_{eff}N \gg 10$, $\mathcal{D} \sim N^{\frac{2}{3}}$ as predicted in the strong segregation

limit (SSL).[46–48] The observed cross-over in Figure 5.13 from weak to strong segregation is consistent with the theory of Uneyama and Doi wherein a monotonic increase in the $\mathcal{D}$ versus N exponent is predicted at the cross-over.[49] The theory of Matsen and Bates predicts a higher exponent for the $\mathcal{D}$ versus N scaling at intermediate segregation strength ($10 < \chi_{eff}N < 100$).[47] The data in Figure 5.13 do not agree with this prediction. It is worth noting that neither theory was developed for salt-containing block copolymers.

In the vicinity of the disordered regime, where $\chi_{eff}N \leq 10$, we can re-arrange Equation 5.9 to give

$$\frac{d}{D} = 0.315N^{\frac{1}{2}} \text{ for } \chi_{eff}N < 10 \tag{5.11}$$

Note, in this limit, normalized domain spacing is independent of χ_{eff}.

In the ordered regime, where $\chi_{eff}N > 10$, we substitute Equation 5.8 into Equation 5.10 and arrive at an explicit expression for the dependence of d on $f_{EO,salt}$, N, and r:

$$\frac{d}{D} = 0.21N^{0.667}(0.047 + 1.67r)^{0.177} \text{ for } \chi_{eff}N \geq 10 \tag{5.12}$$

Note, the right sides of Equations 5.11 and 5.12 are equal at $\chi_{eff}N = 10$.

Equations 5.11 and 5.12 provide explicit predictions of domain spacing as a function of N, r, and $f_{EO,salt}$. It is instructive to re-examine the data in Figure 5.12 in light of these expressions. The data in Figure 5.12 are replotted in Figure 5.14. The solid lines in Figure 5.14 represent Equations 5.11 and 5.12. There are three shaded regions that represent different regimes of segregation strength: $\chi_{eff}N < 10$ (green), $10 \leq \chi_{eff}N < 30$ (orange), and $\chi_{eff}N \geq 30$ (blue). Note, only five SEO copolymers, which lie at the bottom of Figure 5.14, are within the weak segregation limit with $N < 158$ (green region); we see good agreement between these data and Equation 5.11. There are three black arrows in Figure 5.14; they show the cross-over between Equations 5.11 and 5.12 for the low molecular weight SEO copolymers. The remaining SEO copolymers are long enough to have $\chi_{eff}N > 10$ for all studied salt concentrations (orange and blue regions). We see good agreement between experiment data and Equation 5.12 for some of the systems with $10 \leq \chi_{eff}N < 30$ (orange region). At higher segregation strengths (blue region), the predicted increase in $\mathcal{D}$ with r is much stronger than that observed experimentally. These deviations are not evident when the data is presented on a log-log plot (Figure 5.13). There are thus some unresolved issues that arise in the strongly segregated salty block copolymers.

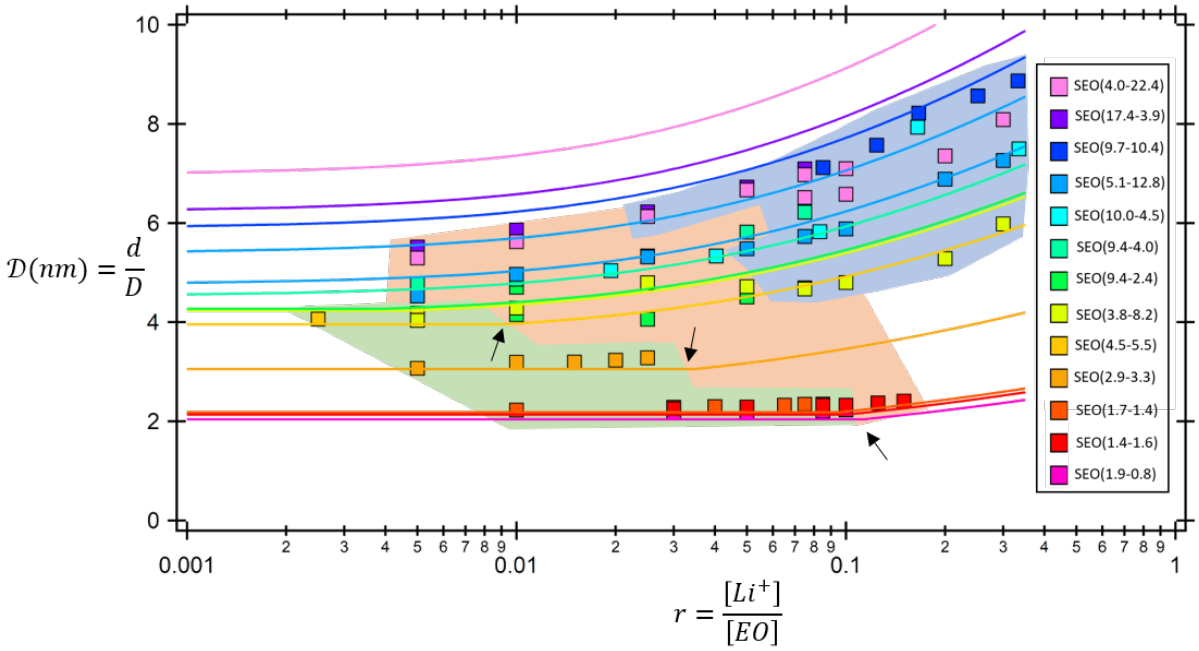

Figure 5.14 Predictions of Normalized Domain Spacing. Comparison of predictions and experiment for normalized domain spacing, $\mathcal{D}$, as a function of salt concentration, *r,* according to Equations 5.11 (WSL) and 5.22 (SSL). The squares show data corresponding to the system indicated in the legend. Curves of the same color indicate theoretical predictions for individual systems. The legend is organized according to the relative magnitude of $\mathcal{D}$. For example, the topmost curve corresponds to SEO(4.0-22.4), the top entry in the legend. The shaded regions represent different regimes of segregation strength: $\chi_{eff}N < 10$ (green), $10 \leq \chi_{eff}N < 30$ (orange), and $\chi_{eff}N \geq 30$ (blue). The three black arrows denote the cross-over from Equations 5.11 to 5.12 at $\chi_{eff}N = 10$ for the low molecular weight SEO copolymers (N < 158). For cases with N > 158, only Equation 5.12 is used; the cross-over is predicted to occur at *r* that is below 0.001.

A possible explanation for the discrepancy between theory and experiments seen in Figure 5.14 is the limited applicability of our expression for $\chi_{eff}N$ (Equation 5.8). The linear relationship between χ_{eff} and r presented in that equation is likely to be valid over a limited range of salt concentrations. This discrepancy has been seen experimentally in salt-containing symmetric SEO copolymers with $f_{EO,salt}$ values in the vicinity of 0.5. Over the limited range of r and N values covered in ref 58, the dependence of χ_{eff} on these parameters was given by

$$\chi_{eff} = A + \frac{B}{N} + \frac{C}{N}\left[1 - \exp\left(-\frac{Dr}{N}\right)\right] \tag{5.13}$$

This expression suggests that χ_{eff} does not increase linearly over an indefinite range of salt concentrations; at concentrations above a certain threshold (e.g. $r = 0.012$ at $N = 100$), χ_{eff} levels off. Based on our analysis thus far, we can assert that this expression does not apply over the range of compositions covered in this review. One may thus view Equations 5.11 and 5.12 as a starting point for organizing domain spacing data from salt-containing block copolymers.

5.6 Conclusions

There is continued interest in studying the effect of salt on the thermodynamics of block copolymers for both fundamental understanding of salt/copolymer mixtures as well as for applications such as solid-state battery electrolytes. We present the phase behavior of SEO/LiTFSI systems over a wide range of compositions, $0.18 \leq f_{EO,salt} \leq 0.84$. Data from weakly and strongly segregated systems are presented; salt concentration is used to tune segregation strength, which is approximated by the product Nr. The relationship between chain length, polymer composition, and salt concentration was examined at the order-to-disorder transition. Our experiments reveal a distinctly non-monotonic relationship between polymer composition and chain length at the order-disorder transition. A linear expression for the dependence of χ_{eff} on salt concentration is obtained by mapping the observed order-disorder phase boundary on to SCFT predictions for uncharged block copolymers. The phase behavior of SEO/LiTFSI mixtures, when plotted on a $\chi_{eff}N$ versus $f_{EO,salt}$ plot is similar to that of a χN versus f_A plot obtained for conventional block copolymers. The only difference is that the phase boundaries are not vertical; they tilt to the right due to the presence of salt swelling of the PEO domain.

These expressions were used to compile phase behavior data from the literature on various SEO/Li salt systems. We hope that our work will allow for discrimination of different theoretical approaches that have been used to describe the effect of electrostatic interactions on block copolymer phase behavior. The dependence of domain spacing, d, on N, r, and $f_{EO,salt}$ for SEO block copolymers collapses on to two universal lines for weak and strong segregation, respectively. This collapse was only obtained after d was normalized by a function that we call $D(f_{EO,salt})$ that was first introduced by Leibler. The dimensionless domain spacing, $\mathcal{D}/(bN^{\frac{1}{2}})$ is a constant in the weak segregation limit and scales with $\chi_{eff}N$ in the strong segregation limit. The same expression for $\chi_{eff}N$ is used to organize both phase behavior and domain spacing data of salty block copolymers. It is likely, however, that the dependence of χ_{eff} on salt concentration deviates from linearity at high salt concentrations. We hope that this effect will be addressed by the community in future studies.

5.7 Nomenclature

5.7.1 Abbreviations:

BCC	body center cubic
DPLS	depolarized light scattering
GYR	gyroid
HEX	hexagonally packed cylinders
LAM	lamellar
LiTf	lithium trifluoromethanesulfonate salt
LiTFSI	lithium bis(trifluoromethanesulfonyl) imide salt
N_A	Avogadro's number
ODT	order-disorder transition

PEO	poly(ethylene oxide)
PI	polyisoprene
PS	polystyrene
RPA	Random Phase Approximation
SAXS	small angle X-ray scattering
SCFT	Self-Consistent Field Theory
SEO	polystyrene-*block*-poly(ethylene oxide)
SIP	polystyrene -*block*-polyisoprene
SSL	strong segregation limit
T_{odt}	order-disorder temperature
WSL	weak segregation limit

5.7.2 Symbols:

b	statistical segment length (nm)
d	domain spacing (nm)
D	periodicity
D_{norm}	normalized periodicity
$\mathcal{D}$	normalized domain spacing (nm)
$f_{EO,salt}$	volume fraction of the PEO/LiTFSI phase
f_A	volume fraction of species A
f_{EO}	volume fraction of PEO phase
f_S	volume fraction of PS phase
M_{PEO}	number-averaged molecular weight of the PEO block (kg mol^{-1})
M_{PS}	number-averaged molecular weight of PS block (kg mol^{-1})
N	number-averaged degree of polymerization (sites chain^{-1})
q	scattering vector (nm^{-1})
q^*	scattering vector at the primary peak (nm^{-1})
r	salt concentration ([Li^+] [EO]$^{-1}$)
R_g	radius of gyration (nm)

5.7.3 Greek Symbols:

ν_i	molar volume of species I i (cm^3 mol^{-1})
ν_{ref}	reference volume (nm^3 site^{-1})
ρ_i	density of spcies species I i (g cm^{-3})
χ	Flory-Huggins interaction parameter
χ_0	Flory-Huggins parameter of salt-free system
χ_{eff}	effective Flory-Huggins interaction parameter
χN	segregation strength
$(\chi N)_{norm}$	normalized segregation strength

5.8 Supporting Information

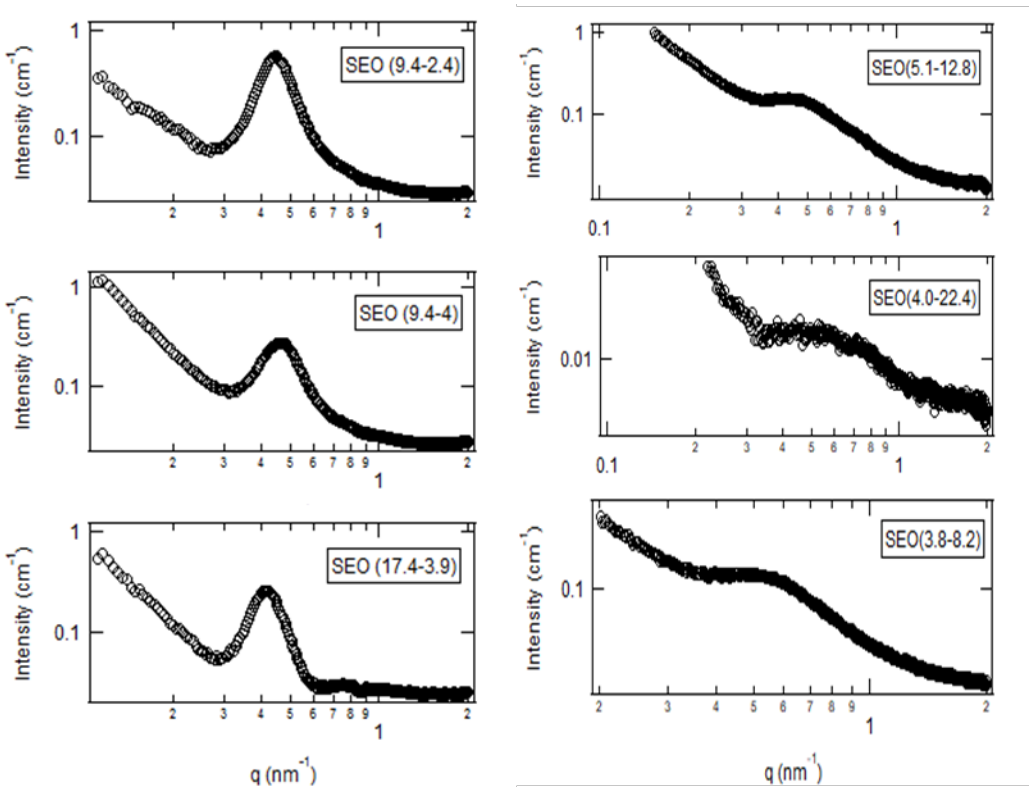

Figure 5.15 Disordered scattering of neat SEO. Disordered scattering from the neat SEO block copolymers at 80 °C for a) SEO(9.4-2.4), b) SEO(9.4-4.0), c) SEO(17.4-3.9), d) SEO(5.1-12.8), e) SEO(4.0-22.4) and f) SEO(3.8-8.2). All six copolymers were disordered as temperatures ranging from 75 °C $\leq T \leq$ 140 °C.

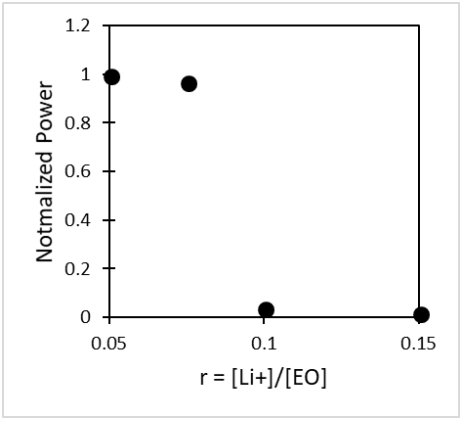

Figure 5.16. Normalized DPLS power: Normalized power from birefringence experiments as a function of salt concentration for SEO(4.0-22.4) at 80 °C

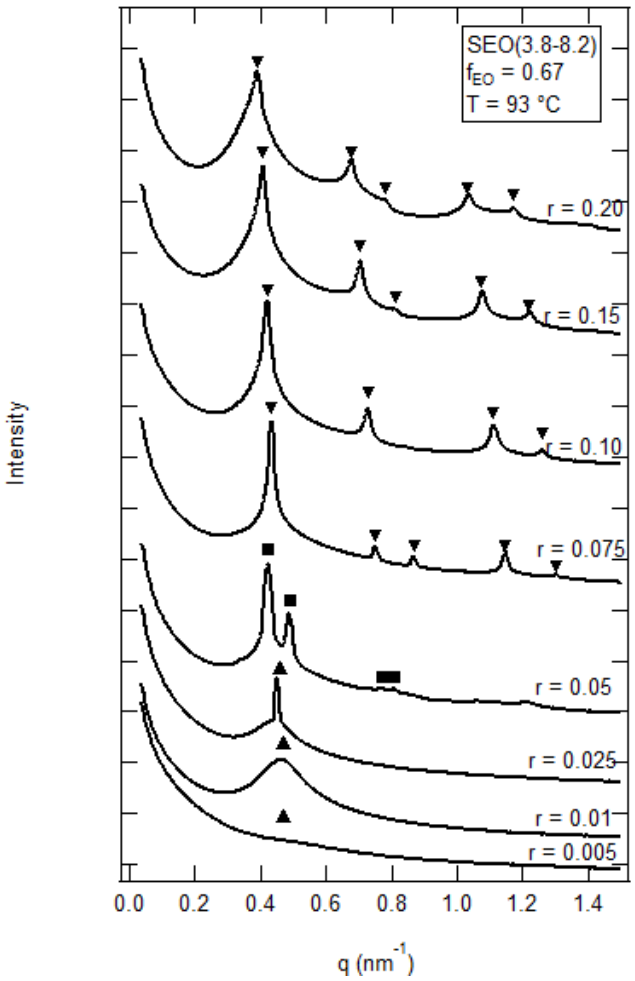

Figure 5.17 SAXS of SEO(3.8-8.2)/LiTFSI: Scattering profiles for electrolytes of SEO(3.8-8.2) from $0.005 \leq r \leq 0.30$ at 93 °C. Profiles were offset vertically for clarity. Morphologies are indicated by Δ, □, and ∇ for DIS, GYR, and HEX respectively.

Table 5.4 Coefficients for polynomial fits to Equation 5.6 for $(\chi N)_{odt}$ and D

	Binary blends	Block copolymers	Periodicity (D)
C_0	2	10.495	3.2292
C_1	0.88073	47.896	-2.3226
C_2	98.693	782.17	-7.6529
C_3	-868.58	-3566.7	33.981
C_4	2631.4	24074	-211.21

6. Composition Dependence of the Flory-Huggins Interaction Parameters and the Isotaksis Point†

ABSTRACT

The thermodynamics of block copolymer/salt mixtures were quantified through the application of Leibler's Random Phase Approximation to disordered small angle X-ray scattering profiles. The experimental system comprises of polystyrene-*block*-poly(ethylene oxide) (SEO) mixed with lithium bis(trifluoromethanesulfonyl) imide salt (LiTFSI), SEO/LiTFSI. The Flory-Huggins interaction parameter determined from scattering experiments, χ_{SC}, was found to be a function of block copolymer composition, chain length, and temperature for both salt-free and salty systems. In the absence of salt, $\chi_{0,SC}$ is a linear function of $(Nf_{EO})^{-1}$; in the presence of salt, a linear approximation is used to describe the effect of salt on $\chi_{eff,SC}$ for a given copolymer composition and chain length. The theory of Sanchez was used to determine χ_{eff} from $\chi_{eff,SC}$ in order to predict the boundary between order and disorder as a function of chain length, block copolymer composition, salt concentration, and temperature. At fixed temperature (100 °C), N_{crit}, the chain length of SEO at the order-disorder transition in SEO/LiTFSI mixtures, was predicted as a function of the volume fraction of the salt-containing poly(ethylene oxide)-rich microphase, $f_{EO,salt}$, and salt concentration. At $f_{EO,salt} > 0.27$, the addition of salt stabilizes the ordered phase; at $f_{EO,salt} < 0.27$, the addition of salt stabilizes the disordered phase. We propose a simple theoretical model to predict the block copolymer composition at which phase behavior is independent of salt concentration ($f_{EO,salt} = 0.27$). We refer to this composition as the "isotaksis point".

6.1 Introduction

There is continued interest in understanding the thermodynamics of polymer/salt mixtures due to their applications as solid electrolytes in rechargeable batteries.[22,24,179,201–204] It is well known that the addition of salt to diblock copolymers greatly affects their thermodynamics and there have been many theoretical and experimental studies on quantifying these effects. A model system is polystyrene-*block*-poly(ethylene oxide) (SEO) mixed with lithium bis(trifluoromethanesulfonyl) imide salt (LiTFSI), SEO/LiTFSI. The transport of Li^+ ions in poly(ethylene oxide) (PEO) has been fully characterized[19] and the addition of polystyrene (PS) introduces mechanical support for the electrolyte.[178]

The phase behavior of pure diblock copolymers has been thoroughly studied, both experimentally and theoretically.[39,41] The equilibrium phase behavior is dictated by two parameters: the volume fraction of one polymer block, f_A, and the segregation strength, χN, where N is the overall degree of polymerization and χ is the Flory-Huggins interaction parameter, a measurement of the

† This chapter was reported in *Macromolecules,* **2019**, 52 (15), 5590-5601.

thermodynamic compatibility between the two polymer constituents. The temperature (T) dependence of χ is often given by

$$\chi = \frac{A}{T} + B \tag{6.1}$$

where A and B are empirically determined constants.[39,42] At high temperatures, entropy dominates leading to the formation of a disordered phase. As temperature decreases, the importance of the energy of interactions between the two polymer blocks increases, and leads to microphase separation and the formation of ordered morphologies. For a given block copolymer, characterized by f_A and N, the transition from disorder-to-order occurs at a critical value of χ. Self-consistent field theory (SCFT) is a powerful tool that can predict the phase behavior of neat block copolymers.[180] At the order-disorder transition (ODT), the product χN may be given by

$$(\chi N)_{ODT} = g(f_A) = 10.495 + C_1(f_A - 0.5)^2 + C_2(f_A - 0.5)^4 + C_3(f_A - 0.5)^6 + C_4(f_A - 0.5)^8 \tag{6.2}$$

where the coefficients, C_i, are obtained by fitting Equation 6.2 to the SCFT results of Cochran et al.[41]: $C_0 = 10.5, C_1 = 47.9, C_2 = 782, C_3 = -3567$ and $C_4 = 24700$. In this theory, χ is an implicit property of the chemical structure of the constituent monomers in the block copolymer and does not depend on N or f_A. For a given block copolymer system at a particular temperature, T, Equation 6.2 can be used to calculate a critical chain length, N_{crit} , as a function of f_A:

$$N_{crit} = \frac{g(f_A)}{\chi(T)} \tag{6.3}$$

Block copolymers of a given composition, f_A, will be ordered if $N \geq N_{crit}$. A common way to measure χ is through the application of Leibler's Random Phase Approximation (RPA)[34], where small angle X-ray (SAXS) experiments can be used to measure concentration fluctuations by fitting the structure factor, $S(q)$, to disordered scattering profiles. The interaction parameters derived from scattering are called χ_{SC}. There has been considerable debate about how the measured χ_{SC} relates to the value of χ that should be used in the SCFT calculations.[36,205–209] An attractive feature of N_{crit} is that it can be measured directly and interpreted without any debate.

The addition of salt is known to alter the thermodynamics of block copolymers due to the introduction of new interactions between the polymer chains and ions, e.g., electrostatic interactions, charge dissociation, ion solvation, ion translational entropy and physical cross-linking between the ions and polymer chains.[59–63,183,210–212] Ions tends to segregate in the phase with higher permittivity, which increases segregation strength between the salt-free and the salt-containing blocks. This was captured in models developed by Wang and coworkers using the concept of Born solvation energy.[50,51,56,213] In these models, χ is replaced with an effective interaction parameter, χ_{eff}, to account for the interactions introduced by salt. In the simplest case

$$\chi_{eff} = \chi_0 + mr \tag{6.4}$$

where χ_0 is the Flory-Huggins parameter for the salt-free system, r is a suitable measure of salt concentration and m is a system-dependent proportionality constant. This form for χ_{eff} in salty systems was first proposed in the pioneering work of Mayes and coworkers.[52]

In this paper, which builds on our previous study of the phase behavior of block copolymer electrolytes[107], we use the standard RPA-based analysis to determine the effective interaction parameter, $\chi_{eff,SC}$, from SAXS profiles of a series of disordered SEO/LiTFSI mixtures. Our experiments cover a wide range of block copolymer compositions, $0.18 \leq f_{EO} \leq 0.84$, and chain lengths, $49 \leq N \leq 414$. We also determine N_{crit} as a function of block copolymer composition. It is generally observed that adding salt stabilizes the ordered phase, i.e., m in Equation 6.4 is positive. This would imply that N_{crit} must decrease with added salt. We show that this is only true over a finite range of copolymer compositions, $0.27 \leq f_{EO} \leq 0.90$. In the range $0.15 \leq f_{EO} < 0.27$, N_{crit} increases with added salt and m is negative. We find that m is a smooth function of f_{EO}. For reasons that we clarify below, we propose using the term isotaksis composition to refer to the point where $m = 0$. For SEO/LiTFSI systems, the isotaksis composition is $f_{EO} = 0.27$.

6.2 Experimental Methods

6.2.1 Polymer Synthesis and Characterization. The polystyrene-*block*-poly(ethylene oxide) (SEO) copolymers in this study were synthesized via anionic living polymerization[83] and purified according to ref 58. The copolymers used in this study are called SEO(*xx*-*yy*), where *xx* and *yy* are the number-averaged molecular weights of the PS, M_{PS}, and PEO, M_{PEO}, in kg mol^{-1}, respectively. Chain length, N, was calculated by $N = N_{PS} + N_{PEO}$ where

$$N_i = \frac{M_i}{\rho_i(T) N_A v_{ref}} \ (i = \text{PS or PEO}) \tag{6.5}$$

and N_A is Avogadro's number and v_{ref} was fixed at 0.1 nm^3. The volume fractions of each block of the copolymers were calculated by

$$f_{EO} = \frac{v_{EO}}{v_{EO} + \frac{M_{PS} M_{EO}}{M_S M_{PEO}} v_S} \tag{6.6}$$

where v_{EO} and v_S are the molar volumes of ethylene oxide and styrene monomer units, respectively, and M_{EO} and M_S are the molar masses of ethylene oxide (44.05 g mol^{-1}) and styrene (104.15 g mol^{-1}), respectively. Molar volumes were calculated by $v = M/\rho$. In this study, the densities (g cm^{-3}) of the PEO and PS blocks were given by $\rho_{PEO} = 1.13$ and $\rho_{PS} = 1.05$, measured values at 90 °C. The neat copolymers are completely transparent and colorless. Table 6.1 gives the properties of the 8 SEO copolymers used in this study.

6.2.2 Electrolyte Preparation. The block copolymer electrolytes used in this study were prepared according to ref 214. The copolymers were dried at 90 °C under vacuum in a glovebox antechamber for at least 12 hours and then immediately brought into an argon environment. Lithium bis(trifluoromethanesulfonyl)imide (LiTFSI) salt (Novolyte) was transferred from its air-free packaging into a vial inside of a glovebox, and then dried at 120 °C under vacuum in a

glovebox antechamber for three days. Due to the hydroscopic nature of the salt, Argon environment gloveboxes (Vacuum Atmosphere Company) with low oxygen and water levels were used for all sample preparation. The salt containing samples were prepared by blending SEO/benzene solutions with the required amount of a 75 wt% solution of LiTFSI/tetrahydrofuran (THF) solution to achieve the calculated salt concentrations.

Table 6.1: Properties of copolymers in the study.

polymer	M_{PS}	M_{PEO}	N	f_{EO}
SEO(17.4-3.9)	17.4	3.9	342	0.18
SEO(9.4-2.4)	9.4	2.4	189	0.20
SEO(9.4-4.0)	9.4	4.0	214	0.29
SEO(1.7-1.4)	1.7	1.4	49	0.44
SEO(2.9-3.3)	2.9	3.3	99	0.52
SEO(3.8-8.2)	3.8	8.2	189	0.68
SEO(5.1-12.8)	5.1	12.8	281	0.71
SEO(4.0-22.4)	4.0	22.4	414	0.84

For the salty samples, we assume that all of the salt resides in the PEO domain.[29–31] Block copolymers containing salt are considered to be pseudo-binary systems where the volume fraction of the salt + PEO component is given by

$$f_{EO,salt} = \frac{\nu_{EO,LiTFSI}(r)}{\nu_{EO,LiTFSI}(r) + \left(\frac{M_{PS}M_{EO}}{M_S M_{PEO}}\nu_S\right)} \tag{6.7}$$

where r is the molar ratio of Li to ethylene oxide (EO) moieties ($r = \frac{[Li]}{[EO]}$) and $\nu_{EO,LiTFSI}$ is the molar volume of the salt-containing PEO phase calculated by

$$\nu_{EO,LiTFSI}(r) = \frac{M_{EO} + rM_{LiTFSI}}{\rho_{EO,LiTFSI}} \tag{6.8}$$

where

$$\rho_{EO,LiTFSI}(r) = 2.008r + 1.13 \tag{6.9}$$

is derived from measured density values at 90 °C taken from ref 19.

6.2.3 Small Angle X-ray Scattering (SAXS) Measurements. Source beamline 7.3.3 at Lawrence Berkeley National Lab[167] and Stanford Synchrotron Radiation Light Source beamline 1-5 at SLAC

National Accelerator Laboratory. Scattering was performed using 10-12 keV X-rays. Silver behenate was used to determine the beam center and sample-to-detector distance. The scattered intensity was corrected for beam transmission, empty cell scattering, as well as for unavoidable air gaps in the system. Glassy carbon (NIST) was used to determine the scaling calibration to obtain absolute intensity scattering. Two-dimensional scattering patterns were integrated azimuthally using the Nika program for IGOR Pro to produce one-dimensional (1D) scattering profiles.[168] In order to compare data collected at each beamline, temperature calibrations were conducted to measure the absolute temperature of the samples by making separate electrolyte samples with a thermocouple running through the sample holder. The data presented in the main text reflects the absolute temperatures of the samples.

6.3 Results

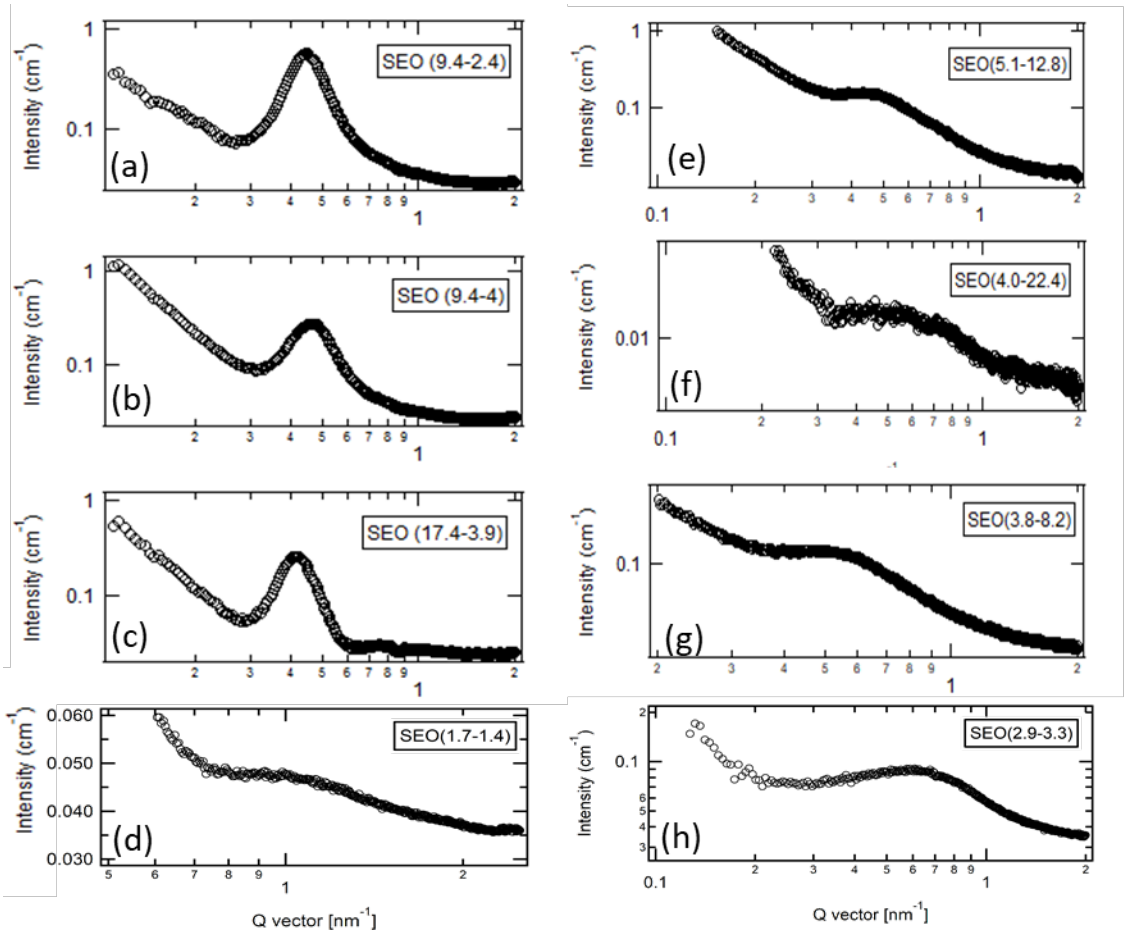

Figure 6.1 Absolute scattering of neat SEO: Absolute scattering for asymmetric copolymers in the neat state ($r = 0$) at 90 °C for (a) SEO(9.4-2.4), (b) SEO(9.4-4.0), (c) SEO(17.4-3.9), (d) SEO(1.7-1.4), (e) SEO(5.1-12.8), (f) SEO(4.0-22.4), (g) SEO(3.8-8.2), and (h) SEO(2.9-3.3).

Figure 6.1 shows the measured absolute scattering intensity (I) as a function of scattering vector, q, of the eight SEO copolymers in the salt-free state at 90 °C. All eight copolymers are disordered,

indicated by a single broad scattering peak, at all accessible temperatures. As the molecular weight of the copolymer increases, the location of the primary scattering peak, q^*, moves to a lower value of q, indicative of an increase in chain dimensions. However, the overall intensity of the scattering is not proportional to *N.* For example, SEO(4.0-22.4) has the lowest scattering intensity, but is the longest copolymer in the study.

The scattering theory of monodisperse disordered diblock copolymers was developed by Leibler.[34] The scattering function $I(q)$ proposed by this theory for a perfectly monodisperse AB diblock copolymer with degree of polymerization *N* can be written as

$$I_{dis}(q) = C\left[\frac{S(q)}{W(q)} - 2\chi\right]^{-1} \tag{6.10}$$

where *C* is the electron contrast calculated by

$$C = \nu_{ref}(B_A - B_B)^2 \tag{6.11}$$

where ν_{ref} is the reference volume, B_i is the X-ray scattering length density of block *i* given by $B_i = \frac{b_i}{\nu_i}$, and ν_i and b_i are the monomer volumes and X-ray scattering lengths of block *i*, respectively; $W(q)$ and $S(q)$ are the determinant and sum of the elements of the structure factor matrix $\|S_{ij}\|$. The expressions for $W(q)$ and $S(q)$ are given by

$$W(q) = S_{AA}^{\circ}S_{BB}^{\circ} - (S_{AB}^{\circ})^2 \tag{6.12}$$

$$S(q) = S_{AA}^{\circ} + S_{BB}^{\circ} + 2S_{AB}^{\circ} \tag{6.13}$$

where

$$S_{ii}^{\circ} = f_i N_i P_i(q) \tag{6.14}$$

$$S_{AB}^{\circ} = S_{BA}^{\circ} = (N_A f_A N_B f_B)^{\frac{1}{2}} F_A(q) F_B(q) \tag{6.15}$$

and

$$P_i(q) = 2\left[\frac{\exp(-x_i) - 1 + x_i}{x_i^2}\right] \tag{6.16}$$

$$F_i = \frac{1 - \exp(-x_i)}{x_i} \tag{6.17}$$

with $x_i = q^2 R_{g,i}^2$. Both blocks are modeled as flexible Gaussian chains and

$$R_{g,i}^2 = \frac{N_i(\alpha a_i)^2}{6} (i = PS, PEO) \tag{6.18}$$

where a_i is the statistical segment length of block i. In order to account for the conformational asymmetry between PS and PEO, we set a_{PS} = 0.50 nm and a_{PEO} = 0.72 nm (conformational asymmetry parameter, $\epsilon = \frac{a_{EO}}{a_S} = 1.44$).[172,200,215] In Equation 6.18, a chain stretching parameter, α, is introduced to match experimental and theoretical values of $R_{g,i}$. N_i in Equations 6.14-6.18 is the number-average degree of polymerization for block i based on v_{ref}, and the calculated values are provided in Table 1. Equations 6.10-6.18 are used to analyze the scattering profiles from disordered block copolymer/salt mixtures. We ignore the fact that these equations were only developed for pure disordered block copolymers.[58,110,216,217]

Figure 6.2 shows a typical SAXS profile obtained from salt-free SEO(9.4-4.0) at 75 °C. The open symbols show the data and the solid green line represents a fit to the equation

$$I_{tot}(q) = I_{dis}(q) + I_{bkgrd}(q) \tag{6.19}$$

where $I_{dis}(q)$ (shown in blue) is Equation 6.10 with χ, α and C as adjustable parameters and $I_{bkgrd}(q)$ (shown in red) is an exponential function to compensate for imperfect background subtraction. We find excellent agreement between the fitted function and the data.

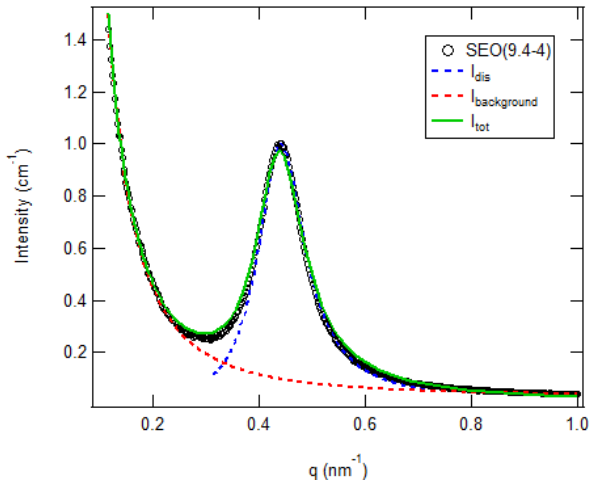

Figure 6.2 Example RPA fit: Example of RPA fit on neat SEO(9.4-4.0) at 75 °C. The open circles show the raw data and the green, blue, and red dashed curves show the fits for the total scattering, RPA fit, and background correction.

We begin with a discussion of the fitted parameter, C. If we assume that the salt molecules remain strongly correlated with the EO segments in the disordered state, then we can consider our mixtures to comprise of two "components": PS and PEO + salt. The density of homopolymer PEO/LiTFSI mixtures, $\rho_{EO,salt}$, as a function of r has been measured experimentally and is provided in Equation 6.9.[19] This can be used to calculate the theoretical scattering length density of these mixtures, $B_{EO,salt}$. If we assume that B_S is given by the known value obtained from homopolymer PS, then the only unknown in Equation 6.11 is $B_{EO,salt}$. The measurements of C thus provide a measurement

of $B_{EO,salt}$, which we refer to as $B_{EO,salt}^{fit}$. This parameter can be used to calculate the effective density of the PEO/LiTFSI component, $\rho_{EO,salt}^{fit}$ using the following equations

$$\rho_{EO,salt}^{fit} = B_{EO,salt}^{fit}\left(\frac{\rho_{EO,salt}}{B_{EO,salt}}\right) \tag{6.20}$$

and

$$B_{EO,salt} = Y_{LiTFSI}B_{LiTFSI} + (1 - Y_{LiTFSI})B_{EO} \tag{6.21}$$

where Y_{LiTFSI} is the volume fraction of LiTFSI in the PEO+salt phase calculated by

$$Y_{LiTFSI} = \frac{r\nu_{LiTFSI}}{(1+r)\nu_{EO,LiTFSI}} \tag{6.22}$$

where ν_{LiTFSI} was calculated from $\rho_{LiTFSI} = 2.023$ g cm^{-3}. These calculations were performed at 90 °C, the applicable temperature for Equation 6.9.

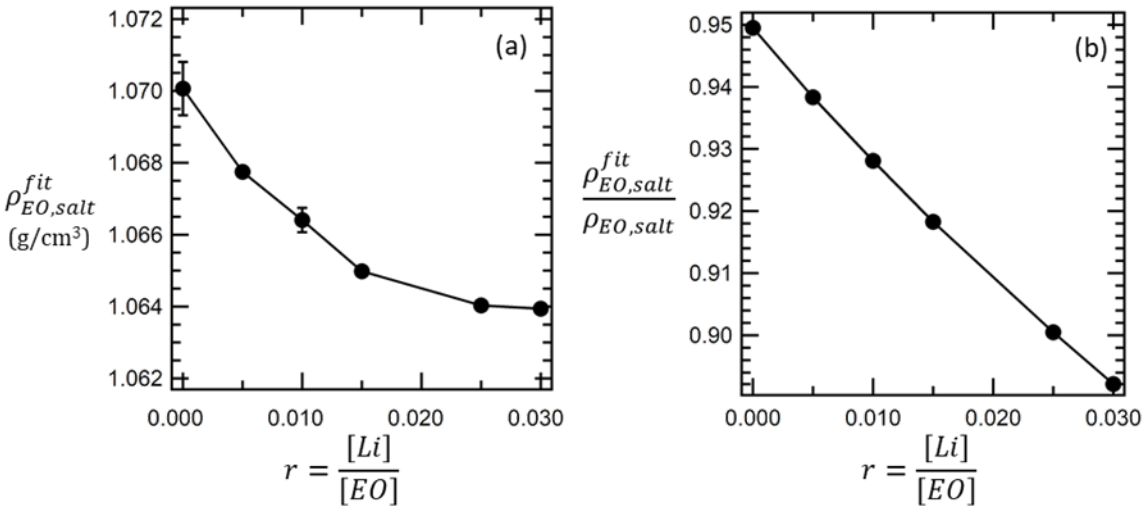

Figure 6.3 Contrast of SEO/LiTFSI: Results from fitting contrast during RPA fits: averaged values for (a) calculated salty PEO density, $\rho_{EO,salt}^{fit}$, and (b) ratio of fitted density to actual density, $\frac{\rho_{EO,salt}^{fit}}{\rho_{EO,salt}}$, as a function of salt concentration, *r*, taken at 90 °C. Error bars show the standard deviations for the data sets. Lines are used to guide the eye.

Figure 6.3a shows the averaged values of $\rho_{EO,salt}^{fit}$ for all eight copolymers as a function of salt concentration at 90 °C. The error bars represent the standard deviation of the averaged data set. First, it is important to note that the individual values for $\rho_{EO,salt}^{fit}$ for all SEO copolymers collapse on to a single point for each salt concentration. This provides justification for our assumption that SEO/LiTFSI mixtures can be approximated as two-component systems. In other words, the change in density of PEO from homopolymer values is dependent only on salt concentration and not on

copolymer properties, N and f_{EO}. The fitted density of PEO/LiTFSI is a weak function of salt concentration, decreasing by < 1% over the experimental salt concentration window (Figure 6.3a). This decrease is opposite to what has been observed in homopolymer PEO/LiTFSI mixtures.[19] Figure 6.3b is a plot of $\frac{\rho_{EO,salt}^{fit}}{\rho_{EO,salt}}$ versus salt concentration. The fitted density values are consistently lower than the homopolymer values. It is important to note that even in the absence of salt, $r = 0$, $\frac{\rho_{EO,salt}^{fit}}{\rho_{EO,salt}} = 0.95$ indicating that the density of PEO is affected by the presence of the PS block. The deviations between the fitted density and that of homopolymer/salt mixtures is less than 10% over the entire salt concentration window. These seemingly insignificant deviations in $\rho_{EO,salt}$ are important during the calculation of the scattering contrast because the electron density of the two phases (PS and PEO/LiTFSI) are similar: a 7% decrease in $\rho_{EO,salt}$ results in a 100% increase in $\left(B_{EO,salt} - B_S\right)^2$ when $r = 0.01$.

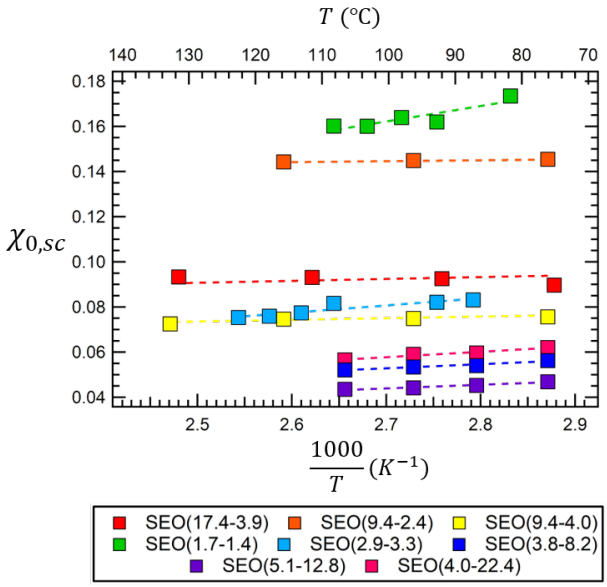

Figure 6.4 Temperature Dependence of $\chi_{0,SC}$: Temperature dependence for the Flory-Huggins interaction parameter for the neat SEO copolymers, $\chi_{0,SC}$. Dashed lines are fits to Equation 6.1.

The main parameter of interest is χ_{SC}, obtained by the fitting procedure depicted in Figure 6.2. Figure 6.4 shows the temperature dependence of $\chi_{0,SC}$, the Flory-Huggins interaction parameter determined from scattering for the salt-free block copolymers. The dashed lines are fits of the extracted $\chi_{0,SC}$ values presented in Figure 6.4 to Equation 6.1. The temperature dependence of $\chi_{0,SC}$ is consistent throughout the copolymers studied: $\chi_{0,SC}$ decreases with increasing temperature. However, the values of A and B obtained vary significantly between the copolymers. In other words, $\chi_{0,SC}$ depends on f_{EO} and N. There are no universally accepted functions for the dependence of $\chi_{0,SC}$ on composition and chain length. A simple function that is consistent with our data is shown in Figure 6.5 where we plot $\chi_{0,SC}$ obtained at 100 °C versus $(f_{EO}N)^{-1}$. When data was not taken at exactly 100 °C, the fits to Equation 6.1 were used to interpolate $\chi_{0,SC}$ to 100 °C. The squares represent the data and the dashed line is a linear regression fit through the data,

$$\chi_{0,SC} = K_1 + \frac{K_2}{Nf_{EO}} \tag{6.23}$$

The regression analysis gives $K_1 = 0.038$ and $K_2 = 2.85$.

The functional form given in Equation 6.23 is motivated by the theory of Fredrickson and Helfand who theoretically examined the effect of concentration fluctuations on the phase behavior of block copolymers.[218] In this theory, the product χN at the ODT, $(\chi N)_{ODT}$, decreases with increasing *N*. For example, in symmetric systems with $f_A = 0.50$, $(\chi N)_{ODT} = 10.495 + 41.002N^{-\frac{1}{3}}$. The mean-field value of $(\chi N)_{ODT}$ is only obtained in the limit of infinite chain length.[34] Equation 6.23 is similar in spirit and for finite f_{EO}, a composition- and chain-length-independent χ is obtained in the limit of infinite chain length. The product Nf_{EO} is equal to N_{EO}, the degree of polymerization of the PEO block. Equation 6.23 implies an implicit asymmetry in the thermodynamics between PS and PEO: a longer PEO block reduces the thermodynamic incompatibility between the two polymer blocks.

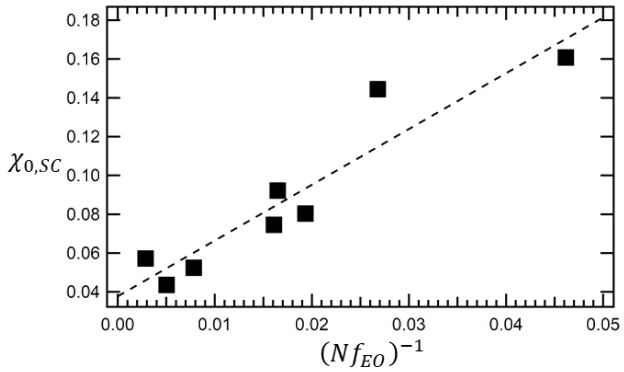

Figure 6.5 Dependence of $\chi_{0,SC}$ on copolymer properties: Chain length, *N*, and composition, f_{EO}, dependence on the Flory-Huggins interaction parameter of the neat copolymers, $\chi_{0,SC}$, at 100 °C. The dashed line is a linear regression through the data: $\chi_{0,SC} = \frac{2.85}{Nf_{EO}} + 0.038$.

We now move to a discussion of the thermodynamics of the salt-containing SEO copolymers. Figure 6.6 shows the temperature dependence of $\chi_{eff,SC}$, the interaction parameter of the salt-containing species derived from scattering, for three SEO copolymers of similar chain lengths ($N \sim 200$) with varying PEO compositions. Solid squares represent experimental measurements and the dashed lines are a fit through the data according to Equation 6.1. The temperature dependence of $\chi_{eff,SC}$ matches what was seen in the salt-free copolymers; *A* in Equation 6.1 remains positive. Figure 6.6a shows the temperature dependence of $\chi_{eff,SC}$ of SEO(9.4-2.4) with $f_{EO} = 0.20$. As salt is added to the system, $\chi_{eff,SC}$ steadily decreases from 0.145 at $r = 0$ to 0.140 at $r = 0.005$ and finally to 0.13 at $r = 0.025$ at 93 °C. In most cases reported in the literature, $\chi_{eff,SC}$ increases with increasing salt concentration.[53–55,219,220] Although the behavior of SEO(9.4-2.4) is unexpected, this trend has been previously reported in ref 58 for a SEO copolymer of a similar composition (SEO(1.9-0.8) with $N = 42$ and $f_{EO} = 0.29$). Figure 6.6b shows the

temperature dependence of $\chi_{eff,SC}$ of SEO(9.4-4.0) with $f_{EO} = 0.29$. Here, we do not see a significant change in $\chi_{eff,SC}$ upon salt addition to $r = 0.005$ indicating that at this copolymer composition, $\chi_{eff,SC}$ is not a strong function of r. Figure 6.6c shows the temperature dependence of $\chi_{eff,SC}$ of SEO(3.8-8.2) with $f_{EO} = 0.67$. This copolymer shows a significant increase in $\chi_{eff,SC}$ upon salt addition (almost a 30% increase, from 0.50 at $r = 0$ to 0.62 at $r = 0.005$ at 100 °C). Figure 6.6 shows that the effect of salt addition on $\chi_{eff,SC}$ is highly dependent on copolymer composition.

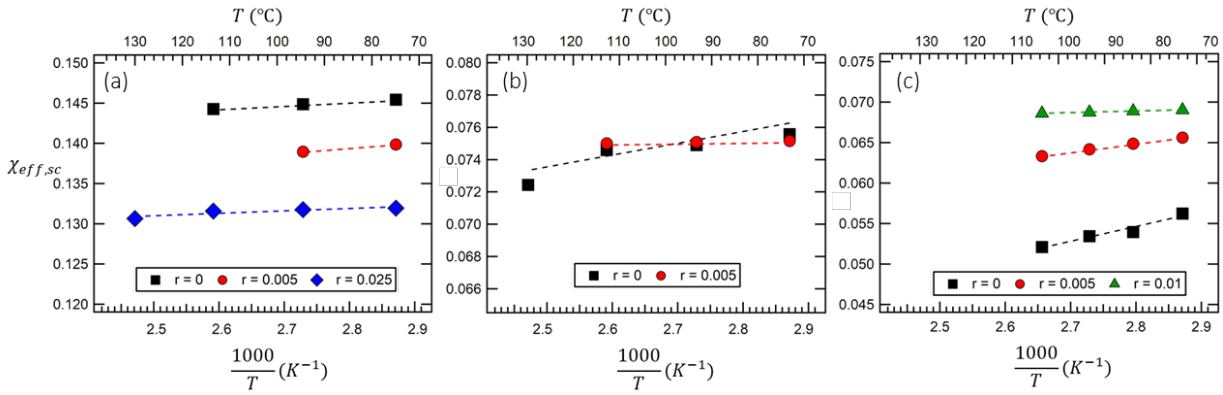

Figure 6.6 Temperature dependence of $\chi_{eff,SC}$: Temperature dependence of effective Flory-Huggins interaction parameter, $\chi_{eff,SC}$, for neat and salty samples of (a) SEO(9.4-2.4), (b) SEO(9.4-4.0), and (c) SEO(3.8-8.2). All copolymers have chain lengths around $N = 200$. Symbols represent the data and dashed lines are fits to Equation 6.1.

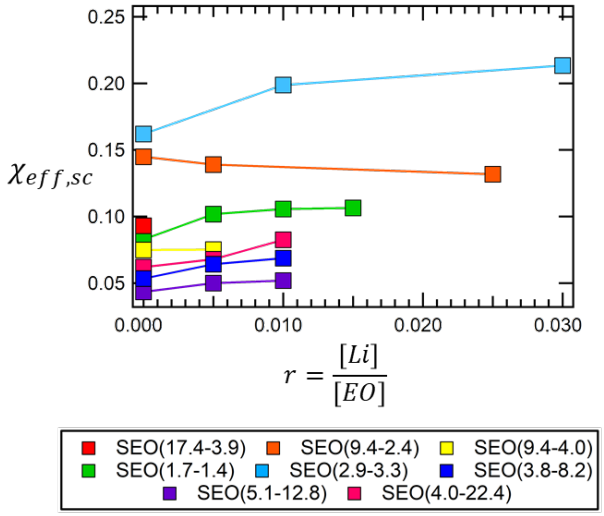

Figure 6.7 Salt concentration dependence of χ_{eff}: Salt concentration dependence for the effective Flory-Huggins interaction parameter, $\chi_{eff,SC}$, at 100 °C for the SEO/LiTFSI mixtures in the study. Lines are drawn to connect data points as a guide for the eye.

Figure 6.7 shows the salt concentration dependence of $\chi_{eff,SC}$ for the eight SEO copolymers taken at 100 °C. Solid lines are used to connect the data points and serve to guide the eye. In general, $\chi_{eff,SC}$ increases with r, except for SEO(9.4-2.4) as described above (shown in orange). For the

low molecular weight SEO copolymers, SEO(1.7-1.4) (cyan) and SEO(2.9-3.3) (green), the effect of salt on $\chi_{eff,SC}$ seems to level-off at a given salt concentration as reported in ref 58, while for the copolymer with the highest PEO composition, SEO(4.0-22.4) (pink), $\chi_{eff,SC}$ increases linearly with salt concentration over the observed salt concentration window. It is obvious from Figure 6.7 that the effect of salt on $\chi_{eff,SC}$ is dependent on both N and f_{EO}.

As a first approximation, each of the datasets presented in Figure 6.7 were fit to Equation 6.4, where m is a copolymer dependent proportionality constant. Figure 6.8 shows the composition dependence of m taken at 100 °C weighted by the interaction parameters of the salt-free systems, $\chi_{0,SC}$. The dashed line is a linear regression through the data according to

$$\frac{m}{\chi_{0,SC}} = K_3 f_{EO} + K_4 \tag{6.24}$$

where $K_3 = 68.3$ and $K_4 = -18.6$. Note, only seven data points are presented in Figure 6.8 because there is no salt containing data for SEO(17.4-3.9), which orders immediately upon salt addition ($r \geq 0.005$). Equation 6.24 quantifies the dependence of rate of change in $\chi_{eff,SC}$ upon salt addition, given by m, on copolymer composition. We see excellent agreement between the data in Figure 6.8 and Equation 6.24. As the volume fraction of PEO increases, $\frac{m}{\chi_{0,SC}}$ increases. It is important to note that at the lowest value of f_{EO}, the ordinate of Figure 6.8 becomes negative, characterized by K_4.

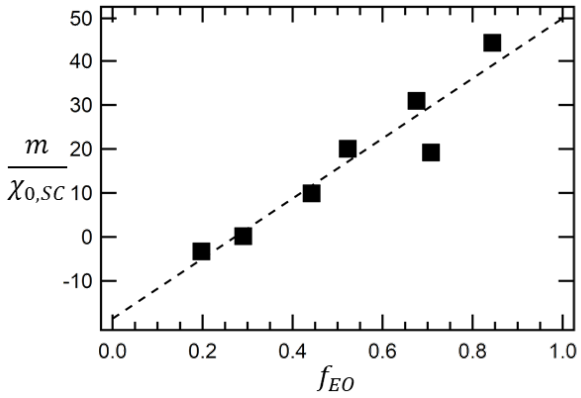

Figure 6.8 Composition dependence of *m*: Composition, f_{EO}, dependence on the weighted slope of Equation 6.4, $\frac{m}{\chi_{0,SC}}$, taken at 100 °C. Dashed line is a fit to $\frac{m}{\chi_{0,SC}} = 68.2 f_{EO} - 18.6$.

Combining Equations 6.4, 6.23 and 6.24, we arrive at

$$\chi_{eff,SC} = \left[K_1 + \frac{K_2}{N f_{EO,salt}}\right]\left[1 + K_3 f_{EO,salt} r + K_4 r\right] \tag{6.25}$$

The comparison between Equation 6.25 and the data are presented in Figure 6.9 on a three-dimensional plot where $\chi_{eff,SC}$ is shown as a function of $f_{EO,salt}$ and r. The solid squares represent

the extracted $\chi_{eff,SC}$ replicated from Figure 6.7, and the dashed lines represent fits to Equation 6.25 in the range of $0 \leq r \leq 0.03$. Overall, we see good agreement between the measured values of $\chi_{eff,SC}$ and Equation 6.25.

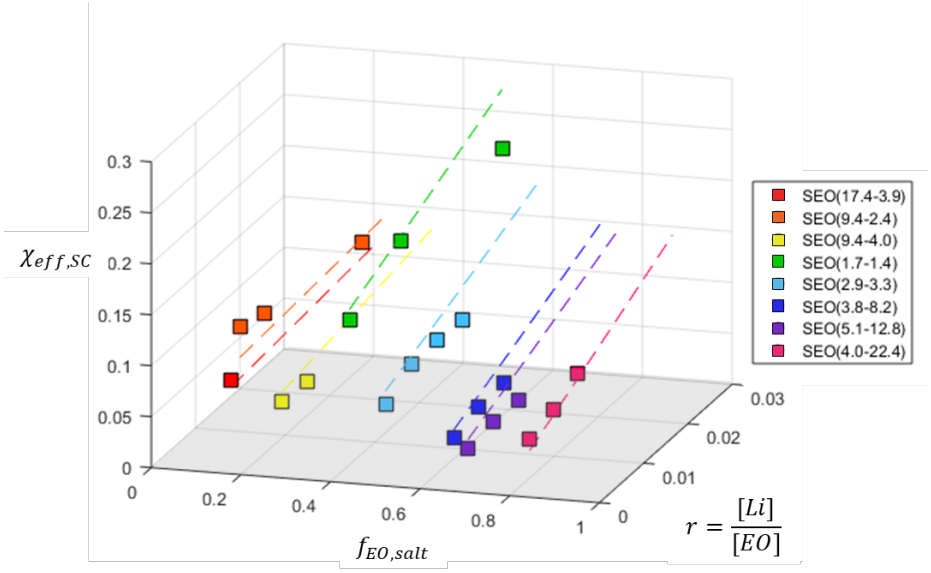

Figure 6.9 Predictions of $\chi_{eff,SC}$: Model predictions for effective Flory-Huggins interaction, $\chi_{eff,SC}$, as a function of salt concentration taken at 100 °C. Dashed lines are the fits to Equation 25, $\chi_{eff,SC} = \left[K_1 + \frac{K_2}{N f_{EO,salt}}\right]\left[1 + K_3 f_{EO,salt} r + K_4 r\right]$. Data points are replicated from Figure 6.7. The slopes of the lines are negative for the block copolymers with $f_{EO,salt} < 0.25$.

The final parameter extracted from the RPA fits is the chain-stretching parameter, α. In most cases, $\alpha > 1$ implying that chains are stretched. In the neat copolymers, as temperature increases, α decreases (Figure 6.13). At fixed tempeature, α for neat copolymers decreases with increasing f_{EO}. Figure 6.14 shows data at 100 °C. At the highest f_{EO}, α is less than one. The addition of salt generally leads to an increase in α as shown in Figure 6.15. The dependence of α on r, shown in Figure 6.15, is very similar to the dependence of $\chi_{eff,SC}$ on r shown in Figure 6.7. In general, the increase in effective repulsion between the blocks, quantified by $\chi_{eff,SC}$, leads to a larger value of α.

6.4 Order-Disorder Transition

The discussion thus far has focused on scattering from disordered SEO/LiTFSI mixtures. Whether or not a particular mixture is ordered depends on four variables: N, $f_{EO,salt}$, r, and T. Our discussion below is restricted to a fixed temperature of 100 °C. At fixed values of $f_{EO,salt}$ and r, one can, in principle, access a transition from disorder to order by increasing N. We define N_{crit} as the chain length at that transition. If χ is known, then Equation 6.3 can be used to determine N_{crit}.

As a first approximation, we assume that the Flory-Huggins interaction parameter extracted from scattering is equivalent to the theoretical parameter, $\chi_{eff,SC} = \chi$, and then use Equation 6.25 in conjunction with Equation 6.2 to calculate N_{crit}:

$$(\chi N)_{odt} = \left[K_1 N_{crit} + \frac{K_2}{f_{EO,salt}}\right]\left[1 + K_3 f_{EO,salt} r + K_4 r\right] = g(f_{EO,salt}) \tag{6.26}$$

Equation 6.26 can be solved to obtain N_{crit} as a function of $f_{EO,salt}$ and r.

The solid curve in Figure 6.10a shows the calculated values of N_{crit} as a function of f_{EO} in the neat state, $r = 0$. The model prediction is asymmetric with respect to copolymer composition, unlike predictions from mean-field theory for conventional block copolymer systems[34], with a minimum at $f_{EO} = 0.37$. The N_{crit} versus f_{EO} curve may be considered a phase boundary: systems below the curve are predicted to be disordered while those above the curve are predicted to be ordered. The squares in Figure 6.10a represent the SEO copolymers considered in this study, characterized by N and f_{EO}. All of the SEO copolymers are disordered in the neat state; however, several of the squares lie above the $N_{crit}(f_{EO})$ curve in Figure 6.10a. Therefore, it is evident that our assumption that $\chi_{SC} = \chi$ leads to an inconsistency in the model.

There are no published results for relating χ_{SC} to χ in block copolymers. However, for the case of polymer blends, Sanchez[205] presented a simple expression relating these two parameters by recognizing that :

$$\chi_{SC} = -\frac{1}{2}\left(\frac{\partial^2 (f_A(1-f_A)\chi)}{\partial f_A^2}\right) \tag{6.27}$$

The solution for Equation 6.27, which was first proposed by de Gennes[36], with appropriate boundary conditions is

$$\chi = \frac{2}{1-f_A}\int_0^{1-f_A} (1-f_A')\chi_{SC}(f_A')d(1-f_A') + \frac{2}{f_A}\int_0^{f_A} (f_A')\chi_{SC}(f_A')df_A' \tag{6.28}$$

When Equation 6.25 for $\chi_{eff,SC}(f_{EO,salt})$ is substituted into Equation 6.28 for $\chi_{SC}(f_A)$, we arrive at the following result

$$\chi_{eff} = \frac{\left(K_2 + K_1 N f_{EO,salt}\right)\left(1 - 2f_{EO} + 2f_{EO,salt}^2\right)\left(1 + K_3 f_{EO,salt} r + K_4 r\right)}{N f_{EO,salt}} \tag{6.29}$$

Equation 6.29 in conjunction with Equation 6.2 is used to calculate N_{crit}:

$$(\chi N)_{odt} = \frac{\left(K_2 + K_1 N_{crit} f_{EO,salt}\right)\left(1 - 2f_{EO} + 2f_{EO,salt}^2\right)\left(1 + K_3 f_{EO,salt} r + K_4 r\right)}{f_{EO,salt}} = g(f_{EO,salt}) \tag{6.30}$$

Equation 6.30 can be solved to obtain N_{crit} as a function of $f_{EO,salt}$ and r. Figure 6.10b shows the results of these calculations for the salt-free case. The predicted phase boundary remains asymmetric with respect to composition, but it moves to higher values of N_{crit} for all values of f_{EO} relative to Figure 6.10a. In Figure 6.10b, all of the data points lie underneath the $N_{crit}(f_{EO})$ curve indicating that all of the copolymers are predicted to be disordered in the absence of salt, consistent with our experiments. It is evident that accounting for the difference between $\chi_{eff,SC}$ and χ_{eff} is essential for quantifying the thermodynamic interactions in SEO/LiTFSI mixtures.

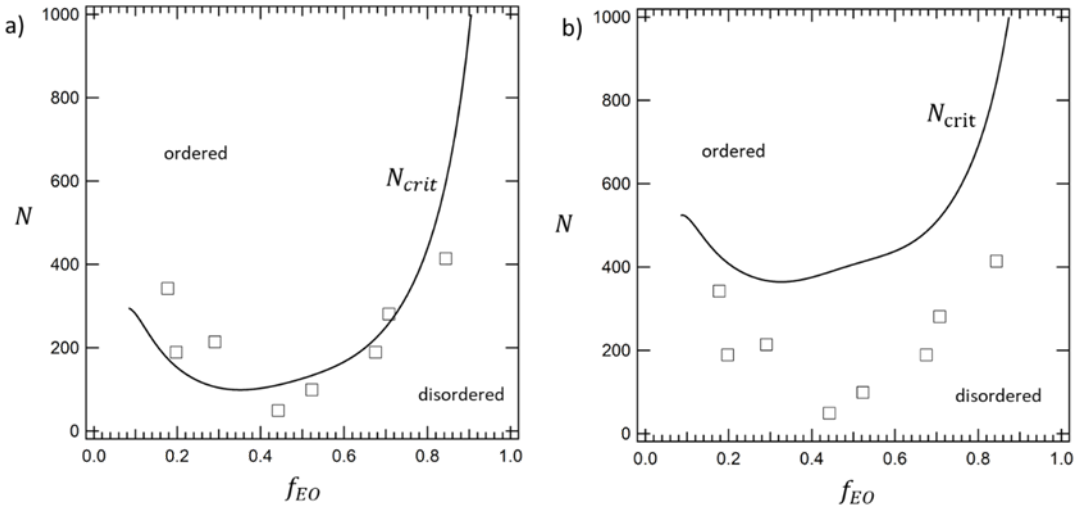

Figure 6.10 Critical chain length predictions: A plot of N versus f_{EO} for neat SEO copolymers ($r = 0$). The curve represents N_{crit} versus f_{EO} using a) Equation 6.25 or b) Equation 6.29 as χ_{eff}. Squares represent the values of N and f_{EO} of the SEO copolymers covered in this study. All of the copolymers are disordered in the neat state and thus we expect the data to lie below the N_{crit} versus f_{EO} curve. This is only the case when Equation 6.29 is used (b).

Based on the findings of Figure 6.10, we take Equation 6.29 to represent the Flory-Huggins interaction parameter in our system and use it to determine the effect of salt on critical chain length. The curves in Figure 6.11 show the composition dependence of N_{crit} for the salt concentrations of interest: $r = 0$ (black), $r = 0.005$ (red), $r = 0.01$ (green) and $r = 0.025$ (blue). The solid squares in Figure 6.11 represent the values of N and $f_{EO,salt}$ for the SEO/LiTFSI mixtures that order at $r \leq 0.025$. In these mixtures, the addition of salt leads to a transition from disorder to order. The color of each square in Figure 6.11 indicates the salt concentration at which the SEO/LiTFSI mixture first forms an ordered morphology and matches the color of the N_{crit} curves. There is excellent quantitative agreement between theory and experiment on the high $f_{EO,salt}$ side. For $f_{EO,salt} \leq 0.58$, the experimental data lie well below the theoretical curves. There is, however, some correspondence between the theoretical curves and experimental data. The curve for $r = 0.025$ (blue) dips to the lowest value of N_{crit}, consistent with the data at $f_{EO,salt} = 0.58$. At $f_{EO,salt} = 0.29$, the curve for $r = 0.01$ (green) is above the $r = 0.025$ curve (blue), consistent with the data.

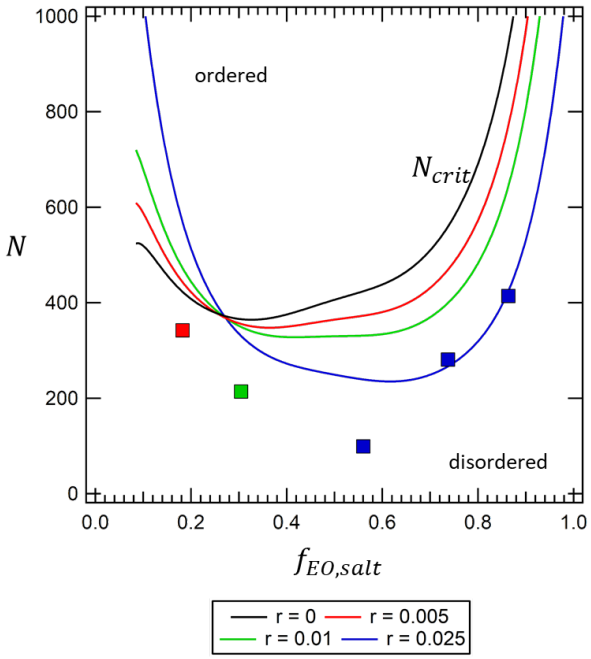

Figure 6.11 Salt concentration dependence of critical chain length: Critical chain length for ordering, N_{crit}, as a function of composition, $f_{EO,salt}$, for SEO/LiTFSI mixtures at 100 °C for different salt concentrations: $r = 0$ (black), $r = 0.005$ (red), $r = 0.01$ (green), and $r = 0.025$ (blue). The lines represent the theoretical curves and the squares represent the SEO copolymers discussed in this study. The color of the squares denotes the salt concentration needed to achieve an ordered phase.

We see the emergence of two regimes of salt-dependent phase behavior on either side of $f_{EO,salt} = 0.27$, which we refer to as the isotaksis point. At this composition, N_{crit} is independent of salt concentration (all curves for N_{crit} intersect at $f_{EO,salt} = 0.27$), i.e., the addition of salt does not affect order in the SEO/LiTFSI mixtures of this composition. We chose the term "isotaksis point" because the word "taksis" means order (spelled τάξις in Greek). At $f_{EO,salt} > 0.27$, the addition of salt stabilizes the ordered phases and the order-disorder boundary drops to lower values of N_{crit}. At $f_{EO,salt} < 0.27$, the addition of salt stabilizes the disordered phase and the order-disorder boundary moves to higher values of N_{crit}.

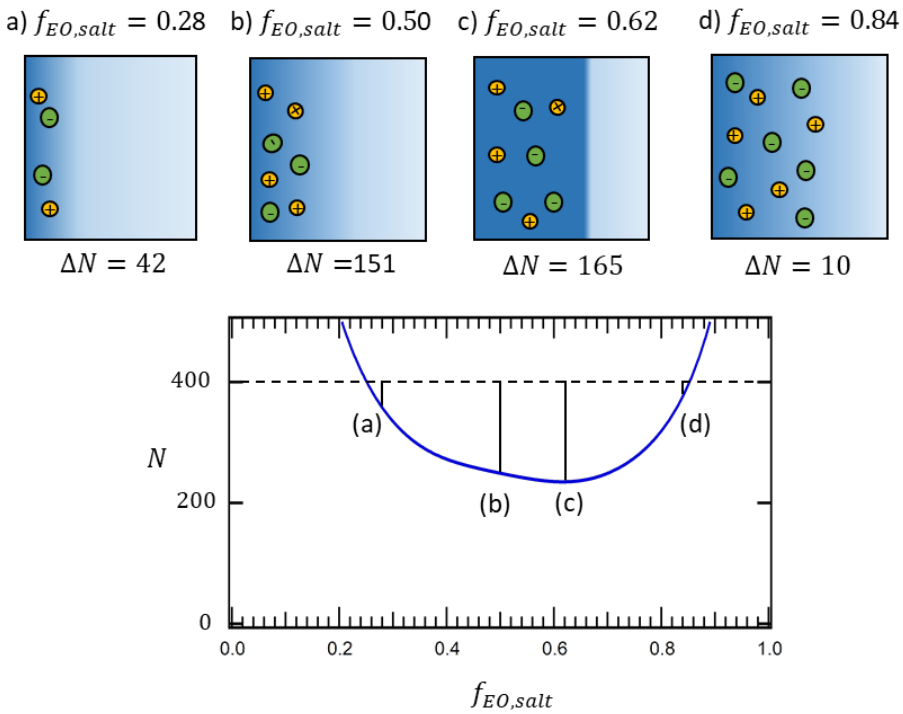

Figure 6.12 Schematic of degree of segregation: Schematic depicting effect of salt on the degree of segregation, ΔN, of microphase separated of SEO/LiTFSI mixtures with increasing $f_{EO,salt}$ at a constant salt concentration, $r = 0.025$, and total chain length, $N = 400$. The curve represents N_{crit} versus $f_{EO,salt}$ taken from Figure 6.11. ΔN is defined as the difference between the chosen N and the curve, and the vertical line segments indicate its value at selected values of $f_{EO,salt}$. The salt is assumed to lie in the PEO-rich microphase, but the degree of mixing between the PS and PEO blocks, governed by the magnitude of ΔN, is indicated by the color contrast and interfacial width in each schematic.

The segregation strength in pure block copolymers is characterized by $\Delta(\chi N)$ defined as $\Delta\chi N = \chi N - (\chi N)_{odt}$. At a given temperature and chain length, $\Delta(\chi N)$ is maximum at $f_A = 0.50$. However, this is only valid if χ is independent on composition and chain length. This simplifcation is not valid for SEO/LiTFSI mixtures, and the effect of composition on segregation strength is, perhaps, non-intuitive. We consider copolymers of different compositions at a single chain length and salt concentration. Such systems are represented by a horizontal line at the chosen value of N in Figure 6.11. For concreteness, we choose $N = 400$ and $r = 0.025$. In Figure 6.12, we re-plot the $N_{crit}(f_{EO,salt})$ curve for $r = 0.025$. Note that the salt concentration under these constraints is proportional to the product $rf_{EO,salt}$. The degree of segregation at 100 °C in systems with different $f_{EO,salt}$ can be quantified by $\Delta N = N - N_{crit}$. We show values of ΔN at selected $f_{EO,salt}$ values in Figure 6.12. Also shown in Figure 6.12, are schematics that illustrate the degree of segregation at each $f_{EO,salt}$ value. For simplicity, we focus on the compositions of the salt-rich and salt-poor microphases. The salt is assumed to lie in the PEO-rich microphase, but the degree of mixing between the PS and PEO blocks, governed by ΔN, is indicated by the color contrast and interfacial width in each schematic. At $f_{EO,salt} = 0.28$ (Figure 6.12a), the SEO/LiTFSI mixture is barely microphase separated as $\Delta N = 42$. Here we see a microphase separated morphology with a broad interfacial region. The interface sharpens and the compositional contrast between the microphases increases when $f_{EO,salt}$ is increased to 0.50 (Figure 6.12b); $\Delta N = 151$ at this composition. Increasing $f_{EO,salt}$ further to 0.62 results in the highest degree of segregation possible in systems

with $N = 400$ and $r = 0.025$ (Figure 6.12c); $\Delta N = 165$ at this composition. This is in contrast with conventional block copolymer melts, where the highest degree of segregation occurs at $f_A = 0.50$.[34] Finally, at $f_{EO,salt} = 0.84$ (Figure 6.12d), the degree of segregation decreases and $\Delta N = 10$. Outside of $0.28 \leq f_{EO,salt} \leq 0.84$, the SEO/LiTFSI mixtures at $r = 0.025$ and $N = 400$ form disordered phases. Qualtitatively different behavior would be obtained at other values of N and r. It is evident from Figures 6.11 and 6.12 that the relationship between segregation strength and copolymer composition in SEO/LiTFSI is complex.

6.6 Model for the Isotaksis Point

As mentioned in the Introduction, the thermodynamic properties of block copolymer/salt mixtures are complex and governed by many effects including electrostatics, ion solvation, ion-ion and ion-polymer correlations. Constructing a quantitative theory that is consistent with our data is outside the scope of this paper. In fact, the origin of the composition dependence of $\chi_{0,SC}$, the interaction parameter in SEO without salt, is unclear. Nevertheless, it seems important to present a plausible explanation for the existance of the isotaksis composition.

We assume that the ions are distributed uniformly in the disordered state, but they are confined to the PEO microphase in the ordered state, similar in spirit to the original work of Marko and Rabin.[221] If we assume that the salt ions are ideal, then the ion entropy change due to order formation, ΔS_{order}, is given by

$$\Delta S_{order} = n k_B \ln f_{EO} \tag{6.31}$$

where n is the number of independent ions and k_B is the Boltzmann constant. For simplicity we ignore the difference between f_{EO} and $f_{EO,salt}$ in this analysis which is a reasonable approximation for $r \leq 0.025$, the range of salt concentrations covered in Figure 6.11. If we assume a lattice model wherein n_t is the total number of lattice sites, n_{EO} is the number of lattice sites occupied by EO and each lattice site is either occupied by a polymer segment or a salt ion, then

$$\frac{\Delta S_{order}}{n_t k_B} = r \frac{n_{EO}}{n_t} \ln(f_{EO}) = r f_{EO} \ln(f_{EO}) \tag{6.32}$$

Note that the entropic contribution is a linear function of r.

We assume that this tendency to disorder is balanced by the solvation energy[51,52] that induces ordering, and is quantified by Equation 6.4. We thus define a theoretical χ, χ_{th}, that is the sum of the two contributions:

$$\chi_{th} = \chi_0 + m_n r + \frac{r f_{EO} \ln(f_{EO})}{f_{EO}(1 - f_{EO})} \tag{6.33}$$

where m_n is a nominal value of m that is assumed to be independent of composition. In many previous studies on mixtures of salt and SEO copolymers[55,107,220], m_n has been shown to be about 1.7. At the isotaksis point ($m = m_{it}$),

$$\frac{d\chi_{th}}{dr} = 0 = m_n + \frac{f_{EO,it}\ln(f_{EO,it})}{f_{EO,it}(1-f_{EO,it})} \tag{6.34}$$

and

$$m_n = -\frac{f_{EO,it}\ln(f_{EO,it})}{f_{EO,it}(1-f_{EO,it})} \tag{6.35}$$

For a system with $m_{it} = 1.7$, the isotakis point according to Equation 6.35 is predicted to occur at $f_{EO} = 0.31$. The quantitative agreement between experiments and the model is probably fortuitious, as the model is highly simplified. For example, one could envision placing a prefactor of 2 on the right hand side of Equation 6.32 to account for salt dissociation. However, the extent to which positively and negatively charged ions are independent in low dielectric media like PEO remains unclear. In addition to this, a complete theory for m_{it} would require inclusion of electrostatic interactions, ion correlations, and physical crosslinking due to interactions between ions and polymer backbones.

6.7 Conclusions

We have characterized thermodynamics of SEO/LiTFSI mixtures by analyzing SAXS scattering patterns from disordered systems. RPA was used to determine χ_{SC}, as a function of block copolymer composition, chain length, temperature and salt concentration. In the neat copolymers, $\chi_{0,SC}$ is a linear function of $(Nf_{EO})^{-1}$. At a given temperature, block copolymer composition and chain length, $\chi_{eff,SC}$ increases linearly with added salt. The data are only weak functions of temperature as shown in Figures 6.4 and 6.6, and therefore these conclusions apply across the entire temperature window studied ($75 < T$ (°C) < 130). The framework of Sanchez[205] was used to determine χ_{eff} from $\chi_{eff,SC}$ in both salty and salt-free systems. We use the term χ_{eff} as it represents interactions between PEO/LiTFSI and PS. SCFT results on pure block copolymers[41] are used to determine the relationship between $\chi_{eff}N$ and composition, $f_{EO,salt}$, at the order-disorder transition. We refer to the value of N at the order-disorder transition as N_{crit}. All of the SEO copolymers used in this study were disordered in the neat state and order upon salt addition. This enables a direct comparison between experimentally determined values of N_{crit} with theoretical predictions. At $f_{EO,salt}$ values greater than 0.27, the addition of salt decreases N_{crit}, i.e., the ordered phase is stabilized. At $f_{EO,salt}$ values less than 0.27, the addition of salt increases N_{crit}, i.e., the disordered phase is stabilized. We propose calling $f_{EO,salt}$ = 0.27 the isotaksis point. A simple theoretical model is proposed to predict the existence of this point. The use of χ to describe the phase behavior of neat block copolymers is strictly valid in the limit of infinite chain length. Fluctuation effects become important at finite chain lengths and this leads to non-trivial changes in phase behavior.[159,192,218] Strictly speaking, the implication of the isotaksis point is that the phase behavior of SEO/LiTFSI mixtures at this composition should be independent of salt concentration.

Instead, experiments show anamalous phase behavior in the vicinity of this composition. In particular the addition of salt to a disordered phase in the vicinity of the isotaksis point gives rise to two coexisting body centered cubic lattices which then disorder before finally ordering into the expected hexagonnally packed cylinder morphology.[106] While further work is required to determine the underpinnings of such observations, the present framework provides a platform to do so.

6.8 Nomenclature

6.8.1 Abbreviations

EO	ethylene oxide
LiTFSI	lithium bis(trifluoromethanesulfonyl) imide salt
N_A	Avogadro's number
ODT	order-disorder transition
PEO	poly(ethylene oxide)
PS	polystyrene
RPA	Random Phase Approximation
S	styrene
SAXS	small angle X-ray scattering
SCFT	Self-Consistent Field Theory
SEO	polystyrene-*block*-poly(ethylene oxide)

6.8.2 Symbols

a_i	statistical segment length of species i (nm)
b_i	X-ray scattering length of species i (nm mer^{-1})
B_i	scattering length density of species i (nm^{-2} mer^{-1})
C_i	Self consistent field theory fitting parameters
C	electron density contrast (cm^{-1})
d	domain size (nm)
f_A	volume fraction of species A
f_{EO}	volume fraction of PEO block
$I(q)$	scattering intensity (cm^{-1})
$I_{dis}(q)$	disordered copolymer scattering intensity (cm^{-1})
k_B	Boltzmann constant
m	proportionality constant
m_{it}	proportionality constant at isotaksis composition
M_i	number-averaged molecular weight of species i (kg mol^{-1})
N_i	number-averaged degree of polymerization of species i (sites chain^{-1})
N_A	Avogadro's number
N_{crit}	critical chain length for ordering
n	number of independent ions
n_{EO}	number of EO sites
n_t	total number of lattice sites

q	scattering vector (nm^{-1})
q^*	primary peak of scattering vector (nm^{-1})
r	salt concentration ($[Li^+]\ [EO]^{-1}$)
$R_{g,i}$	radius of gyration of species *i* (nm)
$S(q)$	scattering structure factor
T	temperature (K)
Y_{LiTFSI}	volume fraction of salt in PEO/LiTFSI microphase

6.8.3 Greek Symbols

α	chain-stretching parameter
ΔS_{order}	change in entropy due to ordering
ΔN	degree of segregation
ϵ	conformational asymmetry parameter
ν_i	molar volume of species *i* ($cm^3\ mol^{-1}$)
ν_{ref}	reference volume ($nm^3\ site^{-1}$)
ρ_i	density of species *i* ($g\ cm^{-3}$)
χ	Flory-Huggins interaction parameter
χ_{SC}	Flory-Huggins interaction parameter from scattering
χ_0	Flory-Huggins interaction parameter of salt free system
χ_{th}	theoretical Flory-Huggins interaction parameter
χ_{eff}	effective Flory-Huggins interaction parameter
χN	segregation strength
$(\chi N)_{odt}$	segregation strength at the ODT

6.9 Supporting Information

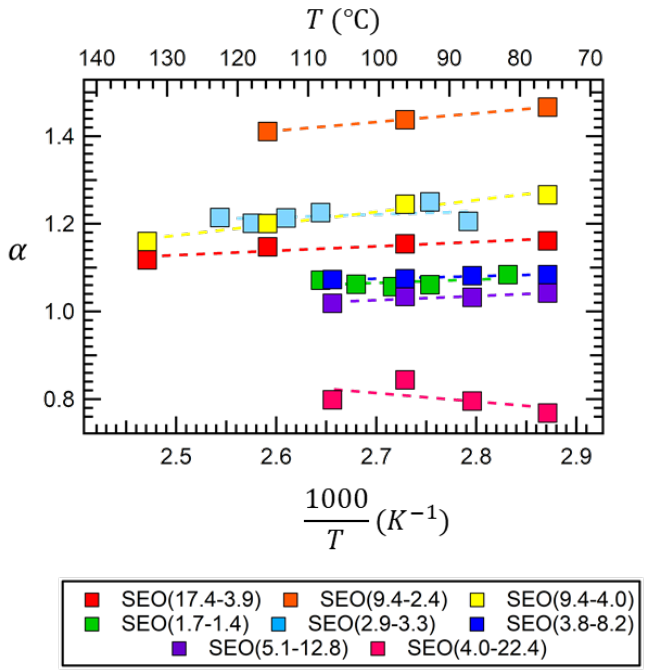

Figure 6.13 Chain stretching parameter for neat SEO: Temperature dependence for the chain-stretching parameter for the neat SEO copolymers, α. Dashed lines are linear regressions through the data.

Figure 6.13 shows the temperature dependence for the chain-stretching parameter, α, for the neat SEO copolymers. The dashed lines are linear regressions through the data. In general, $\alpha > 1$ for the SEO copolymers and α increases with decreasing temperature. Only SEO(4.0-22.4) does not follow this trend, where $\alpha < 1$ and increases with increasing temperature. At fixed tempeature, α for neat copolymers decreases with increasing f_{EO}.

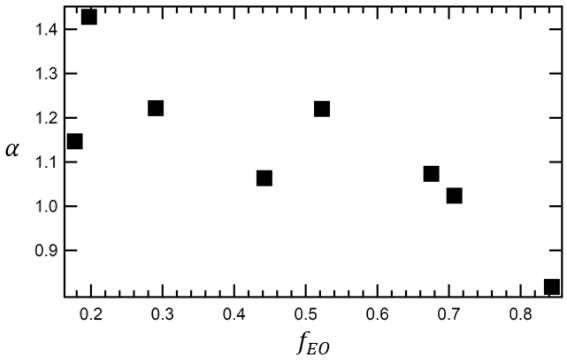

Figure 6.14 Composition dependence of chain stretching parameter: Dependence of the chain-stretching parameter, α, on composition, f_{EO}, of the neat copolymers at 100 °C.

Figure 6.14 shows the composition dependence of the chain-stretching parameter, α, of the neat copolymers at 100 °C. In general, α decreases with increasing f_{EO}. At the highest f_{EO}, α is less than one. This trend mimics the composition dependence of $\chi_{0,SC}$, where copolymers of higher PEO content exhibit weaker degrees of thermodynamic repulsion.

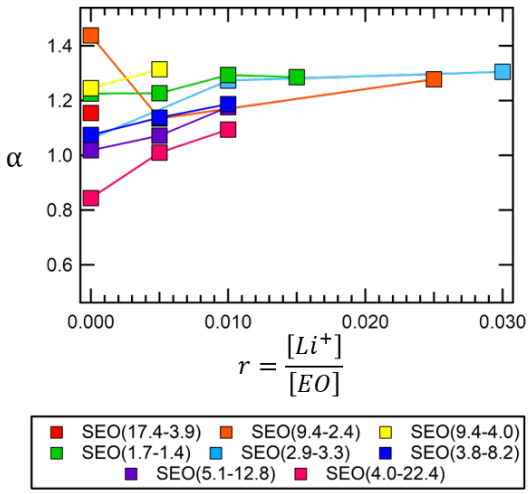

Figure 6.15 Salt concentration dependence of chain stretching parameter: Salt concentration dependence for the chain stretching parameter, α, at 100 °C for the SEO/LiTFSI in the study. Lines are drawn to connect data points as a guide for the eye.

Figure 6.15 shows the salt concentration dependence for the chain-stretching parameter, α, at 100 °C for the SEO/LiTFSI mixtures. Lines are drawn to connect the data points and serve to guide the eye. The trends in Figure 6.15 mimic those seen in Figure 6.7 in the main text. In general, the increase in effective repulsion between the blocks, quantified by $\chi_{eff,SC}$, leads to a larger value of α.

7. The Effect of Salt Concentration on the Chain Dimensions of Poly(ethylene oxide)[†]

ABSTRACT

We have measured the effect of added salt on the chain dimensions of mixtures of poly(ethylene oxide) (PEO) and lithium bis(trifluoromethanesulfonyl)imide salt (LiTFSI) in the melt state through small angle neutron scattering (SANS) experiments. Scattering profiles from blends of hydrogenated and deuterated PEO mixed with LiTFSI were measured as a function of salt concentration. Scattering profiles from pure deuterated PEO/LiTFSI mixtures were used for background subtraction purposes. The densities of PEO/LiTFSI mixtures of varying salt concentrations were measured to calculate partial molar monomer volumes of PEO and LiTFSI to account for non-ideal mixing. Kratky plots of the scattering profiles were used to calculate the salt concentration dependence of statistical segment length. At low salt concentrations, segment length decreases with increasing salt concentration, before increasing with increasing salt concentration in the high salt concentration regime. The Random Phase Approximation was used to predict theoretical scattering profiles from the calculated segment lengths and partial molar volumes; there is excellent agreement between the theoretical and measured scattering profiles at all salt concentrations. There appears to be a correlation between chain dimensions and coordination between lithium ions and EO monomers. The scattering profiles of the pure deuterated PEO/LiTFSI mixtures suggested the presence of ion clusters of characteristic size of 0.6 nm at high salt concentrations.

7.1 Introduction

Solid polymer electrolytes are of significant current interest due to their potential use in rechargeable lithium metal batteries.[6,179,203] The most widely studied polymer electrolyte system is poly(ethylene oxide) (PEO) mixed with lithium bis(trifluoromethanesulfonyl)imide salt (LiTFSI), PEO/LiTFSI. It is well known that the ether oxygens of the PEO backbone solvate Li ions, which leads to high ionic conductivity.[7,17,222] The electrochemical and transport properties of PEO/LiTFSI have been fully characterized at temperatures above the meting temperature of PEO, e.g. 90 °C.[19,20] Ion conduction in amorphous polymer electrolytes takes place through two mechanisms: ion hopping between the polymer chains as well as diffusion of the entire polymer chain, which is coordinated with the ions.[175] It has been previously shown that at high polymer molecular weights ($M_{PEO} \geq 4$ kg mol^{-1}), ion conduction is attributed only to the ion hopping mechanism and the conductivity reaches a plateau as a function of molecular weight.[67,68] It is well known that the ionic conductivity of PEO/LiTFSI increases with increasing salt concentration due to an increase in charge carriers, until it reaches a maximum at moderate salt concentrations.[17] From there, the conductivity decreases with increasing salt concentration, which has been attributed to the decrease in segmental dynamics of the PEO chains.[73,175] As salt concentration

[†] This chapter was reported in *Macromolecules,* **2019**, 52 (22), 8724-8732.

increases, the monomeric friction coefficient of the PEO chain increases, which decreases the segmental motion of the polymer chains. The non-monotonic relationship between salt concentration and ionic conductivity can be attributed to the exponential increase in the friction coefficient experienced by the PEO monomers.[74]

While there have been many theoretical and experimental studies conducted on the ion transport mechanisms in PEO/LiTFSI, very few studies have focused on the effect of added salt on the size of the PEO chains. Annis and co-workers studied the effect lithium iodide (LiI) salt on the radius of gyration, R_g, of PEO in the amorphous state.[223] They showed through small angle neutron scattering (SANS) experiments that at a salt concentration of $r = 0.067$, where r is the molar ratio of Li to ethylene oxide (EO) repeat units ($r = \frac{[Li]}{[EO]}$), there is a 10% decrease in R_g compared to the salt free state at 90 °C. These results were qualitatively confirmed with accompanying molecular dynamics (MD) simulations. MD simulations have shown that the preferred conformation is the coordination of one Li ion to six EO and each Li ion is solvated by at most two PEO chains.[14–16] This increases the population of gauche conformers thereby reducing R_g.[14,174,223] Accurate measurements of R_g, and therefore the statistical segment length, l ($l^2 = \frac{6R_g^2}{N}$), in salt-containing systems are important because they provide insight into the effect of salt on the polymer chain conformations. Unfortunately, the experimental data on this important subject is restricted to a single salt (LiI) and a single salt concentration ($r = 0.067$).

The purpose of this study is to systematically measure the effect of salt on the chain dimensions of PEO/LiTFSI in the melt state through SANS experiments. Our work covers salt concentrations in the range of $0 \leq r \leq 0.30$. In the low salt concentration regime, $r < 0.125$, l decreases monotonically with increasing salt concentration. However, in the high salt concentration regime, $r \geq 0.125$, l increases with increasing salt concentration. The SANS data suggest the presence of ion aggregates with characteristic dimensions of about 0.57 nm at high salt concentrations, $r \geq 0.25$.

7.2 Experimental Methods

7.2.1 Electrolyte Preparation and Density Measurements. Electrolytes were prepared according to ref. 19. The hPEO and dPEO (Polymer Source) used in this study have a molecular weight of 35 kg mol^{-1} and polydispersity of 1.08 and 1.09, respectively. All electrolytes are homogeneous mixtures of hPEO, dPEO, and LiTFSI (Sigma Aldrich). Both isotopes of PEO as well as the LiTFSI were dried in a glovebox antechamber under vacuum at 90 °C and 130 °C for 1 and 3 days, respectively. Electrolytes were prepared by dissolving PEO and LiTFSI in anhydrous tetrahydrofuran (Sigma Aldrich) and stirring at 60 °C until completely dissolved. The composition of the polymer blends was 10% dPEO : 90% hPEO by volume (densities of dPEO and hPEO were assumed to be equivalent). The amount of salt was varied such that the r value ranged from values of 0.03 to 0.30. All polymer/salt solutions were transparent. The solvated electrolytes were subsequently stirred on a hotplate at 60 °C until dry and placed in a glovebox antechamber under vacuum for 24 hours at 90 °C to remove any trace solvent. All dried electrolytes are transparent above 70 °C. Density measurements were conducted according to ref. 19 and conducted at 90 °C on pure hPEO/LiTFSI mixtures for $0.18 \leq r \leq 0.28$ in 0.02 increments. Three measurements

were taken and the average measurement is reported. No measurements were taken for electrolytes with $r \geq 0.30$ because the system phase segregates.

7.2.2 SANS Sample Preparation and Experiments. SANS sample preparation was conducted in inert Argon gloveboxes due to the hygroscopic nature of the Li salt. PEO/LiTFSI mixtures were melted into 1 in. inner diameter, 1 mm thick stainless-steel spacers placed on top of 1.5 mm thick, 25.4 mm outer diameter quartz windows (Esco Optics). Samples were degassed in the glovebox antechamber for 15 minutes at 90 °C before placing the second quartz window on top of the polymer. Quartz-polymer-quartz sandwiches were then sealed in custom built air-free titanium holders.

SANS experiments were conducted on the NG7 and NGB 30m beamlines at the National Institute of Standards and Technology Center for Neutron Research in Gaithersburg, MD. On both instruments, measurements were performed with a neutron wavelength of 6 Å and three sample-to-detector distances of 13, 4, and 1 m were used. Neutron lenses were also used with a neutron wavelength of 8.4 Å on the NGB and 8.09 Å on the NG7, which allowed for access to a scattering wave-vector magnitude, $q = \left(\frac{4\pi}{\lambda}\right) \sin\frac{\theta}{2}$, ranging from 0.03 to 4 nm^{-1}.[224] A 0.5" aperture was used for all measurements. All measurements were conducted at 90 °C. On the NGB a 9 position Peltier cooling/heating block was used and on the NG7 a 10-position heating block with a circulating fluid was used to maintain constant sample temperature. Samples of thickness of 1 mm were employed. The total scattering intensity was corrected for detector sensitivity, background, and empty cell contributions as well as sample transmission and thickness.[128,225]

7.3 Small Angle Neutron Scattering (SANS)

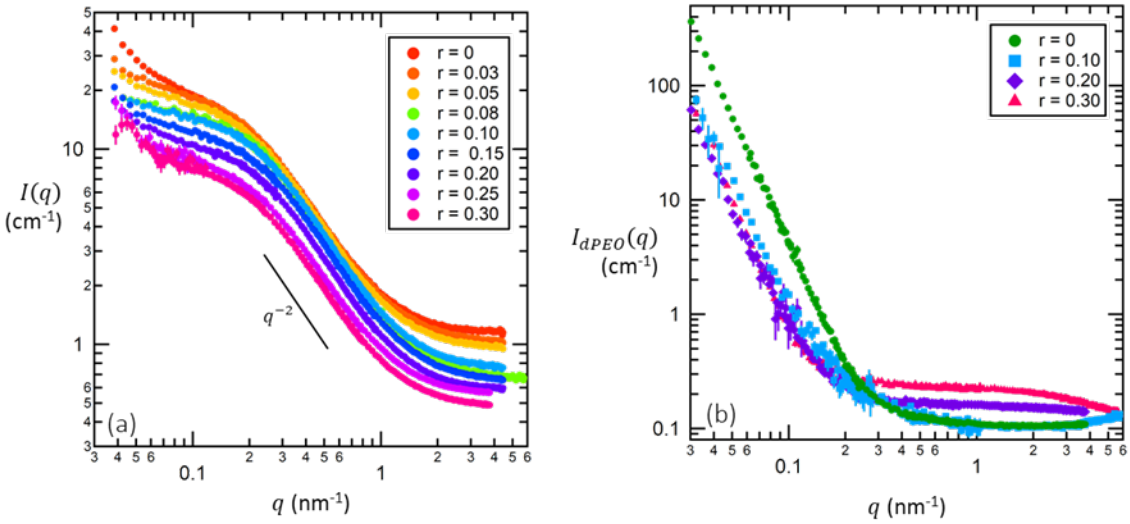

Figure 7.1 Absolute SANS intensities: Measured absolute SANS intensity, $I(q)$, vs q (nm^{-1}) at 90 °C for the (a) blends of hPEO/dPEO/LiTFSI and (b) pure dPEO/LiTFSI samples at varying salt concentrations, r. Error bars represent one standard deviation.

The measured absolute SANS intensity, $I(q)$, for the 10% dPEO/90% hPEO/LiTFSI (referred to as blends) is shown in Figure 7.1a, as a function of the scattering vector, q (nm^{-1}). All of the data in this paper were taken at 90 °C and error bars represent one standard deviation.[128,225] The scattering profiles from all of the blends are similar. Adding salt mainly shifts the curves downward. At high q ($q > 2$ nm^{-1}), the scattering profiles approach a plateau due mainly to incoherent scattering. In the range $0.2 < q$ (nm^{-1}) ≤ 0.9, $I(q)$ is proportional to q^{-2}. The scattering intensity is a much weaker function of q at $q < 0.2$ nm^{-1}. All of these features are generally consistent with scattering from blends of hydrogenous and deuterated polymers obeying random walk statistics.

The measured absolute SANS intensity for the dPEO/LiTFSI mixtures, $I_{dPEO}(q)$, are shown in Figure 7.1b. We mainly use these data for background correction following ref. 226. Note, that the magnitude of the scattering intensity from the dPEO/LiTFSI samples at low q ($q < 0.1$ nm^{-1}) is much larger than that of the blends. While high scattering from pure deuterated samples has been seen previously[125], the reason for this observation has not been fully established. We believe that the scattering intensity of the pure deuterated sample is higher than that of the salt-containing samples due to its higher concentration of dPEO, the main contributor to high intensity scattering. At high q in Figure 7.1b, we see a plateau that is independent of salt concentration when $r < 0.10$. The plateau rises at higher salt concentrations.

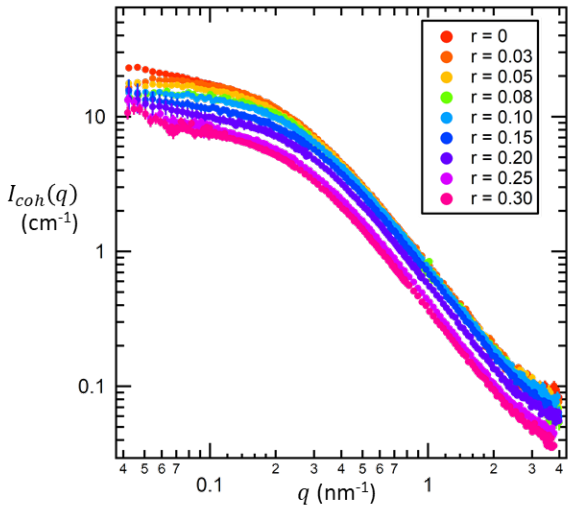

Figure 7.2 Coherent SANS intensity: Coherent SANS intensity, $I_{coh}(q)$, for the blends after dPEO background subtraction taken at 90 °C for varying salt concentrations, r, as function of the scattering vector, q (nm^{-1}). Error bars represent the standard deviation of the scattering data.

Following the analysis in ref. 226, the data in Figure 7.1b were used to subtract the scattering from the fully deuterated chains from the scattering intensity of the blends (Figure 7.1a) to obtain the coherent scattering intensity,

$$I_{coh}(q,r) = I(q,r) - fI_{dPEO}(q,r) - I_{inc}(q,r) \tag{7.1}$$

where f is the volume fraction of dPEO ($f = 0.1$) and $I_{inc}(q)$ is the estimated incoherent scattering from hydrogen atoms in our samples calculated using software provided by NIST.[128] Note that the coherent scattering intensity at a given value of r is obtained after subtracting $I_{dPEO}(q,r)$ at the same r-value. When $I_{dPEO}(q,r)$ was not measured for specific values of r, the interpolated scattering profiles obtained using the weighted average between the appropriate salt concentrations was used. The interpolated scattering profiles for all of the salt concentrations are provided in the Supporting Information.

Figure 7.2 shows the coherent SANS intensities, $I_{coh}(q)$, for all salt concentrations. The relationship between scattering intensity and salt concentration seen in the raw data (Figure 7.1a) persists for $I_{coh}(q)$: mixtures with lower salt concentrations have a higher scattering intensity. Error bars represent the standard deviation of the scattering data.

7.4 Effect of Salt on Chain Dimensions

The coherent scattering intensity for a homogeneous polymer blend can be calculated using the Random Phase Approximation (RPA).[36,43,129,227,228] We assume that the isotopic interaction parameter, $\chi_{dPEO/hPEO}$, as well as the interaction parameter between PEO and LiTFSI, $\chi_{PEO/LiTFSI}$, is negligible and that the salt is randomly distributed throughout the solution. Under these approximations the coherent scattering intensity is given by

$$I_{coh}(q) = (B_1 - B_2)^2 \left(\frac{S_{11}^{\circ} S_{22}^{\circ}}{S_{11}^{\circ} + S_{22}^{\circ}} \right) \tag{7.2}$$

where component 1 is hPEO, component 2 is dPEO, B_i is the neutron scattering length density of component i given by $B_i = \frac{b_i}{\bar{v}_i}$, and $\bar{v}_i$ and b_i are the partial molar monomer volumes and neutron scattering lengths of component i, respectively. The neutron scattering lengths of hPEO and dPEO are 4.13 x 10^{-13} cm and 4.58 x 10^{-12} cm, respectively. Partial molar monomer volumes, $\bar{v}_i$, were used to account for the non-ideal mixing between PEO and LiTFSI if it exists.[19] We note in passing that mixtures of salts and low molecular weight liquids exhibit large volume change of mixing.[229] The structure factor, S_{ii}°, is given by

$$S_{ii}^{\circ} = \phi_i N_i \bar{v}_i P(q) \; (i = 1,2) \tag{7.3}$$

where ϕ_i is the volume fraction of component i, N_i is the degree of polymerization of component i, and

$$P(q) = 2\left[\frac{\exp(-x) - 1 + x}{x^2}\right] \tag{7.4}$$

with $x = q^2 R_g^2$. We assume that the monomer volume and degree of polymerization are the same between the hydrogenated and deuterated PEO samples (e.g. $N_{hPEO} = N_{dPEO} = N = 795$). Both components are modeled as flexible Gaussian chains and

$$R_g^2 = \frac{Nl^2}{6} \tag{7.5}$$

where l is the statistical segment length of both hPEO and dPEO. Note that the reference volume was taken to be the monomer volume for PEO, $\bar{v}_{EO}$. The polymer volume fractions are given by

$$\phi_1 = (1-f)\phi_p \tag{7.6}$$

and

$$\phi_2 = f\phi_p \tag{7.7}$$

where ϕ_p is the volume fraction of polymer in the PEO/LiTFSI mixture calculated from $\phi_p = 1 - \phi_{LiTFSI}$ and

$$\phi_{LiTFSI} = x_{LiTFSI}\frac{\bar{v}_{LiTFSI}}{v_{EO,salt}} \tag{7.8}$$

where $v_{EO,salt}$ is defined as the volume occupied by a mole of a given PEO/LiTFSI mixture divided by Avogadro's number, x_{LiTFSI} is the mole fraction of salt given by

$$x_{LiTFSI} = \frac{r}{1+r} \tag{7.9}$$

and $v_{EO,salt}$ was calculated according to

$$v_{EO,salt} = \frac{(1-x_{LiTFSI})M_{EO}+x_{LiTFSI}M_{LiTFSI}}{\rho(x_{LiTFSI})N_{av}} \tag{7.10}$$

where M_{EO} and M_{LiTFSI} are the molar masses of EO and LiTFSI, 44.05 g mol^{-1} and 287.09 g mol^{-1}, respectively, and N_{av} is Avogadro's number.

Figure 7.3a shows $\rho(x_{LiTFSI})$, the density of a given PEO/LiTFSI mixture, measured at 90 °C as a function of salt mole fraction, x_{LiTFSI}. Some of the data in Figure 7.3a were taken from ref. 19. It is evident that $\rho(x_{LiTFSI})$ is approximately a linear function of x_{LiTFSI}: the dashed line in Figure 7.3a is a linear fit through the data

$$\rho(x_{LiTFSI}) = Ax_{LiTFSI} + B \tag{7.11}$$

The fit in Figure 7.3a gives A = 2635 g L^{-1} and B = 1114 g L^{-1}. Equations 7.10 and 7.11 were used to calculate $v_{EO,salt}$, and this parameter is plotted as a function of x_{LiTFSI} in Figure 7.3b. The solid curve in Figure 7.3b represents a continuous function obtained by combining eq. 7.10 and 7.11. The values of partial molar volumes, $\bar{v}_{EO}$ and $\bar{v}_{LiTFSI}$, at a given salt concentration are calculated by constructing tangents to the solid curve in Figure 7.3b at that salt concentration and noting the intercepts at x_{LiTFSI} = 0 and 1, respectively.[230] The slope of tangent is given by the analytical expression

$$\frac{dv_{EO,salt}}{dx_{LiTFSI}} = \frac{B[M_{LiTFSI} - M_{EO}] - AM_{EO}}{N_{av}(Ax_{LiTFSI} + B)^2} \tag{7.12}$$

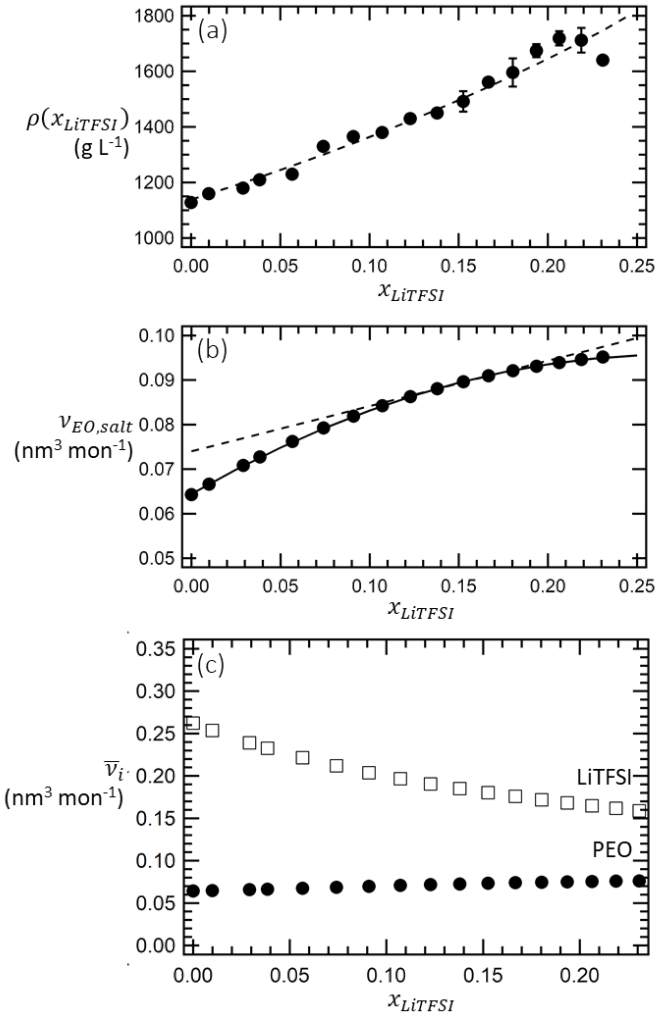

Figure 7.3 Volume Properties of PEO/LiTFSI: (a) Dependence of density, $\rho(x_{LiTFSI})$, on salt mole fraction, x_{LiTFSI}. Error bars represent the standard deviation of measured samples. Molar properties are calculated on the basis of EO monomers (not PEO chains). (b) The volume occupied by a mole of a given PEO/LiTFSI mixture divided by Avogadro's number, $v_{EO,salt}$, as a function of salt mole fraction, x_{LiTFSI}. Solid curve represents eq. 7.10 and the dashed line is an example of a tangent, constructed at $r = 0.20$ using eq. 7.12. (c) Partial molar volumes of EO monomer (circles), LiTFSI (squares) divided by Avogadro's number as a function of salt mole fraction, x_{LiTFSI}. These volumes are used to compute the scattering length densities and volume fractions of the two components in our mixture.

An example of a tangent is shown for $r = 0.20$ as a dashed line in Figure 7.3b. The partial molar volumes thus obtained are plotted as a function of x_{LiTFSI} in Figure 7.3c. The partial molar volumes of both components are monotonic functions of salt concentration. We found that $\bar{v}_{EO}$ increases with increasing salt concentration from $\bar{v}_{EO} = 0.064$ to 0.076 nm^3 mon^{-1} from r = 0 to 0.30. In

contrast, $\bar{v}_{LiTFSI}$ exhibits a more pronounced dependence on salt concentration, decreasing with increasing salt concentration from 0.26 to 0.16 nm^3 mon^{-1} in the same salt concentration window. In a previous study, where volume change of mixing was ignored, the values of volumes used were $v_{EO} = 0.069$ nm^3 mon^{-1} and $v_{LiTFSI} = 0.24$ nm^3 mon^{-1}.[58] To our knowledge, the data presented in Figure 7.3 represents the most exhaustive measurement of density as a function of salt concentration in PEO/LiTFSI mixtures.

Based on equations 7.2-7.10, eq. 7.2 can be rewritten as

$$I_{coh}(q) = (B_1 - B_2)^2 \phi_p f(1-f) \bar{v}_{EO} NP(q) \tag{7.13}$$

Note that the all of the parameters on the right side of eq. 7.13 have been determined independently except for l, which is found in $P(q)$. We do not expect the LiTFSI to have any preference for dPEO relative to hPEO. Thus, the scattering length density of LiTFSI is irrelevant. In addition, $I_{coh}(q)$ is directly proportional to ϕ_p, which monotonically decreases with salt concentration. Equation 7.13 explains the trend in low-q SANS intensity seen in Figures 7.1 and 7.2, where $I(q = 0)$ decreases with increasing salt concentration due to the decrease in polymer concentration, which is the main contributor to scattering in these systems.[231] It is convenient to define the structure factor, $S(q)$ as

$$S(q) = \frac{I_{coh}(q)}{(B_1 - B_2)^2} \tag{7.14}$$

In the limit of large q, $S(q)$ is proportional to q^{-2} and thus the product $q^2 S(q)$ is given by[126,132]

$$\frac{q^2 S(q)}{\bar{v}_{EO}} = \frac{12 \phi_p f(1-f)}{l^2} \tag{7.15}$$

Figure 7.4a shows a plot of $\frac{q^2 S(q)}{\bar{v}_{EO}}$ versus q, for different salt concentrations. Such plots are referred to as Kratky plots.[232] The Kratky plots in Figure 7.4a are typical of polymeric samples. They begin at the origin, level off to a give a plateau at intermediate q, and at large q values ($q > 2$ nm^{-1}), we see deviations from the plateau. All of the features except the high-q deviations are consistent with eq. 7.13. On monomeric length-scales, deviations from random-walk statistics become evident due to correlations between neighboring bonds within a repeat unit.[135]

The height of the intermediate-q plateau of a Kratky plot can be used to determine l as all other parameters in eq. 7.14 have been independently determined.[233] It is important to note that the height of the plateau does not decrease monotonically with salt concentration like the scattering profiles seen in Figures 7.1 and 7.2. For example, the Kratky plateau for $r = 0$ is not that different from that of $r = 0.15$ (Figure 7.4a). To focus on this fact, Figure 7.4b shows normalized Kratky plots where $\frac{q^2 S(q)}{\bar{v}_{EO} \phi_p f(1-f)}$ is plotted versus q for selected salt concentrations in the q range where the Kratky plateau is observed ($0.6 \leq q\ (nm^{-1}) \leq 1.6$). Normalized Kratky plots for the remaining salt concentrations are provided in the Supporting Information (Figure 7.9). The circles in Figure 7.4b represent the SANS data and the solid horizontal lines show the averaged value of

$\frac{q^2S(q)}{\bar{v}_{EO}\phi_p f(1-f)}$ in the range of $0.6 < q$ (nm^{-1})< 1.6. This value is then used to determine l using eq. 7.15.

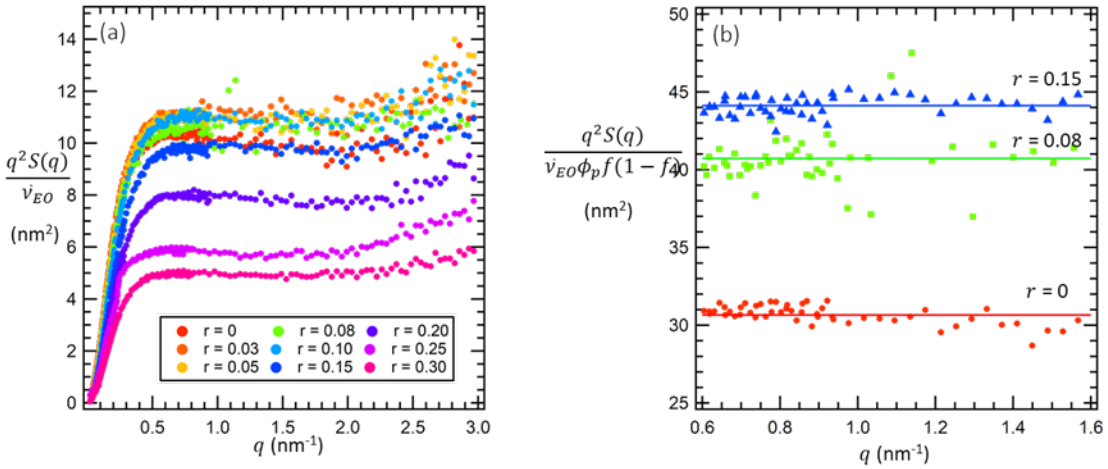

Figure 7.4 Kratky plots: a) Kratky plots, $\frac{q^2S(q)}{\bar{v}_{EO}}$, and b) normalized Kratky plots, $\frac{q^2S(q)}{\bar{v}_{EO}\phi_p f(1-f)}$, vs q (nm^{-1}), for the blends at different salt concentrations. Error bars represent the standard deviation of the scattering data and are smaller than the symbols.

In a related study, Hayashi et al.[134] studied mixtures of deuterated and hydrogenated polyisobutylene as a function of composition. They used an expression to similar to eq. 7.15 to analyze their data and found that the plateau in the normalized Kratky plot was independent of composition indicating that the statistical segment length of that system was also independent of composition. This is clearly not the case in the present study (Figure 7.4b).

Figure 7.5 shows the results for the salt concentration dependence of the statistical segment length, l (left axis), calculated using eq. 7.15 and the normalized Kratky plateau (Figure 7.4b). The right axis of Figure 7.5 shows the salt concentration dependence of the radius of gyration, R_g (right axis), calculated with eq. 7.5. Error bars represent the standard deviation between the data and the fit in Figure 7.4b. The PEO statistical segment length decreases linearly upon salt addition in the range $0 < r < 0.125$, before linearly increasing with increasing salt concentration. The dashed lines in Figure 7.5 represent two linear regressions through the data at $r \leq 0.125$ and $r \geq 0.125$. The magnitude of the slope of these lines is approximately equal and it appears that the maximum reduction in l might occur at $r = 0.125$ where the two dashed lines intersect. The statistical segment length at this salt concentration is 19% lower than that of neat PEO. At $r = 0.067$, there is a 10% decrease in segment length relative to the neat state, which is in excellent agreement with refs. 14 and 15 where the decrease in segment length relative to the neat state in PEO/LiI mixtures at $r =$ 0.067 is also 10%.

The top y-axis in Figure 7.5 plots selected values of $1/r$, which quantifies the number of EO present per Li atom. MD simulations of dilute mixtures of Li salts in PEO show that the Li ions are each coordinated with six ether oxygens.[17] In other words, when $1/r = 6$, all of the oxygen atoms in the mixture are coordinated with Li ions. It is difficult to pinpoint the exact location of the crossover from chain contraction to chain expansion using the data in Figure 7.5, however, we

believe it is close to $r = 0.125$ as denoted by the dashed lines in Figure 7.5, which intersect at $1/r = 8$. There appears to be a correlation between chain dimensions and coordination between lithium ions and EO monomers.

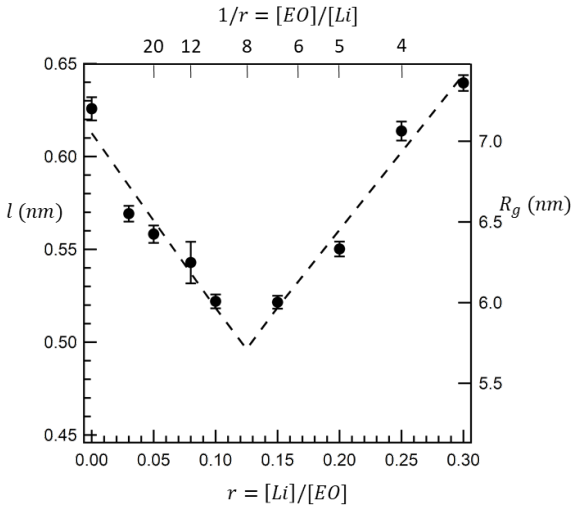

Figure 7.5 Statistical segment length: Statistical segment length, l (nm) (left axis), and radius of gyration, R_g (nm) (right axis), of PEO/LiTFSI blends at 90 °C as a function of salt concentration. l was calculated according to eq. 7.15 from the Kratky plateau values and R_g was calculated according to eq. 7.5. Error bars represent the standard deviation between the data and the fit in Figure 7.4b. The top y-axis shows selected values of $1/r$, which quantifies the ratio of Li ions to EOs.

7.5 Comparison between Theory and Experiment

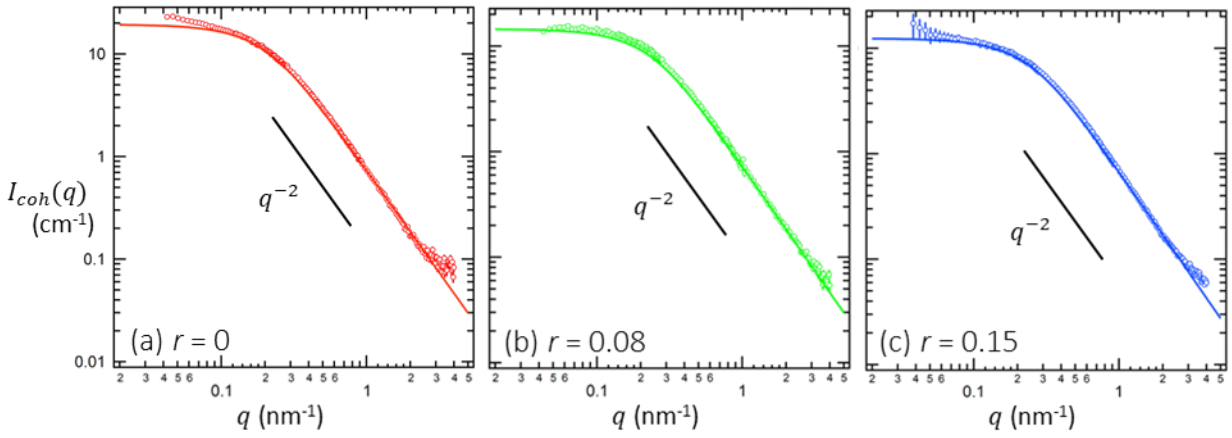

Figure 7.6 Comparisons of theory vs experiment: Comparisons between theoretical and experimental scattering profiles for (a) $r = 0$, (b) $r = 0.08$, and (c) $r = 0.15$. Circles represent the coherent SANS intensity reproduced from Figure 7.2 and the solid lines represent the Dilution model, eq. 7.13, when l was calculated according to eq. 7.15. Error bars represent one standard deviation.

Figure 7.6 shows the comparison between theory and experimental data for the PEO/LiTFSI mixtures at selected salt concentrations: (a) $r = 0$, (b) $r = 0.08$, and (c) $r = 0.15$ (the remaining salt concentrations are presented in the Supporting Information). The circles represent the coherent scattering data, $I_{coh}(q)$, reproduced from Figure 7.2, and the solid curves represent eq. 7.13 where l is obtained from the Kratky analysis (Figure 7.5) and all other parameters are determined independently. We will refer to this expression as the "dilution model". The agreement between theory and experiment is remarkable. The experimental data exhibit two regimes, a high-q Kratky regime where $I_{coh}(q)$ scales with q^{-2} and a low-q Zimm regime where $I_{coh}(q)$ is a weak function of q. The crossover between the Zimm and Kratky regimes is accurately predicted by eq. 7.13. At $r = 0.08$, the measured $I_{coh}(q)$ at low q is very close to theoretical predictions. At $r = 0$ and $r = 0.15$, however, we see significant upturns in the scattering data that is inconsistent with eq. 7.13. We attribute this to imperfect background subtraction. It is clear that the dPEO sample contains some impurity that gives rise to significant scattering at low-q, which in turn complicates background subtraction.

In addition to the dilution model (eq. 7.13), a second model using multicomponent RPA was developed following Hammouda et. al[234] wherein the scattering from the salt, which was treated as a common solvent, was explicitly accounted for. The random walk statistics for a homogeneous blend of two polymers, (1) dPEO and (2) hPEO, and one solvent, (3) LiTFSI, with $\chi_{ij} = 0$ for all i and j was calculated. The properties of the two polymers were identical except for their scattering lengths, b_i, and volume fractions, ϕ_i. The bare structure factors, S_{ii}°, for components 1 and 2 follow eq. 7.11 and S_{33}° can be written as

$$S_{33}^{\circ}(q) = \phi_3 \bar{v}_{LiTFSI} \tag{7.16}$$

because the form factor, $P(q)$, and the degree of polymerization, N, of a small molecule is 1. S_{ij}° was taken to be zero for all $i \neq j$. Although the interaction parameters, $\chi_{i,j}$, between the components are neglected, the volume occupied by the salt molecules is included in the excluded volume matrix as given by

$$V = \frac{1}{\phi_{LiTFSI}\bar{v}_{LiTFSI}} \tag{7.17}$$

Following the procedure outlined in section 6 of ref. 234, $I_{coh}(q)$ can be calculated according to

$$I_{coh}(q) = B^T(S^{\circ -1} + V)^{-1}B \tag{7.18}$$

where S° is the bare structure factor matrix (given by eq. 7.3 and is zero for the cross terms where $i \neq j$), V is the excluded volume matrix (where all elements are given by eq. 7.17) and B is the contrast matrix. The product inside the parenthesis on the right hand side of eq. 7.18 is known as the interacting structure factor matrix or S. The contrast matrix was calculated according to

$$B_i = \left(\frac{b_i}{\bar{v}_i}\right) - \left(\frac{b_{LiTFSI}}{\bar{v}_{LiTFSI}}\right) \text{ for } i = 1,2 \tag{7.19}$$

to directly account for the scattering contributions of the salt species. The elements of the interacting structure factor matrix, S, are calculated as

$$S_{ij} = \frac{P_i(1+VP_j)}{1+V(P_i+P_j)} \text{ for } i = j \tag{7.20}$$

and

$$S_{ij} = -\frac{VP_iP_j}{1+V(P_i+P_j)} \text{ for } i \neq j \tag{7.21}$$

where

$$P_i = N\bar{v}_{EO}\phi_i P(Q) \text{ for } i = 1,2 \tag{7.22}$$

The resulting expression for $I_{coh}(q)$, calculated according to eq. 7.18, is given by

$$I_{coh}(q) = \frac{(B_1-B_2)^2 S_{11}^{\circ} S_{22}^{\circ} + \frac{1}{V}(B_1^2 S_{11}^{\circ} + B_2^2 S_{22}^{\circ})}{S_{11}^{\circ} + S_{22}^{\circ} + \frac{1}{V}} \tag{7.23}$$

We will refer to this model as "multicomponent-RPA". In the neat state, this model reduces to the dilution model as $\frac{1}{V} = 0$ when $\phi_{LiTFSI} = 0$.

Finally, a third model was taken from ref. 234, the "high concentration model", which describes a polymer solution consisting of protonated and deuterated polymers with the same degree of polymerization, *N*. In this model, the structure factors are explicitly split into single-chain, $P_i^S(Q)$, and interchain, $P_{ij}^I(Q)$, parts such that

$$\frac{\nu_i^2 S_{ii}(Q)}{V} = N_i\phi_i\nu_i[P_i^S(Q) + \phi_i P_{ii}^I(Q)] \text{ for } i = 1,2 \tag{7.24}$$

and

$$\frac{\nu_1\nu_2 S_{12}(Q)}{V} = (N_1\phi_1\nu_1 N_2\phi_2\nu_2)^{\frac{1}{2}}(\phi_1\phi_2)^{\frac{1}{2}} P_{12}^I(Q) \tag{7.25}$$

It was assumed that deuteration does not affect chain conformations and interactions, and therefore $P_1^S(Q) = P_2^S(Q) = P_S(Q)$ and $P_{11}^I(Q) = P_{22}^I(Q) = P_{12}^I(Q) = P_I(Q)$. A "total" polymer-polymer structure factor is defined according to

$$P_T(Q) = P_S(Q) + \phi_p P_I(Q) \tag{7.26}$$

The resulting expression for the scattering intensity is given by

$$I_{coh}(Q) = \frac{(B_1-B_2)^2\phi_1\phi_2 N\bar{v}_{EO} P_S(Q)}{\phi_p} + \left[B_2^2\phi_2\phi_p + B_1^2\phi_1\phi_p\right]^2 N\phi_p\bar{v}_{EO}P_T(Q) \tag{7.27}$$

where the contrast is defined according to eq. 7.19. Typically, one would design SANS experiments to determine the analytical expressions for $P_s(Q)$ and $P_T(Q)$ by changing the ratio of ϕ_1/ϕ_2 and keeping ϕ_p constant.[234] Instead, we used our multicomponent-RPA model (eq. 7.23) to solve for $P_s(Q)$ and $P_T(Q)$ explicitly. Based on the equations provided in ref. 234, $P_s(Q)$ and $P_T(Q)$ can be solved for from the elements in the interacting structure factor matrix, given by eq. 7.20 and 7.21. The expressions for $P_s(Q)$ and $P_I(Q)$ are therefore given by

$$P_I(Q) = -\frac{\bar{v}_{EO}NP(Q)^2}{1+V(P_1+P_2)} \tag{7.28}$$

and

$$P_S(Q) = \frac{P(Q)}{1+V(P_1+P_2)} \tag{7.29}$$

where P_i is given by eq. 7.22. These expressions are plugged into eq. 7.27 for $I_{coh}(Q)$ to predict the SANS profiles. The resulting expression is referred to as the "high concentration model".

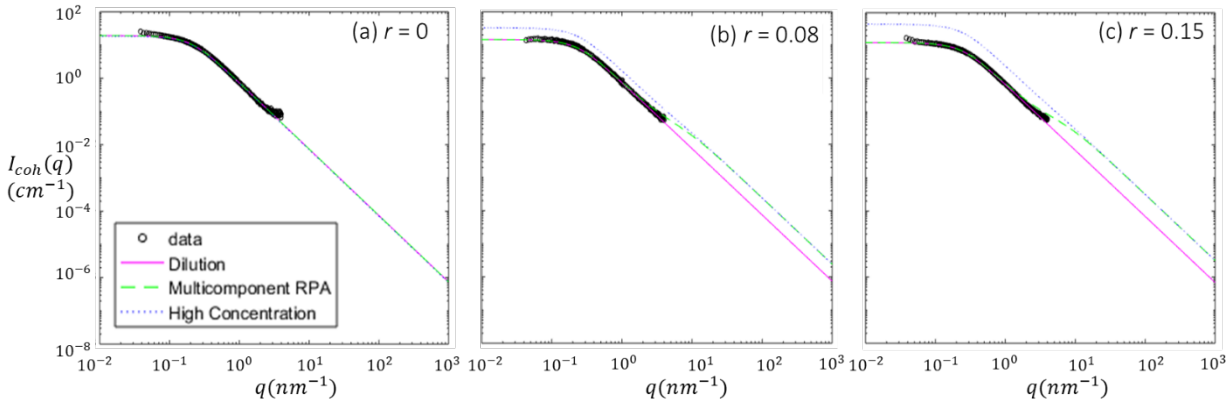

Figure 7.7 Comparison of RPA-based theories: Comparisons between the three RPA models, dilution (eq. 7.13), multicomponent-RPA (eq. 23) and the high concentration (eq. 7.27) models, and the experimental data for (a) r = 0, (b) r = 0.08, and (c) r = 0.15. Circles represent the coherent SANS intensity reproduced from Figure 7.2 and the solid lines represent the dilution model, the dashed lines represent the multicomponent-RPA model, and the dotted lines represent the high concentration model. l calculated according to eq. 7.15 (Figure 7.5) was used in all equations.

Figure 7.7 shows comparisons of the three models based on RPA, (eq. 7.13, 7.23 and 7.27), as well as the experimental data at selected salt concentrations: (a) r = 0, (b) r = 0.08, and (c) r = 0.15. Similar to the theoretical predictions shown in Figure 7.6, l used in the multicomponent-RPA and high concentration models was taken from Figure 7.5, and all other parameters were determined independently. In the absence of salt, the three theories are identical for all q and overlap well with the experimental data (Figure 7.7a). As salt concentration increases, only the dilution model matches the experimental data over the entire q-range. The multicomponent RPA model matches well with the experimental data at in the low-q Zimm region as well as the intermediate-q regimes ($q < 2$ nm^{-1}). At higher q values, the multicomponent RPA model deviates from the classical q^{-2} scaling of a random walk and the two curves separate. This deviation manifests as a "kink" in the tail of eq 7.23. The slope of eq. 7.23 resumes the q^{-2} scaling shortly

after the kink. As salt concentration increases, the q-value at which the kink occurs decreases and the deviations between the multicomponent RPA model and the experimental data increase. In contrast, the high concentration model obeys the expected q^{-2} scaling throughout the entire q-range. However, there are significant deviations between the experimental data and high concentration model for $r > 0$ at all q-values. In the low-q Zimm region, the high concentration model consistently overestimates the scattering intensity and the deviations between experiment and theory increase with increasing salt concentration. Interestingly, the high concentration model and the multicomponent RPA model overlap at high q-values after the observed kink in the multicomponent RPA model. Therefore, the multicomponent RPA is essentially a combination of the random-walk statistics described in both the dilution and high concentration model. We hypothesize that the discrepancies between the models arise from the definitions of the contrast terms and whether the scattering lengths of the salt species were accounted more (use of eq. 7.19). However, more work is needed to understand the implications of these results.

7.6 Ion Clusters

Returning to Figure 7.1b, it is clear that the scattering profiles of dPEO/LiTFSI at $r \geq 0.20$ contain features at high q ($q > 0.2$ nm^{-1}) that are absent in the samples with lower salt concentrations. We posit that these features arise due to the presence of ionic clusters. In order to investigate the nature of these clusters, the scattering from the neat dPEO was subtracted from the salt containing samples:

$$I_{clusters}(q) = I_{dPEO}(q,r) - \phi_P I_{dPEO}(q,r=0) \tag{7.30}$$

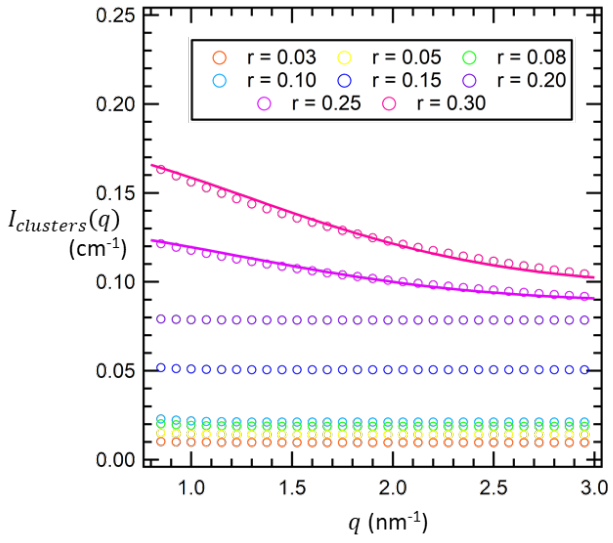

Figure 7.8 Ion Clusters: Scattering data from ion clusters, $I_{clusters}(q) = I(q,r) - \phi_P I(q,r=0)$, for the pure dPEO/LiTFSI mixtures at high salt concentrations. Circles represent the data and lines represent a fit to eq. 7.31. Only salt concentrations $r \geq 0.25$ could be fit to eq. 7.31. Error bars represent the standard deviation of the scattering data and are smaller than the symbols.

In Figure 7.8 we plot $I_{clusters}(q)$ versus q at different salt concentrations as circles. For $r \leq 0.20$, $I_{clusters}$ is independent of q. The solid curves through the high salt concentration data ($r \geq 0.25$) are fits to

$$I_{clusters}(q) = y_0 + I_0 \exp(-R^2 q^2) \tag{7.31}$$

which represents the Guinier equation for scattering from random irregular objects with characteristic size R.[95,235] The origin of the background term, y_0, is not clear. The data in Figure 7.8 indicate that y_0 increases monotonically with salt concentration, suggesting that the additional scattering in the dPEO/LiTFSI mixtures arises from the presence of salt. The fact that $I_{clusters}(q)$ is q-independent for $r \leq 0.20$ may be an indication that the salt is uniformly distributed in the samples. The Guinier equation has been used to account for deviations from eq. 7.13 at high q for systems where structure overlaps with Debeye scattering.[236] The fitted parameters, y_0 and R, are similar for $r = 0.25$ and $r = 0.30$ (with $y_0 = 0.090 \pm 0.0004$ and 0.097 ± 0.0007 and $R = 0.58 \pm 0.01$ nm and 0.56 ± 0.01 nm for $r = 0.25$ and $r = 0.30$, respectively, where the error represents one standard deviation from the fits). However, I_0 is approximately twice as high for the $r = 0.30$ sample versus the $r = 0.25$ sample (0.04 ± 0.0006 vs 0.08 ± 0.0010 cm^{-1}, respectively where the error represents one standard deviation from the fits). In theory, I_0 is proportional to the product of the volume fraction of aggregates and average aggregation number.[236,237] The volume fraction of salt increases by 8% when r is increased from 0.25 to 0.30 (from 0.36 to 0.38). The measured value of I_0 suggests that the average aggregation number at $r = 0.30$ is a factor of 1.9 larger than that of $r = 0.25$; the average aggregate size remains constant at 0.57 nm between these two salt concentrations. These results are supported by MD simulations, which have shown that the number of ion clusters increases at these salt concentrations.[14,15] Further characterization of ion clusters in PEO/LiTFSI using techniques such as X-ray scattering and Raman spectroscopy seem warranted.

7.7 Conclusions

We have determined the effect of added salt on the chain dimensions of PEO/LiTFSI mixtures through SANS experiments on ternary mixtures comprising hPEO, dPEO and LiTFSI salt, conducted at 90 °C, above the melting transition of the mixtures. Scattering profiles were corrected for impurities present in the dPEO through background subtraction as described in ref. 226. Partial molar monomer volumes of EO and LiTFSI were calculated from measured density values in order to account for non-ideal mixing between PEO and LiTFSI salt. The partial molar volume of EO increases with increasing salt concentration while the partial molar volume of LiTFSI decreases with increasing salt concentration. The salt concentration dependence of statistical segment length was calculated through the Kratky analysis of the intermediate-q scattering plateaus, which were normalized by polymer volume fraction. At low salt concentrations, $r < 0.125$, l linearly decreases with increasing salt concentration; in the high salt concentration region, $r \geq 0.125$, l increases with increasing salt concentration. When the calculated value of l is used in the Random Phase Approximation, along with the independently determined partial molar monomer volumes and chain length, we see good agreement between theory and experiment. The SANS data suggested the presence of ion clusters of characteristics size of 0.57 nm in electrolytes with $r \geq 0.25$.

7.8 Nomenclature

7.8.1 Abbreviations

EO	ethylene oxide
LiTFSI	lithium bis(trifluoromethanesulfonyl) imide salt
MD	molecular dynamics
N_A	Avogadro's number
PEO	poly(ethylene oxide)
RPA	random phase approximation
SANS	small angle neutron scattering

7.8.2 Symbols

b_i	neutron scattering length of species *i* *c*m mon^{-1})
B_i	scattering length density of species *i* (cm^{-2} mon^{-1})
C	electron density contrast (cm^{-1})
f	volume fraction of deuterated species
$I(q)$	scattering intensity (cm^{-1})
$I_{coh}(q)$	coherent scattering intensity (cm^{-1})
$I_{inc}(q)$	incoherent scattering intensity (cm^{-1})
$I_{clusters}(q)$	ionic cluster scattering intensity (cm^{-1})
l	statistical segment length (nm)
M_i	number-averaged molecular weight of species *i* (kg mol^{-1})
N_i	number-averaged degree of polymerization of species *i* (sites chain^{-1})
N_A	Avogadro's number
$P(q)$	scattering form factor
$P_S(Q)$	single-chain structure factor
$P_I(Q)$.	inter-chain structure factor
$P_T(Q)$	total polymer structure factor
q	scattering vector (nm^{-1})
r	salt concentration ([Li] [EO]$^{-1}$)
R_g	radius of gyration (nm)
$S(q)$	scattering structure factor
S°	bare structure factor matrix
S	interacting structure factor matrix
T	temperature (K)
V	excluded volume matrix
x_i	mole fraction of species *i*

7.8.3 Greek Symbols

ν_i	molar volume of species *i* divided by Avogadro's number (nm^3 mon^{-1})

$\overline{v_i}$	partial molar volume of species *i* divided by Avogadro's number (nm^3 mon^{-1})
ρ_i	density of species *i* (g cm^{-3})
ϕ_i	volume fraction of component *i*
χ_{ij}	Flory-Huggins interaction parameter

7.9 Supporting Information

7.9.1 Interpolated SANS Curves

In order to remove the low-q upturn from the blends SANS intensity, pure dPEO SANS profiles were generated at each of the salt concentrations of interest. Pure dPEO SANS was collected at $r = 0, 0.10, 0.20$ and 0.30 at 90 °C. Each of these scattering profiles were fit to two power law functions ($I(q) = y_0 + Aq^B$) in the regions of $q(nm^{-1}) < 0.005$ and $0.005 \leq q(nm^{-1}) < 0.02$. Data for $q(nm^{-1}) \geq 0.02$ was fit to an exponential equation ($I(q) = y_0 + A\exp(-\tau q)$). The constants for the fits are provided in Table 7.1. Curves for each salt concentration shown in Figure 7.8 were generated by taking the weighted averaged of the fitted SANS profiles at known salt concentrations for $0.002 < q\ (nm^{-1}) < 4$ for $0 \leq r \leq 0.30$.

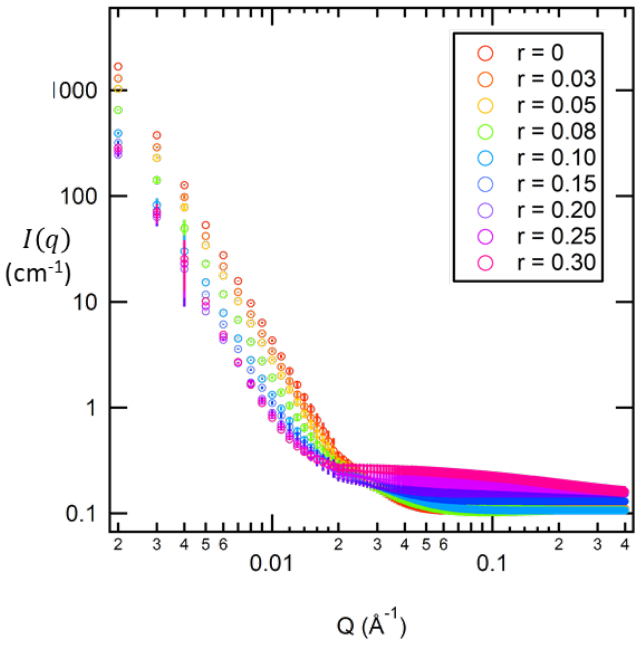

Figure 7.12 Interpolated SANS intensities: Interpolated SANS intensity for pure dPEO/LiTFSI mixtures at varying salt concentrations, *r*, at 90 °C. These curves were used to background subtract the scattering from pure dPEO from the blends data. Error bars represent the standard deviations based on the fits.

Table 7.1. Fitting constants for dPEO SANS: Constants for fitted pure dPEO SANS profiles at $r = 0, 0.10, 0.20$ and 0.30. Error bars represent standard deviations from the fits.

	$r = 0$	$r = 0.10$	$r = 0.20$	$r = 0.30$
	$q(nm^{-1}) < 0.005$			
y_0	-8.08 ± 1.9	5.56 ± 12.4	-9.08 ± 11.5	-1.35 ± 12.8
A	2.4 x 10^{-7} ± 1.0 x 10^{-8}	7.00 x 10^{-9} ± 3.4 x 10^{-7}	1.07 x 10^{-6} ± 1.3 x 10^{-9}	1.68 x 10^{-7} ± 1.3 x 10^{-10}
B	-3.64 ± 0.01	-3.98 ± 0.23	-3.10 ± 0.009	-3.42 ± 0.001
	$0.005 \leq q(nm^{-1}) < 0.02$			
y_0	-0.038 ± .12	0.16 ± .04	0.20 ± 0.05	0.24 ± 0.01
A	2.59 x 10^{-7} ± 5.2 x 10^{-8}	4.35 x 10^{-8} ± 8.4x 10^{-9}	7.19 x 10^{-8} ± 2.2 x 10^{-7}	2.83 x 10^{-9} ± 2.2 x 10^{-10}
B	-3.61 ± 0.04	-3.71 ± 0.09	-3.49 ± 0.10	-4.15 ± 0.02
	$q(nm^{-1}) \geq 0.02$			
y_0	0.11 ± 0.007	0.11 ± 0.001	0.15 ± 0.0009	0.15 ± 0.01
A	2.95 ± 0.26	0.61 ± 0.06	0.32 ± 0.04	0.14 ± 0.009
τ	125.38 ± 3.9	68.07 ± 4.2	72.381 ± 6.0	6.07 ± 0.78

7.9.2 RPA at additional salt concentrations

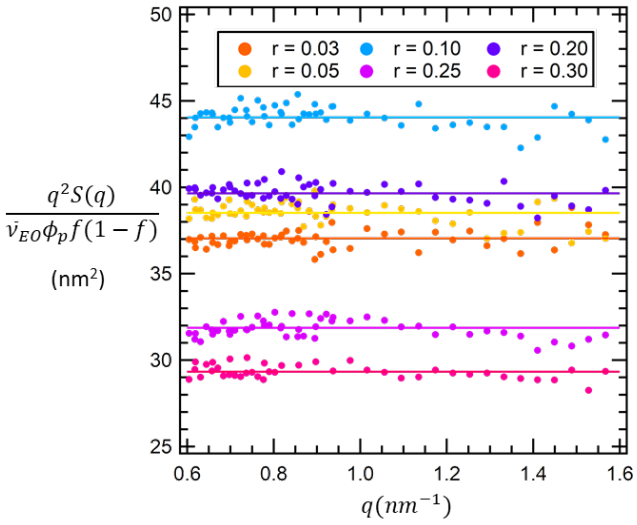

Figure 7.13 Normalized Kratky plots: Normalized Kratky plots, $\frac{q^2S(q)}{\bar{v}_{EO}\phi_p f(1-f)}$ vs q (nm^{-1}), for the PEO/LiTFSI mixtures at different salt concentrations. Error bars represent the standard deviation of the scattering data and are smaller than the symbols.

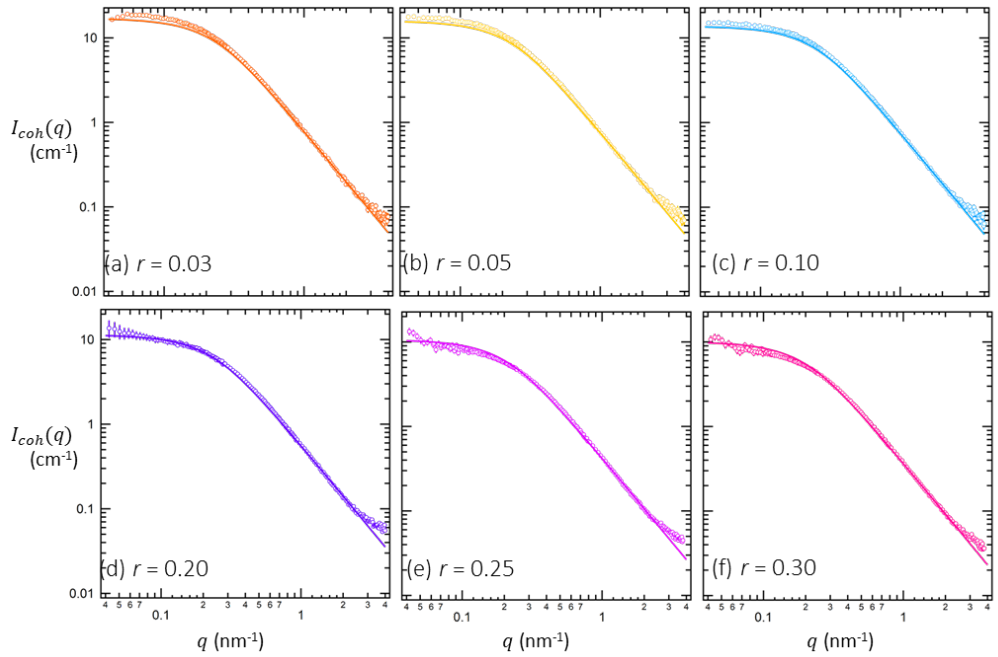

Figure 7.14 Comparison theory vs experiment: Comparison between theoretical predictions and scattering data for the blends of PEO/LiTFSI at 90 °C for (a) r = 0.03, (b) r = 0.05, (c) r = 0.10, (d) r = 0.15, (e) r = 0.20 and (f) r = 0.30. The circles represent $I_{coh}(q)$ replicated from Figure 2 and the solid lines represent eq. 7.14 when segment length, l, is taken from Figure 7.5. Error bars represent one standard deviation.

8. Polymer Dynamics in Block Copolymer Electrolytes Detected by Neutron Spin Echo[†]

ABSTRACT

Polymer chain dynamics of a nanostructured block copolymer electrolyte, polystyrene-*block*-poly(ethylene oxide) (SEO) mixed with lithium bis(trifluoromethanesulfonyl)imide (LiTFSI) salt, are investigated by neutron spin-echo spectroscopy on the 0.1-100 ns timescale and analyzed using the Rouse model at short times ($t \leq 10$ ns) and the reptation tube model at long times ($t \geq 50$ ns). In the Rouse regime, the monomeric friction coefficient increases with increasing salt concentration as seen previously in homopolymer electrolytes. In the reptation regime, the tube diameters, which represent entanglement constraints, decrease with increasing salt concentration. The normalized longest molecular relaxation time, calculated from the NSE results, increases with increasing salt concentration. We argue that quantifying chain motion in the presence of ions is essential for predicting the behavior of polymer-electrolyte-based batteries operating at large currents.

8.1 Introduction

It is becoming increasingly clear that the next generation of rechargeable batteries for the emerging clean energy landscape will require electrolytes that are fundamentally different from those used in today's lithium-ion batteries. Current electrolytes in lithium ion batteries are comprised of mixtures of cyclic and linear carbonates and a lithium salt. Polymer electrolytes, i.e., mixtures of polymers and a lithium salt, have the potential to improve battery safety as they are less flammable than the organic solvents used currently.[2]

Efforts to characterize polymer electrolytes have focused on quiescent systems or systems under very small applied potentials (e.g. 10 mV).[17,238] Under these conditions, it is reasonable to focus on the motion of ions; the motion of polymer chains on larger length scales can be safely neglected. However, in electrolytic applications such as batteries in electric vehicles, ion transport occurs under large applied dc potentials (e.g. 4 V). Under these conditions, significant salt concentration gradients develop due to the well-established competition between diffusion and migration.[18] Since the salt concentration in the electrolyte must be uniform before the polymer-electrolyte-based battery is turned on, the polymer chains must diffuse away from regions of high salt concentration toward regions of low salt concentration during battery operation. We aim to elucidate the molecular underpinnings of this process. We present the first study of polymer electrolytes using neutron spin echo (NSE) spectroscopy.

A popular approach for characterizing ion transport in electrolytes is ac impedance spectroscopy, which reflects the oscillation of ions in response to a small ac potential.[17,68,239] Another popular approach is pulse-field gradient NMR wherein the Brownian motion of ions is quantified in the

[†] This chapter was reported in *ACS Macro Lett.* **2020**, 9, 639-645.

absence of an applied potential.[67,238,240–242] In these cases, the translation of ions can be accommodated by segmental relaxation of the polymer chains.[15,65,72–79] Thus, ionic conductivity of a well-studied polymer electrolyte, a mixture of poly(ethylene oxide) (PEO) and lithium bis(trifluoromethanesulfonyl)imide (LiTFSI) salt measured by ac impedance spectroscopy, can be explained entirely by the segmental relaxation quantified by quasi-elastic neutron scattering (QENS).[74] To our knowledge, no attempt has been made to study the relaxation processes that govern polymer electrolytes under large applied potentials.

One advantage of polymer electrolytes over liquid electrolytes is their ability to exert stress on the electrodes. This is believed to be the key to enabling rechargeable batteries with lithium metal anodes,[21] which is a promising approach to significantly increase the energy density of rechargeable batteries.[10,11] Linear polymers are viscoelastic liquids and thus are unable to withstand stress in the long-time limit. Crosslinking can increase their mechanical properties but slows down segmental relaxation, which in turn slows down ion transport.[243] A better approach for creating solid polymer electrolytes is through the self-assembly of block copolymers, which can microphase separate into ionically conductive and mechanically rigid domains.[22–25]

Here, we quantify segmental motion and polymer dynamics in a series of block copolymer electrolytes using NSE. The time-scales covered by our experiments range from 0.1-100 ns, which correspond to polymer dynamics on the Angstrom to nanometer length-scales. At short times (0.1-10 ns), polymer chains obey Rouse dynamics and their segmental motion is quantified by an effective friction coefficient, ζ, of the monomer units.[66,70] At longer times (10-100 ns), the motion of polymer segments of a "test-chain" is constrained by the presence of neighboring chains. In the theory of Doi, Edwards, and de Gennes, these constraints are represented by a tube with diameter, *d,* that runs down the primitive path of the "test-chain".[69,70] We are not aware of any prior studies on either polymer electrolytes or block copolymers (with or without salt) that cover both regimes. Previous studies on these systems using NSE are limited to the Rouse regime ($t \leq 20$ ns).[74,77,152] Previous studies on nanostructured block copolymer electrolytes are limited to studying the cooperative grain dynamics on the 10^{-2}-10^{2} s time-scale.[82]

8.2 Experimental Methods

8.2.1 Synthesis and preparation of the block copolymer electrolytes. The block copolymer electrolyte of interest is a well-studied model system: polystyrene-*block*-poly(ethylene oxide) (SEO) mixed with LiTFSI, SEO/LiTFSI. Two SEO copolymers with similar compositions were synthesized by living anionic polymerization:[83,84,86] deuterated PS-*b*-deuterated PEO (ddSEO) ($M_{n,dPS}$ = 4.9 kg mol^{-1}, $M_{n,dPEO}$ = 23.6 kg mol^{-1}, ϕ_{EO} = 0.82, PDI = 1.05) and deuterated PS-*b*-hydrogenated PEO (dhSEO) ($M_{n,dPS}$ = 5.1 kg mol^{-1}, $M_{n,hPEO}$ = 14.4 kg mol^{-1}, ϕ_{EO} = 0.73, PDI = 1.05). Detailed information on the synthesis is provided in the Supporting Information. The PEO blocks of both copolymers are well above the entanglement molecular weight, M_e = 2 kg mol^{-1}. The preparation of the SEO/LiTFSI electrolytes is described in ref 108. The samples used were blends of 20% dhSEO and 80% ddSEO by volume (the densities of dhSEO and ddSEO are 1.10 and 1.11 g cm^{-3}, respectively, at 90 °C). LiTFSI was added to the copolymer blends such that the final molar salt ratios, $r = [Li]/[EO]$, were 0, 0.025, 0.075, and 0.10. The block copolymer system was designed such that the NSE data are dominated by relaxation of the PEO segments as they

interact with salt ions; in particular, the incoherent background from the PEO chains is minimized at the scattering vectors, Q, chosen for NSE.[244]

8.2.2 Small Angle Neutron Scattering (SANS). Small-angle neutron scattering (SANS) experiments were performed at 363 K on the NGB-30m beamline at the NIST Center for Neutron Research (NCNR, Gaithersburg, MD). Sample preparation for the SANS experiments is described in ref [137]. Measurements were performed with a neutron wavelength of 6 Å and three sample-to-detector distances of 13, 4, and 1 m were used. Measurements were performed such that the Q range covered was from 0.003 to 0.4 Å^{-1}.[224] A 9 position Peltier cooling/heating block was used. Samples of thickness of 1 mm were employed. The total scattering intensity was corrected for detector sensitivity, background, and empty cell contributions as well as sample transmission and thickness.[128,225]

8.2.3 Neutron Spin Echo (NSE) Spectroscopy. Single-chain PEO dynamics were obtained using the NGA Neutron Spin Echo Spectrometer (NSE) at the NIST Center for Neutron Research (NCNR, Gaithersburg, MD). Sample preparation was similar to that of the SANS samples. The measurements were performed at 363 and 393 K using wavelengths of $\lambda = 11$ Å for Fourier times up to 100 ns and a wave vector range of Q = 0.11 Å^{-1} to 0.20 Å^{-1}. Additional measurements were performed at $\lambda = 6$ Å for Fourier times up to 20 ns for Q = 0.11 Å^{-1} to 0.20 Å^{-1}. Overlapping NSE data taken at $\lambda = 6$ and 11 Å for $0.1 \leq t$ (ns) ≤ 30 are shown in the Supporting Information. A standard carbon sample was used to determine the instrument resolution. Data were corrected for background using an empty holder using the software DAVE.[245]

8.3 Results and Discussion

The SANS profiles for SEO/LiTFSI mixtures after subtracting the incoherent background, $I_{coh}(Q)$, at 90 °C for r = 0, 0.025, 0.075 and 0.10 are shown in Figure 8.1. All profiles contain a primary peak at $Q = Q^*$ and a higher order peak at $Q = \sqrt{3}Q^*$. At $r \geq 0.075$, an additional higher order peak at $Q = \sqrt{7}Q^*$is seen. The SANS data indicate that the SEO/LiTFSI mixtures order into hexagonally packed PS cylinders in a salt-containing PEO matrix at all salt concentrations as expected based on previous studies of the phase behavior of SEO/LiTFSI.[107] As salt concentration increases, the scattering intensities of the Bragg scattering peaks increase due to increased segregation between the PS and PEO/LiTFSI blocks with increasing salt concentration.[55,58,107] The domain spacing, given by $D = \frac{2\pi}{Q^*}$, increases from 18.5 to 25.5 nm as r increases from 0 to 0.10, as expected.[56,220] The SANS data show that the ddSEO/dhSEO/LiTFSI blends are macroscopically homogeneous at all salt concentrations; at high-Q the scattering intensity scales with Q^{-2} indicative of scattering from polymer chains obeying random walk statistics (see Supporting Information, Section 8.5).[36] The bar at high-Q in Fig. 8.1 shows the range of scattering vectors covered by the NSE experiments, which corresponds to intra-domain length-scales ensuring that the NSE experiments selectively probe the PEO/LiTFSI matrix phase.

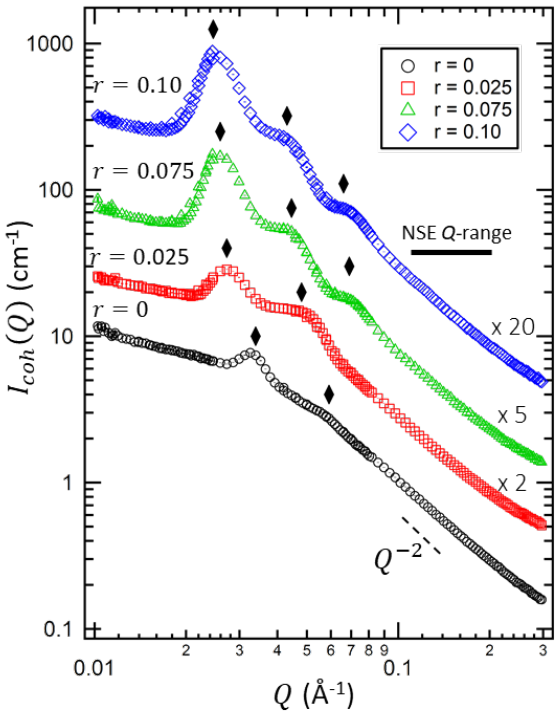

Figure 8.1 SANS of SEO/LiTFSI: SANS profiles, $I_{coh}(Q)$, of SEO/LiTFSI mixtures at different salt concentrations, $0 \leq r \leq 0.10$, at 90 °C. Error bars represent one standard deviation and are smaller than the data points. Curves are offset vertically for clarity (scaling factors are given at the high-Q intercept). Diamonds represent the primary scattering peak, Q^*, and the higher order scattering peaks at $Q = \sqrt{3}Q^*$ and $\sqrt{7}Q^*$. The bar at high-Q represents the scattering vector range chosen for the NSE experiments, $0.11 \leq Q\ (\text{Å}^{-1}) \leq 0.20$. An example of the scaling for a Gaussian chain, Q^{-2}, is shown in the high-Q regime.

The dynamic scattering function measured by NSE, $\frac{S(Q,t)}{S(Q,0)}$, is shown as a function of salt concentration and temperature in Figure 8.2. At short times, $t \leq 10$ ns, the data are consistent with the Rouse model,[66] which has been shown by Richter and coworkers[71] to be approximated by

$$\frac{S(Q,t)}{S(Q,0)} = \frac{12}{Q^2 l^2} \int_0^\infty du \exp\left\{-u - (\Omega_R t)^{\frac{1}{2}} h\left(u(\Omega_R t)^{-\frac{1}{2}}\right)\right\} \tag{8.1}$$

with

$$h(y) = \frac{2}{\pi} \int_0^\infty dx \left(\frac{\cos xy}{x^2}\right) [1 - \exp(-x^2)] \tag{8.2}$$

and

$$(\Omega_R t)^{\frac{1}{2}} = \frac{Q^2 l^2}{6} \sqrt{Wt} \tag{8.3}$$

where the Rouse parameter is given by Wl^4 (l is the statistical segment length of the polymer and W is the elementary Rouse rate). The curves through the short time data in Fig. 8.2 represent fits to Eq. 8.1-8.3 for all Q values simultaneously with Wl^4 as the only adjustable parameter at both temperatures (see Eq. 8.3). A magnified view of the fits of Eq. 8.1-8.3 through the low-t data is provided in the Supporting Information, Section 8.5.

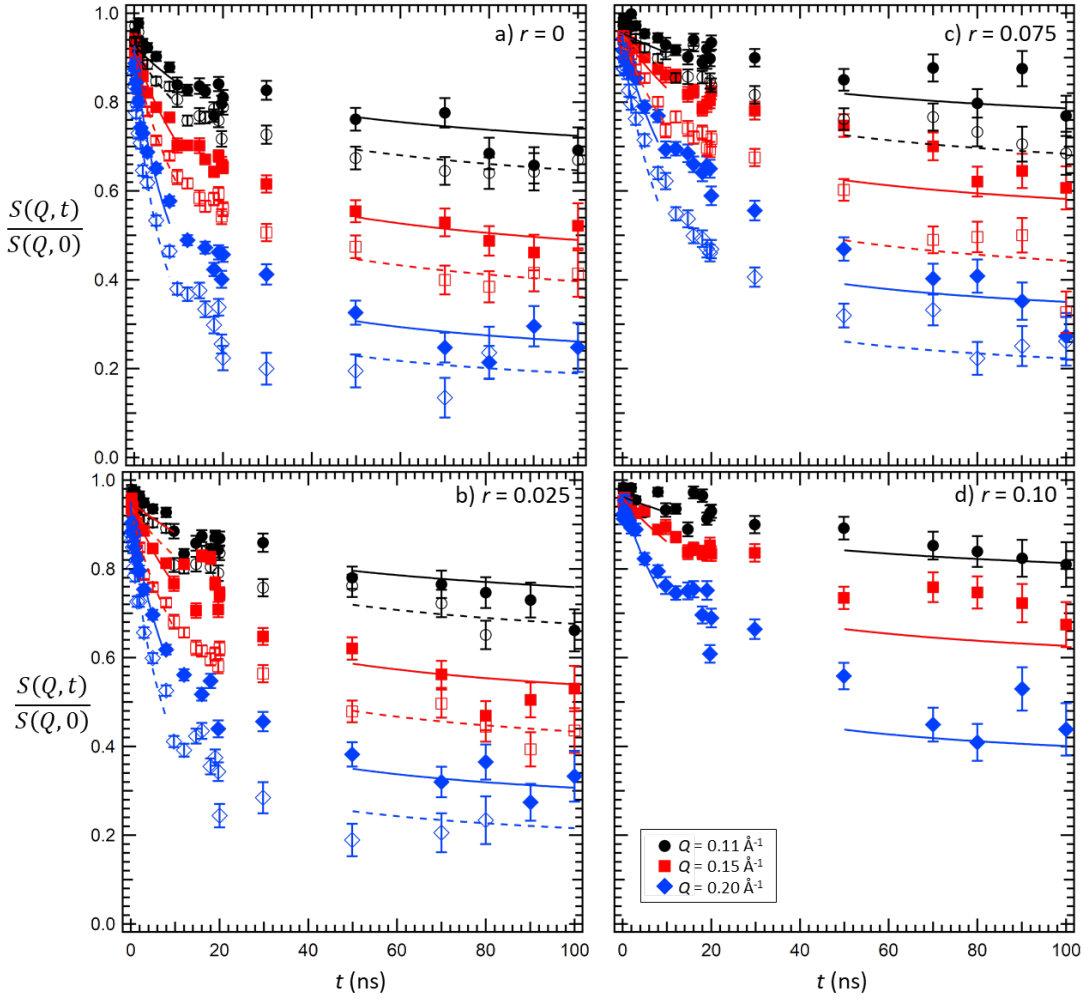

Figure 8.2 Dynamic Scattering Function: Dynamic scattering functions, $\frac{S(Q,t)}{S(Q,0)}$, determined from NSE for SEO/LiTFSI mixtures for $Q = 0.11$, 0.15 and 0.20 Å^{-1} at 90 °C (filled symbols) and 120 °C (open symbols) for different salt concentrations: (a) $r = 0$, (b) 0.025, (c) 0.075 and (d) 0.10. The error bars represent one standard deviation of the NSE data. At short times, $t \leq 10$ ns, the curves correspond to the Rouse model (Eq. 8.1-8.3). At long times, $t \geq 50$ ns, the curves correspond to the tube model for reptation (Eq. 8.4). Solid lines represent fits to data taken at 90 °C and dashed lines represent fits to data taken at 120 °C.

The data in Figure 8.2 show deviations from Rouse dynamics at $t \geq 20$ ns for all salt concentrations signaling the slowing down of segmental motion due to constraints imposed by the presence of other chains (see Supporting Information, Section 8.5). The tube diameter, d, quantifies these constraints. The crossover from Rouse dynamics to local reptation occurs over the

window from 20-50 ns. At long times, $t \geq 50$ ns, the data in Fig. 8.2 were fit to the tube model proposed by de Gennes[70,246] which gives

$$\frac{S(Q,t)}{S(Q,0)} = \left[1 - \exp\left(-\frac{Q^2 d^2}{36}\right)\right] S_{local}(Q,t) + \exp\left(-\frac{Q^2 d^2}{36}\right) S_{esc}(Q,t) \tag{8.4}$$

where $S_{local}(Q,t) = \exp\left(\frac{t}{\tau_0}\right) \mathrm{efrc}\left(\sqrt{\frac{t}{\tau_0}}\right)$ describes local reptation within the tube with characteristic time scale $\tau_0 = \frac{36}{Wl^4Q^4}$. $S_{esc}(Q,t)$ is related to the long-time dynamics of the confined chain and was neglected in this study ($S_{esc}(Q,t) = 1$). The Rouse parameter, Wl^4, was taken from the fits of Eq. 8.1-8.3 in the low-*t* regime and used in Eq. 8.4 to determine the tube diameter, *d*. Eq. 8.4 was fit simultaneously for all Q values at a given temperature leaving *d* as the only free parameter. The results and statistics for the fitting of Eq. 8.1-8.4 are provided in the Supporting Information. We note that Eq. 8.1-8.4 are derived for salt-free homopolymer systems and that no models currently exist for describing segmental dynamics and reptation of salt-containing polymer systems.

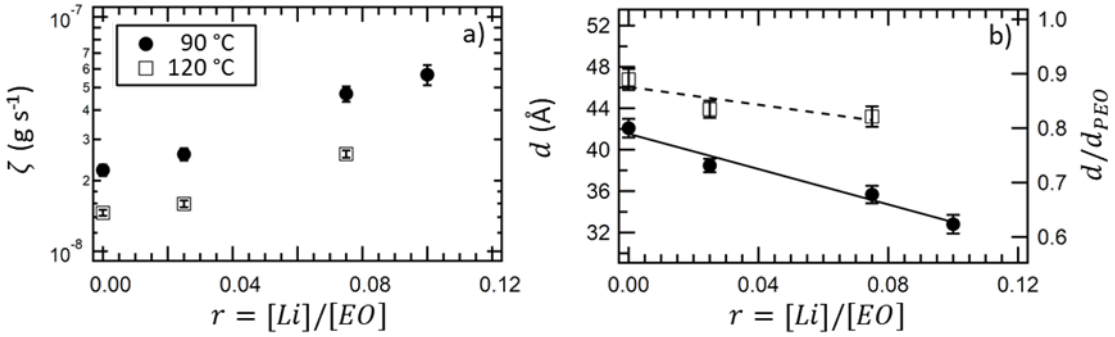

Figure 8.3 NSE Results: Results from fitting $\frac{S(Q,t)}{S(Q,0)}$ (Fig. 2) in both the low and high *t* regions: (a) monomeric friction coefficient, ζ, (Eq. 8.5), (b) tube diameter (left axis), d, and normalized tube diameter (right axis), d/d_{PEO}, as a function of salt concentration, *r*, at 90 °C (filled symbols) and 120 °C (open symbols). Error bars represent one standard deviation from the fits. The lines in (b) are least-squares fits of the data through the equation, $\frac{d}{d_{PEO}} = ar + b$, where $a = -1.63 \pm 0.21$ and -0.82 ± 0.48 and $b = 0.80 \pm 0.01$ and 0.88 ± 0.02 for 90 °C and 120 °C, respectively, and the confidence intervals represent the standard deviations from the fits of $\frac{d}{d_{PEO}}$.

Figure 8.3 shows the results from the fits shown in Figure 2. The monomeric friction coefficient, ζ, is calculated from Wl^4 using Eq. 8.5,[71]

$$\zeta = \frac{3k_BT}{Wl^4} l^2 \tag{8.5}$$

where k_B is the Boltzmann constant and *T* is absolute temperature. The dependence of l on salt concentration for PEO/LiTFSI mixtures is reported in ref 137 at 90 °C. These values of l were used to calculate ζ according to Eq. 8.5 assuming that l is independent of temperature. The dependence of ζ on salt concentration is shown in Fig. 8.3a at 90 °C (solid circles) and 120 °C (open squares). In the absence of salt ($r = 0$), ζ decreases with increasing temperature. These results

are consistent with literature values for PEO homopolymer.[247] The monomeric friction coefficient increases with increasing salt concentration at a similar rate for both temperatures. At 90 °C, this rate matches that seen in PEO/LiTFSI systems.[74] The segmental dynamics on short-time scales, $t \leq 10$ ns, in a microphase separated block copolymer electrolyte is indistinguishable from that of the homopolymer electrolyte; see Supporting Information for details. In a related study, it has been shown that the presence of nanoparticles does not affect the segmental dynamics in polymer nanocomposites,[150] consistent with our finding that the PS-rich phase does not affect the segmental dynamics of the PEO-rich phase.

The dependence of tube diameter, *d*, on salt concentration is shown in Figure 8.3b. Our measured values of d increase with increasing temperature as typically seen in homopolymers due to a decrease in the number of entanglement constraints from increased chain mobility.[248] The tube diameter of PEO homopolymer, d_{PEO}, in the absence of salt at 125 °C is 52.6 Å.[247] The right *y*-axis in Fig. 8.3b shows the ratio d/d_{PEO} as a function of salt concentration, where all data are normalized by d_{PEO} at 125 °C. In the neat state, *d* for SEO/LiTFSI at 120 °C is lower than that of PEO/LiTFSI at 125 °C. This deviation is more pronounced than what can be explained by temperature differences.[248–250] We attribute the decrease in tube diameter to the geometric constraints introduced by the PS microphase. It is thermodynamically unfavorable for portions of entangled chains near the interface of the two microphases to undergo reptation; in order to move around the entanglement constraints, portions of the PS block will need to enter the PEO/LiTFSI-rich phase.[81,251,252] This is consistent with previous findings that geometric confinement contracts tube diameters in polymer mixtures.[151] In addition, the tube diameter decreases with increasing salt concentration. As salt concentration increases, the coordination between Li^+ ions and the ether oxygens on the PEO backbone increases. Molecular dynamics simulations indicate that the Li^+ ions coordinate with either one or two PEO chains.[253] It is likely that coordination with two chains, which may be regarded as a temporary crosslink, has a more significant effect on chain entanglement. The decrease in d with *r* seen in Fig. 8.3b is a reflection of this effect. The effect of salt concentration on the tube diameter is more pronounced at 90 °C relative to 120 °C by a factor of 2. This suggests that coordination effects are more significant at 90 °C, which is supported by MD simulations.[14,254] To our knowledge, these results provide the first measurements of the entanglement constraints, represented by tube diameters, as well as insight into polymer chain conformation in polymer electrolytes as well as block copolymers.

In a melt of entangled homopolymers with degree of polymerization *N*, the longest molecular relaxation time, τ_d, is given by[71]

$$\tau_d = \frac{\zeta N^3}{\pi^2 k_B T}\left(\frac{l^4}{d^2}\right) \tag{8.6}$$

which quantifies the time needed for a confined chain to escape the tube created by neighboring chains. This time-scale also determines the viscosity of the polymer melt.[255] Note that $\zeta, l,$ and d are all functions of *r*. The fact that both parameters, ζ and d, obtained from the neat block copolymer are similar to that of PEO homopolymer indicates that Equation 8.6 is a reasonable starting point to quantify the long-time dynamics of SEO/LiTFSI. In SEO electrolytes, there will be additional contributions to τ_d due to the presence of the PS microphase. Escape of SEO chains from their tubes will involve dragging PS segments through the PEO-rich microphase.[81,251,252] This

factor is not accounted for in our estimate of τ_d. Due to this limitation, it is best to examine a normalized relaxation time, $\tau_{d,n}$, defined as

$$\tau_{d,n} = \frac{\tau_d(r)}{\tau_d(r=0)} \tag{8.7}$$

to quantify the effect of salt concentration on chain dynamics. At 90 °C, d^2 decreases by 39% over the range $0 \leq r \leq 0.10$, while ζ increases by a factor of 2.5 over the same window. Both factors slow down chain diffusion. However, the chain shrinks with added salt, l^4 decreases by 52% over the same window,[137] which will speed up chain diffusion. Therefore, the net effect of salt concentration on the polymer chain dynamics is that $\tau_{d,n}$ increases by a factor of 1.7 across our salt concentration window at 90 °C, as shown in Figure 8.4. The effect of salt concentration of chain diffusion is less pronounced at 120 °C. It is important to note that these factors are lower bounds on the effect of added salt on the longest relaxation time of block copolymer electrolytes as we have neglected contributions arising from the presence of the PS block.

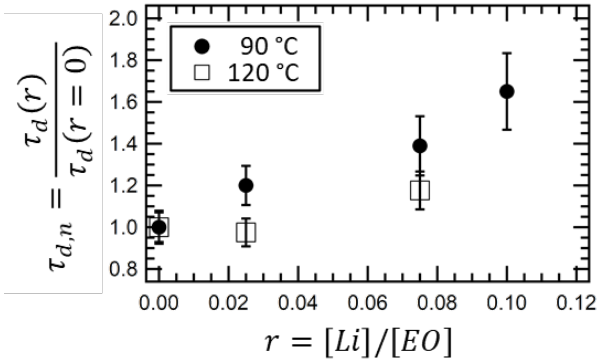

Figure 8.4 Normalized Relaxation Time: Normalized longest molecular relaxation time, $\tau_{d,n} = \tau_d(r)/\tau_d(r=0)$, as a function of salt concentration, *r*, for SEO/LiTFSI at 90 °C (filled circles) and 120 °C (open squares) calculated from Eq. 8.6 and 8.7. Error bars are propagations of the standard deviations of the fits of ζ and d from Eq. 8.1-8.4.

Let us return to the discussion of a polymer-electrolyte-based battery operating at a large current. For completeness, we consider an SEO/LiTFSI electrolyte with r = 0.05 in a battery operating at 90 °C. The volume fraction of salt in this electrolyte is 0.16.[137] When a large enough current is applied, the volume fraction of the salt near the cathode will approach zero due to the well-established concept of concentration polarization.[18,256,257] Based on the data in ref 256, for a symmetric Li-SEO/LiTFSI-Li cell with a 250 micron-thick electrolyte and a PEO volume fraction of 0.80, the current density at which the salt concentration in our SEO electrolyte would be zero at the cathode is 0.75 mA cm^{-2}, and the potential drop across the electrolyte would be 125 mV. In this case, the 16% of the electrolyte volume that was originally occupied by salt must be replaced by polymer due to the incompressibility constraint. Similarly, the salt concentration at the anode will increase to about r = 0.10, displacing polymer chains. The data in Fig. 8.4 suggest that relaxation processes at the anode will be about 1.7 times slower than those at the cathode. While further work is necessary to substantiate this effect, the NSE results presented in Figures 8.3 and 8.4 provide the first insights into factors that may limit the performance of polymer-electrolyte-based batteries operating at high currents.

8.4 Conclusions

In conclusion, the effect of added salt on the polymer dynamics of a nanostructured block copolymer electrolyte are investigated using NSE on the 0.1-100 ns timescale and analyzed using the Rouse model at short times ($t \leq 10$ ns) and the reptation model at long times ($t \geq 50$ ns). The effect of salt concentration on the segmental dynamics in the Rouse regime matches the results of previous experiments on homopolymer electrolytes: monomeric friction increases with increasing salt concentration.[15,72–75] In the reptation regime, the tube diameter decreases with increasing salt concentration. We attribute this trend to temporary crosslinks between neighboring chains arising from Li^+ ion coordination. The normalized longest molecular relaxation time, $\tau_{d,n}$, was calculated from the NSE results, and was found to increase with increasing salt concentration. All of the rich literature on polymer electrolytes is narrowly focused on the transport of ions under small applied fields or in the absence of applied fields.[25,65,76–79,240] We posit that our measurements of dynamics at long times (50-100 ns) are relevant to the operation of polymer-electrolyte-containing batteries at high currents wherein the diffusion of salt ions in one direction must induce diffusion of polymer chains in the opposite direction.

8.5 Nomenclature

8.5.1 Abbreviations

ddSEO	deuterated polystyrene-*b*-deuterated poly(ethylene oxide)
dhSEO	deuterated polystyrene-*b*-hydrogenated poly(ethylene oxide)
LiTFSI	lithium bis(trifluoromethanesulfonyl) imide salt
MD	molecular dynamics
NSE	neutron spin echo
PEO	poly(ethylene oxide)
PS	polystyrene
QENS	quasi elastic neutron scattering
SANS	small angle neutron scattering
SEO	polystyrene-*b*-poly(ethylene oxide)

8.5.2 Symbols

d	tube diameter (Å)
D	domain spacing (nm)
d_{PEO}	tube diameter of PEO homopolymer (Å)
$I_{coh}(Q)$	coherent scattering intensity (cm^{-1})
k_B	the Boltzmann constant
l	statistical segment length (Å)
M_e	entanglement molecular weight (kg mol^{-1})
$M_{n,i}$	number-averaged molecular weight of species i (kg mol^{-1})
N	number-averaged degree of polymerization (sites $chain^{-1}$)
Q	scattering vector ($Å^{-1}$)
r	salt concentration ([Li] $[EO]^{-1}$)

$\frac{S(Q,t)}{S(Q,0)}$	dynamic scattering function
t	time (ns)
T	temperature (K)
W	elementary Rouse rate (ns^{-1})
Wl^4	Rouse parameter ($Å^4ns^{-1}$)

8.5.3 Greek Symbols

λ	neutron wavelength (Å)
ζ	monomeric friction coefficient ($g\ s^{-1}$)
τ_d	longest molecular relaxation time (s)
$\tau_{d,n}$	normalized molecular relaxation time
τ_0	characteristic time scale (ns)

8.6 Supporting Information

8.6.1 Electrochemical Characterization. Ion transport properties were determined by performing electrochemical measurements on symmetric cells made with blocking electrodes assembled in an Ar glovebox. Conductivity samples for the blends of SEO/LiTFSI were prepared by pressing the polymer into a 508 μm thick silicone spacer and sandwiching it between two 200 μm thick stainless steel electrodes. Nickel tabs were secured to the stainless steel shims to serve as current collectors. The assembly was vacuum sealed in laminated pouch material (Showa-Denko) prior to removal from the glovebox. Electrochemical impedance spectroscopy was performed within a frequency range of 1 MHz to 1 Hz at a sinusoidal amplitude of 60 mV. The final electrolyte thickness was determined by subtracting the electrode thickness from the total cell thickness after the experiments were completed. Conductivity was then determined according to the equation

$$\kappa = \frac{l}{A \cdot R_b} \tag{8.8}$$

where l is the electrolyte thickness, A is the sample area, and R_b is the bulk resistance determined from the low frequency minimum in the resulting Nyquist impedance plot.

8.6.2 NSE and SANS Analysis

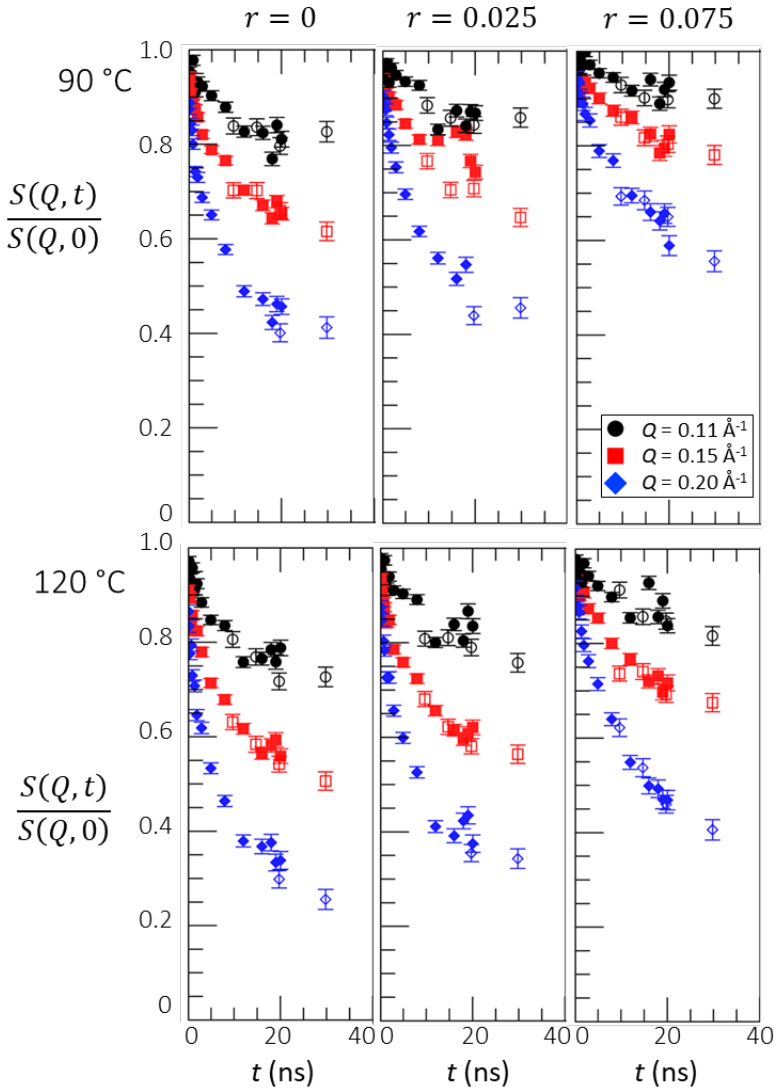

Figure 8.5 Overlap of NSE data: Dynamic scattering functions, $\frac{S(Q,t)}{S(Q,0)}$, determined from NSE for SEO/LiTFSI mixtures for $Q = 0.11$, 0.15, and 0.20 Å^{-1} at $\lambda = 6$ (filled symbols) and 11 Å (open symbols) for different salt concentrations (columns) and temperatures (rows) to show the overlap in data taken at the two wavelengths near $t =$ 20 ns.

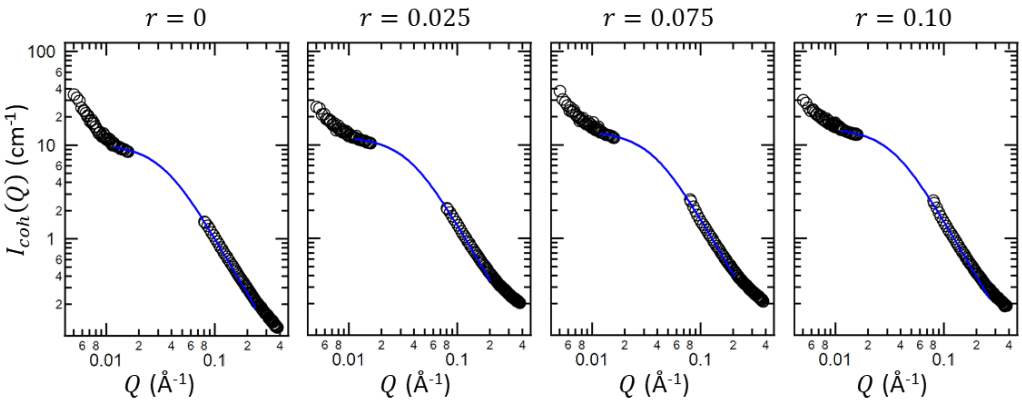

Figure 8.6 Quantitative Analysis of SANS: SANS profiles of SEO/LiTFSI mixtures at different salt concentrations, $0 \leq r \leq 0.10$, at 90 °C. The data surrounding the structured peaks shown in Figure 8.1 were removed and the data were fit to the form factor for a Gaussian coil, the Debeye function. At all salt concentrations, the data are consistent with the Debeye function in the Q-range of the NSE experiments. The results for the radius of gyration, R_g, range from 4.1-4.3 nm, which are in reasonable agreement with ref 137.

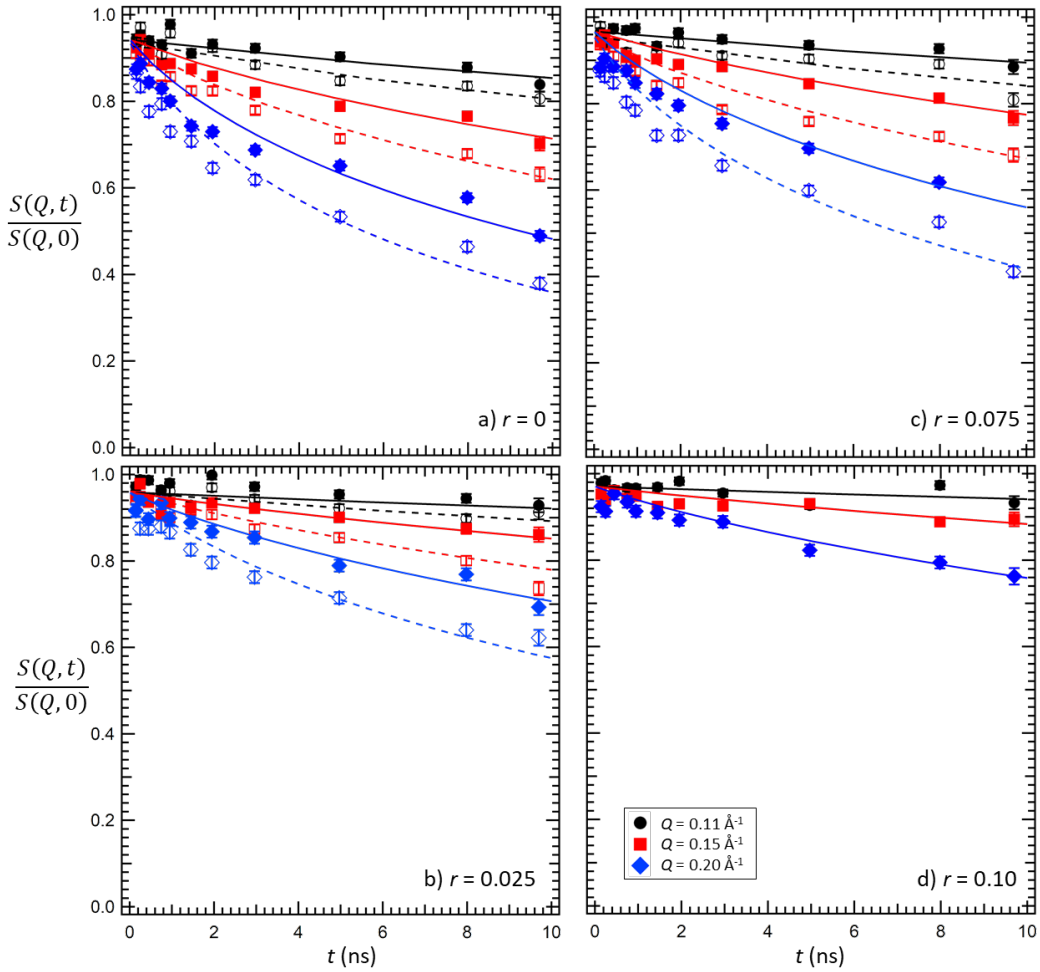

Figure 8.7 Magnified Rouse Fits: Dynamic scattering functions, $\frac{S(Q,t)}{S(Q,0)}$, determined from NSE for SEO/LiTFSI mixtures for $Q = 0.11$, 0.15, and 0.20 Å^{-1} at 90 °C (filled symbols) and 120 °C (open symbols) for different salt concentrations: (a) $r = 0$, (b) 0.025, (c) 0.075 and (d) 0.10. The error bars represent one standard deviation of the NSE data. The curves correspond to the Rouse model (Eq. 8.1-8.3 in main text). Solid lines represent fits to data taken at 90 °C and dashed lines represent fits to data taken at 120 °C.

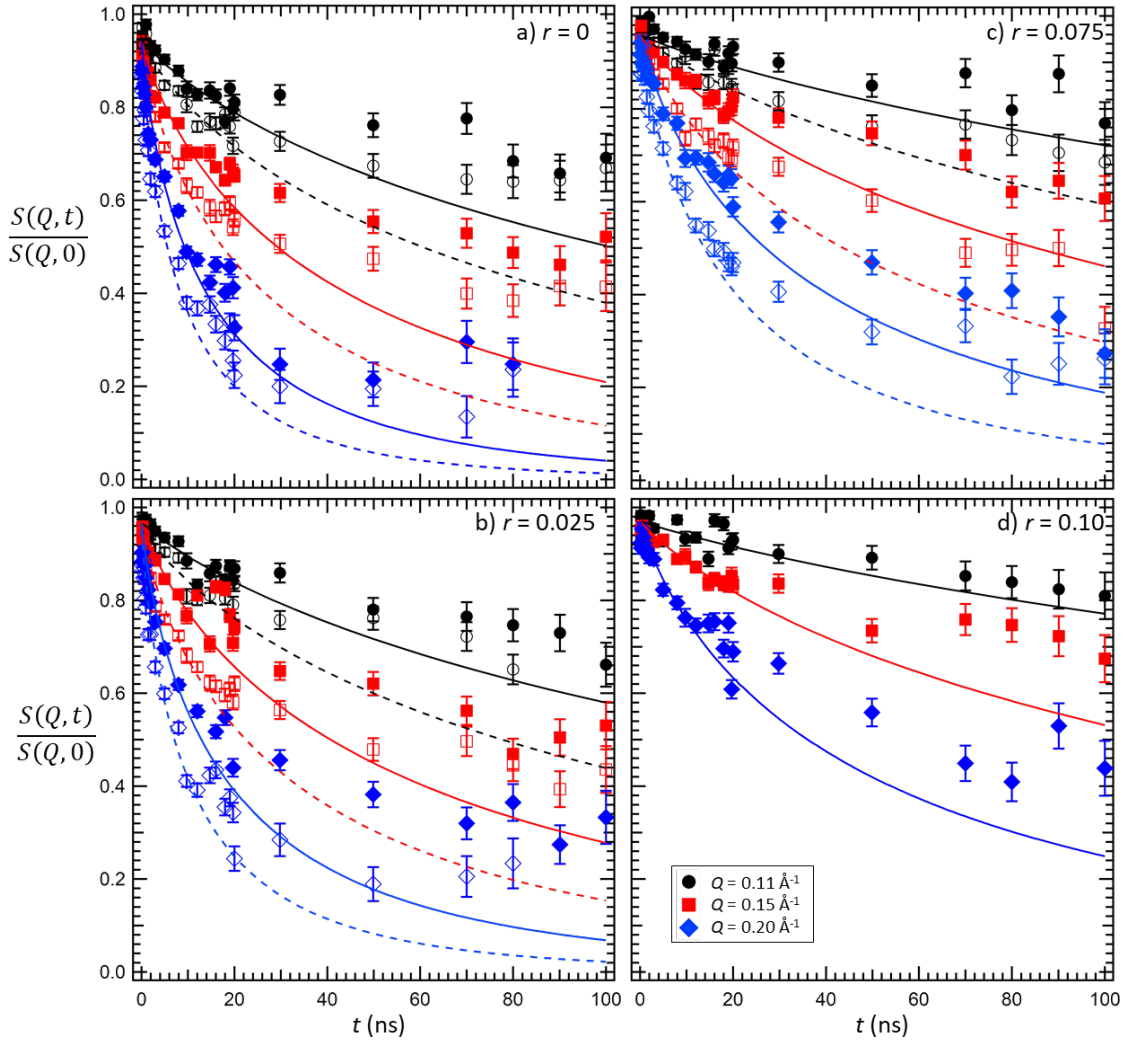

Figure 8.8 Extrapolated Rouse Fits: Dynamic scattering functions, $\frac{S(Q,t)}{S(Q,0)}$, determined from NSE for SEO/LiTFSI mixtures for $Q = 0.11$, 0.15, and 0.20 Å^{-1} at 90 °C (filled symbols) and 120 °C (open symbols) for different salt concentrations: (a) $r = 0$, (b) 0.025, (c) 0.075 and (d) 0.10. The error bars represent one standard deviation of the NSE data. The curves correspond to the Rouse model (Eq. 8.1-8.3 in main text) and are reproduced from the main text but are extrapolated out to $t = 100$ ns to show the deviations from Rouse dynamics at $t > 20$ ns. Solid lines represent fits to data taken at 90 °C and dashed lines represent fits to data taken at 120 °C.

Table 8.1 Fits and statistics for Rouse parameter and tube diameter at 90 °C: Confidence intervals represent one standard deviation from the fits.

r	Wl^4 [Å^4 s^{-1}]	χ^2	d [Å]	χ^2
0	$5.56\text{x}10^{12} \pm 1.43\text{x}10^{11}$	8.00	46.8 ± 1.0	1.19
0.025	$4.52\text{x}10^{12} \pm 1.22\text{x}10^{11}$	8.41	43.9 ± 0.8	3.89
0.075	$2.34\text{x}10^{12} \pm 8.80\text{x}10^{10}$	3.30	43.2 ± 1.0	2.66

Table 8.2 Fits and statistics for Rouse parameter and tube diameter at 120 °C: Confidence intervals represent one standard deviation from the fits.

r	Wl^4 [Å^4 s^{-1}]	χ^2	d [Å]	χ^2
0	$3.38\text{x}10^{12} \pm 9.65\text{x}10^{10}$	7.28	42.1 ± 0.9	3.48
0.025	$2.56\text{x}10^{12} \pm 8.63\text{x}10^{10}$	4.31	38.5 ± 0.7	4.31
0.075	$1.20\text{x}10^{12} \pm 6.68\text{x}10^{10}$	2.18	35.7 ± 0.8	4.29
0.10	$9.20\text{x}10^{11} \pm 5.72\text{x}10^{10}$	2.71	32.8 ± 0.9	3.70

8.6.3 Comparison between PEO/LiTFSI and SEO/LiTFSI

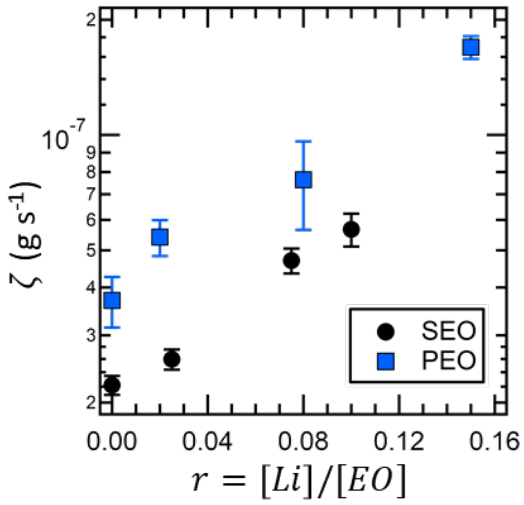

Figure 8.9 Friction for SEO/LiTFSI and PEO/LiTFSI: Monomeric friction coefficients at 90 °C for PEO/LiTFSI and SEO/LiTFSI as a function of salt concentration. Values for PEO/LiTFSI were taken from ref 74 and re-calculated to account for the effect of salt on the statistical segment length, l, from ref 137.

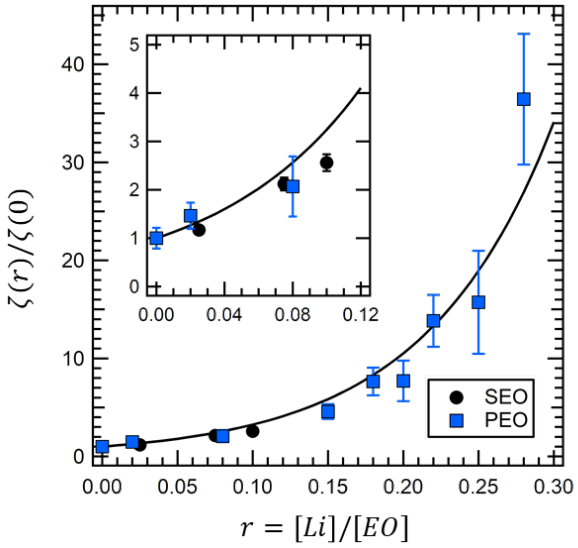

Figure 8.10 Normalized Friction: Comparison between normalized friction coefficient, $\zeta(r)/\zeta(0)$, as a function of salt concentration taken at 90 °C for PEO/LiTFSI and SEO/LITFSI (reproduced from Fig. 8.9). Solid line is the equation, $\frac{\zeta(r)}{\zeta(0)} = \frac{r}{0.085}$, taken from ref 74. Error bars represent one standard deviation.

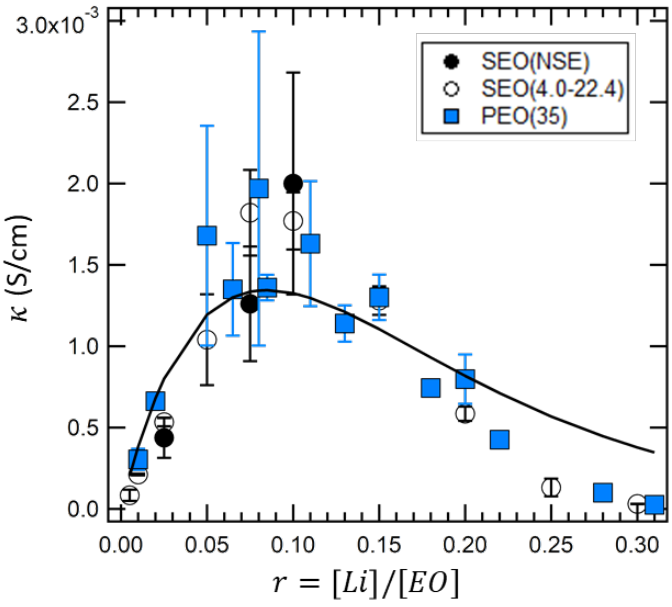

Figure 8.11 Ionic Conductivity Predictions: Ionic conductivity, κ, as a function of salt concentration taken at 90 °C for PEO/LiTFSI (blue squares), SEO/LiTFSI from this study (black circles), and a comparable SEO/LiTFSI (white circles) (reproduced from ref 25). Error bars represent standard deviations from the ≥ 3 measurements taken. The solid line is the equation: $\kappa = 0.043r\left[\exp\left(-\frac{r}{0.085}\right)\right]$ taken from ref 74.

9. Summary

The purpose of the work presented in this dissertation is to develop a molecular-level understanding of the effect of salt on the thermodynamics and dynamics of block copolymer electrolytes. Throughout this work, we apply theories developed for salt-free polymer systems to experimental data taken on block copolymer/salt mixtures to gain insight on how the presence of salt affects polymer behavior such as self-assembly, thermodynamics, and chain motion. Our model system is polystyrene-*block*-poly(ethylene oxide) (SEO) mixed with lithium bis(trifluoromethanesulfonyl) imide (LiTFSI) salt, SEO/LiTFSI. In these systems, we quantify the salt concentration, r, as the ratio of Li ions to ethylene oxide repeat units: $r = [Li]/[EO]$. In Chapter 2, we describe the synthetic procedures used to synthesize the SEO block copolymers used in this study. In Chapter 3, we give a brief review on the variety of X-ray and neutron scattering techniques used in the present study and highlight other relevant applications for the techniques.

Chapters 4 and 5 focus on the phase behavior of SEO/LiTFSI. The morphologies of SEO/LiTFSI were determined using temperature-resolved small angle X-ray scattering (SAXS) experiments. All SEO copolymers considered in these studies form disordered morphologies in the salt-free state and microphase separate upon the addition of salt. In Chapter 4, we focus on SEO copolymers with a majority polystyrene (PS) phase. We find that the addition of salt drives the copolymers to form ordered morphologies, which increases the domain spacing of the electrolytes. In one copolymer, with a poly(ethylene oxide) (PEO) volume fraction (f_{EO}) equal to 0.20, we find a reentrant phase transition where the addition of a small volume of salt first orders the copolymer. The ordered phase formed at this salt concentration contains coexistence of the same lattice type – two body center cubic lattices with different lattice constants. Upon further salt addition, the copolymer disorders before undergoing a final disorder-to-order phase transition at even higher salt concentrations. Neither this reentrant phase transition nor the coexistence of the same ordered morphology has been previously seen in block copolymers (with or without salt). We use electron tomography and resonant soft X-ray scattering (RSoXS) to probe the nature of the coexisting spheres. We hypothesize that a difference in salt concentration in the PEO spheres leads to the emergence of two dominant domain spacings.

Chapter 5 focuses on the creation of the largest experimental dataset of the phase behavior of block copolymer electrolytes. Through SAXS experiments, we determine the morphology of a library of SEO/LiTFSI mixtures with copolymer compositions ranging from $0.18 \leq f_{EO} \leq 0.85$, chain lengths ($N$) ranging from 50-500 repeat units, and salt concentrations ranging from $0 \leq r \leq 0.30$. For simplicity, we focus on the phase behavior at a single temperature of 100 °C. We use a simple framework to create phase diagrams of segregation strength versus copolymer composition for SEO/LiTFSI and find that the phase behavior of SEO/LiTFSI is qualitatively similar to that of salt-free block copolymers predicted by mean-field theory. Also included in this chapter is a compiled dataset from the literature on the phase behavior of SEO copolymers mixed with a variety of Li salts as well as a study on the effect of salt concentration on the domain spacing of SEO-based electrolytes. Expressions for the domain spacing as a function of copolymer chain length, composition and salt concentration were developed for both the weak and strong segregation regimes.

In Chapter 6, we focus on the effect of salt concentration and copolymer composition on the thermodynamics of SEO/LiTFSI through quantification of the Flory-Huggins interaction parameter, χ. The interaction parameters were quantified through application of Leibler's Random Phase Approximation to SAXS profiles of the electrolytes in the disordered phase. In the absence of salt, we find that the thermodynamics are dependent on both *N* and f_{EO}. The effect of salt on χ_{eff} is also asymmetric and at a fixed temperature of 100 °C, an expression for χ_{eff} was developed for SEO/LiTFSI as a function of chain length, copolymer composition, and salt concentration. This expression was used to determine the critical chain length for ordering, N_{crit}, as a function of copolymer composition and salt concentration. At $f_{EO} > 0.27$, the addition of salt stabilizes the ordered phase; at $f_{EO} < 0.27$, the addition of salt stabilizes the disordered phase. We propose a simple theoretical model to predict the block copolymer composition at which phase behavior is independent of salt concentration ($f_{EO} = 0.27$). We refer to this composition as the "isotaksis point".

Chapter 7 is the first section to introduce neutron scattering and is the only section that focuses on homopolymer electrolytes, PEO/LiTFSI. We use small angle neuron scattering (SANS) to determine the effect of salt concentration on the statistical segment length of PEO in the melt state at 90 °C. In the prior sections we used nanostructure to determine the effect of salt on the thermodynamics or chain conformation of SEO corresponding to length-scales on the ~10 nm length-scale. In Chapter 7, we determine the effect of salt concentration on a significantly smaller length-scale (approximately 0.5 nm) to quantify how the effect of salt concentration on the chain dimensions. We find that the effect is non-monotonic: for $r \leq 0.125$, the chain size decreases and for $r > 0.125$, the chain size increases. We hypothesize that this relationship is due to the preferred coordination environment of Li ions with PEO where each Li ion prefers to be coordinated by six ether oxygens. As salt concentration increases, the ether oxygens become saturated with Li ions, which we hypothesize leads to the formation of ion clusters, which increase the chain dimensions. We use additional SANS studies to probe the nature of the ion clusters and found that they had a characteristic size of 0.6 nm.

Chapter 8 expands on the use of neutron scattering techniques. We used neutron spin echo (NSE) spectroscopy to probe the effect of salt concentration on the polymer chain dynamics of a SEO/LiTFSI electrolyte that microphase separates into cylinders of PS in a salt-containing PEO matrix determined by SANS. The main advantage to using NSE is the wide range of timescales it can probe: 0.1-100 ns. This allows for examination of segmental dynamics in the Rouse regime at $t \leq 10$ ns as well as polymer chain dynamics in the reptation regime at $t \geq 50$ ns. We find that the dynamics in both regimes decreases with increasing salt concentration as quantified by the increase in the monomeric friction coefficient in the Rouse regime and decrease in tube diameter in the reptation regime. Based on these measurements, we calculate a normalized longest molecular relaxation time and find that block copolymers with flow more slowly with increasing salt concentration. This is important in a battery operating at high current wherein the diffusion of salt ions in one direction must induce diffusion of polymer chains in the opposite direction.

10. References

(1) Balsara, N. P.; Newman, J. Comparing the Energy Content of Batteries, Fuels, and Materials. *J. Chem. Educ.* **2013**, *90* (4), 446–452 DOI: 10.1021/ed3004066.

(2) Tarascon, J. M.; Armand, M. Issues and Challenges Facing Rechargeable Lithium Batteries. *Nature* **2001**, *414* (6861), 359–367 DOI: 10.1038/35104644.

(3) Goodenough, J. B.; Park, K.-S. S. The Li-Ion Rechargeable Battery: A Perspective. *J. Am. Chem. Soc.* **2013**, *135* (4), 1167–1176 DOI: 10.1021/ja3091438.

(4) Goodenough, J. B.; Kim, Y. Challenges for Rechargeable Li Batteries. *Chem. Mater.* **2010**, *22* (3), 587–603 DOI: 10.1021/cm901452z.

(5) Scrosati, B.; Vincent, C. a. Polymer Electrolytes: The Key to Lithium Polymer Batteries. *MRS Bull.* **2000**, *25* (March), 28 DOI: 10.1557/mrs2000.15.

(6) Armand, M. B. Polymer Electrolytes. *Annu. Rev. Mater. Sci.* **1986**, *16* (1), 245–261 DOI: 10.1146/annurev.ms.16.080186.001333.

(7) Fenton, D. E.; Parker, J. M.; Wright, P. V. Complexes of Alkali Metal Ions with Poly(Ethylene Oxide). *Polymer (Guildf).* **1973**, *14* (11), 589 DOI: 10.1016/0032-3861(73)90146-8.

(8) Armand, M. B.; Chabahno, J. M.; Dulcot, M. J. Poly-Ethers as Solid Electrolytes. In *Fast Ion Transport in Solids*; Vashishta, P. M., Mundy, J. M., Shenoy, G. K., Eds.; North-Holland, 1979; pp 131–136.

(9) Armand, M. B.; Gorecki, W.; Andreani, R. Second International Symposium on Polymer Electrolytes. In *Second International Symposium on Polymer Electrolytes;* Scrosati, B., Ed.; Elsevier Applied Science: New York, NY, 1990; p 91.

(10) Gallagher, K. G.; Goebel, S.; Greszler, T.; Mathias, M.; Oelerich, W.; Eroglu, D.; Srinivasan, V. Quantifying the Promise of Lithium-Air Batteries for Electric Vehicles. *Energy Environ. Sci.* **2014**, *7* (5), 1555–1563 DOI: 10.1039/c3ee43870h.

(11) Lin, D.; Liu, Y.; Cui, Y. Reviving the Lithium Metal Anode for High-Energy Batteries. *Nat. Nanotechnol.* **2017**, *12* (3), 194–206 DOI: 10.1038/nnano.2017.16.

(12) Shriver, D. F.; Papke, B. L.; Ratner, M. A.; Dupon, R.; Wong, T.; Brodwin, M. Structure and Ion Transport in Polymer-Salt Complexes. *Solid State Ionics* **1981**, *5*, 83–88 DOI: 10.1016/0167-2738(81)90199-5.

(13) Ratner, M. A.; Shriver, D. F. Ion Transport in Solvent-Free Polymers. *Chem. Rev.* **1988**, *88*, 109–124.

(14) Borodin, O.; Smith, G. D. Molecular Dynamics Simulations of Poly(Ethylene Oxide)/LiI Melts. 1. Structural and Conformational Properties. *Macromolecules* **1998**, *31* (23), 8396–8406 DOI: 10.1021/ma980838v.

(15) Fullerton-Shirey, S. K.; Maranas, J. K. Effect of LiClO 4 on the Structure and Mobility of PEO-Based Solid Polymer Electrolytes. *Macromolecules* **2009**, *42* (6), 2142–2156 DOI: 10.1021/ma802502u.

(16) Webb, M. A.; Jung, Y.; Pesko, D. M.; Savoie, B. M.; Yamamoto, U.; Coates, G. W.; Balsara, N. P.; Wang, Z. G.; Miller, T. F. Systematic Computational and Experimental Investigation of Lithium-Ion Transport Mechanisms in Polyester-Based Polymer Electrolytes. *ACS Cent. Sci.* **2015**, *1* (4), 198–205 DOI: 10.1021/acscentsci.5b00195.

(17) Lascaud, S.; Perrier, M.; Vallke, A.; Besner, S.; Prud ’homme, J.; Armand, M. Phase Diagrams and Conductivity Behavior of Poly(Ethy1ene Oxide)-Molten Salt Rubbery

Electrolytes. *Macromolecules* **1994**, *27* (25), 7469–7477.
(18) Newman, J.; Thomas-Alyea, K. E. *Electrochemical Systems*; John Wiley & Sons: Hoboken, NJ, 2004.
(19) Pesko, D. M.; Timachova, K.; Bhattacharya, R.; Smith, M. C.; Villaluenga, I.; Newman, J.; Balsara, N. P. Negative Transference Numbers in Poly(Ethylene Oxide)-Based Electrolytes. *J. Electrochem. Soc.* **2017**, *164* (11), E3569–E3575 DOI: 10.1149/2.0581711jes.
(20) Villaluenga, I.; Pesko, D. M.; Timachova, K.; Feng, Z.; Newman, J.; Srinivasan, V.; Balsara, N. P. Negative Stefan-Maxwell Diffusion Coefficients and Complete Electrochemical Transport Characterization of Homopolymer and Block Copolymer Electrolytes. *J. Electrochem. Soc.* **2018**, *165* (11), A2766–A2773 DOI: 10.1149/2.0641811jes.
(21) Monroe, C.; Newman, J. Dendrite Growth in Lithium/Polymer Systems. *J. Electrochem. Soc.* **2003**, *150* (10), A1377 DOI: 10.1149/1.1606686.
(22) Soo, P. P.; Huang, B.; Jang, Y.-I.; Chiang, Y.-M.; Sadoway, D. R.; Mayes, A. M. Rubbery Block Copolymer Electrolytes for Solid-State Rechargeable Lithium Batteries. *J. Electrochem. Soc.* **1999**, *146* (1), 32–37.
(23) Panday, A.; Mullin, S.; Gomez, E. D.; Wanakule, N.; Chen, V. L.; Hexemer, A.; Pople, J.; Balsara, N. P. Effect of Molecular Weight and Salt Concentration on Conductivity of Block Copolymer Electrolytes. *Macromolecules* **2009**, *42* (13), 4632–4637 DOI: 10.1021/ma900451e.
(24) Young, W. S.; Kuan, W. F.; Epps, T. H. Block Copolymer Electrolytes for Rechargeable Lithium Batteries. *J. Polym. Sci. Part B Polym. Phys.* **2014**, *52* (1), 1–16 DOI: 10.1002/polb.23404.
(25) Galluzzo, M. D.; Loo, W. S.; Wang, A. A.; Walton, A.; Maslyn, J. A.; Balsara, N. P. Measurement of Three Transport Coefficients and the Thermodynamic Factor in Block Copolymer Electrolytes with Different Morphologies. *J. Phys. Chem. B* **2020**, *124* (5), 921–935 DOI: 10.1021/acs.jpcb.9b11066.
(26) Harry, K. J.; Hallinan, D. T.; Parkinson, D. Y.; MacDowell, A. a; Balsara, N. P. Detection of Subsurface Structures underneath Dendrites Formed on Cycled Lithium Metal Electrodes. *Nat. Mater.* **2014**, *13* (1), 69–73 DOI: 10.1038/nmat3793.
(27) Maslyn, J. A.; Frenck, L.; Loo, W. S.; Parkinson, D. Y.; Balsara, N. P. Extended Cycling through Rigid Block Copolymer Electrolytes Enabled by Reducing Impurities in Lithium Metal Electrodes. *ACS Appl. Energy Mater.* **2019**, *2* (11), 8197–8206 DOI: 10.1021/acsaem.9b01685.
(28) Schauser, N. S.; Harry, K. J.; Parkinson, D. Y.; Watanabe, H.; Balsara, N. P. Lithium Dendrite Growth in Glassy and Rubbery Nanostructured Block Copolymer Electrolytes. *J. Electrochem. Soc.* **2015**, *162* (3), 398–405 DOI: 10.1149/2.0511503jes.
(29) Gomez, E. D.; Panday, A.; Feng, E. H.; Chen, V.; Stone, G. M.; Minor, A. M.; Kisielowski, C.; Downing, K. H.; Borodin, O.; Smith, G. D.; Balsara, N. P. Effect of Ion Distribution on Conductivity of Block Copolymer Electrolytes. *Nano Lett.* **2009**, *9* (3), 1212–1216 DOI: 10.1021/nl900091n.
(30) Gilbert, J. B.; Luo, M.; Shelton, C. K.; Rubner, M. F.; Cohen, R. E.; Epps, T. H. Determination of Lithium-Ion Distributions in Nanostructured Block Polymer Electrolyte Thin Films by X-Ray Photoelectron Spectroscopy Depth Profiling. *ACS Nano* **2015**, *9* (1), 512–520 DOI: 10.1021/nn505744r.

(31) Gartner, T. E.; Morris, M. A.; Shelton, C. K.; Dura, J. A.; Epps, T. H. Quantifying Lithium Salt and Polymer Density Distributions in Nanostructured Ion-Conducting Block Polymers. *Macromolecules* **2018**, *51* (5), 1917–1926 DOI: 10.1021/acs.macromol.7b02600.
(32) Flory, P. J. Thermodynamics of High Polymer Solutions. *J. Chem. Phys.* **1942**, *10* (1), 51–61 DOI: 10.1063/1.1723621.
(33) Huggins, M. L. Theory of Solutions of High Polymers [1]. *J. Am. Chem. Soc.* **1942**, *64* (7), 1712–1719 DOI: 10.1021/ja01259a068.
(34) Leibler, L. Theory of Microphase Separation in Block Copolymers. *Macromolecules* **1980**, *13* (10), 1602–1617 DOI: 10.1021/ma60078a047.
(35) de Gennes, P. G. Qualitative Features of Polymer Demixtion. *J. Phys. Lett.* **1977**, *38* (21), 441–443 DOI: 10.1051/jphyslet:019770038021044100.
(36) de Gennes, P. G. *Scaling Concepts in Polymer Chemsitry*; Cornell University Press: Ithaca, NY, 1979.
(37) Fredrickson, G. H.; Liu, a J.; Bates, F. S. Entropic Corrections to the Flory-Huggins Theory of Polymer Blends - Architectural and Conformational Effects. *Macromolecules* **1994**, *27* (9), 2503–2511 DOI: Doi 10.1021/Ma00087a019.
(38) Helfand, E. Block Copolymer Theory. III. Statistical Mechanics of the Microdomain Structure. *Macromolecules* **1975**, *8* (4), 552–556.
(39) Bates, F. S.; Fredrickson, G. H. Block Copolymer Thermodynamics: Theory and Experiment. *Annu. Rev. Phys. Chem.* **1990**, *41* (1), 525–557 DOI: 10.1146/annurev.physchem.41.1.525.
(40) Kawasaki, K.; Kawakatsu, T. Equilibrium Morphology of Block Copolymer Melts. *Macromolecules* **1990**, *23* (17), 4006–4019 DOI: 10.1021/ma00219a022.
(41) Cochran, E. W.; Garcia-Cervera, C. J.; Fredrickson, G. H. Stability of the Gyroid Phase in Diblock Copolymers at Strong Segregation. *Macromolecules* **2006**, *39* (7), 2449–2451 DOI: 10.1021/ma0527707.
(42) Knychała, P.; Timachova, K.; Banaszak, M.; Balsara, N. P. 50th Anniversary Perspective: Phase Behavior of Polymer Solutions and Blends. *Macromolecules* **2017**, *50* (8), 3051–3065 DOI: 10.1021/acs.macromol.6b02619.
(43) De Gennes, P. G. Theory of X-Ray Scattering by Liquid Macromolecules with Heavy Atom Labels. *J. Phys. TOME* **1970**, *31* (3) DOI: 10.1051/jphys:01970003102-3023500.
(44) Hamley, I. W.; Castelletto, V. Small-Angle Scattering of Block Copolymers. In *Soft Matter Characterization*; pp 1021–1081.
(45) Flory, P. J. *Principles of Polymer Chemistry*; Cornell University Press: Ithaca, 1953.
(46) Semenov, A. N. Theory of Block Copolymer Interfaces in the Strong Segregation Limit. *Macromolecules* **1993**, *26* (24), 6617–6621 DOI: 10.1021/ma00076a047.
(47) Matsen, M. W.; Bates, F. S. Unifying Weak-and Strong-Segregation Block Copolymer Theories. *Macromolecules* **1996**, *29* (4), 1091–1098 DOI: 10.1021/ma951138i.
(48) Matsen, M. W. Strong-Segregation Limit of the Self-Consistent Field Theory for Diblock Copolymer Melts. *Eur. Phys. J. E* **2010**, *33* (4), 297–306 DOI: 10.1140/epje/i2010-10673-4.
(49) Uneyama, T.; Doi, M. Density Functional Theory for Block Copolymer Melts and Blends. *Macromolecules* **2005**, *38* (1), 196–205 DOI: 10.1021/ma049385m.
(50) Wang, Z. G. Effects of Ion Solvation on the Miscibility of Binary Polymer Blends. *J. Phys. Chem. B* **2008**, *112* (50), 16205–16213 DOI: 10.1021/jp806897t.

(51) Nakamura, I.; Balsara, N. P.; Wang, Z. G. Thermodynamics of Ion-Containing Polymer Blends and Block Copolymers. *Phys. Rev. Lett.* **2011**, *107* (19), 1–5 DOI: 10.1103/PhysRevLett.107.198301.
(52) Ruzette, G.; Soo, P. P.; Sadoway, D. R.; Mayes, A. M. Melt-Formable Block Copolymer Electrolytes for Lithium Rechargeable Batteries. *J. Electrochem. Soc.* **2001**, *148* (6), A537–A543 DOI: 10.1149/1.1368097.
(53) Young, W.; Epps, T. H. Salt Doping in PEO-Containing Block Copolymers: Counterion and Concentration Effects. *Macromolecules* **2009**, *42* (7), 2672–2678 DOI: 10.1021/ma802799p.
(54) Gunkel, I.; Thurn-Albrecht, T. Thermodynamic and Structural Changes in Ion-Containing Symmetric Diblock Copolymers: A Small-Angle X-Ray Scattering Study. *Macromolecules* **2012**, *45* (1), 283–291 DOI: 10.1021/ma201334h.
(55) Wanakule, N. S.; Virgili, J. M.; Teran, A. A.; Wang, Z. G.; Balsara, N. P. Thermodynamic Properties of Block Copolymer Electrolytes Containing Imidazolium and Lithium Salts. *Macromolecules* **2010**, *43* (19), 8282–8289 DOI: 10.1021/ma1013786.
(56) Nakamura, I.; Wang, Z.-G. Salt-Doped Block Copolymers: Ion Distribution, Domain Spacing and Effective χ Parameter. *Soft Matter* **2012**, *8* (36), 9356 DOI: 10.1039/c2sm25606a.
(57) Nakamura, I.; Balsara, N. P.; Wang, Z. G. First-Order Disordered-to-Lamellar Phase Transition in Lithium Salt-Doped Block Copolymers. *ACS Macro Lett.* **2013**, *2* (6), 478–481 DOI: 10.1021/mz4001404.
(58) Teran, A. a.; Balsara, N. P. Thermodynamics of Block Copolymers with and without Salt. *J. Phys. Chem. B* **2014**, *118* (1), 4–17 DOI: 10.1021/jp408079z.
(59) Sing, C. E.; Zwanikken, J. W.; de la Cruz, M. O. Electrostatic Control of Block Copolymer Morphology. *Nat. Mater.* **2014**, *13*, 694–698 DOI: 10.1038/NMAT4001.
(60) Sing, C. E.; Zwanikken, J. W.; De La Cruz, M. O. Theory of Melt Polyelectrolyte Blends and Block Copolymers: Phase Behavior, Surface Tension, and Microphase Periodicity. *J. Chem. Phys.* **2015**, *142* (3), 1–18 DOI: 10.1063/1.4905830.
(61) Pryamitsyn, V. A.; Kwon, H.-K.; Zwanikken, J. W.; Olvera de la Cruz, M. Anomalous Phase Behavior of Ionic Polymer Blends and Ionic Copolymers. *Macromolecules* **2017**, *50* (13), 5194–5207 DOI: 10.1021/acs.macromol.7b00523.
(62) Brown, J. R.; Seo, Y.; Hall, L. M.; Lowrie, W. G. Ion Correlation Effects in Salt-Doped Block Copolymers. *Phys. Rev. Lett.* **2018**, *120* (12), 1–7 DOI: 10.1103/PhysRevLett.120.127801.
(63) Hou, K. J.; Qin, J. Solvation and Entropic Regimes in Ion-Containing Block Copolymers. *Macromolecules* **2018**, *51* (19), 7463–7475 DOI: 10.1021/acs.macromol.8b01616.
(64) Grzetic, D. J.; Delaney, K. T.; Fredrickson, G. H. Field-Theoretic Study of Salt-Induced Order and Disorder in a Polarizable Diblock Copolymer. *ACS Macro Lett.* **2019**, *23*, 962–967 DOI: 10.1021/acsmacrolett.9b00316.
(65) Choo, Y.; Halat, D. M.; Villaluenga, I.; Timachova, K.; Balsara, N. P. Diffusion and Migration in Polymer Electrolytes. *Progress in Polymer Science*. 2020.
(66) Rouse, P. E. A Theory of the Linear Viscoelastic Properties of Dilute Solutions of Coiling Polymers. *J. Chem. Phys.* **1953**, *21* (7), 1272–1280 DOI: 10.1063/1.1699180.
(67) Shi, J.; Vincent, C. A. The Effect of Molecular Weight on Cation Mobility in Polymer Electrolytes. *Solid State Ionics* **1993**, *60* (1–3), 11–17 DOI: 10.1016/0167-2738(93)90268-8.

(68) Teran, A. a.; Tang, M. H.; Mullin, S. a.; Balsara, N. P. Effect of Molecular Weight on Conductivity of Polymer Electrolytes. *Solid State Ionics* **2011**, *203* (1), 18–21 DOI: 10.1016/j.ssi.2011.09.021.
(69) De Gennes, P. G. Reptation of a Polymer Chain in the Presence of Fixed Obstacles. *J. Chem. Phys.* **1971**, *55* (2), 572–579 DOI: 10.1063/1.1675789.
(70) Doi, M.; Edwards, S. F. *The Theory of Polymer Dynamics*; Oxford University Press: Oxford, U.K., 1986.
(71) Richter, D.; Monkenbusch, M.; Arbe, A.; Colmenero, J. Neutron Spin Echo in Polymer Systems. *Adv. Polym. Sci.* **2005**, *174*, 1–221 DOI: 10.1007/b106578.
(72) Mao, G.; Perea, R. F.; Howells, W. S.; Price, D. L.; Saboungi, M.-L. Relaxation in Polymer Electrolytes on the Nanosecond Timescale. *Nature* **2000**, *405*, 163–165.
(73) Mao, G.; Saboungi, M. L.; Price, D. L.; Armand, M.; Mezei, F.; Pouget, S. α-Relaxation in PEO-LiTFSI Polymer Electrolytes. *Macromolecules* **2002**, *35* (2), 415–419 DOI: 10.1021/ma010108e.
(74) Mongcopa, K. I. S.; Tyagi, M.; Mailoa, J. P.; Samsonidze, G.; Kozinsky, B.; Mullin, S. A.; Gribble, D. A.; Watanabe, H.; Balsara, N. P. Relationship between Segmental Dynamics Measured by Quasi-Elastic Neutron Scattering and Conductivity in Polymer Electrolytes. *ACS Macro Lett.* **2018**, *7* (4), 504–508 DOI: 10.1021/acsmacrolett.8b00159.
(75) Webb, M. A.; Yamamoto, U.; Savoie, B. M.; Wang, Z. G.; Miller, T. F. Globally Suppressed Dynamics in Ion-Doped Polymers. *ACS Macro Lett.* **2018**, *7* (6), 734–738 DOI: 10.1021/acsmacrolett.8b00237.
(76) Frischknecht, A. L.; Paren, B. A.; Middleton, L. R.; Koski, J. P.; Tarver, J. D.; Tyagi, M.; Soles, C. L.; Winey, K. I. Chain and Ion Dynamics in Precise Polyethylene Ionomers. *Macromolecules* **2019**, *52* (20), 7939–7950 DOI: 10.1021/acs.macromol.9b01712.
(77) Do, C.; Lunkenheimer, P.; Diddens, D.; Götz, M.; Weiß, M.; Loidl, A.; Sun, X. G.; Allgaier, J.; Ohl, M. Li+ Transport in Poly(Ethylene Oxide) Based Electrolytes: Neutron Scattering, Dielectric Spectroscopy, and Molecular Dynamics Simulations. *Phys. Rev. Lett.* **2013**, *111* (1), 1–5 DOI: 10.1103/PhysRevLett.111.018301.
(78) Bresser, D.; Lyonnard, S.; Iojoiu, C.; Picard, L.; Passerini, S. Decoupling Segmental Relaxation and Ionic Conductivity for Lithium-Ion Polymer Electrolytes. *Mol. Syst. Des. Eng.* **2019**, *4* (4), 779–792 DOI: 10.1039/c9me00038k.
(79) Seo, Y.; Shen, K. H.; Brown, J. R.; Hall, L. M. Role of Solvation on Diffusion of Ions in Diblock Copolymers: Understanding the Molecular Weight Effect through Modeling. *J. Am. Chem. Soc.* **2019** DOI: 10.1021/jacs.9b07227.
(80) Mongcopa, K. I. S.; Gribble, D. A.; Loo, W. S.; Tyagi, M.; Mullin, S. A.; Balsara, N. P. Segmental Dynamics Measured by Quasi-Elastic Neutron Scattering and Ion Transport in Chemically Distinct Polymer Electrolytes. *Macromolecules* **2020**, *53* (7), 2406–2411 DOI: 10.1021/acs.macromol.0c00091.
(81) Dalvi, M. C.; Eastman, C. E.; Lodge, T. P. Diffusion in Microstructured Block Copolymers: Chain Localization and Entanglements. *Phys. Rev. Lett.* **1993**, *71* (16), 2591–2594 DOI: 10.1103/PhysRevLett.71.2591.
(82) Oparaji, O.; Narayanan, S.; Sandy, A.; Ramakrishnan, S.; Hallinan, D. Structural Dynamics of Strongly Segregated Block Copolymer Electrolytes. *Macromolecules* **2018**, *51* (7), 2591–2603 DOI: 10.1021/acs.macromol.7b01803.
(83) Hadjichristidis, N.; Iatrou, H.; Pispas, S.; Pitsikalis, M. Anionic Polymerization: High Vacuum Techniques. *J. Polym. Sci. Part A Polym. Chem.* **2000**, *38* (18), 3211–3234 DOI:

10.1002/1099-0518(20000915)38:18<3211::AID-POLA10>3.0.CO;2-L.
(84) Hadjichristidis, N.; Pitsikalis, M.; Pispas, S.; Iatrou, H. Polymers with Complex Architecture by Living Anionic Polymerization. *Chem. Rev.* **2001**, *101* (12), 3747–3792 DOI: 10.1021/cr9901337.
(85) Teran, A. A. Block Copolymer Electrolytes: Thermodynamics, Ion Transport, and Use in Solid- State Lithium/Sulfur Cells, 2013.
(86) Quirk, R. P.; Kim, J.; Kausch, C.; Chun, M. Butyllithium-Initiated Anionic Synthesis of Well-Defined Poly(Styrene-Block-Ethylene Oxide) Block Copolymers with Potassium Salt Additives. *Polym. Int.* **1996**, *39* (1), 3–10 DOI: 10.1002/(SICI)1097-0126(199601)39:1<3::AID-PI436>3.0.CO;2-O.
(87) Brocas, A.-L.; Deffieux, A.; Le Malicot, N.; Carlotti, S. Combination of Phosphazene Base and Triisobutylaluminum for the Rapid Synthesis of Polyhydroxy Telechelic Poly(Propylene Oxide). *Polym. Chem.* **2012**, *3* (5), 1189–1195 DOI: 10.1039/c2py20014g.
(88) Herzberger, J.; Niederer, K.; Pohlit, H.; Seiwert, J.; Worm, M.; Wurm, F. R.; Frey, H. Polymerization of Ethylene Oxide, Propylene Oxide, and Other Alkylene Oxides: Synthesis, Novel Polymer Architectures, and Bioconjugation. *Chem. Rev.* **2015**, acs.chemrev.5b00441 DOI: 10.1021/acs.chemrev.5b00441.
(89) Maslyn, J. A.; Loo, W. S.; McEntush, K. D.; Oh, H. J.; Harry, K. J.; Parkinson, D. Y.; Balsara, N. P. Growth of Lithium Dendrites and Globules through a Solid Block Copolymer Electrolyte as a Function of Current Density. *J. Phys. Chem. C* **2018**, *Under revi*, acs.jpcc.8b06355 DOI: 10.1021/acs.jpcc.8b06355.
(90) Izunobi, J. U.; Higginbotham, C. L. Polymer Molecular Weight Analysis by 1 H NMR Spectroscopy. *J. Chem. Educ.* **2011**, *88* (8), 1098–1104 DOI: 10.1021/ed100461v.
(91) Teran, A. A.; Balsara, N. P. Thermodynamics of Block Copolymers with and without Salt. *J. Phys. Chem. B* **2014**, *118* (1), 4–17 DOI: 10.1021/jp408079z.
(92) de Gennes, P. G. Theory of Long-Range Correlations in Polymer Melts. *Faraday Discuss. Chem. Soc.* **1979**, *68*, 96 DOI: 10.1039/dc9796800096.
(93) Roe, R.-J. *Methods of X-Ray and Neutron Scattering in Polymer Science*, 1st ed.; Oxford University Press, 2000.
(94) Andrews, D. *Molecular Photophysics and Spectroscopy*; Morgan & Claypool Publishers, 2014.
(95) Guinier, A.; Fournet, G. *Small Angle Scattering of X-Rays*; John Wiley & Sons: New York, 1955.
(96) Ilavsky, J.; Zhang, F.; Andrews, R. N.; Kuzmenko, I.; Jemian, P. R.; Levine, L. E.; Allen, A. J. Development of Combined Microstructure and Structure Characterization Facility for in Situ and Operando Studies at the Advanced Photon Source. *J. Appl. Crystallogr.* **2018**, *51* (3), 867–882 DOI: 10.1107/S160057671800643X.
(97) Chintapalli, M.; Chen, X. C.; Thelen, J. L.; Teran, A. A.; Wang, X.; Garetz, B. A.; Balsara, N. P. Effect of Grain Size on the Ionic Conductivity of a Block Copolymer Electrolyte. *Macromolecules* **2014**, *47* (15), 5424–5431 DOI: 10.1021/ma501202c.
(98) Chintapalli, M.; Le, T. N. P.; Venkatesan, N. R.; Mackay, N. G.; Rojas, A. A.; Thelen, J. L.; Chen, X. C.; Devaux, D.; Balsara, N. P. Structure and Ionic Conductivity of Polystyrene-Block-Poly(Ethylene Oxide) Electrolytes in the High Salt Concentration Limit. *Macromolecules* **2016**, *49* (5), 1770–1780 DOI: 10.1021/acs.macromol.5b02620.
(99) Mullin, S. A.; Stone, G. M.; Teran, A. A.; Hallinan, D. T.; Hexemer, A.; Balsara, N. P. Current-Induced Formation of Gradient Crystals in Block Copolymer Electrolytes. *Nano*

Lett. **2012**, *12* (1), 464–468 DOI: 10.1021/nl203826s.
(100) Bates, F. S. Measurement of the Correlation Hole in Homogeneous Block Copolymer Melts. *Macromolecules* **1985**, *18* (3), 525–528 DOI: 10.1021/ma00145a037.
(101) Zhang, F.; Ilavsky, J.; Long, G. G.; Quintana, J. P. G.; Allen, A. J.; Jemian, P. R. Glassy Carbon as an Absolute Intensity Calibration Standard for Small-Angle Scattering. *Metall. Mater. Trans. A* **2010**, *41* (5), 1151–1158 DOI: 10.1007/s11661-009-9950-x.
(102) Liu, J.; Lhermitte, J.; Tian, Y.; Zhang, Z.; Yu, D.; Yager, K. G. Healing X-Ray Scattering Images. *IUCrJ* **2017**, *4* (4), 455–465 DOI: 10.1107/S2052252517006212.
(103) Wang, B.; Yager, K.; Yu, D.; Hoai, M. X-Ray Scattering Image Classification Using Deep Learning. In *2017 IEEE Winter Conference on Applications of Computer Vision (WACV)*; IEEE, 2017; pp 697–704.
(104) He, H.; Liu, C.; Liu, H. Model Reconstruction from Small-Angle X-Ray Scattering Data Using Deep Learning Methods. *iScience* **2020**, *23* (3), 100906 DOI: 10.1016/j.isci.2020.100906.
(105) Thelen, J. L. The Influence of Charged Species on the Phase Behavior, Self-Assembly, and Electrochemical Performance of Block Copolymer Electrolytes, 2016.
(106) Loo, W. S.; Jiang, X.; Maslyn, J. A.; Oh, H. J.; Zhu, C.; Downing, K. H.; Balsara, N. P. Reentrant Phase Behavior and Coexistence in Asymmetric Block Copolymer Electrolytes. *Soft Matter* **2018**, *14* (15), 2789–2795 DOI: 10.1039/C8SM00175H.
(107) Loo, W. S.; Galluzzo, M. D.; Li, X.; Maslyn, J. A.; Oh, H. J.; Mongcopa, K. I.; Zhu, C.; Wang, A. A.; Wang, X.; Garetz, B. A.; Balsara, N. P. Phase Behavior of Mixtures of Block Copolymers and a Lithium Salt. *J. Phys. Chem. B* **2018**, *122* (33), 8065–8074 DOI: 10.1021/acs.jpcb.8b04189.
(108) Loo, W. S.; Sethi, G. K.; Teran, A. A.; Galluzzo, M. D.; Maslyn, J. A.; Oh, H. J.; Mongcopa, K. I.; Balsara, N. P. Composition Dependence of the Flory–Huggins Interaction Parameters of Block Copolymer Electrolytes and the Isotaksis Point. *Macromolecules* **2019**, *52* (15), 5590–5601 DOI: 10.1021/acs.macromol.9b00884.
(109) Ameh, E. S. A Review of Basic Crystallography and X-Ray Diffraction Applications. *Int. J. Adv. Manuf. Technol.* **2019**, *105* (7–8), 3289–3302 DOI: 10.1007/s00170-019-04508-1.
(110) Thelen, J. L.; Inceoglu, S.; Venkatesan, N. R.; Mackay, N. G.; Balsara, N. P. Relationship between Ion Dissociation, Melt Morphology, and Electrochemical Performance of Lithium and Magnesium Single-Ion Conducting Block Copolymers. *Macromolecules* **2016**, *49* (23), 9139–9147 DOI: 10.1021/acs.macromol.6b01886.
(111) Gann, E.; Young, A. T.; Collins, B. A.; Yan, H.; Nasiatka, J.; Padmore, H. A.; Ade, H.; Hexemer, A.; Wang, C. Soft X-Ray Scattering Facility at the Advanced Light Source with Real-Time Data Processing and Analysis. *Review of Scientific Instruments*. 2012, p 45110.
(112) Virgili, J. M.; Tao, Y. F.; Kortright, J. B.; Balsara, N. P.; Segalman, R. A. Analysis of Order Formation in Block Copolymer Thin Films Using Resonant Soft X-Ray Scattering. *Macromolecules* **2007**, *40* (6), 2092–2099 DOI: 10.1021/ma061734k.
(113) Wong, D. T.; Wang, C.; Beers, K. M.; Kortright, J. B.; Balsara, N. P. Mesoporous Block Copolymer Morphology Studied by Contrast- Matched Resonant Soft X-ray Scattering. DOI: 10.1021/ma3019206.
(114) Aplan, M. P.; Grieco, C.; Lee, Y.; Munro, J. M.; Lee, W.; Gray, J. L.; Seibers, Z. D.; Kuei, B.; Litofsky, J. H.; Kilbey, S. M.; Wang, Q.; Dabo, I.; Asbury, J. B.; Gomez, E. D. Conjugated Block Copolymers as Model Systems to Examine Mechanisms of Charge Generation in Donor-Acceptor Materials. *Adv. Funct. Mater.* **2019**, *29* (1), 1804858 DOI:

10.1002/adfm.201804858.
(115) Hamid, Z.; Wadsworth, A.; Rezasoltani, E.; Holliday, S.; Azzouzi, M.; Neophytou, M.; Guilbert, A. A. Y.; Dong, Y.; Little, M. S.; Mukherjee, S.; Herzing, A. A.; Bristow, H.; Kline, R. J.; DeLongchamp, D. M.; Bakulin, A. A.; Durrant, J. R.; Nelson, J.; McCulloch, I. Influence of Polymer Aggregation and Liquid Immiscibility on Morphology Tuning by Varying Composition in PffBT4T-2DT/Nonfullerene Organic Solar Cells. *Adv. Energy Mater.* **2020**, *10* (8), 1903248 DOI: 10.1002/aenm.201903248.
(116) Wang, C.; Lee, D. H.; Hexemer, A.; Kim, M. I.; Zhao, W.; Hasegawa, H.; Ade, H.; Russell, T. P. Defining the Nanostructured Morphology of Triblock Copolymers Using Resonant Soft X-Ray Scattering. *Nano Lett.* **2011**, *11* (9), 3906–3911 DOI: 10.1021/nl2020526.
(117) Litofsky, J. H.; Lee, Y.; Aplan, M. P.; Kuei, B.; Hexemer, A.; Wang, C.; Wang, Q.; Gomez, E. D. Polarized Soft X-Ray Scattering Reveals Chain Orientation within Nanoscale Polymer Domains. *Macromolecules* **2019**, *52* (7), 2803–2813 DOI: 10.1021/acs.macromol.8b02198.
(118) Grubel, G.; Madsen, A. X-Ray Photon Correlation Spectroscopy (XPCS). In *Soft Matter Characterization*; pp 953–990.
(119) Zhang, Q.; Dufresne, E. M.; Grybos, P.; Kmon, P.; Maj, P.; Narayanan, S.; Deptuch, G. W.; Szczygiel, R.; Sandy, A. Submillisecond X-Ray Photon Correlation Spectroscopy from a Pixel Array Detector with Fast Dual Gating and No Readout Dead-Time. *J. Synchrotron Radiat.* **2016**, *23* (3), 679–684 DOI: 10.1107/S1600577516005166.
(120) Nogales, A.; Fluerasu, A. X Ray Photon Correlation Spectroscopy for the Study of Polymer Dynamics. *Eur. Polym. J.* **2016**, *81*, 494–504 DOI: 10.1016/j.eurpolymj.2016.03.032.
(121) Lewis, R. M.; Beech, H. K.; Jackson, G. L.; Maher, M. J.; Kim, K.; Narayanan, S.; Lodge, T. P.; Mahanthappa, M. K.; Bates, F. S. Dynamics of a Supercooled Disordered Sphere-Forming Diblock Copolymer as Determined by X-Ray Photon Correlation and Dynamic Mechanical Spectroscopies. **2018**, *17*, 55 DOI: 10.1021/acsmacrolett.8b00740.
(122) Ruegg, M. L.; Patel, A. J.; Narayanan, S.; Sandy, A. R.; Mochrie, S. G. J.; Watanabe, H.; Balsara, N. P. Condensed Exponential Correlation Functions in Multicomponent Polymer Blends Measured by X-Ray Photon Correlation Spectroscopy. *Macromolecules* **2006**, *39* (25), 8822–8831 DOI: 10.1021/ma061183y.
(123) Carpenter, J. M.; Loong, C.-K. *Elements of Slow Neutron Scattering: Basics, Techniques, and Applications*; Cambridge University Press, 2015.
(124) Ballard, D. G. H.; Cheshire, P.; Longman, G. W.; Schelten, J. Small-Angle Neutron Scattering Studies of Isotropic Polypropylene. *Polymer (Guildf).* **1978**, *19* (4), 379–385 DOI: 10.1016/0032-3861(78)90241-0.
(125) Qiu, J.; Mongcopa, K. I.; Han, R.; López-Barrón, C. R.; Robertson, M. L.; Krishnamoorti, R. Thermodynamic Interactions in a Model Polydiene/Polyolefin Blend Based on 1,2-Polybutadiene. *Macromolecules* **2018**, *51* (8), 3107–3115 DOI: 10.1021/acs.macromol.7b02181.
(126) Wignall, G. D.; Bates, F. S. Absolute Calibration of Small-Angle Neutron Scattering Data of a Double-Crystal Diffractometer. *J. Appl. Crystallogr.* **1987**, *30* (5), 857–861 DOI: 10.1107/s0021889897001179.
(127) Brûlet, A.; Lairez, D.; Lapp, A.; Cotton, J.-P. Improvement of Data Treatment in Small-Angle Neutron Scattering. *J. Appl. Crystallogr.* **2007**, *40* (1), 165–177 DOI:

10.1107/S0021889806051442.
(128) Kline, S. SANS Data Reduction Tutorial. NIST Center for Neutron Research., 2001.
(129) Hammouda, B. Random Phase Approximation for Compressible Polymer Blends. *J. Non. Cryst. Solids* **1994**, *172–174*, 927–931.
(130) Balsara, N. P.; Jonnalagadda, S. V; Lin, C. C.; Han, C. C.; Krishnamoorti, R. Thermodynamic Interactions and Correlations in Mixtures of Two Homopolymers and a Block Copolymer by Small Angle Neutron Scattering. *J. Chem. Phys.* **1993**, *99* (12), 10011–10020 DOI: 10.1063/1.465505.
(131) Lin, C. C.; Jonnalagadda, S. V; Balsara, N. P.; Han, C. C.; Krishnamoorti, R. Thermodynamic Interactions in Multicomponent Polymer Blends. *Macromolecules* **1996**, *29*, 661–669.
(132) Balsara, N. P.; Fetters, L. J.; Hadjichristidis, N.; Lohse, D. J.; Han, C. C.; Graessley, W. W.; Krishnamoorti, R. Thermodynamic Interactions in Model Polyolefin Blends Obtained by Small-Angle Neutron Scattering. *Macromolecules* **1992**, *25* (23), 6137–6147.
(133) Balsara, N. P.; Lin, C. C.; Dai, H. J.; Krishnamoorti, R. Effect of Saturation on Thermodynamics of Polystyrene-Polyisoprene Block Copolymers. *Macromolecules* **1994**, *27* (5), 1216–1220 DOI: 10.1021/ma00083a021.
(134) Hayashi, H.; Flory, P. J.; Wignall, G. D. Configuration of the Polyisobutylene Chain According to Neutron and X-Ray Scattering. *Macromolecules* **1983**, *16* (8), 1328–1335 DOI: 10.1021/ma00242a013.
(135) Daoud, M.; Cotton, J. P.; Farnoux, B.; Jannink, G.; Sarma, G.; Benoit, H.; Duplessix, C.; Picot, C.; de Gennes, P. G. Solutions of Flexible Polymers. Neutron Experiments and Interpretation. *Macromolecules* **1975**, *8* (6), 804–818 DOI: 10.1021/ma60048a024.
(136) Crist, B.; Graessley, W. W.; Wignall, G. D. Chain Dimensions of Crystallizable Polymers in the Solid and Melt States. *Polymer (Guildf).* **1982**, *23* (11), 1561–1567 DOI: 10.1016/0032-3861(82)90172-0.
(137) Loo, W. S.; Mongcopa, K. I.; Gribble, D. A.; Faraone, A. A.; Balsara, N. P. Investigating the Effect of Added Salt on the Chain Dimensions of Poly(Ethylene Oxide) through Small-Angle Neutron Scattering. *Macromolecules* **2019**, *52*, 8724–8732 DOI: 10.1021/acs.macromol.9b01509.
(138) Bee, M. *Quasielastic Neutron Scattering: Principles and and Applications in Solid State Chemistry, Biology and Materials Science*; IOP Publishing, 1988.
(139) Bée, M. Localized and Long-Range Diffusion in Condensed Matter: State of the Art of QENS Studies and Future Prospects. *Chem. Phys.* **2003**, *292* (2–3), 121–141 DOI: 10.1016/S0301-0104(03)00257-X.
(140) Hoffmann, S.; Willner, L.; Richter, D.; Arbe, A.; Colmenero, J.; Farago, B. Origin of Dynamic Heterogeneities in Miscible Polymer Blends: A Quasielastic Neutron Scattering Study. *Phys. Rev. Lett.* **2000**, *85* (4), 772–775 DOI: 10.1103/PhysRevLett.85.772.
(141) Brodeck, M.; Alvarez, F.; Arbe, A.; Juranyi, F.; Unruh, T.; Holderer, O.; Colmenero, J.; Richter, D. Study of the Dynamics of Poly(Ethylene Oxide) by Combining Molecular Dynamic Simulations and Neutron Scattering Experiments. *J. Chem. Phys.* **2009**, *130* (9) DOI: 10.1063/1.3077858.
(142) Doxastakis, M.; Chrissopoulou, K.; Aouadi, A.; Frick, B.; Lodge, T. P.; Fytas, G. Segmental Dynamics of Disordered Styrene-Isoprene Tetrablock Copolymers. *J. Chem. Phys.* **2002**, *116* (11), 4707–4714 DOI: 10.1063/1.1452109.
(143) Doxastakis, M.; Kitsiou, M.; Fytas, G.; Theodorou, D. N.; Hadjichristidis, N.; Meier, G.;

Frick, B. Component Segmental Mobilities in an Athermal Polymer Blend: Quasielastic Incoherent Neutron Scattering versus Simulation Molecular Dynamics of Polyisoprene/Polystyrene Oligomer Blends: The Role of Self-Concentration and Fluctuations on Blend Dynamics Com. *J. Chem. Phys. J. Chem. Phys. J. Chem. Phys.* **2000**, *1121* (10) DOI: 10.1063/1.1603720.

(144) Mongcopa, K. I. S.; Gribble, D. A.; Loo, W. S.; Tyagi, M.; Mullin, S. A.; Balsara, N. P. Segmental Dynamics Measured by Quasi-Elastic Neutron Scattering and Ion Transport in Chemically Distinct Polymer Electrolytes. *Macromolecules* **2020** DOI: 10.1021/acs.macromol.0c00091.

(145) Mezei, F. Neutron Spin Echo: A New Concept in Polarized Thermal Neutron Techniques. *Zeitschrift für Phys. A Hadron. Nucl.* **1972**, *255* (2), 146–160 DOI: 10.1007/BF01394523.

(146) Gardner, J. S.; Ehlers, G.; Faraone, A.; Garcamp, V. High-Resolution Neutron Spectroscopy Using Backscattering and Neutron Spin-Echo Spectrometers in Soft and Hard Condensed Matter. *Nat. Rev. Phys.* **2020**, *2*, 103–116 DOI: 10.1038/s42254-019-0128-1.

(147) Gooßen, S.; Krutyeva, M.; Sharp, M.; Feoktystov, A.; Allgaier, J.; Pyckhout-Hintzen, W.; Wischnewski, A.; Richter, D. Sensing Polymer Chain Dynamics through Ring Topology: A Neutron Spin Echo Study. *Phys. Rev. Lett.* **2015**, *115* (14), 1–5 DOI: 10.1103/PhysRevLett.115.148302.

(148) Malo De Molina, P.; Alegría, A.; Allgaier, J.; Kruteva, M.; Hoffmann, I.; Prévost, S.; Monkenbusch, M.; Richter, D.; Arbe, A.; Colmenero, J. Direct Observation of Dynamic Tube Dilation in Entangled Polymer Blends: A Combination of Neutron Scattering and Dielectric Techniques. *Phys. Rev. Lett.* **2019**, *123* (18), 1–5 DOI: 10.1103/PhysRevLett.123.187802.

(149) Niedzwiedz, K.; Wischnewski, A.; Allgaier, J.; Richter, D. Chain Dynamics and Viscoelastic Properties of Poly (Ethylene Oxide). *Macromolecules* **2008**, *41* (13), 4866–4872.

(150) Senses, E.; Ansar, S. M.; Kitchens, C. L.; Mao, Y.; Narayanan, S.; Natarajan, B.; Faraone, A. Small Particle Driven Chain Disentanglements in Polymer Nanocomposites. *Phys. Rev. Lett.* **2017**, *118* (14), 147801 DOI: 10.1103/PhysRevLett.118.147801.

(151) Senses, E.; Tyagi, M.; Pasco, M.; Faraone, A. Dynamics of Architecturally Engineered All-Polymer Nanocomposites. *ACS Nano* **2018**, *12* (11), 10807–10816 DOI: 10.1021/acsnano.8b02514.

(152) Montes, H.; Monkenbusch, M.; Willner, L.; Rathgeber, S.; Fetters, L.; Richter, D. Neutron Spin Echo Investigation of the Concentration Fluctuation Dynamics in Melts of Diblock Copolymers. *J. Chem. Phys.* **1999**, *110* (20), 10188–10202 DOI: 10.1063/1.478891.

(153) Loo, W. S.; Faraone, A.; Grundy, L. S.; Gao, K. W.; Balsara, N. P. Polymer Dynamics in Block Copolymer Electrolytes Detected by Neutron Spin Echo. *ACS Macro Lett.* **2020**, *9* (5), 639–645 DOI: 10.1021/acsmacrolett.0c00236.

(154) Naidu, S.; Ahn, H.; Gong, J.; Kim, B.; Ryu, D. Y. Phase Behavior and Ionic Conductivity of Lithium Perchlorate-Doped Polystyrene- b -Poly(2-Vinylpyridine) Copolymer. *Macromolecules* **2011**, *44* (15), 6085–6093 DOI: 10.1021/ma200429v.

(155) Nakamura, I.; Wang, Z.-G. Salt-Doped Block Copolymers: Ion Distribution, Domain Spacing and Effective χ Parameter. *Soft Matter* **2012**, *8* (36), 9356 DOI: 10.1039/c2sm25606a.

(156) Mai, S.; Fairclough, J. P. A.; Hamley, I. W.; Matsen, M. W.; Denny, R. C.; Liao, B.;

Booth, C.; Ryan, A. J. Order - Disorder Transition in Poly (Oxyethylene) - Poly (Oxybutylene) Diblock Copolymers. *Macromolecules* **1996**, *29* (19), 6212–6221.
(157) Thelen, J. L.; Teran, A. A.; Wang, X.; Garetz, B. A.; Nakamura, I.; Wang, Z.-G.; Balsara, N. P. Phase Behavior of a Block Copolymer/Salt Mixture through the Order-to-Disorder Transition. *Macromolecules* **2014**, *47* (8), 2666–2673 DOI: 10.1021/ma500292n.
(158) Irwin, M. T.; Hickey, R. J.; Xie, S.; So, S.; Bates, F. S.; Lodge, T. P. Structure-Conductivity Relationships in Ordered and Disordered Salt-Doped Diblock Copolymer/Homopolymer Blends. *Macromolecules* **2016**, *49* (18), 6928–6939 DOI: 10.1021/acs.macromol.6b01553.
(159) Medapuram, P.; Glaser, J.; Morse, D. C. Universal Phenomenology of Symmetric Diblock Copolymers near the Order-Disorder Transition. *Macromolecules* **2015**, *48* (3), 819–839 DOI: 10.1021/ma5017264.
(160) Hamley, I. W.; Gehlsen, M. D.; Khandpur, A. K.; Koppi, K. A.; Rosedale, J. H.; Schulz, M. F.; Bates, F. S.; Almdal, K.; Mortensen, K. Complex Layered Phases Asymmetric Copolymers. *J. Phys. II Fr.* **1994**, *4* (12), 2161–2186 DOI: https://doi.org/10.1051/jp2:1994254.
(161) Karim, A.; Singh, N.; Sikka, M.; Bates, F. S.; Dozier, W. D.; Felcher, G. P. Ordering in Asymmetric Poly (Ethylene–Propylene)–Poly (Ethylethylene) Diblock Copolymer Thin Films. *J. Chem. Phys.* **1994**, *100* (2), 1620 DOI: 10.1063/1.466589.
(162) Floudas, G.; Vazaiou, B.; Schipper, F.; Ulrich, R.; Wiesner, U.; Iatrou, H.; Hadjichristidis, N. Poly(Ethylene Oxide-b-Isoprene) Diblock Copolymer Phase Diagram. *Macromolecules* **2001**, *34* (9), 2947–2957 DOI: 10.1021/ma001957p.
(163) Gillard, T. M.; Lee, S.; Bates, F. S. Dodecagonal Quasicrystalline Order in a Diblock Copolymer Melt. *Proc. Natl. Acad. Sci.* **2016**, *11* (5), 201601692 DOI: 10.1073/pnas.1601692113.
(164) Adams, J.; Quiram, D. Ordering Dynamics of Compositionally Asymmetric Styrene-Isoprene Block Copolymers. … **1996**, *29* (8), 2929–2938 DOI: 10.1021/ma951261+.
(165) Listak, J.; Jakubowski, W.; Mueller, L.; Plichta, A.; Matyjaszewski, K.; Bockstaller, M. R. Effect of Symmetry of Molecular Weight Distribution in Block Copolymers on Formation of "Metastable" Morphologies. *Macromolecules* **2008**, *41* (15), 5919–5927 DOI: 10.1021/ma800816j.
(166) Yuan, R.; Teran, A. A.; Gurevitch, I.; Mullin, S. A.; Wanakule, N. S.; Balsara, N. P. Ionic Conductivity of Low Molecular Weight Block Copolymer Electrolytes. *Macromolecules* **2013**, *46* (3), 914–921 DOI: 10.1021/ma3024552.
(167) Hexemer, A.; Bras, W.; Glossinger, J.; Schaible, E.; Gann, E.; Kirian, R.; MacDowell, A.; Church, M.; Rude, B.; Padmore, H. A SAXS/WAXS/GISAXS Beamline with Multilayer Monochromator. In *Journal of Physics: Conference Series*; 2010; Vol. 247, pp 1–11.
(168) Ilavsky, J. Nika: Software for Two-Dimensional Data Reduction. *J. Appl. Crystallogr.* **2012**, *45* (2), 324–328 DOI: 10.1107/S0021889812004037.
(169) Kremer, J. R.; Mastronarde, D. N.; McIntosh, J. R. Computer Visualization of Three-Dimensional Image Data Using IMOD. *J. Struct. Biol.* **1996**, *116* (1), 71–76 DOI: 10.1006/jsbi.1996.0013.
(170) Mastronarde, D. N. Dual-Axis Tomography: An Approach with Alignment Methods That Preserve Resolution. *J. Struct. Biol.* **1997**, *120* (3), 343–352 DOI: 10.1006/jsbi.1997.3919.
(171) Mastronarde, D. N.; Held, S. R. Automated Tilt Series Alignment and Tomographic Reconstruction in IMOD. *J. Struct. Biol.* **2017**, *197* (2), 102–113 DOI:

10.1016/j.jsb.2016.07.011.
(172) Irwin, M. T.; Hickey, R. J.; Xie, S.; Bates, F. S.; Lodge, T. P. Lithium Salt-Induced Microstructure and Ordering in Diblock Copolymer/Homopolymer Blends. *Macromolecules* **2016**, *49* (13), 4839–4849 DOI: 10.1021/acs.macromol.6b00995.
(173) Chintapalli, M.; Le, T. N. P.; Venkatesan, N. R.; Mackay, N. G.; Rojas, A. A.; Thelen, J. L.; Chen, X. C.; Devaux, D.; Balsara, N. P. Structure and Ionic Conductivity of Polystyrene- Block -Poly(Ethylene Oxide) Electrolytes in the High Salt Concentration Limit. *Macromolecules* **2016**, *49* (5), 1770–1780 DOI: 10.1021/acs.macromol.5b02620.
(174) Muller-Plathe, F.; van Gunsterene, W. F. Computer Simulation of a Polymer Electrolyte: Lithium Iodide in Amorphouse Poly(Ethylene Oxide). *J. Chem. Phys.* **1995**, *103* (11), 4745–4756 DOI: 10.1063/1.2400221.
(175) Borodin, O.; Smith, G. D. Mechanism of Ion Transport in Amorphous Poly(Ethylene Oxide)/ LiTFSI from Molecular Dynamics Simulations. *Macromolecules* **2006**, *39* (4), 1620–1629 DOI: 10.1021/ma052277v.
(176) Ganesan, V.; Pyramitsyn, V.; Bertoni, C.; Shah, M. Mechanisms Underlying Ion Transport in Lamellar Block Copolymer Membranes. *ACS Macro Lett.* **2012**, *1* (4), 513–518 DOI: 10.1021/mz300051x.
(177) Qin, J.; de Pablo, J. J. Ordering Transition in Salt-Doped Diblock Copolymers. *Macromolecules* **2016**, *49* (9), 3630–3638 DOI: 10.1021/acs.macromol.5b02643.
(178) Singh, M.; Odusanya, O.; Wilmes, G. M.; Eitouni, H. B.; Gomez, E. D.; Patel, a J.; Chen, V. L.; Park, M. J.; Fragouli, P.; Iatrou, H.; Hadjichristidis, N.; Cookson, D.; Balsara, N. P. Effect of Molecular Weight on the Mechanical and Electrical Properties of Block Copolymer Electrolytes. *Macromolecules* **2007**, *40* (13), 4578–4585 DOI: 10.1021/ma0629541.
(179) Hallinan, D. T.; Balsara, N. P. Polymer Electrolytes. *Annu. Rev. Mater. Res* **2013**, *43*, 503–525 DOI: 10.1146/annurev-matsci-071312-121705.
(180) Matsen, M. W.; Schick, M. Stable and Unstable Phases of a Diblock Copolymer Melt. *Phys. Rev. Lett.* **1994**, *72* (16), 2660–2663 DOI: 10.1103/PhysRevLett.72.2660.
(181) Epps, T. H.; Bailey, T. S.; Waletzko, R.; Bates, F. S. Phase Behavior and Block Sequence Effects in Lithium Perchlorate-Doped Poly (Isoprene- b -Styrene- b -Ethylene Oxide) and Poly (Styrene- b -Isoprene- b -Ethylene Oxide) Triblock Copolymers. *Macromolecules* **2003**, *36* (8), 2873–2881.
(182) Sing, C. E.; Olvera De La Cruz, M. Polyelectrolyte Blends and Nontrivial Behavior in Effective Flory-Huggins Parameters. *ACS Macro Lett.* **2014**, *3* (8), 698–702 DOI: 10.1021/mz500202n.
(183) Ren, C. L.; Nakamura, I.; Wang, Z. G. Effects of Ion-Induced Cross-Linking on the Phase Behavior in Salt-Doped Polymer Blends. *Macromolecules* **2016**, *49* (1), 425–431 DOI: 10.1021/acs.macromol.5b02229.
(184) Sing, C. E.; Zwanikken, J. W.; Olvera De La Cruz, M. Ion Correlation-Induced Phase Separation in Polyelectrolyte Blends. *ACS Macro Lett.* **2013**, *2* (11), 1042–1046 DOI: 10.1021/mz400511r.
(185) Chintapalli, M.; Timachova, K.; Olson, K. R.; Mecham, S. J.; Devaux, D.; DeSimone, J. M.; Balsara, N. P. Relationship between Conductivity, Ion Diffusion, and Transference Number in Perfluoropolyether Electrolytes. *Macromolecules* **2016**, acs.macromol.6b00412 DOI: 10.1021/acs.macromol.6b00412.
(186) Wang, X.; Chintapalli, M.; Newstein, M. C.; Balsara, N. P.; Garetz, B. A. Characterization

of a Block Copolymer with a Wide Distribution of Grain Sizes. *Macromolecules* **2016**, *49* (21), 8198–8208 DOI: 10.1021/acs.macromol.6b01380.
(187) Wang, X.; Li, X.; Loo, W.; Newstein, M. C.; Balsara, N. P.; Garetz, B. A. Depolarized Scattering from Block Copolymer Grains Using Circularly Polarized Light. *Macromolecules* **2017**, *50* (13), 5122–5131 DOI: 10.1021/acs.macromol.7b01048.
(188) Balsara, N. P.; Perahia, D.; Safinya, C. R.; Tirrell, M. V.; Lodge, T. P. Birefringence Detection of the Order-to-Disorder Transition in Block Copolymer Liquids. *Macromolecules* **1992**, *25* (15), 3896–3901 DOI: 10.1021/ma00041a011.
(189) Wang, X.; Thelen, J. L.; Teran, A. A.; Chintapalli, M.; Nakamura, I.; Wang, Z. G.; Newstein, M. C.; Balsara, N. P.; Garetz, B. A. Evolution of Grain Structure during Disorder-to-Order Transitions in a Block Copolymer/Salt Mixture Studied by Depolarized Light Scattering. *Macromolecules* **2014**, *47* (16), 5784–5792 DOI: 10.1021/ma501166p.
(190) Teran, A. A.; Mullin, S. A.; Hallinan, D. T.; Balsara, N. P. Discontinuous Changes in Ionic Conductivity of a Block Copolymer Electrolyte through an Order-Disorder Transition. *ACS Macro Lett.* **2012**, *1* (2), 305–309 DOI: 10.1021/mz200183t.
(191) Balsara, N. P.; Garetz, B. a.; Dai, H. J. Relationship between Birefringence and the Structure of Ordered Block Copolymer Materials. *Macromolecules* **1992**, *25* (22), 6072–6074 DOI: 10.1021/ma00048a036.
(192) Grzywacz, P.; Qin, J.; Morse, D. C. Renormalization of the One-Loop Theory of Fluctuations in Polymer Blends and Diblock Copolymer Melts. *Phys. Rev. E - Stat. Nonlinear, Soft Matter Phys.* **2007**, *76* (6), 1–33 DOI: 10.1103/PhysRevE.76.061802.
(193) Morse, D. C.; Chung, J. K. On the Chain Length Dependence of Local Correlations in Polymer Melts and a Perturbation Theory of Symmetric Polymer Blends. *J. Chem. Phys.* **2009**, *130* (22), 224902–284902 DOI: 10.1063/1.3108460.
(194) Spencer, R. K. W.; Matsen, M. W. Critical Point of Symmetric Binary Homopolymer Blends. *Macromolecules* **2016**, *49* (16), 6116–6125 DOI: 10.1021/acs.macromol.6b01437.
(195) Shultz, A. R.; Flory, P. J. Phase Equilibria in Polymer-Solvent Systems1,2. *J. Am. Chem. Soc.* **1952**, *74*, 4760−4767.
(196) Bae, Y. C.; Shim, J. J.; Soane, D. S.; Prausnitz, J. M. Representation of Vapor–Liquid and Liquid–Liquid Equilibria for Binary Systems Containing Polymers: Applicability of an Extended Flory–Huggins Equation. *J. Appl. Polym. Sci.* **1993**, *47* (7), 1193–1206 DOI: 10.1002/app.1993.070470707.
(197) Khandpur, A. K.; Förster, S.; Bates, F. S.; Hamley, I. W.; Ryan, A. J.; Bras, W.; Almdal, K.; Mortensen, K. Polyisoprene-Polystyrene Diblock Copolymer Phase Diagram near the Order-Disorder Transition. *Macromolecules* **1995**, *28* (26), 8796–8806 DOI: 10.1021/ma00130a012.
(198) Helfand, E.; Tagami, Y. Theory of the Interface between Immiscible Polymers. II. *J. Chem. Phys.* **1972**, *56* (7), 3592–3601 DOI: 10.1063/1.1677735.
(199) Helfand, E. Theory of Unsymmetric Polymer–Polymer Interfaces. *J. Chem. Phys.* **1975**, *62* (4), 1327 DOI: 10.1063/1.430632.
(200) Eitouni, H. B.; Balsara, N. P. CHAPTER 19 Thermodynamics of Polymer Blends. *Phys. Prop. Polym. Handb. 2e* **2006**, 339–356 DOI: 10.1007/978-0-387-69002-5_19.
(201) Mizushima, K.; Jones, P. C.; Wiseman, P. J.; Goodenough, J. B. LixCoO 2 (0<x<1): A New Cathode Material for Batteries of High Energy Density. *Mat. Res. Bull* **1980**, *15* (6), 783–789.
(202) Morris, M. A.; An, H.; Lutkenhaus, J. L.; Epps, T. H. Harnessing the Power of Plastics:

Nanostructured Polymer Systems in Lithium-Ion Batteries. *ACS Energy Letters*. 2017, pp 1919–1936.
(203) Miller, T. F.; Wang, Z. G.; Coates, G. W.; Balsara, N. P. Designing Polymer Electrolytes for Safe and High Capacity Rechargeable Lithium Batteries. *Acc. Chem. Res.* **2017**, *50* (3), 590–593 DOI: 10.1021/acs.accounts.6b00568.
(204) Glynos, E.; Petropoulou, P.; Mygiakis, E.; Nega, A. D.; Pan, W.; Papoutsakis, L.; Giannelis, E. P.; Sakellariou, G.; Anastasiadis, S. H. Leveraging Molecular Architecture To Design New, All-Polymer Solid Electrolytes with Simultaneous Enhancement in Modulus and Ionic Conductivity. *Macromolecules* **2018**, *51* (7), 2542–2550 DOI: 10.1021/acs.macromol.7b02394.
(205) Sanchez, I. C. Relationships between Polymer Interaction Parameters. *Polymer (Guildf).* **1989**, *30* (3), 471–475 DOI: 10.1016/0032-3861(89)90016-5.
(206) Bates, F. S.; Muthukumar, M.; Wignall, G. D.; Fetters, L. J. Thermodynamics of Isotopic Polymer Mixtures: Significance of Local Structural Symmetry. *J. Chem. Phys.* **1988**, *89* (1), 535–544 DOI: 10.1063/1.455442.
(207) Nedoma, A. J.; Lai, P.; Jackson, A.; Robertson, M. L.; Wanakule, N. S.; Balsara, N. P. Phase Diagrams of Blends of Polyisobutylene and Deuterated Polybutadiene as a Function of Chain Length. *Macromolecules* **2011**, *44* (8), 3077–3084 DOI: 10.1021/ma200258w.
(208) Ellison, C. J.; Meuler, A. J.; Qin, J.; Evans, C. M.; Wolf, L. M.; Bates, F. S. Bicontinuous Polymeric Microemulsions from Polydisperse Diblock Copolymers †. *J. Phys. Chem. B* **2009**, *113* (12), 3726–3737 DOI: 10.1021/jp807343b.
(209) Meuler, A. J.; Ellison, C. J.; Qin, J.; Evans, C. M.; Hillmyer, M. A.; Bates, F. S. Polydispersity Effects in Poly(Isoprene-b-Styrene-b-Ethylene Oxide) Triblock Terpolymers. *J. Chem. Phys.* **2009**, *130* (23), 234903 DOI: 10.1063/1.3140205.
(210) Nakamura, I. Ion Solvation in Polymer Blends and Block Copolymer Melts: Effects of Chain Length and Connectivity on the Reorganization of Dipoles. *J. Phys. Chem. B* **2014**, *118* (21), 5787–5796 DOI: 10.1021/jp502987a.
(211) Liu, L.; Nakamura, I. Solvation Energy of Ions in Polymers: Effects of Chain Length and Connectivity on Saturated Dipoles near Ions. *J. Phys. Chem. B* **2017**, *121* (14), 3142–3150 DOI: 10.1021/acs.jpcb.7b00671.
(212) Nakamura, I. Effects of Dielectric Inhomogeneity and Electrostatic Correlation on the Solvation Energy of Ions in Liquids. *J. Phys. Chem. B* **2018**, *122* (22), 6064–6071 DOI: 10.1021/acs.jpcb.8b01465.
(213) Nakamura, I.; Wang, Z. G. Thermodynamics of Salt-Doped Block Copolymers. *ACS Macro Lett.* **2014**, *3* (8), 708–711 DOI: 10.1021/mz500301z.
(214) Thelen, J. L.; Wang, A. A.; Chen, X. C.; Jiang, X.; Schaible, E.; Balsara, N. P. Correlations between Salt-Induced Crystallization, Morphology, Segmental Dynamics, and Conductivity in Amorphous Block Copolymer Electrolytes. *Macromolecules* **2018**, *51* (5), 1733–1740 DOI: 10.1021/acs.macromol.7b02415.
(215) Matsen, M. W.; Bates, F. S. Conformationally Asymmetric Block Copolymers. *J. Polym. Sci. Part B Polym. Phys.* **1997**, *35* (6), 945–952 DOI: 10.1002/(SICI)1099-0488(19970430)35:6<945::AID-POLB9>3.0.CO;2-G.
(216) Zhang, W.; Huang, M.; Abdullatif, S. al; Chen, M.; Shao-Horn, Y.; Johnson, J. A. Reduction of (Meth)Acrylate-Based Block Copolymers Provides Access to Self-Assembled Materials with Ultrasmall Domains. *Macromolecules* **2018**, *51* (17), 6757–6763 DOI: 10.1021/acs.macromol.8b01588.

(217) Jung, H. Y.; Kim, S. Y.; Kim, O.; Park, M. J. Effect of the Protogenic Group on the Phase Behavior and Ion Transport Properties of Acid-Bearing Block Copolymers. *Macromolecules* **2015**, *48* (17), 6142–6152 DOI: 10.1021/acs.macromol.5b01237.
(218) Fredrickson, G. H.; Helfand, E. Fluctuation Effects in the Theory of Microphase Separation in Block Copolymers. *J. Chem. Phys.* **1987**, *87* (1), 697–705 DOI: 10.1063/1.453566.
(219) Zardalidis, G.; Ioannou, E. F.; Gatsouli, K. D.; Pispas, S.; Kamitsos, E. I.; Floudas, G. Ionic Conductivity and Self-Assembly in Poly(Isoprene- b -Ethylene Oxide) Electrolytes Doped with LiTf and EMITf. *Macromolecules* **2015**, *48* (5), 1473–1482 DOI: 10.1021/acs.macromol.5b00089.
(220) Loo, W. S.; Balsara, N. P. Organizing Thermodynamic Data Obtained from Multicomponent Polymer Electrolytes: Salt-containing Polymer Blends and Block Copolymers. *J. Polym. Sci. Part B Polym. Phys.* **2019**, *57* (18), 1177–1187 DOI: 10.1002/polb.24800.
(221) Marko, J.; Rabin, Y. Microphase Separation of Charged Diblock Copolymers: Melts and Solutions. *Macromolecules* **1992**, *25*, 1503–1509.
(222) Mao, G.; Saboungi, M. L.; Price, D. L.; Armand, M. B.; Howells, W. S. Structure of Liquid PEO-LiTFSI Electrolyte. *Phys. Rev. Lett.* **2000**, *84* (24), 5536–5539 DOI: 10.1103/PhysRevLett.84.5536.
(223) Annis, B. K.; Kim, M. H.; Wignall, G. D.; Borodin, O.; Smith, G. D. Study of the Influence of LiI on the Chain Conformations of Poly(Ethylene Oxide) in the Melt by Small-Angle Neutron Scattering and Molecular Dynamics Simulations. *Macromolecules* **2000**, *33* (20), 7544–7548 DOI: 10.1021/ma000452w.
(224) Glinka, C. J.; Barker, J. G.; Hammouda, B.; Krueger, S.; Moyert, J. J.; Orts, W. J. The 30 m Small-Angle Neutron Scattering Instruments at the National Institute of Standards and Technology. *J. Appl. Crystallogr.* **1998**, *31* (3), 430–445 DOI: 10.1107/S0021889897017020.
(225) Kline, S. R. Reduction and Analysis of SANS and USANS Data Using IGOR Pro. *J. Appl. Crystallogr.* **2006**, *39* (6), 895–900 DOI: 10.1107/S0021889806035059.
(226) Balsara, N. P.; Lohse, D. J.; Graessley, W. W.; Krishnamoorti, R. Small-Angle Neutron Scattering by Partially Deuterated Polymers and Their Blends. *J. Chem. Phys.* **1994**, *100* (5), 3905–3910 DOI: 10.1063/1.466325.
(227) Akcasu, A. Z.; Tombakoglu, M. Dynamics of Copolymer and Homopolymer Mixtures in Bulk and in Solution via the Random Phase Approximation. *Macromolecules* **1990**, *23* (2), 607–612 DOI: 10.1021/ma00204a038.
(228) Benoit, H.; Benmouna, ·7 M; Wu, W.-L. Static Scattering from Multicomponent Polymer and Copolymer Systems. *Macromolecules* **1990**, *23*, 1511–1517 DOI: 10.1021/ma00207a045.
(229) Marcus, Y.; Hefter, G. Standard Partial Molar Volumes of Electrolytes and Ions in Nonaqueous Solvents. *Chem. Rev.* **2004**, *104* (7), 3405–3452 DOI: 10.1021/cr030047d.
(230) Smith, J. M.; Van Ness, H. C.; Abbot, M. *Introduction to Chemical Engineering Thermodynamics*, 7th ed.; McGraw-Hill Education: New York, 2004.
(231) Kirste, R. G.; Kruse, W. A.; Ibel, K. Determination of the Conformation of Polymers in the Amorphous Solid State and in Concentrated Solution by Neutron Diffraction. *Polymer (Guildf).* **1975**, *16*, 120–124.
(232) Kratky, O. Possibilities of X-Ray Small Angle Analysis in the Investigation of Dissolved

and Solid High Polymer Substances. *Pure Appl. Chem.* **1966**, *12* (1–4), 483–524 DOI: 10.1351/pac196612010483.
(233) Crist, B.; Wignall, G. D. Small-Angle Neutron Scattering Studies of Chain Conformation in Semicrystalline Hydrogenated Polybutadiene. *J. Appl. Crystallogr.* **1988**, *21* (6), 701–706 DOI: 10.1107/S0021889888006818.
(234) Hammouda, B. SANS from Homogeneous Polymer Mixtures: A Unified Overview. *Adv. Polym. Sci.* **1993**, *106*, 86–133 DOI: 10.1007/bfb0025862.
(235) Garetz, B. A.; Balsara, N. P.; Dai, H. J.; Wang, Z.; Newstein, M. C.; Majumdar, B. Orientation Correlations in Lamellar Block Copolymers. *Macromolecules* **1996**, *29* (13), 4675–4679 DOI: 10.1021/ma9600724.
(236) Beaucage, G. Small-Angle Scattering from Polymeric Mass Fractals of Arbitrary Mass-Fractal Dimension. *J. Appl. Cryst* **1996**, *29*, 134–146.
(237) Bushell, G.; Amal, R. Measurement of Fractal Aggregates of Polydisperse Particles Using Small- Angle Light Scattering. *J. Colloid Interface Sci.* **2000**, *221* (2), 186–194 DOI: 10.1006/jcis.1999.6532.
(238) Hayamizu, K.; Sugimoto, K.; Akiba, E.; Aihara, Y.; Bando, T.; Price, W. S. An NMR and Ionic Conductivity Study of Ion Dynamics in Liquid Poly(Ethylene Oxide)-Based Electrolytes Doped with LiN(SO2CF3)2. *J. Phys. Chem. B* **2002**, *106* (3), 547–554 DOI: 10.1021/jp013035+.
(239) Galluzzo, M. D.; Maslyn, J. A.; Shah, D. B.; Balsara, N. P. Ohm's Law for Ion Conduction in Lithium and beyond-Lithium Battery Electrolytes. *J. Chem. Phys.* **2019**, *151* (2), 20901 DOI: 10.1063/1.5109684.
(240) Timachova, K.; Watanabe, H.; Balsara, N. P. Effect of Molecular Weight and Salt Concentration on Ion Transport and the Transference Number in Polymer Electrolytes. *Macromolecules* **2015**, *48* (21), 7882–7888 DOI: 10.1021/acs.macromol.5b01724.
(241) Becher, M.; Becker, S.; Hecht, L.; Vogel, M. From Local to Diffusive Dynamics in Polymer Electrolytes: NMR Studies on Coupling of Polymer and Ion Dynamics across Length and Time Scales. *Macromolecules* **2019**, *52* (23), 9128–9139 DOI: 10.1021/acs.macromol.9b01400.
(242) Devaux, D.; Bouchet, R.; Glé, D.; Denoyel, R. Mechanism of Ion Transport in PEO/LiTFSI Complexes: Effect of Temperature, Molecular Weight and End Groups. *Solid State Ionics* **2012**, *227*, 119–127 DOI: 10.1016/j.ssi.2012.09.020.
(243) Hasan, N.; Pulst, M.; Samiullah, M. H.; Kressler, J. Comparison of Li+-Ion Conductivity in Linear and Crosslinked Poly(Ethylene Oxide). *J. Polym. Sci. Part B Polym. Phys.* **2019**, *57* (1), 21–28 DOI: 10.1002/polb.24750.
(244) Richter, B. D.; Ewzn, B. Neutron Spin-Echo Investigations on the Dynamics of Polymers. *Appl. Cryst* **1988**, *21*, 715–728 DOI: 10.1107/S002188988800487X.
(245) Azuah, R. T.; Kneller, L. R.; Qiu, Y.; Tregenna-Piggott, P. L. W.; Brown, C. M.; Copley, J. R. D.; Dimeo, R. M. DAVE: A Comprehensive Software Suite for the Reduction, Visualization, and Analysis of Low Energy Neutron Spectroscopic Data. *J. Res. Natl. Inst. Stand. Technol.* **2009**, *114* (6), 341 DOI: 10.6028/jres.114.025.
(246) De Gennes, P. G. Coherent Scattering by One Reptating Chain. *J. Phys.* **1981**, *42* (5), 735–740 DOI: 10.1051/jphys:01981004205073500.
(247) Niedzwiedz, K.; Wischnewski, A.; Pyckhout-Hintzen, W.; Allgaier, J.; Richter, D.; Faraone, A. Chain Dynamics and Viscoelastic Properties of Poly(Ethylene Oxide). *Macromolecules* **2008**, *41* (13), 4866–4872 DOI: 10.1021/ma800446n.

(248) Richter, D.; Farago, B.; Butera, R.; Fetters, L. J.; Huang, J. S.; Ewen, B. On the Origins of Entanglement Constraints. *Macromolecules* **1993**, *26* (4), 795–804 DOI: 10.1021/ma00056a034.
(249) Fetters, L. J.; Lohse, D. J.; Richter, D.; Witten, T. A.; Zirkel, A. Connection between Polymer Molecular Weight, Density, Chain Dimensions, and Melt Viscoelastic Properties. *Macromolecules*. 1994, pp 4639–4647.
(250) Wittmer, J.; Paul, W.; Binder, K. Rouse and Reptation Dynamics at Finite Temperatures: A Monte Carlo Simulation. *Macromolecules* **1992**, *25* (26), 7211–7219 DOI: 10.1021/ma00052a023.
(251) Lodge, T. P.; Dalvi, M. C. Mechanisms of Chain Diffusion in Lamellar Block Copolymers. *Phys. Rev. Lett.* **1995**, *75* (4), 657–660 DOI: 10.1103/PhysRevLett.75.657.
(252) Lodge, T. P.; Hamersky, M. W.; Milhaupt, J. M.; Kannan, R. M.; Dalvi, M. C.; Eastman, C. E. Diffusion in Microstructured Block Copolymer Melts. *Macromol. Symp.* **1997**, *121* (1), 219–233 DOI: 10.1002/masy.19971210119.
(253) Molinari, N.; Mailoa, J. P.; Kozinsky, B. Effect of Salt Concentration on Ion Clustering and Transport in Polymer Solid Electrolytes: A Molecular Dynamics Study of PEO-LiTFSI. *Chem. Mater.* **2018**, *30* (18), 6298–6306 DOI: 10.1021/acs.chemmater.8b01955.
(254) Brooks, D. J.; Merinov, B. V; Goddard, W. A.; Kozinsky, B.; Mailoa, J. Atomistic Description of Ionic Diffusion in PEO-LiTFSI: Effect of Temperature, Molecular Weight, and Ionic Concentration. *Macromolecules* **2018**, *51* (21), 8987–8995 DOI: 10.1021/acs.macromol.8b01753.
(255) Rubinstein, M.; Colby, R. H. *Polymer Physics*; Oxford University Press: Oxford, U.K., 2003.
(256) Gribble, D. A.; Frenck, L.; Shah, D. B.; Maslyn, J. A.; Loo, W. S.; Mongcopa, K. I. S.; Pesko, D. M.; Balsara, N. P. Comparing Experimental Measurements of Limiting Current in Polymer Electrolytes with Theoretical Predictions. *J. Electrochem. Soc.* **2019**, *166* (14), A3228–A3234 DOI: 10.1149/2.0391914jes.
(257) Pesko, D. M.; Feng, Z.; Sawhney, S.; Newman, J.; Srinivasan, V.; Balsara, N. P. Comparing Cycling Characteristics of Symmetric Lithium-Polymer-Lithium Cells with Theoretical Predictions. *J. Electrochem. Soc.* **2018**, *165* (13), A3186–A3194 DOI: 10.1149/2.0921813jes.

Appendix A1. RSoXS Running Manual

Beamline 11.0.1.2 provides an excellent user manual to the beamline, which should be read thoroughly before beamtime and consulted frequently during beamtime. These notes serve to supply specific details about conducting RSoXS experiments on air-free samples as well as provide a few details that are not in the user manual.

A1.1 Sample Preparation

RSoXS samples are typically thin film polymer membranes that have been drop-cast from solution on to silicon nitride (Si_3N_4) windows. A few tips for the most successful sample preparation:

- If possible, use tweezers with rubber tips when handing Si_3N_4 windows. They break very easily.
- Purchase Si_3N_4 windows with smaller windows for easier handling inside of the glovebox and create more uniform films. The frame should be 5x5 mm in dimensions and the window can be between 1x1 mm and 1.5x1.5 mm in dimensions. The smaller the window, the larger the exposed frame area, and the easier the window is to handle.
- The most uniform films were achieved by pre-treating the Si_3N_4 windows in an ozone chamber for 15 minutes. The ALS chemistry labs have one that can be used.
- Use double sided carbon tape to stick the window frames to the stage. If using the heat stage, secure the windows with double sided copper tape to allow for heat conduction to the samples.
- Pre-load the windows on to the stage outside of the glovebox. The windows can be pre-treated once attached to the stage as well. This eliminates the need to handle individual windows inside of the glovebox. Ensure the windows are far apart enough to drop-cast solution, but within the range of usable stage at the beamline. If you need extra space, consider getting an extra stage made at the machine shop to use for sample prep.
- Create a sample map of the stage prior to drop-casting samples. Use the asymmetries of the stage to orient the samples. Once the samples are drop-cast, it is impossible to distinguish them from one another.
- NMP wets the Si_3N_4 windows better than THF. Thin films cast from NMP solutions appear more uniform in surface roughness compared to those cast from THF solutions.
- Films can be as thick as 1-2 microns for scattering experiments. By assuming the film will cover the entire window area, one can approximate the thickness of the resulting film based on the polymer concentration of the solution and the volume of solution used.
- At most, 4 μL of solution should be drop-cast on to the Si_3N_4 window at a time. For best results, place the pipette tip in one of the corners of the window and release the solution from the pipette only until the first “click”. Fully expunging the pipette of solution will also release Ar from the pipette tip which can disturb the solution.
- If thicker films are desired that what can be created with 4 μL of solution, repeat the drop-cast procedure two to three times after allowing all of the visible solution to be evaporated from the window (approximately 10-15 min on a hotplate at 120 °C). After sufficient

material has been drop-cast to the window, the thin films can go into the glovebox antechamber for annealing.

- Lightly press on the frames of all of the samples before moving into the glovebox antechamber for annealing. The initial evacuation is intense, and the samples can move or become disconnected from the stage if not secured tightly.
- Use a beaker to secure the stage inside of the antechamber. Anneal the samples for as long as possible, preferably 3-5 days at 160 °C. Make sure there is enough time to do a controlled cooling to RT under vacuum, approximately 12 hours.
- Visibly inspect all of the samples and compare with the sample map immediately after removing the stage from the antechamber.

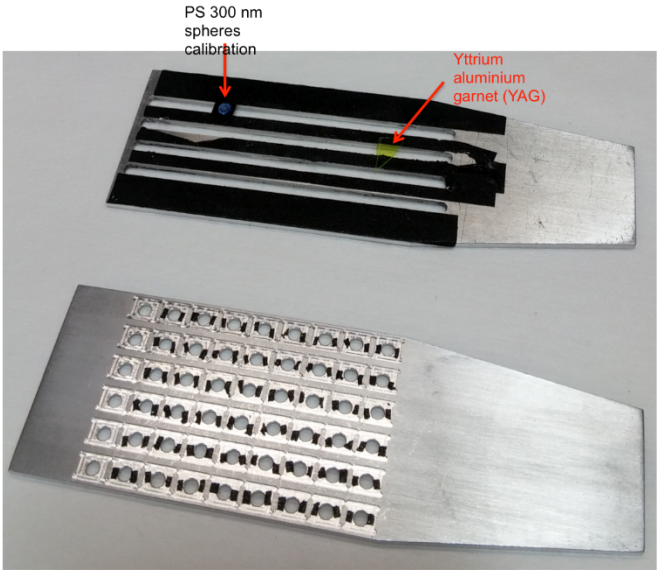

Figure A.1.1 Sample Stages Provided by 11.0.1.2: Example of two sample stages provided by 11.0.1.2 beamline scientists with an example PS 300 nm spheres calibration and piece of YAG.

A1.2 Transferring Samples to the Beamline

Unfortunately, the transfer process of the samples from the glovebox to the beamline cannot happen in completely air-free environments. Therefore, it is extremely important to be prepared while doing the sample transfer:

- Bring your calibration samples (ordered block copolymers, PS spheres of known size, etc.), blank pre-treated Si_3N_4 window, and a piece of yttrium aluminum garnet (YAG) into the glovebox. Place the standards, blank window and YAG on the sample stage and add them to the sample map.
- Bring a large desiccator into the glovebox and place the sample stage inside of it. Secure the lid and bring the whole desiccator to the beamline.
- Vent the sample chamber at the beamline. Do not open the desiccator until the sample chamber is vented.

- Open the desiccator and quickly transfer the sample stage into the sample chamber. Pump down the sample chamber as quickly as possible. If using the heat stage, secure the plug into the adaptor present within the sample chamber.
- Again, the evacuation of the sample chamber is intense. Make sure all of the samples are secured to the stage prior to inserting into the desiccator in the glovebox.

A1.3 Running Experiments

There are two types of experiments to run Beamline 11.0.1.2: NEXAFS and scattering experiments. NEXAFS experiments can be run in two detection modes: Transmission and Total Electron Yield (TEY). Transmission detection is more suited for thicker samples and provides information on the sample transmission to determine if the samples are too thick. Scattering experiments, called "CCD Scan" in the LabView program, are extremely similar to SAXS experiments conducted elsewhere, although there is the option to collect scattering profiles as a function of incident beam energy. Some useful tips for data acquisition:

- NEXAFS experiments are used to determine suitable energies for conducting scattering experiments. This means a NEXAFS spectra should typically be taken for each sample with a different chemical structure or chemical components. In theory, the NEXAFS spectra for a given copolymer of different molecular weights or compositions will have the same peaks as these samples contain the same chemical structure. Note, peak intensity will change with copolymer composition.
- NEXAFS experiments are also used to calculate the absolute scattering intensity of the sample. At each given energy, NEXAFS spectra should be taken of the blank window and the direct beam to calibrate the beam intensity.
- If running absolute scattering intensity, a NEXAFS scan of each sample is needed in addition to calibrate the scattering intensity.
- CCD Scan collects the scattering data. This should be done for every sample at the energy range identified from the NEXAFS scans. Note, the optimal exposure time for a sample at a given energy is inversely proportional to the NEXAFS intensity. Run a few test CCD scan experiments to make sure the exposure time isn't too high and will not oversaturate the detector.
- Collect a CCD Scan for dark images (no beam) at all exposure times used. Often times, it's easiest to do this first, for a wide window of exposure times.
- Conduct all experiments, NEXAFS and CCD Scan, in a given energy range (Carbon K-edge, for example) before moving to the next energy range (Nitrogen K-edge, for example). Often times the beam will "move" if the incident beam energy is change drastically and it will be hard to re-gain the exact beam properties (i.e., sharpness, intensity, placement).
- It's possible to write scripts in Excel (.csv or .txt. formats) to automate the energy scans and exposure times for both NEXAFS and CCD Scan experiments. The scripts can be saved on the beamline computer and used at all future beamtimes as well. Refer to the Beamline User Manual on how to write scripts for each type of experiment.

- If one is not familiar with 2D scattering data, it is helpful to process the collected 2D data into 1D profiles through Igor at the beamline on the data reduction computer. The most time-efficient way of doing this is for two people to be present throughout the beamtime: one to run data acquisition and one to process the data.

A1.4 Reducing Scattering Data

The beamline provides an altered version of the Nika program to reduce RSoXS scattering data efficiently. They have an excellent data analysis manual that walks through the process of reducing scattering data correctly. A few tips:

- A separate Igor Program Files is provided to reduce RSoXS scattering data. This package relies on an older version of Nika. Therefore, it is useful to house two sets of Igor Program Files on your computer and only "call upon" the one needed when reducing RSoXS versus SAXS or SANS data.
- If you are not familiar with reducing 2D scattering patterns into 1D profiles in Nika prior to running RSoXS, it is prudent to learn on standard SAXS data first. This will help you understand what information is really necessary, e.g., absolute intensity, to provide you with the data that you need as well as some of the useful keyboard shortcuts in Igor.
- Use the quick key, "Ctrl+Y" or "Cmd+Y" to highlight the window preferences on a selected graph. This will allow you to rename the window of recently reduced data to an identifier. Then, when you go to reduce the next set of data, it will open up a new window to populate with 1D scattering profiles.

:

A1.5 Additional Notes

Here are additional notes that were gathered over the course of many nights on the beamline:

- Be extremely careful when in "camera mode" while you are viewing the sample stage. It is extremely easy to move the beam away from the cursor, and it is a huge pain to re-locate the beam. The YAG piece on the sample stage is used to "find" the beam.
- Often times the filename is not updated while collected NEXAFS data. It is important write down the five-digit number associated with each NEXAFS scan or it can become impossible to deconvolute the collected data after beamtime.
- Keep track of the photodiode reading at a given energy range. If it changes significantly throughout the course of experiments over a specific energy window, a new direct beam and blank NEXAFS scan will be needed to calibrate the scattering intensity.
- Sometimes the beam intensity changes drastically during beamtime. This is easy to track by keeping an eye on the photodiode reading while in the NEXAFS configuration or tracking the beamstop intensity while in the CCD Scan configuration. If this happens, adjust the mirrors upstream of the sample chamber to re-center and focus the beam. This usually requires opening the upstream slits to allow more of the beam into the sample chamber. Ask a beamline scientist how to do this before they abandon you for the night.

- If you plan to use a wide range of incident beam energies. Make sure the beam can "get" to all of the desired energies before the beamline scientist leaves you. Often times, more adjustments are needed, such as changing the slits and higher order suppressors, than simply changing the incident beam energy on LabView. Record the photodiode or beamstop reading that is achieved at these energy levels. When returning to these energies later, refer to the beamstop reading to make sure you are achieving the "best" possible incident beam profile.
- The beam physically moves if the incident beam energy changes drastically, say from the Carbon to the Fluorine K-edge. Record the position of the beamstop at each configuration. This will inform you how far the beam has moved. If you use the same x,y positions for CCD Scans at one energy, they will most likely not collect scattering at the same place on the sample at the other energy. If your films are uniform in thickness and composition, this shouldn't be an issue unless the beam is now off the sample window. However, this can cause problems if your films are rough and non-uniform. The best way to overcome this is to take CCD scan calibration images of well-ordered block copolymer to use while calibrating beam center and sample-to-detector distance in Igor. Then, create separate Igor calibrations for each energy range (i.e., Carbon, Oxygen, Fluorine). The intensities of the scattering profiles will change with energy, but the peak positions should remain at constant q-values due to the Bragg scattering.
- Always calculate the transmission of each sample and the blank window when reducing the data. It can be easy to miss a change in beam intensity during a long beamtime, and this serves as a good "sanity check" when comparing scattering intensities between samples.